THE UNIVERSITY
of EDINBURGH

Development and Utility of Magnetic Nanoparticles Production by Mammalian Cells

Lisa Lungaro

(BSc, MSc)

Doctor of Philosophy (PhD)

The University of Edinburgh

2017

To my husband Paolo, who left his job to follow my dreams, who supported me for all this time, who cooked my dinners when I was too tired and who made me happy even when outside it was raining and the experiments were difficult.

Thank you for believing in me.

Declaration

I hereby declare that:

a) This thesis has been composed by me.

b) The work presented in this thesis was carried out entirely by me or otherwise as stated below:

- The experiments measuring cellular hyperthermia in Chapter 3 and Chapter 4 were performed by Dr. Franca Albertini's group, Magnetic Materials Group IMEM-CNR in Parma, Italy.
- Superconducting Quantum Interference Devices (SQUID) measurements performed on MG63 cells in Chapter 3 were carried out by Dr. Marc Uhlarz, Dresden High Magnetic Field Laboratory (HLD-EMFL), Helmholtz-Zentrum Dresden-Rossendorf, Dresden, Germany.
- All the mice implantations and cullings described in Chapter 7 were undertaken by Mrs Morwenna Muir, Centre for Cancer Research, The University of Edinburgh, Edinburgh.

c) The work is submitted for the fulfilment of the degree of Doctor of Philosophy, and not for any other degree or professional qualification.

Lisa Lungaro

July 2017

Abstract

Magnetic hyperthermia (MH) is an anti-cancer treatment which exploits the heat produced by tumour-targeted magnetic nanoparticles (MNPs) subjected to an alternating magnetic field (AMF). A problem limiting the clinical use of MH, however, is the inability to adequately localise the MNPs at the tumour site. A cellular approach using mesenchymal stem cells (MSCs) as carriers has been proposed as these cells are believed to home to sites of tissue injury and tumour growth, however problems with MNPs uptake and toxicity retard progress and need to be overcome. The aim of this project was to find an alternative approach in MH treatment, creating engineered human MSCs able to biosynthesise MNPs. To achieve this goal, MSCs were transfected with either, or both, M. magneticum AMB-1 *mms6* and *mmsF* genes. M. magneticum AMB-1 is a genus of magnetotactic bacteria, containing magnetosomes, which are lipidic organelles containing single crystals of magnetite. M. magneticum-AMB1 *mms6* and *mmsF* genes are important for final crystal morphology and are known to play a role in crystal synthesis and growth respectively. The originality of this study was in using *mms6* and *mmsF* genes, which were codon-optimized for mammalian expression, alone or in combination, for transfection of human MSCs, which have known tumour homing capacity. The transfected MNPs-bearing MSCs, able to migrate into the tumour tissue, were subjected to AMF in MH experiments in an attempt to induce cancer cell death. *mms6* and *mmsF* gene expression, following transfection, was investigated in the human osteosarcoma cell line MG63 by reverse transcription polymerase chain reaction (RT-PCR). The cellular ultrastructure of transfected MG63 cells was investigated by transmission electron microscopy (TEM), revealing the presence of nanoparticles. The magnetism of transfected MG63 cells was proved by superconducting quantum interference device (SQUID) and supported by in vitro MH experiments. Then, human MSCs were transfected with *mms6* and *mmsF* genes, alone or in combination. The effect of transfection experiments and MNPs synthesis on MSCs markers of stemness, cell proliferation and differentiation ability were investigated. The MTB genes expression in human MSCs was assessed by RT-PCR

and cell magnetism was confirmed by SQUID, in vitro MH experiments and by magnetic force microscopy (MFM). Then, *in vitro* studies of MH were undertaken to establish whether *mms6* transfected MSCs expressing MNPs supported a MH effect when exposed to an AMF. Cells were initially exposed to an AMF of 565.3 kHz frequency in monolayers and in 3D arrangements and cell death/viability was assessed. Subsequently, the effect of the same AMF on 3D models of mixed populations of *mms6*-expressing MSCs and cancer cells was assessed. The results indicate that viability of MNPs-expressing MSCs and adjacent cancer cells is reduced following AMF exposure. *In vivo* studies of MH were undertaken following intracardiac injection of *mms6*-expressing MSCs in tumour-bearing mice (epidermoid carcinoma). The expression of *mms6*-expressing MSCs inside mice organs was confirmed by RT-PCR, fluorescence microscopy and immunohistochemistry. The effect of the application of an AMF of 565.3 kHz on mice tumours was studied with different techniques (tumour size and volume measurement, multiphoton microscopy, haematoxylin and eosin staining, and activated Caspase 3 expression), to understand if MNPs created inside *mms6*-expressing MSCs, following AMF exposure, could lead to cancer cell death. Results indicate that mice tolerate the treatment well, however no appreciable tumour reduction or necrosis was evident.

Overall the results suggest that *mms6* transfection alone confers the highest magnetisation to MSCs compared to *mmsF* alone or *mms6+mmsF* co-transfected, and that *mms6* expression in human MSCs does not have an adverse effect on important cell functions. *mms6*-expressing MSCs, when exposed to an AMF, show reduced viability and enhanced cell cytotoxicity in vitro. When co-cultured with cancer cells in 3D models *in vitro*, *mms6*-expressing MSCs are able to reduce viability of adjacent cancer cells confirming the potential applicability of *mms6*-expressing MSCs for MH treatment. *In vivo* proof of concept experiments show that *mms6*-expressing MSCs can locate to the tumour tissue, and *mms6*-expressing intracardiac injected MSCs mice exposed to AMF tolerate the treatment well. However, the number of *mms6*-expressing MSCs able to localize to the tumour tissue in this experiment was too low to give an appreciable tumour reduction, so more experiments are needed to enhance the experimental protocol. A number of

improvements are required to progress this novel technique towards clinical application. Gene transfection and MNPs production need to be optimised, the best frequency for MH needs to be established and MSCs delivery to the tumour has to be significantly increased to allow concentration of MNPs. The study has helped to increase our knowledge on the creation of magnetic human MSCs to potentially use these cells in MH cancer treatment.

Lay Summary

Magnetic hyperthermia (MH) is a new treatment for cancer, in which synthetic magnetic nanoparticles (MNPs) are delivered to the tumour. When the tumour is exposed to an alternating magnetic field (AMF), MNPs release heat and kill it. A problem limiting the clinical use of MH, however, is the inability to adequately localise the MNPs at the tumour site. A cellular approach using mesenchymal stem cells (MSCs) as carriers has been proposed as these cells are believed to home to sites of tissue injury and tumour growth, however problems with MNPs uptake and toxicity retard progress and need to be overcome.

Magnetotactic bacteria produce and contain crystals of magnetic iron. The mechanism by which these structures are created is becoming clear, and two genes, named *mms6* and *mmsF*, are particularly involved. The aim of this work was to establish whether it was possible to insert these bacterial genes into MSCs, to see whether these cells can produce MNPs and to establish whether they can be used for MH and killing of cancer cells. Following insertion of the genes into MSCs, I was able to show that the MSCs expressed the genes and formed MNPs, something they could not do without the genes. *mms6* appeared to be the best gene for producing MNPs, so it was chosen for the next experiments. Importantly, experiments suggested that the treatment used to express the *mms6* gene inside MSCs did not have adverse effects on the function of these cells.

Experiments in the laboratory demonstrated that the MNPs produced inside *mms6*-expressing MSCs were subsequently found to be heated and kill the MSCs when exposed to a magnetic field and, significantly, also tumour cells that were grown alongside the MSCs. However, when these MNPs bearing MSCs were injected in mice which had tumours, and then exposed to AMF, no significant evidence of tumour killing was seen.

Overall, results indicate that the *mms6* gene can be used to make MSCs produce MNPs without interfering with the function of these cells. Moreover, *mms6*-expressing MSCs and adjacent tumour cells are killed by AMF in laboratory

experiments. However, a similar effect could not be seen in live animals. A number of optimisations are required before it will be possible to use this novel technique for treating cancers in patients. These include improving the way the bacterial genes are expressed inside MSCs and the MSCs homing to tumour site, increasing the number of MNPs that are being made by MSCs and establishing with certainty the best form of AMF which produces the greatest magnetic hyperthermia effect.

Acknowledgements

I would like to express my sincere gratitude to my mentor Professor Donald Salter. He kindly guided me from the beginning to the end of my PhD with his precious advice, support, patience and immense knowledge.

I would also thank Professor Alistair Elfick for his support and for helping me to widen my research from various perspectives.

A special thank goes to Dr Asim Azfer, who was more than a bench tutor, but a Teacher of Life and has become a sincere friend. His passion for Science, his dedication to Biology and his kindness will always remain with me. Without his precious support it would not be possible to conduct this research. I could not have imagined having a better bench tutor for my Ph.D study.

I would also thank Helen Caldwell and Elein McClay for being always friendly and helpful. I will miss our fast food lunches.

Last but not least, I thank my fellow labmates: Natalia Harasymowicz, Dimitrios Tsikritsis, Micaela Rios Visconti and Kerans Fransiscus for all the fun and for the great time spent together.

Abbreviations

A431 ecad-GFP - Human squamous carcinoma e-cadherin GFP expressing

AC - Alternating Current

AFM - Atomic-force microscopy

ddH_20 - Distilled water

DMEM - Dulbecco's Modified Eagle's medium

DNA - Deoxyribonucleic Acid

FACS - Fluorescence-activated cell sorting

FBS- Fetal Bovine Serum

GFP- Green Fluorescent Protein

H&E - Hematoxylin & Eosin

HT - Hyperthermia

IF - Immunofluorescence

IHC- Immunohistochemistry

MFH - Magnetic Fluid Hyperthermia

MFM- magnetic force microscopy

MG63- Homo sapiens bone osteosarcoma

MH - Magnetic Hyperthermia

MHT - Magnetic Hyperthermia Therapy

MM - Magnetosomes Membrane

MNPs - Magnetic nanoparticles

MSCs - Mesenchymal stem cells

MTB- Magnetotactic Bacteria

O/N-overnight

P/S - Penicillin/Streptomycin

PBS- Phosphate buffered saline

RNA - Ribonucleic Acid

ROS - Reactive Oxygen Species

RT-PCR- Reverse transcription polymerase chain reaction

SHP -Specific Heating Power

SOD - Superoxide Dismutase

SQUID - Superconducting Quantum Interference Device

TEM - Transmission Electron Microscopy

TNF- Tumour Necrosis Factor

Contents

List of Figures

List of Tables

1. Introduction

1.1. Magnetic Hyperthermia

1.1.1. Magnetic Hyperthermia: a possible cancer therapy

Hyperthermia (HT) is a therapeutic tumour treatment which increases the temperature at the tumour site. The temperature raising changes the physiology of the tumour cells leading to selective death through apoptosis (Moy & Tunnell, 2017; Peeken et al., 2017; van Loo et al., 2002). Accordingly to the temperature values reached during the treatment, HT could be classified in three categories: diathermia, where temperature is lower than 41°C, typically employed for rheumatic diseases; moderate hyperthermia, which causes stress to the cells in the temperature range of 41–46 °C; and thermoablation, where the temperature goes up to 56 °C, causing cells necrosis (Kumar & Mohammad, 2011; Mallory et al., 2016).

Depending on the area of interest, HT treatments could also be grouped into local, regional, or whole body. Local HT refers to a delimited area of interest; regional HT considers a larger area, such as the whole organ; whereas in whole body HT the entire body is exposed to HT treatment, when metastasis occurs. Among all three treatments, local HT is the most studied due to the possibility to treat a defined area of the body (Habash et al., 2006; Toraya-Brown & Fiering, 2014).

After the HT treatment, several alterations occur in the cell, such as the reduction in the transmembrane transport, the destabilisation of the membrane potential and the changes in the structural proteins (Coss & Linnemans, 1996; Lepock, 2003; Moy & Tunnell, 2017). Furthermore, also the synthesis of the nucleic acid and the DNA repairing enzymes are affected by the temperature increase, altering the conformation of the DNA and leading to cell death (A. C. Silva et al., 2011).

In Magnetic Hyperthermia Therapy (MHT), the heating of the target tissue is obtained by injecting Magnetic Nanoparticles (MNPs) *in situ* and then exposing the body part to an alternating current (AC) magnetic field (Mertz et al., 2017; Shaterabadi et al., 2017; Suriyanto et al., 2017). Magnetic energy is converted in heat by MNPs and transferred to the tumour tissue, as illustrated in **Figure 1** (Cole et al.,

2011; Deatsch & Evans, 2014; Pollert et al., 2009). Temperature, which can reach up to 56°C, affects cancer cell function and metabolism, leading to cell apoptosis. Cancer cells, indeed, are more sensitive to the increases in temperature than the surrounding healthy cells.The reason for this enhanced sensibility could be ascribed to the chaotic cancerous tissue blood vasculature. Indeed, while the vascular architecture of the healthy tissue is hierarchically organised into arteries, capillaries and veins, the fast proliferation of cells inside the tumour tissue leads to an inefficient and leaky vasculature (Hervault & Thanh, 2014; Mallory et al., 2016). The dysregulation in the vasculature organisation is also responsible for the 'enhanced permeability and retention (EPR) effect', a typical feature of the solid tumors characterised by a limited lymphatic drainage and wider fenestrations and gaps between endothelial cells, which favour the nanoparticles accumulation into the tumour tissue due to "passive targeting" (Aslan et al., 2013; Maeda et al., 2006).

Moreover, tumours show a poor heat dissipation when a temperature above 42°C is applied, due to a reduced blood flow in comparison to the normal tissues (Bogart et al., 2014).The reduced blood flow favours the rising of temperature in the tumour tissue, favouring cancer cells apoptosis and the creation of hypoxia, acidosis and energy deprivation, all factors which contribute to the enhancement of the hyperthermia effect on cancer cells.(Corbet & Feron, 2017; Damaghi et al., 2015; Hervault & Thanh, 2014).

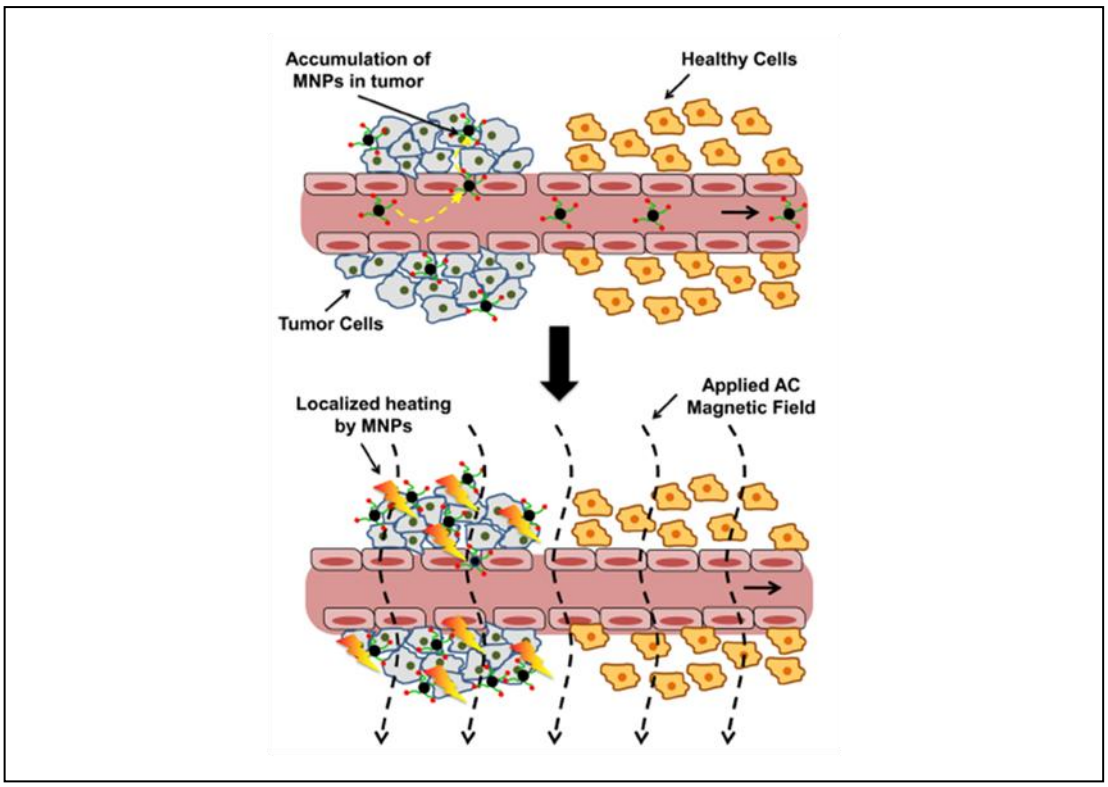

Figure 1. Schematic representation of the MHT treatment in tumour tissue.

Solid tumours are characterised by a poor lymphatic drainage and wider fenestrations and gaps between endothelial cells, all factors contributing to the "enhanced permeability and retention (EPR) effect". For this reason, the accumulation of MNPs is favoured in tumour tissue respect to the healthy tissue: MNPs in circulation passively enter the tumour tissue through the gaps and fenestration between endothelial cells and there are retained because of the limited lymphatic drainage.

When the body part is exposed to an alternating current (AC) magnetic field, the magnetic energy is converted in heat by MNPs and transferred to the tumour cells, which die, while the surrounding healthy cells are not affected by the treatment.

Original image taken from (Cole et al., 2011).

1.1.2. Cellular modifications induced by Hyperthermia

HT treatment impairs cellular environment, from the cell membrane, which becomes more fluidic and less stable, to the DNA and RNA repair system. Although all these cellular changes do not seem to be strictly linked with the cell death *in vitro*, cells exposed to HT treatment show membrane blebbing, a typical feature of apoptosis. (Hildebrandt et al., 2002).

When HT occurs, membrane potential changes, the presence of sodium and calcium in the cytoplasm increases as well as the potassium-efflux (Calderwood & Hahn, 1983; Konings & Ruifrok, 1985; Majda et al., 1994; Stevenson et al., 1981). Very little is known about pH fluctuations happening during HT treatments. Karino et al. registered pH values of tissues exposed to different temperatures (41°C, 43°C and 45°C), showing that the pH of tissues slightly elevates at the beginning of heating at 41°C and 43°C, to gradually reduce, whereas at 45°C the pH decreases (Karino et al., 1988).

The cytoskeleton is another cell component affected by HT application. Cytoskeleton orchestrates many cell functions, such as cell division, macromolecules transport, protein synthesis regulation and intracellular organelles distribution and anchoring. The three systems composing cytoskeleton are actin filaments, intermediate filaments and microtubules. HT exposure re-arranges all these three systems: actin microfilaments disassemble, intermediate filaments aggregate in a tight ring around the nucleus and microtubule network weakens (Pawlik et al., 2013).

1.1.3. Hyperthermia activates heat shock proteins (HSPs)

Heat shock unfolds proteins, which become insoluble and concentrate at the nuclear matrix, influencing DNA synthesis and repair mechanism (Hildebrandt et al., 2002). Among all the cellular proteins, Heat Shock Proteins (HSPs) are probably the most representative of the cell response when a changing of temperature occurs in the cell environment. These chaperones are divided among families, depending on their molecular mass: the small HSPs with a molecular mass< 40 kDa, and the HSPs with a molecular mass>40 kDa, which are HSP60, HSP70, HSP90 and HSP100 proteins families. In addition to act in the regular protein synthesis and in many stress-related cellular responses, HSPs have also been observed to cover a prominent role in cell protection from heat. When a heat shock occurs, the proteins of the cell matrix denature, liberating many hydrophobic protein sequences that could potentially interact with other proteins, leading to a loss of protein function. HSPs bind unselectively these hydrophobic regions, saving the proteins function. In moderate

HT, it was observed that the production of HSPs increases, a mechanism that seems aimed at the cell protection against hyperthermic cell death (Buchner, 1996; Ciocca et al., 1993; Fuller et al., 1994; Jaattela, 1999; Kaur et al., 2000; Samali et al., 1999). However, a high heat shock can overwork the HSPs function, so that the proteins aggregation and the misfolding phenomenon can no longer being stopped. In certain cancer cells, HSPs were found to create complexes with the tumour specific peptides, which are presented by antigen presenting cells with major histocompatibility complex (MHC) class I molecules (Menoret & Chandawarkar, 1998; Suto & Srivastava, 1995; Tamura et al., 1997). Multhoff and Issels suggested that the HSP70 and HSP72 could appear on the cell surface of some types of cancer cells after heat exposure, probably acting as foreign antigens by themselves and trigging the immune response against tumour cell (Botzler, Li, et al., 1998; Botzler, Schmidt, et al., 1998; Multhoff et al., 1997; Multhoff et al., 1995; Multhoff et al., 1999; Roigas et al., 1998). A correlation between HSPs and p53 protein (transcription factor) or retinoblastoma (Rb) was proposed, suggesting that HSP 70/72 can interact with the mutated form of p53, but not with the wild-type p53. These findings suggest that tumours in which p53 or Rb is mutated are more thermoresistant than those with wild-type proteins (Agoff et al., 1993; Finlay et al., 1988; Matsumoto et al., 1994; Matsumoto et al., 1997; van Bree et al., 1999).

Besides, the heat stress influences also the endoplasmic reticulum (ER), in which unfolded proteins accumulate leading to cell death (Han et al., 2013; F. J. Li et al., 2001). The stress on ER could be monitored by the increasing levels of cytosolic calcium and glucose related proteins (GRP) 78 and 94 (Hou et al., 2014).

1.1.4. Hyperthermia stimulates the Reactive Oxygen Species (ROS) production

Reactive Oxygen Species (ROS) arise from normal cell respiration and are a common by-product in all the aerobic organisms. Although ROS determine damages in lipids, protein, and affects mitochondrial membranes constituents, their presence in cell cytosol is well tolerated when it is balanced by the neutralising action of

antioxidants and of superoxide dismutase 1 (SOD-1), an enzyme involved in the destruction of superoxide radicals. The SOD-1 level is consistently lowered by heat stress, with the consequent enhancing of free ROS (El-Orabi et al., 2011). HT reduces SOD-1 protein levels and activity. As a consequence, the superoxide anion O^{-}_{2}, precursor of many ROS, remains free to react with other radicals in the cytosol, like nitric oxide (NO), creating the potentially harmful oxidant peroxynitrite (ONOO-), detrimental for the cell (Beckman & Koppenol, 1996).

1.1.5. The effects of Hyperthermia on gene modulation, cell cycle and DNA

The effect of HT on gene modulation was studied by Ahmed et al., who unveiled two gene networks in U937 cells, called A and B (Ahmed et al., 2015). In gene network A, the pathway is anti-apoptotic, and the core gene is IL1B, involved in cellular maintenance; while in gene network B, the pathway is pro-apoptotic and it is centred around the gene MAPK8, which belongs to the MAP kinase family. In gene network A, many HSPs proteins are involved to protect the cell from heat stress, whereas in gene network B act caspases proteins, which lead to cell death.

Heat stress also modulates the cell cycle. The thermal shock stimulates the serine/threonine-specific protein kinase ATM-and Rad3 related (ATR) which activates Checkpoint kinase 1 (Chk1), determining the arrest of the cycle progression at the G2/M phase (Furusawa et al., 2012). The *ATR-Chk1* pathway is thought to play a pivotal role in the apoptosis inhibition after HT: its inactivation triggers the caspase-3 cleavage, promoting apoptosis.

The damages of HT on DNA have been object of discordant reports; however, the current idea is that HT induces double strand brakes (DSB) in G1 and G2 cells, as indicated by the presence of γH2AX, a typical mark of DSB. Moreover, HT stops the replication of cell in S phase in a temperature-dependent manner (Velichko et al., 2012).

1.1.6. Hyperthermia-induced apoptosis

It is known that HT kills the cells by inducing apoptosis, a programmed cellular suicide program; however, more work is needed to clarify the mechanism underlying the whole process (van Loo et al., 2002). Tumour cells of solid tumours are more prone to HT damages, due to their vascular architecture, rich of hypoxic and low-pH regions and definitively more complex than normal cells (Reinhold & Endrich, 1986; Song et al., 1995; Vaupel & Kelleher, 1995).

The effect of HT can either affect or not cell survival, depending on the signal pathway that is trigged after heat shock: if HSPs are activated, the cell can survive below an acceptable threshold of temperature; otherwise, it can undergo apoptosis. The apoptosis mechanism can be triggered by the extrinsic or the intrinsic pathway (**Figure 2**). In the extrinsic apoptotic pathway, HT activates Fas ligands, the cytokine tumor necrosis factor (TNF)-related apoptosis-inducing ligand TRAIL, and the TNF-α ligand that stimulate death receptors on the cell surface (Ahmed et al., 2015; Reap et al., 1997). Fas could either activate the downstream caspases-a situation which seems favoured by the heat stress- or the mitochondrial amplification loop. In the last case, other effectors such as caspase-8, Bid and cytochrome c release are involved, until cytochrome-c binds to Apaf-1 and caspase-9 apoptosome complex (Tran et al., 2003).

The ligand TRAIL binds to death receptor TRAILR1 (DR4), and TRAILR2 (DR5) expressed prevalently on the surface of the tumour cells, triggering the apoptosis signal. When it happens, the surface of the Fas-associated death domain is exposed, recruiting caspase-8 and caspase-10 with the formation of the death signalling complex. Caspase-8 can either activate caspase-3 in cooperation with Caspase-10 or participate in the mitochondrial apoptosis pathway (Yoo & Lee, 2007). TNF-α binds THFR1 and TNFR2 receptors, inducing apoptosis through extrinsic pathway. When HT is repeated, FLIP protein, which inhibits caspase-8, is down-regulated, favouring the TNFR-mediated apoptosis signalling.

Regarding the intrinsic apoptosis pathway, Caspase-2 plays a pivotal role in cell death by acting on microtubules organisation and forming a complex with the

adaptor protein named RAIDD. The complex Caspase-2/RAIDD cleaves Bid, forming tBid, which stimulates a cascade of events: mitochondrial outer membrane potential (MOMP), cytochrome c release, the formation of Apaf-1-caspase-9 apoptosome (Bonzon et al., 2006; Bouchier-Hayes et al., 2009; Ho et al., 2008; Tu et al., 2006). Bim is another actor involved in the intrinsic apoptosis signalling, following an independent pathway and activating the Bax/Bak cascade. Bim triggers Bax/Bak-independent activation of caspase-3 in the absence of MOMP, and it is also destroyed by heat stress, together with actin and tubulin (Kuwana et al., 2005).

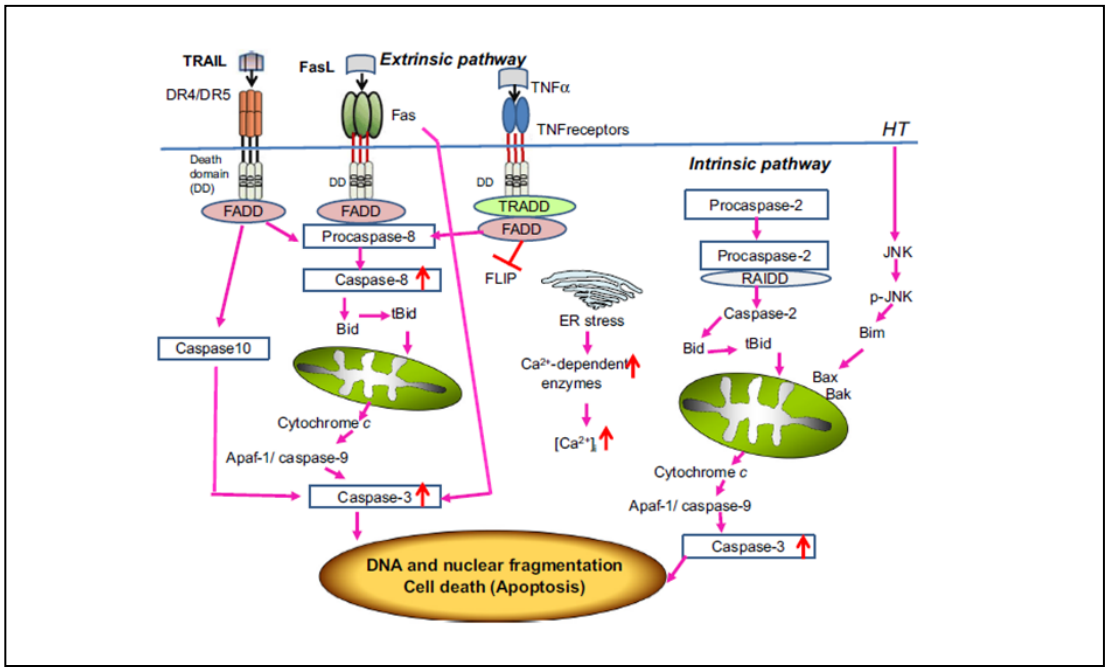

Figure 2. Extrinsic and intrinsic apoptotic pathways triggered by HT.

Extrinsic apoptotic pathway: HT activates the ligand TRAIL, Fas ligands, and the TNF-α ligand. TRAIL binds to death receptor DR4 and DR5, starting the apoptosis signal; as a consequence, the surface of FADD is exposed, and forms the death signalling complex with the help of caspase-8 and caspase-10. Caspase-8 can either activate caspase-3 in cooperation with Caspase-10 or participate in the mitochondrial apoptosis pathway. Fas could either activate the mitochondrial amplification loop (involving caspase-8, Bid and cytochrome c) or the downstream caspases. TNF-α binds THFR1 and TNFR2 receptors, inducing apoptosis through extrinsic pathway. The repetition of HT favours the down-regulation of the FLIP protein, which inhibits caspase-8 and favours the TNFR-mediated apoptosis signalling.

Intrinsic apoptosis pathway: Caspase-2 acts on microtubules and forms a complex with RAIDD. The complex Caspase-2/RAIDD cleaves Bid, creating tBid, which stimulates the mitochondrial outer membrane potential (MOMP), cytochrome c release, and the formation of Apaf-1-caspase-9 apoptosome. The intrinsic apoptosis signalling could be triggered also by the independent pathway which involves Bim. Bim favours the Bax/Bak-independent activation of caspase-3 in the absence of MOMP, and it is also destroyed by heat stress, together with actin and tubulin.

Original picture taken from (Ahmed et al., 2015).

1.2. Basic Physics concepts of Magnetic Hyperthermia

1.2.1. Magnetic field induced by a coil

Before to start with the description of the main mechanisms that underlay the heat transmission in MHT, it is worth to state the basic concepts of the magnetism induced by a coil (solenoid). A current **I**, which flows through a long coil, called solenoid, creates a uniform magnetic field inside the coil, like the one generated by a bar magnet. The magnetic field is indicated by the symbol **B**, and it is expressed in Tesla, **T** (**Figure 3**). The magnetic field is more concentrated and uniform in the centre of a long solenoid, and it could be calculated as (hyperPhysics, n.d.):

$$B = \mu * n * I$$

where μ is the permeability, n is the number of coils, called "turn density" of the solenoid, and I is the current flowing inside the coil.

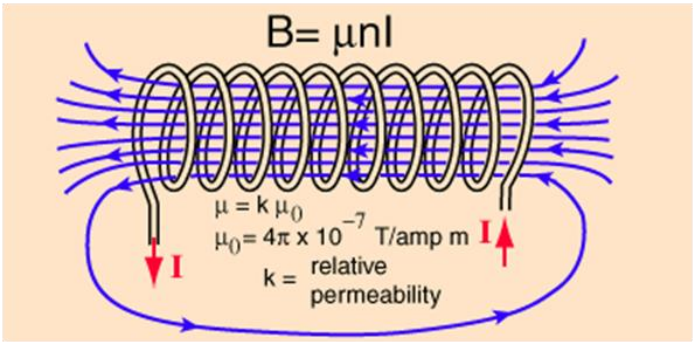

Figure 3. Representation of the magnetic field generated by a current flowing in a solenoid. The current I (red arrows), flows through the solenoid (the long coil with many turns) and creates a uniform magnetic field inside the coil. The magnetic field is indicated by the symbol B and it is represented in the picture by the blue lines. The magnetic field is more concentrated and uniform in the centre of a long solenoid.

From (hyperPhysics, http://hyperphysics.phy-astr.gsu.edu/hbase/magnetic/solenoid.html).

The parameters that define the magnetic strength **H** of an electromagnet, are:

- number of the turns of the coil (*n*);
- current (*I*) flowing through the coil;
- type of core material used.

The magnetic field strength could be increased by increasing the current or the number of turns. Flux density ϕ (defined as the magnetic field produced in a given area), the magnetic field *B* and the magnetic strength *H* are related by the formula (Electronics-Tutorials, n.d.):

$$B = \frac{\boldsymbol{\phi}}{A} \; and \; \frac{B}{H} = \mu$$

where *A* is the area and μ is the permeability, considered constant (μ_0) for non-magnetic material, such as wood or plastic, but it varies with the flux density for ferrimagnetic materials.

B and **H** could be plotted in a graphic, and the resulting curve is called *Magnetisation Curve, Magnetic Hysteresis Curve, or B-H curve.* The curves are different for each material investigated (**Figure 4**). In **Figure 4**, the flux density increases with the magnetic field strength until a point in which the flux density reaches the magnetic saturation. This happens because, at molecular levels, all the molecular magnets of the material are aligned with the magnetic field: at this point, the flux density will not increase anymore, even if the magnetic field strength increases. At the same time, the magnetic field strength H increases until a saturation point.

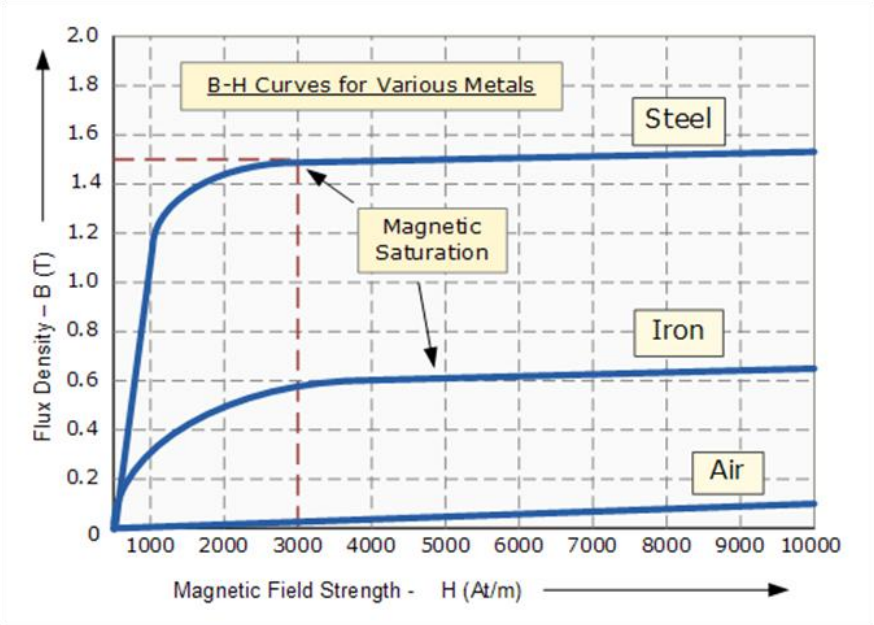

Figure 4. Representation of *B-H curves* (Magnetisation curves) of different materials.

In all the materials investigated, the flux density (y axis) increases with the magnetic field strength (x axis) until a point in which the flux density reaches a "plateau", called magnetic saturation. This happens when, at molecular levels, all the molecular magnets of the material are aligned with the magnetic field: at this point, the flux density will not increase further, even if the magnetic field strength is increased.

Adapted from (electronics-tutorials, http://www.electronics-tutorials.ws/electromagnetism/magnetic-hysteresis.html).

1.2.2. Magnetic Hyperthermia heating is due to magnetic hysteresis loss and relaxations losses.

The two main challenges of MHT are: 1) to deliver MNPs to the tumour region through a safe and reproducible method and 2) to improve the specific heating power (SHP) of the MNPs, in order to use the minimum amount of MNPs (Dutz & Hergt, 2014). When MHT is clinically applied, MNPs need to absorb an efficient amount of energy to be therapeutic: a condition achieved when MNPs are subjected to an AMF generated by a coil outside the patient's body.

However, speaking of induction heating is misleading. Indeed, the inductive heat production mechanism depends on: 1) the electrical conductivity of the medium and 2) the induced electrical voltage, both of them too low for MNPs to give rise to a sensible heating effect. The induced electrical voltage, in particular, is determined by the eddy current loops in the MNPs, which are too small for MNPs, but could become considerable when treating a human body, leading to serious consequences (Dutz & Hergt, 2014).

Nowadays, two mechanisms are recognised as responsible for the tumour heating by MNPs in an external magnetic field: the magnetic hysteresis loss, occurring in particles with multi-magnetic domains, and the relaxation losses, that are present in superparamagnetic or single-domain particle (**Figure 5**), (Beik et al., 2016).

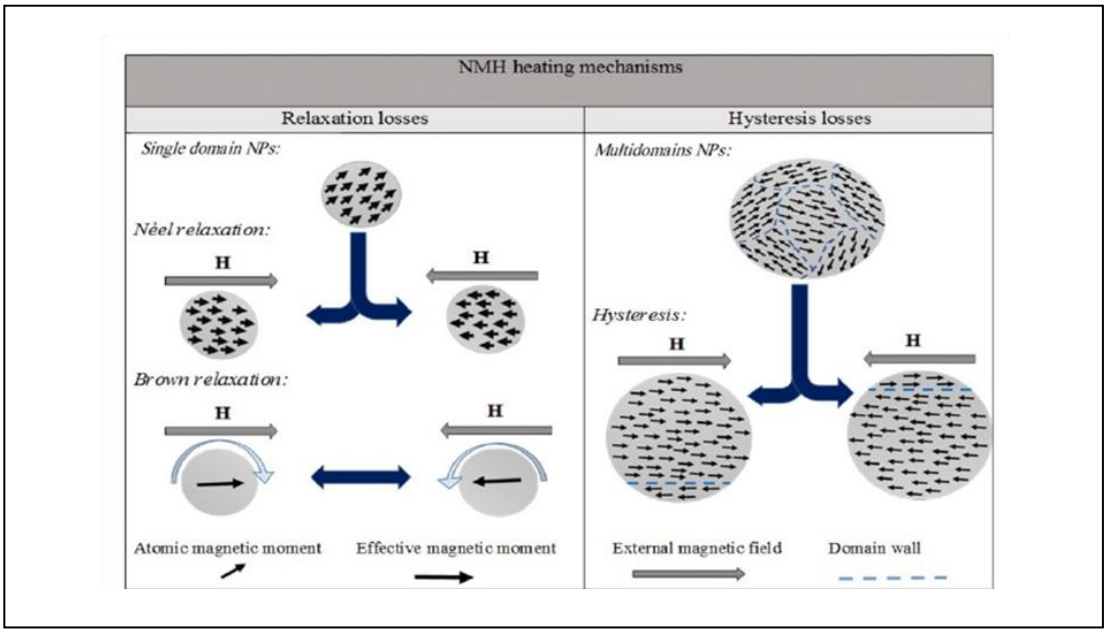

Figure 5. Relaxation losses and hysteresis loss.

These two mechanisms are responsible for MNPs heat generation under AMF. The relaxation losses (Néel and Brownian) are present in superparamagnetic or single-domain particle, while the magnetic hysteresis loss is typical in particles with multi-magnetic domains. Picture taken from (Beik et al., 2016).

1.2.3. The magnetic hysteresis loss

Large ferro- or ferri-magnetic particles contain different sub-domains, each of them with a precise magnetisation direction. When a magnetic field is applied, the domains with the same magnetic direction of the magnetic field axis *grow*, while the others with different direction *shrink*. The phenomenon, also knew as "domain wall displacements", is not reversible: the curve to increase the magnetic field amplitude is not coincident with the one to reverse the magnetisation. Such behaviour is called 'hysteresis behaviour' and produces heat under an AC magnetic field (Mornet et al., 2004). Magnetic hysteresis loss is defined as the coupling of magnetic spin with crystal lattice. The electromagnetic energy is transferred to the lattice under the form of heat, often named magnetic loss. The amount of energy loss during one cycle of the magnetic field is given by the area of hysteresis loop (**Figure 6**), which is defined by the formula (Carrey et al., 2011a):

$$A = \int_{-Hmax}^{H\,max} \mu_0 M(H) dH$$

where *M(H)* is the magnetisation of the magnetic materials, *H* is the magnetic field strength and μ_0 is the permeability constant.

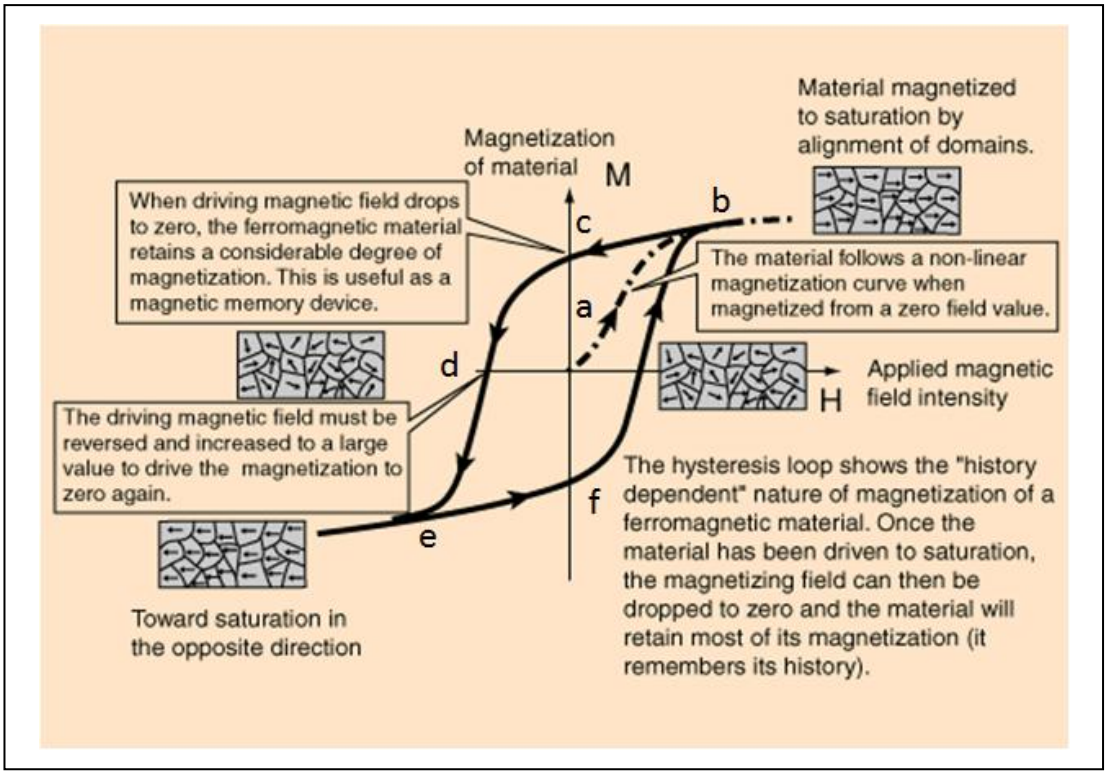

Figure 6. Representation of magnetic hysteresis loop.

a) A not magnetised material, put in a magnetic field, will show a magnetisation that increases to a maximum point (b), the magnetic saturation. c) When the magnetic field intensity is decreased to 0, in the material there will be still a residual magnetic field (remanence). d) In order to bring the material magnetisation to 0, a certain amount of magnetic field oriented in the opposite direction is required. This will flip the magnetic field direction (e). Decreasing the magnetic field intensity, there will be a residual magnetic field direction in the opposite direction (f). To get rid of the magnetic field, it should be increased and it will drop the magnetic field intensity to 0. Then, the material can be magnetised again and the cycle will start again (b).

Image adapted from (hyperPhysics, http://hyperphysics.phy-astr.gsu.edu/hbase/Solids/hyst.html.).

Three parameters define the hysteresis loop of magnetised materials: saturation magnetisation (Ms), the remanent magnetisation (Mr) and coercivity (Hc), all involved in the hysteresis heating mechanism. Saturation magnetisation is the maximum magnetisation that could be achieved by increasing the external magnetic field, the remanent magnetisation is the magnetisation retained by ferrimagnetic materials when the magnetic field is slowly reduced to zero and coercivity is the remanent field lost by the ferrimagnetic material when the negative field is applied to demagnetised the material (Shi et al., 2015). In macroscopic magnetic materials, it is possible to find magnetic domains, which are regions in which all the individual magnetic moments of the atoms are aligned in the same direction, resulting in a uniform magnetic direction. When the magnetic particle size decreases, these multi-domains are no longer energetically favoured, and so each nanoparticle represents only a single magnetic domain. According to Heider et al., the transition from multidomain to the single domain of magnetite, one of the most used materials for MNPs creation, is achieved when the particles have a diameter of 30 nm (Heider et al., 1987). The single domain particle shows an energy barrier that prevents the moment alignment toward the magnetic field, a condition which could be reversed with a great amount of energy. The energy barrier that should be overcome to reverse the total magnetisation of single domains particles is higher than the one of multi-domains particles (Heider et al., 1987).

1.2.4. Néel relaxation and the Brownian relaxation.

The second mechanism involved in the dissipation of heat is present when single-domain superparamagnetic particles are in an AC magnetic field. These particles do not show any domain wall, and so there is no hysteresis loss, but heating is provided by Néel and Brownian relaxation losses (**Figure 7**). Again, it should be done a distinction between nanoparticles immobilised, only subjected to the Néel relaxation loss, and particles free to move in a suspension, which show Brownian relaxation losses (Mornet et al., 2004).

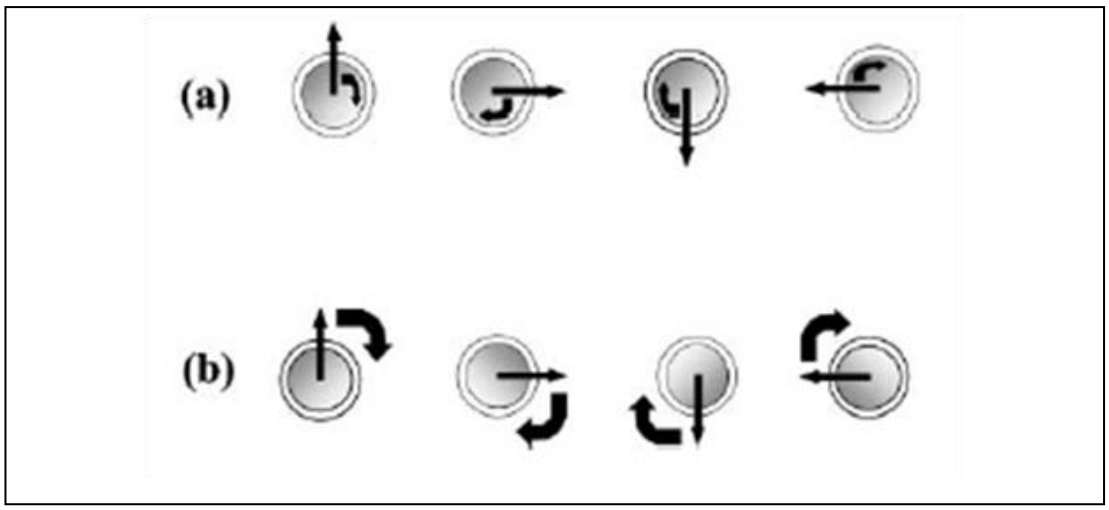

Figure 7. Schematic representation of the Néel and Brownian relaxations in a magnetic particle. (a) Néel rotation (the magnetic moment rotates within each particle, but the particle does not rotate); (b) Brown rotation (the particle rotates as a whole). Picture taken from (Mornet et al., 2004).

MNPs with a diameter comprised between 10 and 60 nm show two antiparallel crystallographic directions, separated by energy barriers: this behaviour is due to their magnetic anisotropy (magnetism that varies from point to point of the MNPs). The two magnetic stable orientations determine the magnetic axis of the nanoparticle which could flip and reverse its direction. Let's call τN the average time necessary for the nanoparticle magnetisation to randomly flip as a result of thermal fluctuations, and τm the time at which the magnetisation of the nanoparticle is measured. If $\tau m >> \tau N$, the magnetisation will flip many times during measurement, leading to a total magnetisation equal to zero, while if $\tau m << \tau N$, the magnetisation will not have the time to flip, and so the measured magnetisation will be the one registered at the beginning of the measurement. The temperature at which $\tau m = \tau N$ is called the *blocking temperature* (T_B). In this case, the state of the nanoparticle- superparamagnetic or blocked- will be determined by the measurement time: below the T_B, nanoparticles are in the superparamagnetic state, characterized by single domain behaviour, with the system coercivity and retentivity equal to zero; above the T_B the direction is randomized, due to the small nanoparticles size (Shi et al., 2015). The blocking temperature is influenced by the volume of nanoparticles and the anisotropy constant of the material, called the energy barrier.

Néel relaxation occurs when a particle overcome an energy barrier in the presence of an AMF. The magnetisation of the nanoparticle does not vanish immediately when the magnetic field ceases, but the microscopic magnetisation vanishes with the typical relaxation time *τN* (Dutz & Hergt, 2014):

$$\tau N = \tau 0 * e^{\frac{K*V}{k*T}},\ \tau_0 \sim 10^{-9}\ \text{s}$$

Where *τ0* is a length of time, characteristic of the material, called the attempt time, *K* is the magnetic anisotropy, and *V* is the particle volume, *k* is the Boltzmann constant, *T* the temperature and *k*T* the thermal energy. Typical values for *τ0* are between 10^{-9} and 10^{-10} seconds. *K*V* determines the energy barrier against reversal of magnetisation.

The relaxation time decreases with the decreasing particle volume. Néel relaxation is the only relaxation process present when the nanoparticles are immobilised, as in tumour tissue (Shi et al., 2015).

When the magnetic nanoparticles are in suspension, and so they can rotate freely, another process of relaxation occurs, called Brownian relaxation. In this case, it should be taken into account the fractional losses due to the viscosity of the carrier liquid. The Brownian relaxation time is described by Beik et al. in the formula (Dutz & Hergt, 2014):

$$\tau B = \tau_0 * \frac{3\eta * V_h}{k * T}$$

where V_h is the hydrodynamically effective volume, which could differ from the geometrical volume, due for example to the adhering fluids layers.

Nanoparticles tend to reverse the magnetisation by either the Néel or the Brownian process, following the energetically easiest way, that is the one which shows the smaller relaxation time (**Figure 8**). The effective relaxion time (*τ*) is described by the formula (E. Moros, 2012):

$$\tau = \frac{\tau_N \tau_B}{\tau_N + \tau_B}$$

The transition between Néel or Brownian relaxations happens when $\tau_N = \tau_B$, but for smaller diameter, the Néel relaxation is favoured instead of the Brownian relaxation. When nanoparticles are dispersed in blood vessels, the Brown relaxation is present, while when the nanoparticles are injected directly in the tumour, and so are not freely movable in a suspension, the Brown relaxation is suppressed.

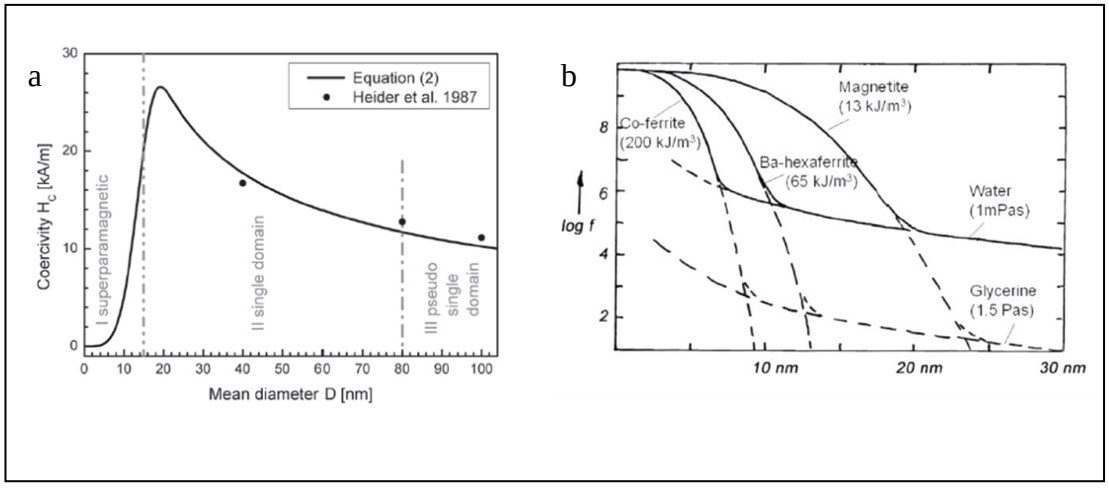

Figure 8. Coercivity and relaxation losses dependency on particle size.

a) Maghemite nanoparticles coercivity depends on particle size, taken from (R. Hergt et al., 2008).

b) Particles relaxation frequency depends on their size, magnetic type and suspension media. Adapted from (Dutz & Hergt, 2014; Staniland & Rawlings, 2016).

1.2.5. The Specific Absorption Rate (SAR)

In clinical applications, the measure of the rate at which the energy is absorbed by the human body, when it is exposed to an AMF, is determined by Specific Absorption Rate (SAR). SAR is defined as (Mornet et al., 2004):

$$SAR = C \cdot \frac{\Delta T}{\Delta t}$$

where C is the specific heat capacity of the heated medium and $\frac{\Delta T}{\Delta t}$ is the initial slope of the temperature versus time dependence.

SAR is influenced by a multitude of other parameters, such as viscosity and heat capacity of the tissue/liquid in which nanoparticles are suspended, size, size distribution, shape and chemical composition of nanoparticles (Mornet et al., 2004). Indeed, with the nanoparticles size reduction, thermal fluctuations are more frequent. If the changes in the external magnetic field are too slow respect to the relaxation time, particles show superparamagnetism, and so it can be assumed that frequency of the external magnetic field is responsible also for the transition from stable ferromagnetic[1] to superparamagnetic[2] behaviour. The transition is also influenced by Néel and Brownian relaxation.

In general, when frequency is low, the nanoparticles magnetisation *M* follows the driving AMF *H*, and it is said that *M* and *H* are in phase; however, when the frequency increases, *M* and *H* are no longer in phase, because *M* cannot follow the rapid increase of *H*. In magnetic multi-domains materials, in addition to that, when the frequency is high, loss peaks due to the domain wall resonance could appear (Dutz & Hergt, 2014).

[1] Ferromagnetic behaviour is displayed by materials which have a high susceptibility to magnetisation. Their susceptibility depends on the applied magnetizing field and could persist also after the magnetic field ceases. Iron is a ferromagnetic material, in which all the neighbouring atoms display parallel magnetic alignments (oxforddictionaries, n.d.).

[2] Superparamagnetic behaviour is a form of magnetism displayed by small ferromagnetic or ferrimagnetic nanoparticles. When nanoparticles are small, their magnetisation can randomly flip direction under the influence of temperature, with a typical time between two flips called the Néel relaxation time (Wikipedia, n.d.).

1.2.6. Physical parameters which influence nanoparticle interaction

The nanoparticles size and volume have been correlated to the heat dissipation in a model which defines the hysteresis losses as the primary mechanism of MNPs heating of any size (Carrey et al., 2011b). The heating properties of MNPs are influenced by several parameters: the frequency and amplitude of magnetic field, the particle geometry and shape, the particles size and distribution, the anisotropy (Hergt et al., 2004; Hugounenq et al., 2012; Vallejo Fernandez & O'Grady, 2013; Walter et al., 2014). Magnetic dipoles, in particular, play an important role in HT. When present in a complex biological system, indeed, the nanoparticles tend to be inhomogeneously distributed, creating the intercellular clustering of nanoparticles, bunched up in the endosomes or another cellular compartment (Branquinho et al., 2013; Lunov et al., 2011). A study on different configurations of nanoparticles, respectively homogeneously dispersed in water or blocked in a polystyrene matrix, shows that when the nanoparticles are blocked inside the matrix, the strong dipole interactions impeded the magnetic moment, so Néel relaxation contribute to heating is reduced and the heating is caused by hysteresis loss (Sadat et al., 2014). Also the concentration influences nanoparticle behaviour. Indeed, at high concentration, nanoparticles tend to create magnetic dipoles with an enhanced heat dissipation from magnetic hysteresis loss, lowering the SAR (Fortin et al., 2007; Gudoshnikov et al., 2012; Haase & Nowak, 2012; Urtizberea et al., 2010). Instead, when nanoparticles are normally concentrated, the superparamagnetic particles follow the Néel and Brownian relaxations, according to the classical Langevin behaviour, that is reversible magnetisation curve with zero retentivity and coercivity. When the nanoparticles concentration is high, however, they do not follow anymore the Langevin function, but instead the dipole interactions change their anisotropy and their magnetic behaviour. It was also observed that in the presence of an AC field, nanoparticles tend to create chains, lowering the SAR (Branquinho et al., 2013). The dimerization of the nanoparticles and their arrangement into chains, as well as the behaviour of the nanoparticles in complex biological systems, are still objects of study.

1.3. MNPs required features for Magnetic Hyperthermia applications

There is a vast research aimed to create MNPs with the highest SAR and the minimum toxic effect for the body. The most interesting MNPs features are: 1) type of magnetic material they are made of, 2) particle size, and 3) particle coating.

For the MNPs creation, metals as iron, cobalt and nickel and metal oxides as Fe_3O_4, γ-Fe_2O_3, $MnFe_2O_4$ and $CoFe_2O_4$ are normally used. However, their degradation when introduced inside the body could produce reactive oxygen species (ROS) and free radicals. These products trigger lipid peroxidation, DNA damages, protein alteration, and cell apoptosis (Liu et al., 2015). To overcome these issues, MNPs are usually subjected to surface treatments that make them stable and safe for biomedical application. According to Nandwana et al., MNPs surface modifications should satisfy different requirements, as: 1) do not agglomerate, 2) be biocompatible and possibly be able to be functionalized, 3) avoid nonspecific cell interaction, and 4) increase the MNPs pharmacokinetics. MNPs are normally coated with dimercaptosuccinic acid (DMSA), Polyethylene glycol (PEG), dextran, chitosan, liposomes, gold and silica (Nandwana et al., 2015).

The preferred MNPs size for clinical application is below 20–30 nm, under the superparamagnetic limit. Nanoparticles could be created either by mechanical attrition (top-down method) or by chemical synthesis (bottom-up method), but the latter method is the most used as it creates MNPs of uniform composition and size. Chemical methods typically used for MNPs creation are co-precipitation, microemulsion, thermal decomposition and/or reduction, hydrothermal synthesis, and polyol synthesis (Nandwana et al., 2015).

1.3.1. *In vitro* and *in vivo* Magnetic Hyperthermia application

Magnetic Fluid Hyperthermia (MFH) refers to Hyperthermia treatment that uses MNPs suspended in a fluid. MFH has frequently been used in synergy with other

treatments, such as chemotherapy and radiotherapy. It was observed that MFH increases Caco-2 cell membrane fluidity, enhancing the effect of chemotherapy, in MFH-treated cells (Alvarez-Berrios et al., 2013; Hernandez et al., 2010; Meenach et al., 2012). The effect of the combined treatments also affects the immune system: indeed there is a production of heat shock proteins, which stimulate the immune system against melanoma tumour cells, opening new routes for the treatments of the metastasis (Sato et al., 2010). Sadhasivam et al. used surface modified carbon-encapsulated iron oxide nanoparticles (CEIO-NPs) with polyethylene glycol-folic acid (PEG-FA) against HeLa cells. The folate receptors expressed on the surface of the cell were targeted by the nanoparticles, which entered inside the cell, leading to cell damage after MFH (Sadhasivam et al., 2015).

MFH was successfully employed as a single treatment using poly (lactic-co-glycolic acid) (PLGA)-functionalised magnetic nanocapsules, effectively killing neoplastic 4T1 and MCF-7 breast cell lines by apoptotic cell death (Estevanato et al., 2012). Cell apoptosis was also obtained by delivering herceptin-conjugated MNPs to SK-BR-3 cells and exposing the cells to an AMF (J. Zhang et al., 2011).

In vivo experiments of MFH on mice bearing pancreatic cancer locally injected with 20-nm MNPs, determined the tumour growth inhibition and the survival prolongation. After 30 minutes of exposure, it was also registered an increase in temperature up to 47-51 °C (L. Wang, Dong, et al., 2012). Wang et al. applied NMH to ultra-small magnetic iron oxide (USPIO) on cervical lymph node metastasis of rabbit pyriform sinus carcinoma, obtaining an apoptosis of 100% of treated cells. It was also reported chromatin and cytoplasm condensation, endoplasmic reticulum membrane fusion, and bubble formation. Studies regarding the *in vivo* and *in vitro* application of MFH are summarized in **Table 1** and **Table 2** (Beik et al., 2016).

Reference	Experiment medium	Nanoparticles; size (nm)	Exposure condition (KHz;KA/m; min)	SAR[1] (W/g)	Cell death (%)
Liao et al., 2015	Hepatocellular carcinoma cells	Fe_3O_4-Alginate-galactosamine; 128	780;19; 20	308	95
Sadhasivam et al.,2015	Cervix cancer cells	CEIO[2]-PEG[3]-FA[4];74	750;0.8; 10	Not Informed	>75
Meenach et al, 2010.	Glioblastoma cells	Fe_3O_4;20-30	297;25; 5	Not Informed	>90
Shinkai et al., 1996	Glioma cells	Fe_3O_4-cationic liposomes;35	118;30.6; 60	140	100
Sahu et al., 2015	Cervix cancer cells	DOX-magnetic nanocomposite;65	250;36.6; 25	Not Informed	>80
Yan et al., 2014	Hepatocellular carcinoma cells	γ-Fe_2O_3-10-20	200; Not Informed;60	Not Informed	~82
Pala et al., 2014	Adenocarcinoma cells	γ-Fe_2O_3-Dextran-Her2[5]-20;10	280; Not Informed;60	Not Informed	60
Kruse et al., 2014	Lung cancer cells	Fe_3O_4-Dextran-CREKA[6]-Cisplatin;52	292;58; 30	83.5	>75

Table 1. List of *in vitro* experiments in which MFH was applied.

[KHz; KA/m; min] indicates [Kilo Hertz; Kilo Ampere per meter; minutes]. [1]Specific Absorption Rate (SAR). [2]Carbon-encapsulated iron oxide nanoparticles. [3]Polyethylene glycol. [4]Folic acid. [5]Anti-human epidermal growth factor receptor (HER2) aptamer as a targeting moiety. [6]CREKA is a tumour homing peptide that recognizes fibrin associated plasma proteins overexpressed in cancer cells. Table adapted from (Beik et al., 2016).

Reference	Tumour model	Nanoparticles; size (nm)	Exposure condition (KHz;KA/m;min)	Therapeutic gain; index
Jordan et al. (2001)	Glioma	Fe_3O_4-Amilosilane;15	100;18;30	4.5-fold Survival prolongation
Balivada et al. (2010)	Melanoma	Fe_3O_4-Porphyrin;12	366;5;10	>75% Tumour inhibition
Wang et al. (2015)	Pyriform sinus carcinoma	Fe_3O_4;20	Not Informed; Not Informed; 45	5-fold; Apoptosis
Rachakatla et al. (2010)	Melanoma	Fe-Fe_3O_4-Porphyrin; 25	366;5;10	~40%; Tumour inhibition
Kossatz et al. (2014)	Breast	Fe_3O_4-DMSA[1]-3;12	435;15.4;60	>80%; Tumour inhibition
Kossatz et al.(2) (2015)	Breast	Fe_3O_4-DMSA-DOX[2]-[3]N6L;12	435;15.4;60	~85%; Tumour inhibition
Johannsen et al. (2005)	Prostate	Fe_3O_4;15	100;12.6;30	~50%; Tumour inhibition
Bae et al. (2012)	Lung	Chito-FIONSs[4];103	1000;0.208; 20	~70%; Tumour inhibition

Table 2. List of in vivo experiments in which MFH was applied.

[KHz; KA/m; min] indicates [Kilo Hertz; Kilo Ampere per meter; minutes].[1]Dimercaptosuccinic acid. [2]Doxorubicin. [3]Nucant multivalent pseudopeptide. [4]Chitosan oligosaccharide-stabilized ferrimagnetic iron oxide nanocubes. Table adapted from (Beik et al., 2016).

1.4. Non-thermal effect in Magnetic Hyperthermia

Observations from different research groups suggest that the heating effect due to the AMF application to the cells bearing MNPs seems not to be the exclusive mechanism involved in the cell death, but that at least another non-thermal mechanism exists, generated by AMF, which leads to cell death. Indeed, Villanueva et al. (Villanueva et al., 2010) observed that 30 minutes of AMF application (f¼100 kHz, H¼15 mT) on HeLa cells using perovskite-based MNPs were sufficient to cause cell apoptosis, even if the observed temperature increase was less than 0.5 °C. Along with Villanueva et al., Asin et al. in 2012 , obtained 100% of cell dead when an AMF of 260 kHz and 12.7 kA/m was applied for 15 min to magnetically loaded dendritic cells (DCs), with a temperature rise of only 1-2 °C. All these findings show that some other non-thermal mechanism should happen in cells exposed to MH, as observed by Asin et al. in 2013 (Asin et al, 2013), where the supernatant of the AMF-exposed cells was used to kill control cells, not exposed to AMF. The controls death was explained as a mechanical effect: the MNPs, due to AMF exposure, cause the breakage of the endocytic vesicles/lysosomes in which are confined, determining the release of toxic content in the cytoplasmic medium.

Many scientific works investigated the cellular heating, thought as the simple consequence of the so-called "intracellular hyperthermia". Huang et al. found an increase of temperature only in the cell membrane, while the cytoplasm temperature was unchanged; others studies calculated that the temperature of MNPs is reduced below one tenth if measured at a distance of 3nm from the nanoparticle, making difficult to attribute the excessive peak temperature registered for MNPs only to the magnetic heating effect (Huang et al., 2010; Riedinger et al., 2013). Probably other actors, not yet unveiled, are involved in the cellular heating process. The cell heating represents still a mystery, and until now the models that tried to estimate the heating effect inside the cell environment appeared too naive, and macroscopic temperature sensors are probably not sensitive enough to adequately describe the MNPs cellular surrounding. It was also theoretically hypothesised that MNPs, under the effect of an

AMF, could generate ultrasound waves that could enrich the panorama of therapeutic applications (Carrey et al., 2013).

Wild-type cells loaded with MNPs and exposed to AMF could have phenotypic responses. Indeed, the interaction between the MNPs and the magnetic field influences the ROS generation, which increases in cells exposed to the AMF (Connord et al., 2015). ROS exert their detrimental effects on all the cell macromolecules, such as protein, carbohydrate, lipids and DNA, causing damages to the cells (L. Chen et al., 2017).

The catalytic ROS production is favoured by the release of Fe^{2+} produced by MNPs by Fenton reaction, that is increased by the exposure to the magnetic field(Connord et al., 2015; Domenech et al., 2013). The ROS production is also favoured by the magnetic field generated by MNPs in their immediate proximity, that changes the pair spin states and promotes the free radical production. (Binhi & Chernavskii, 2005; Jia et al., 2014), It was shown that Fe_3O_4 MNPs could promote ROS generation both in the presence of an AMF (60 kA/m,292 kHz) than in a statical magnetic field (Binhi & Chernavskii, 2005; Wydra et al., 2015).

Other effects promoted by AMF application are lysosomal membrane permeabilization (Domenech et al., 2013), cell cytotoxicity and apoptosis, as seen in hepatocytes exposed to a static magnetic field (0.4 T) for 1 h (Bae et al., 2011), and in rat pheochromocytoma cells incubated with MNPs-SiO_2 and then exposed to extremely low frequency magnetic field (50Hz, 400 μT) (Jia et al., 2014).

1.5. Clinical application of Magnetic Hyperthermia

Magnetic Hyperthermia was firstly applied clinically by Jordan et al. (Jordan et al., 2001).

After that, the technique was employed in many different applications, summarised by Beik et al. in **Table 3** (Beik et al., 2016). In all of them, the magnetic field strength was modulated accordingly with the area subjected to the treatment, from 2 to 18 KA/m.

The efficacy of the thermal therapy approach is measured by the thermal dose unit, a method by which "*the time-temperature profile of an arbitrary treatment regime is normalised to cumulative equivalent minutes (CEM) of treatment at 43 °C"*, and which is defined by the formula (Sapareto, 1982; Sapereto et al., 1978):

$$CEM_{45} = \int_0^t R_{CEM^{43-T}}\ \delta t$$

Where t indicates the time spent at temperature *T*, and R_{CEM} stands for the ratio of exposure times required to result in the same survival for a 1 °C rise in temperature T. For many cell types, R_{CEM} is considered to be 0.5 above 43 °C and 0.25 below 43 °C.

Regarding application of MHT in human, Maier-Hauff et al. tested a combined treatment of Nano-Magnetic Hyperthermia (NMH) and radiotheraphy (RT) on 14 patients suffering of recurrent glioblastoma multiforme (Maier-Hauff et al., 2007). During the treatment, repeated in average 6 times for each patient, the thermotherapy was combined with 30 Gy of radiotherapy dose. In 90% of the tumours (T90), temperature was 40.5 °C and the survival rate of patients increased.

Ref.	MNPs Size (nm)	Trial Phase	Cancer	Exposure condition (KHz; KA/m; min)	Median T90 (°C)	Median CEM43 (min)	Outcome Survival (months)
Maier-Hauff et al.(2007)	15	I	GMB2	100; 8.5; 60	40.5	7.7	2.7-11.5 for RT[1]; 14.5 for RT+NMH
Maier-Hauff et al. (2011)	12	II	GMB[2]	100; 15; 60	Not Informed	Not Informed	6.2 for RT1;13.4 for RT+NMH
Joannsen et al. (2010)	<20	I	Prostate	100; 15; 60	39.9	5.8	Not Informed
Joannsen et al. (2007)	15	I	Prostate	100; 18; 60	40.1	7.8	Not Informed
Bonvalot et al. (2017)	NBTXR3[3]	I	Soft Tissue sarcoma	50 Gy	Not Informed	Not Informed	tumor shrinkage was 40%
Matsumine et al. (2011)	Calcium phosphate cement with magnetite	Not informed	bone metastases	300 Oe; 100 kHz. (7 kW @ 1.5 MHz)	Not Informed	15 min per day.	32% tumour reduction
Jimbow et al.(2012)	NPrCAP/M	I	Melanoma patients	118 kHz	Not informed	43°C for 30 min x3 times every other day intervals	30 months for stage 4 patients 32 months for stage III patients
Lübbe et al. (1996)	100 with epirubicin	I	Breast cancer Chondrosarcoma Schwannoma Ewing sarcoma	0.5-0.8 tesla 60-120 min	Not Informed	Not Informed	2 deaths out of 14 in 5-6 weeks

Table 3. Summary of clinical trials on NMH using MNPs.

The table compares the median T90, median CEM43, and patient survival for radiotherapy alone or radiotherapy in combination with NMH. [Median T90] indicates temperature exceeded for 90% of tumour volume. Median CEM 43°C indicates cumulative equivalent minutes at 43°C. [1]Radiotherapy. [2]Glioblastoma Multiforme. [3]NBTXR3 are hafnium oxide crystallites and phosphate groups in an aqueous medium.Table adapted from (Beik et al., 2016).

1.6. Magnetotacic Bacteria

1.6.1. The discovery of Magnetotactic bacteria (MTB)

Magnetotactic Bacteria (MTB) are Gram-negative organisms able to align with external magnetic fields. This ability is given by chains of linearly arranged subcellular magnetic organelles, called magnetosomes (**Figure 9**), (Barber-Zucker et al., 2016; Bazylinski & Frankel, 2004; Blakemore et al., 1980; Nudelman & Zarivach, 2014). Magnetosomes are lipidic membranes filled within crystals of magnetite (Fe_3O_4), greigite (Fe_3S_4) or maghemite (γ-Fe_2O_3), that are believed to originate from MTB cytoplasmic membrane (Gorby et al., 1988; Rong et al., 2012). Magnetosomes in MSR-1 species are formed principally by proteins, which surround the magnetosome, and by lipids (Grunberg et al., 2001).

The length of the magnetosome crystal iron oxide core, determined by Transmission Electron Microscopy (TEM) investigation, measures between 5 and 120 nm (Kolinko et al., 2012). *Magnetospirillum AMB-1 and MSR-1* strains are characterised by magnetosomes of cubo-octaedral geometry, sized between 30 and 50 nm (Alphandéry et al., 2008). This size makes magnetosomes single-domain crystals, that are crystals with the maximum possible magnetic moment per unit volume. In *AMB-1* and *MSR-1*, there is only one magnetosome chain composed by 15-30 magnetosomes, while *Magnetobacterium bavaricum (Mbav)* strain shows more chains, each of them consisting of more strands of magnetosomes (Komeili, 2012).

MTB were discovered by Salvatore Bellini, a medical doctor at the University of Pavia, who for first noticed MTB in fresh waters around Pavia in a period which spans from the late 1950s to 1963. He observed that those bacteria were able to accumulate in water droplets following the North direction. Bellini performed different experiments to demonstrate the sensitivity of the MTB to the magnetic field, but the findings of his researches, written in Italian, were only diffused to the small audience of a few Italian universities. It was only several years later that Bellini's discoveries were translated into English, with the help of Frankel (Bellini, 2009; Bellini, 2009; Frankel., 2009). The men who introduced MTB to the scientific

audience was Blakemore, who found the bacteria in sediments collected near Woods Hole (Massachusetts) and noticed that their swimming direction was always the same, independently from the external stimulus given, but it changed when a magnet was brought near. Blakemore also studied the internal morphology of MTB, describing the magnetosome and the chains of the magnetosomes, providing an explanation for the MTB movement along the magnetic field (R. Blakemore, 1975; Komeili, 2012).

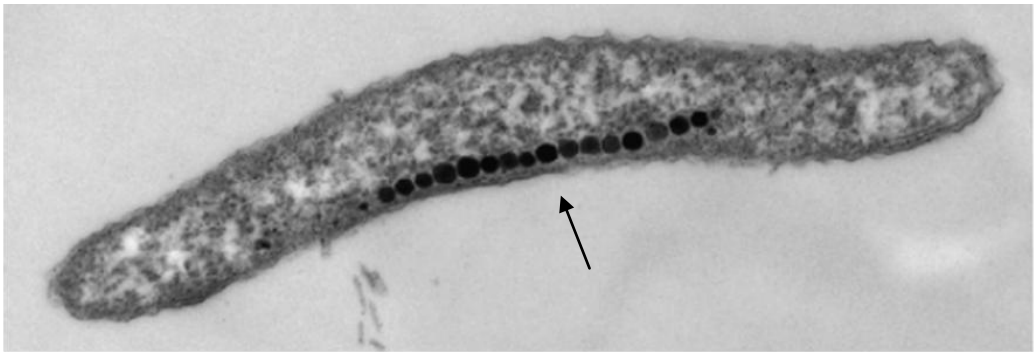

Figure 9 Transmission Electron Microscopy (TEM) pictures of *Magnetospirillum gryphiswaldense*.

The central chain made of single magnetosomes is visible in the cell body, indicated by the arrow. Picture adapted from (Schuler, 2008).

1.6.2. Ecology of Magnetotatic Bacteria

The ecology of MTB reveals that these bacteria prefer to live in aquatic zones where oxygen and redox compounds are horizontally stratified, gathering close to or below the oxic-anoxic transition zone (OATZ). OATZ is a particular zone created by two opposite gradients, one formed by the oxygen coming from the surface and another created by the sulphide produced by the sediments of the bottom (**Figure 10**). In OATZ, oxygen levels are very low, creating the perfect environment for MTB, which dislike increasing oxygen conditions (Bazylinski & Frankel, 2004; Frankel et al., 1997). Moreover, it was found by Blakemore that MTB of the North hemisphere swim northwards, while MTB of the South hemisphere swim southwards, and in both the cases MTB point to the lower part of their habitat, where oxygen levels are very low (Blakemore et al., 1980). In both the hemispheres, MTB on the oxic side of OATZ move across different stratifications by swimming down geomagnetic field lines, whereas those on the anoxic side swim up. The MTB located on oxic side of OATZ rotate their flagella counterclockwise (CCW), whereas the ones present on the anoxic side swim up along geomagnetic field lines (Bgeo) by rotating their flagella clockwise (CW). MTB showing north or south-seeking behaviour show also different magnetic polarity. This typical MTB mechanism of moving toward OATZ, exploiting magnetic field through their magnetosomes, is called "magneto-aerotaxis". According to the "magneto-aerotaxis" hypothesis, moving along the magnetic field, MTB follow a vertical route toward different stratifications, being helped in this sense to find OATZ respect to other bacteria that possess only chemotactic and aerotactic mechanisms. However, this hypothesis is not fully validated by evidences. Frankel et al. found out magnetosomes also in the Equator, very far from North and South Poles, while MTB believed to migrate toward south were found in the North hemisphere (Frankel et al., 1981; Shapiro et al., 2011; Simmons et al., 2006).

Moreover, Spring et al. observed that the number of magnetosomes inside MTB exceeds the one required for MTB movement along magnetic field (Spring et al., 1993). Taken together, these findings are not completely against the "magneto-

aerotaxis" hypothesis: it could be possible indeed that MTB follow other routes to find other chemical compounds more abundant in areas which are different from OATZ. Due to the ambiguity of the magnetosomes role, other hypotheses have been raised about the presence of magnetosomes in MTB. For example, it is possible that magnetosomes participate to iron storage or cell detoxification, but this assumption is not convincing (Shapiro et al., 2011; Simmons et al., 2006), or maybe magnetosomes could be involved in the cell movement, helping the MTB to turn along the magnetic field (Philippe & Wu, 2010). Another hypothesis is that magnetosomes could be involved in MTB energy production, exploiting the redox changes to oxidise magnetite in maghemite and producing energy for the cell ("magnetosome battery hypothesis", proposed by (Kopp & Kirschvink, 2008).

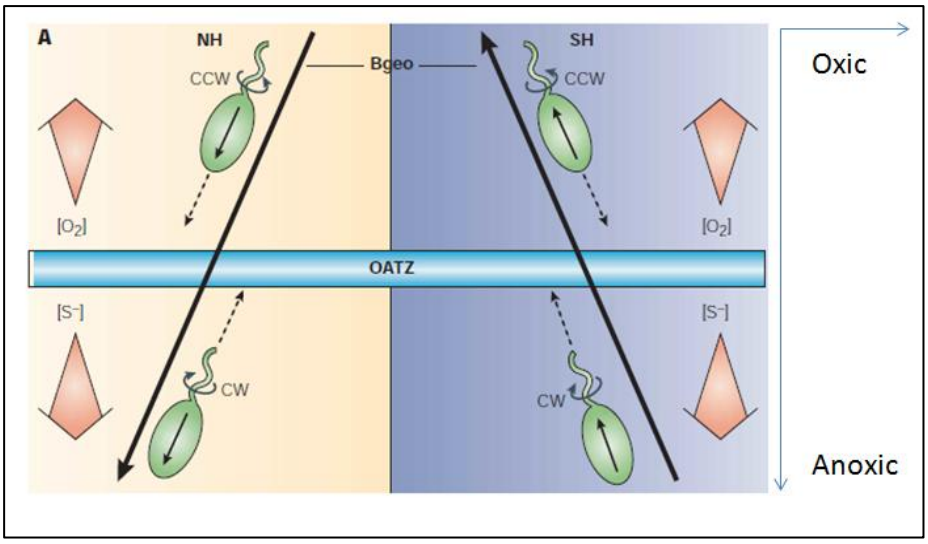

Figure 10. Schematic representation of Magneto-aerotaxis in the northern (NH) and southern (SH) hemispheres.

MTB exploit magnetic field to find their optimal oxygen concentration at the microaerobic oxic–anoxic transition zone (OATZ). To move across different stratifications, in both the hemispheres, MTB on the oxic side of OATZ swim down geomagnetic field lines (Bgeo), whereas those on the anoxic side swim up along Bgeo. The MTB on oxic side of OATZ rotate their flagella counterclockwise (CCW), whereas the ones on the anoxic side rotate their flagella clockwise (CW). MTB showing north or south-seeking behaviour show also different magnetic polarity, indicated by arrows. Image adapted from (Bazylinski & Frankel, 2004)

1.6.3. The magnetosome formation

The magnetosome formation is a well-modulated process, orchestrated by a high number of genes, most of which belong to a genomic area that is highly conserved among different species, called Magnetosomes Island (MAI). The MAI is a region of 130 kb (Ullrich et al., 2005) which contains 106 annotated Open Reading Frame (ORF). To better understand its function, the MAI was divided into 14 independent regions, named R1-R14 by Murat et al. (Murat et al., 2010). The MAI contains five different polycistronic operons, named: *mamAB*, *feoAB1*, *mamGFDC*, *mms6*, *mamXY*, the most conserved of which is *mamAB* (Figure 11). Without MAI or the operon *mamAB*, there is no magnetic phenotype (Murat et al., 2010; Lohsse et al., 2011). The other operons, such as *mamGFDC*, *mamXY* and *mms6* in *MSR-1*, vary from strain to strain, so to explore magnetosome formation researchers preferred to focus on genes of *MSR-1*, considered as a model of MTB-related and specific genes. The magnetosome formation is a multi-steps process. The major ones are named: *magnetosome membrane formation*, *magnetosome protein sorting*, *magnetosome alignment into chains*, and *biomineralization*. The principal genes involved in these processes are all contained in the conserved *mamAB* region (Murat et al., 2010). The MAI is such a critical region, which could recreate alone the entire pathway of magnetosome biogenesis. Indeed, when the 30 genes of which MAI is composed were introduced using expression cassettes in *Rhodospirillum rubrum*, a non-magnetic bacterium, it became magnetic (Kolinko et al., 2014). This experiment is the proof of principle that it is possible to transfer the magnetic properties of MTB in a non-magnetic bacteria.

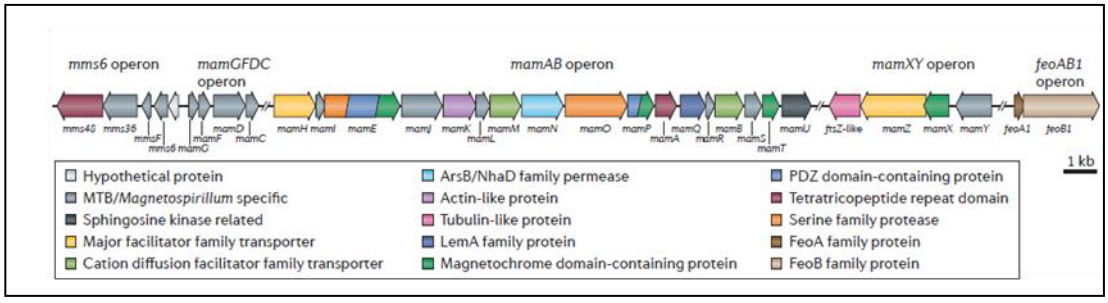

Figure 11. Schematic representation of the genomic magnetosome island (MAI).

In the MAI are present the five operons containing the genes involved in the magnetosome biogenesis. The genes are coloured according to the features of their encoded proteins. Original image adapted from (Uebe & Schuler, 2016)

1.6.4. The magnetosome membrane formation

Magnetosomes membrane (MM) has been investigated for a long time, as it is believed to be one of the major players in magnetosomes biomineralization and cell protection from magnetosomes toxic products. The MM creates a specialised environment inside the bacterium, where pH, iron and redox are finely tuned, acting as a "nano-reactor" for crystals formation (Uebe & Schuler, 2016). However, the fragility of the magnetosome membranes made investigations arduous. The magnetosome membrane biogenesis was clarified by using Electrical capacitance tomography (ECT). ECT is a technique which takes images from frozen samples at different angles using an electron beam; images are then assembled in a 3D reconstruction by using an algorithm. ECT images reveal that magnetosome membrane could originate as an invagination of the inner membrane (Komeili et al., 2006; Tocheva et al., 2010). Magnetosome vesicles remain as invagination along all the entire mineralisation process, either empty or filled with iron. Moreover, invaginations originate from different non-specific spots of the MTB inner membrane, suggesting that vesicles formation process is less regulated respect to the vesicles formation in the eukaryotic cell (Faini et al., 2013). The formation of vesicles seems a necessary condition for the biomineralization process happening; however, the opposite is not true, as MTB show vesicles in iron deprived conditions (Fukuda et al., 2006; Grunberg et al., 2004; Komeili et al., 2004; Murat et al., 2010; Scheffel et al., 2006). It was speculated that magnetosomes, integrating within the inner cell membrane, could guide cell movements along the magnetic field, without any additional mechanism. However, the proposed mechanism is not valid for all the magnetic bacteria, as in uncultured magnetic cocci and in *Mbav*, magnetosomes were found clearly far from the inner membrane (Jogler et al., 2011).

The genes involved in membrane invagination are *mamB, I, L, Q* and *Y*, as their deletion cause the absence of magnetosomes vesicles in *AMB-1*. Their presence is necessary but not sufficient for membrane invagination, as they are unable to restore wild-type magnetosomes membranes in *ΔmamAB* experiments (Murat et al., 2010).

In particular, MamB seems to have a function in magnetosome membrane invagination and iron transportation; whereas mamI and mamL are integral membrane proteins associated with the MM (Uebe et al., 2011). MamB is believed to act as a landmark protein, which directs the formation of multiprotein complexes to induce invagination in the later steps of magnetosome biogenesis. MamY is another protein associated with membrane invagination (Tanaka et al., 2010), and it is believed to be involved in constriction of the cell membrane to create the magnetosome cell membrane, in deformation of MM and in magnetite growth. MamQ is an MM integrated protein; it is well conserved among different MTB phyla, and it is believed to have a role in membrane bending.

1.6.5. The magnetosome protein sorting

Magnetosomes proteins are usually targeted to the MM, or to the cytosolic side of it, as a consequence of a process which is still ignored. MamA, a highly conserved magnetosome-associated protein, moves freely and independently from magnetite formation (Barber-Zucker et al., 2016). When MamA is removed in *AMB-1*, a large number of magnetosomes is empty; however, it does not influence magnetosome formation (Komeili et al., 2004). In vitro, MamA binds different proteins, forming a multiprotein complex that surrounds the magnetosome membrane. MamA acts as a multiprotein interaction site, forming homo-oligomers with central pore cavity (Pan et al., 2012; Yamamoto et al., 2010; Zeytuni et al., 2011).

MamE, a predicted integral membrane protein containing a transmembrane region (TM), has a role in protein sorting and crystal biomineralization initiation (Quinlan et al., 2011; W. Yang et al., 2010). As MamE deletion in *AMB-1* causes misplacing of different proteins, it is likely that MamE physically interacts with the other proteins (Murat et al., 2010).

1.6.6. The magnetosome alignment into chains

MTB sense the magnetic field by aligning their magnetosomes, each of them made of a single-magnetic domain, in a linear chain. Unlike the single magnetosome, insufficient to detect the magnetic field, the magnetosome chain forms a larger magnetic dipole that can identify and respond to the magnetic field, functioning as a needle (Frankel & Bazylinski, 2006). Two proteins are suggested to be involved in magnetosome alignment, MamK and MamJ. MamK, an actin-like protein, is supposed to have a crucial role in magnetosomes alignment, providing a track to which magnetosomes could move on (Bennet et al., 2015; Draper et al., 2011; Pradel et al., 2006). MamK, containing an ATP-binding site with ATPase activity, guides singles magnetosomes in a single chain located in the mid-cell, and it is also believed to be involved in the filaments dissociation (Draper et al.,2011; Sonkaria et al., 2012; Ozyamak et al., 2013; Pradel et al., 2006; Rioux et al., 2010; Taoka et al., 2007; Uebe & Schuler, 2016). In *AMB-1* mutants lacking MamK, the protein function is partially replaced by a MamK-like protein, codified outside the MAI region (Rioux et al., 2010), but the resulting magnetosomes show a reduction in size and are not well organised (Katzmann et al., 2010).

MamJ is a protein not conserved within all MTB, which is co-transcribed with MamK. MamJ is present on a structure which connects the two ends of the cells, and it is believed to play a role in magnetosome chain organisation (Draper et al., 2011; Katzmann et al., 2010; Scheffel et al., 2006). It is assumed that MamJ cooperates with MamK in the organisation of magnetosomes into chains (Scheffel et al., 2006). Strong magnetic field disturbs MamJ and MamJ/MamK interaction (Körnig et al., 2014), but not the filaments created by MamK. It was also demonstrated that MamJ relies on other magnetosomes proteins for its localisation, such as MamE and MamK, whose presence is essential for MamJ correct localisation in MSR-1, but not the opposite (Katzmann et al., 2010; Scheffel et al., 2006).

1.6.7. Biomineralization

Biomineralization is a process lead by living organisms that exploit organic molecules for crystal nucleation and growth under mild condition (Amemiya et al., 2007). The MM protects the internal environment of the magnetosome, which provides the chemical conditions required for the biomineralization. The process of crystal maturation is fine tuned and depends on extracellular iron: to explain it, the following mechanisms have been proposed. In the first one, the extracellular iron enters into cell cytoplasm by cytoplasmic membrane transporters and then it is transported into MM vesicles by magnetosome-specific transporters; in the second proposed model iron is transported across the cytoplasmic membrane, then it is bound to organic compounds and lately it is released into the magnetosome without the transport of free iron through the cytoplasm. The third mechanism proposes that iron is directly imported into vesicles from the periplasm of the cell envelope (Uebe & Schuler, 2016). The steps of biomineralization have been defined and are: *nucleation*, *growth* and *morphological regulation* (Tanaka et al., 2011).

Nucleation is a well-orchestrated process that in the most of the cases ends up with the formation of a single iron crystal for each magnetosome. Nucleation occurs when inside the magnetosome there are the right conditions -pH should be $\geq$7, and the redox potential should be low- that favour the formation of crystalline iron phase from soluble $Fe2^{+}$and $Fe3^{+}$ (Uebe & Schuler, 2016). To date, two proposed models of nucleation of magnetite crystals have been proposed: the first one suggests that $Fe2^{+}$and $Fe3^{+}$ precipitate, forming the magnetite straight away; while the second one suggests that the magnetite formation occurs by several discrete steps, involving the creation of precursor mineral phases that are transformed into magnetite (Faivre & Godec, 2015). The definition of the mechanisms which lead to the growth and to the morphological regulation of crystals are still obscure, and experiments conducted so far are based on the creation of mutants lacking the proteins believed to be involved in such process, but a complete picture is still missing (Uebe & Schuler, 2016).

The proteins involved in magnetosome biomineralization process so far discovered are: MamM, MamB, MamO, MamE, MamP, MamT, MamX, MamZ, MamH, MamN, MamS, MamR and the FtsZ-like proteins.

MamM is an integral membrane protein localised to MM. MamM is believed to be involved in iron transport, magnetite nucleation, crystals growth and in other MM proteins localisation (Murat et al., 2010). The first function was attributed to MamM due to the protein homology with cation diffusion facilitator (CDF) protein family and because MamM single point mutation leads to magnetite biomineralization alterations (Murat et al., 2010). MamM seems to participate in many different activities, like accumulating iron in the magnetosome lumen and keeping high the magnetosome pH for magnetite/greigite biomineralization (Barber-Zucker et al., 2016). It was found that MamM is responsible also for MamB stability, a protein taking part to both the iron accumulation and to the MM invagination processes. In *MSR-1*, the dependence of MamB stability from MamM suggests a possible interaction between the two proteins, maybe forming heterodimers (Uebe et al., 2011).

MamO is an integral membrane protein believed to be involved in crystal nucleation, as mutants lacking MamO possess magnetosomes without iron content and low magnetism (Guo et al., 2012; W. Yang et al., 2010).

Besides being involved in protein sorting (Quinlan et al., 2011; W. Yang et al., 2010), MamE takes part also in the biomineralization process. It was demonstrated that MamE deletion causes magnetosomes deprived of the iron content and without magnetite synthesis (Murat et al., 2010), so it is supposed that MamE could mediate biomineralization acting as a molecular switch together with other proteins, such as MamO (W. Yang et al., 2010). MamE, as well as MamP, T and X, possess the CXXCH motif, that is a c-type cytochrome motif which binds a haem, acting in iron reduction/oxidation (Quinlan et al., 2011; Raschdorf et al., 2013). The CXXCH motif seems to be unique of MTB, and so it was called "magnetochrome", defining a new class of cytochromes (Siponen et al., 2013). Since MamE, P, T and X are the only redox proteins, it was supposed that their role could be determinant in MTB crystal

shape and MTB evolution (Siponen et al., 2012). MamE is also expected to direct the synthesis and in the maturation of 20 nm iron-oxide crystals (Quinlan et al., 2011).

MamP is an integral membrane protein believed to be involved in crystal size and number determination as well as in cell-cycle regulation and stoichiometry optimisation of $Fe2^{+}$ and $Fe3^{+}$, (Taoka et al., 2014). MamT is another integral protein believed to influence the magnetite crystal growth and electron-redox chain (Jones et al., 2015; Murat et al., 2010; Siponen et al., 2013). Also MamX is believed to arrange crystal shape and maturation and to be involved in redox control (Barber-Zucker et al., 2016; J. Yang et al., 2013).

MamH is suggested to act in the magnetite biomineralization and magnetosomal iron transport (Uebe et al., 2011; Zeytuni et al., 2011). MamZ is believed to take part in iron transport (Zeytuni et al., 2011) and in electron shutting and redox reactions ions (Brokx et al., 2005). Mutants lacking both MamH and MamZ show more severe phenotypes than mutants for only one protein, suggesting a redundant function of the two proteins (Zeytuni et al., 2011). MamN is a TM protein suspected to be an antiporter, which extrudes protons released from magnetosome precipitation, and increases the pH inside the magnetosome- a necessary condition for in vitro magnetite synthesis (Komeili, 2012; Nudelman & Zarivach, 2014). Indeed, MamN deletion causes mutants containing empty magnetosomes and no magnetic response (Murat et al., 2010).

FtsZ-like proteins are a copy of FtsZ, defined as bacterial tubulin-like cell division proteins found in three *Magnetospirillum* species (Ding et al., 2010; Richter et al., 2007). FtsZ-like proteins genes are localised into the MAI region, in *MamXY* operon, a feature that suggests a possible involvement of these proteins in magnetosome chains assembly or in *Magnetospirillum* cells division (Jogler & Schuler, 2009; Müller et al., 2014).

MamS and MamR are MTB specific proteins: MamS is thought to regulate magnetosome size and morphology, while MamR is believed to be involved in the magnetosome size and number determination (Murat et al., 2010; Richter et al., 2007).

1.6.8. Proteins involved in arrangement of magnetosome crystal size and morphology

Some proteins, even if not directly involved in magnetosomes biomineralization process, play a role in the determination of magnetosomes size and morphology (Barber-Zucker et al., 2016). The protein discovered so far associated with magnetite in *AMB-1* are: MamC, MamD, MamG (that in this strain are respectively named Mms13, Mms7 and Mms5) and protein Mms6. These proteins are supposed to localise in MM and to tightly interact with magnetite surface (Arakaki et al., 2014; Tanaka et al., 2011). As these genes are present only in *AMB-1* strain, which synthesise octahedral shaped magnetite, it was supposed that their function is linked to this particular feature (Arakaki et al., 2014).

MamC (Mms13) protein structure is predicted to be composed of two TM helices and one acidic alpha-helical loop present in magnetosome lumen, which is believed to bind iron and to participate to iron accumulation, creating the proper conditions for the magnetite nucleation (Valverde-Tercedor et al., 2015). Moreover, MamC is the most abundant protein exclusively found in MM (Arakaki et al., 2003; Grunberg et al., 2004; Grunberg et al., 2001; Lang & Schüler, 2008). MamD, also called Mms7, is also abundant in MM and his function is believed to be associated with the crystal morphology, as AMB-1 mutants for MamD show crystals reduced in size and with different faces respect to wild-type (Arakaki et al., 2014; Grunberg et al., 2001). MamG (also called Mms5) is another abundant protein localised in MM, predicted to be formed by two TM helices and a charged connecting loop between them that contacts magnetite crystals. (Lang & Schüler, 2008; Nudelman & Zarivach, 2014). As MamG deletion causes crystals reductions, it is possible that the protein has a role in crystal growth control, maybe interacting with the crystal face (Arakaki et al., 2014).

MamF is similar to MmsF (61% amino acid identity between the products), and it is the second most abundant protein in MM after MamC (Lohsse et al., 2014; Richter et al., 2007). The magnetosomes number and size is more affected in double mutants for MamF and MmsF, respect to mutants with single MmsF deletion, suggesting that

MamF could influence these magnetosome features (Lohsse et al., 2014). The secondary structure of MamF is predicted to be formed by three TM helices, two of whom connected by a loop with charged residues that could interact with magnetite crystals (Nudelman & Zarivach, 2014). Also Mms6 and MmsF are involved in crystal size and morphology determination, however, due to the interest they have raised, they will be described in a separate section. The different steps of magnetosome formation to which the described proteins take part are shown **Figure 12**.

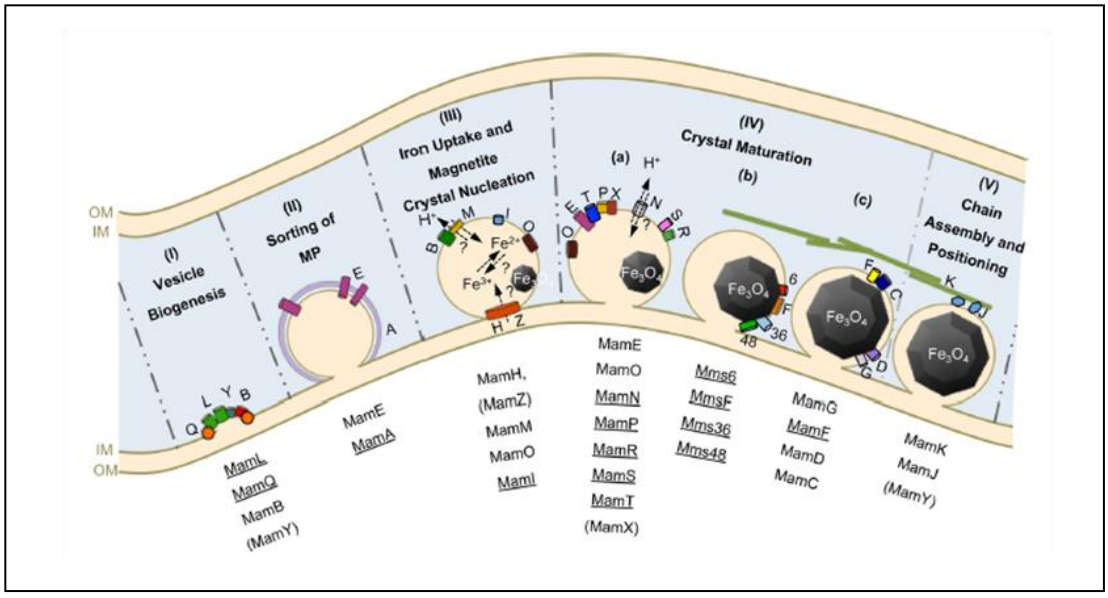

Figure 12. Hypothetical representation of magnetosome biogenesis with proteins which take part to the process in *M. gryphiswaldense*.

OM stands for outer membrane, while IM stands for inner membrane and MP stands for magnetosome protein. Original image taken from (Lohsse et al., 2014).

1.7. Mms6 and MmsF: two interesting proteins involved in MNPs biosynthesis

Rationale for using Mms6 and MmsF proteins:

MHT is a promising tumour treatment, but it is still far from optimal, due to the use of synthetic MNPs, which display cell toxicity and poor tumour localisation. The need of finding an alternative to chemical MNPs in MHT is of primary importance to improve the whole treatment.

A possible approach is to use MTB magnetosomes, which are characterised by high SAR and a better heat distribution, but this idea has raised concernings regarding the application of bacterial structures inside the human body. An alternative to the magnetosomes use is the creation of engineered human MSCs able to biosynthesise MNPs. MSCs, indeed, could be easily engineered and show an exceptional tumour homing ability.

The final purpose of this study was to create MSCs able to biosynthesise MNPs, and to deliver them directly inside the tumour. Then, tumours will be exposed to AMF, determining the killing of both the magnetic MSCs and of the tumour cells.

Mms6 and MmsF are two proteins believed to play a **paramount role in iron crystal morphology regulation in MTB** (Amemiya et al.,2007; Murat et al.,2012).

For this purpose, MTB *mms6* and *mmsF* genes, alone or in combination, were transfected in human MSCs, following codon-optimization for mammalian expression.

The protein Mms6, firstly introduced to the scientific audience by Arakaki et al. in 2003, was isolated from magnetosomes of *M. magneticum AMB-1* together with the others magnetosomes associated proteins, after lipid membranes stripping and treatments based on detergent and heat (Arakaki et al., 2003). The extracted proteins were named "*Mms*", which stands for "*magnetosome membrane specific*", and were numbered according to their molecular mass (Arakaki et al., 2003). Among the four proteins discovered, named Mms5, 6, 7 and Mms13, Mms6 presents a negative charge at neutral pH, being different from all the other Mms proteins, that are positively charged (Arakaki et al., 2003). Mms6 gene sequence shows a high consensus among different MTB species (Staniland & Rawlings, 2016), especially in the C-terminal region (**Figure 13a**). The mass of the protein codified by the *mms6* gene is 12-15 kDa, larger than the 6 kDa Mms6 protein identified by SDS/PAGE, suggesting that Mms6 undergoes in vivo protease cleavage (Arakaki et al., 2003; Grunberg et al., 2004). Mms6 has a predicted secondary structure formed by an unstructured N-terminal domain, a transmembrane helix and a C-terminal, which may form a α-helix structure (Nudelman & Zarivach, 2014), (**Figure 13b**). The presence of the helix is supported by protein model structure and sequence analysis, while 3D models show a negative patch on its carboxy-terminal domain (CTD) that is believed to be an iron binding site (Nudelman & Zarivach, 2014), (**Figure 13c**).

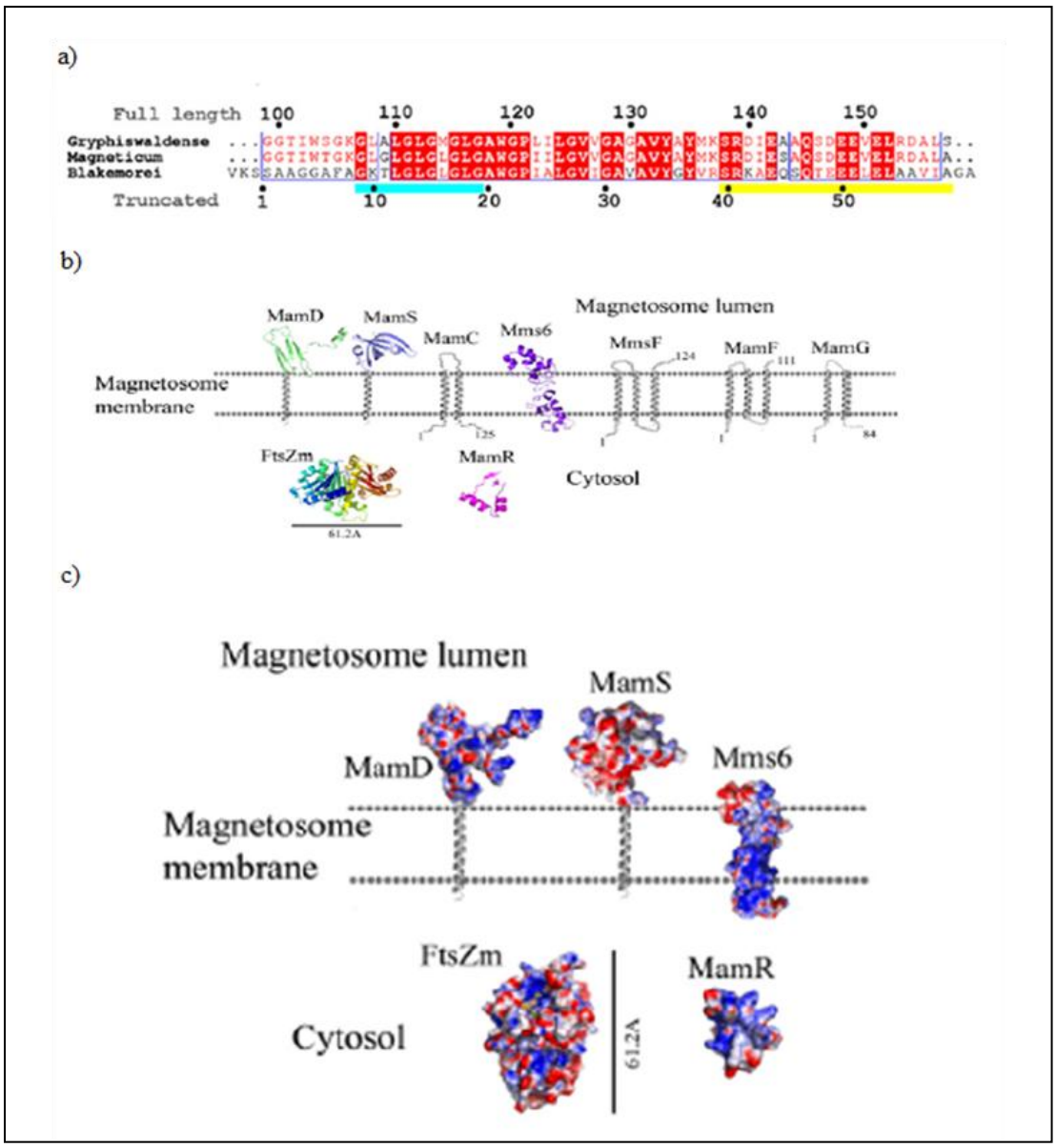

Figure 13. Mms6 protein description.

a) Mms6 truncated protein sequence alignment from different MTB species. Residues conserved are highlighted in red boxes, and similar residues are in red font. The first 98 residues are not shown, but are less conserved. The glycine-leucine repeated sequences are indicated by blue bar, and the C-terminal amino-acid region are highlighted in yellow. Original picture taken from (Staniland & Rawlings, 2016). b) Ribbon representation of Mms6 protein structure among other proteins involved in magnetosomes size and shape control. TM helix are represented in grey and protein size is indicated in Angstroms, by black bar. c) 3D prediction of Mms6 protein structure among other proteins involved in magnetosomes size and shape control. Negative charges are in red and positive charges are in blue. Protein size is indicated in Angstroms, by black bar. Original pictures taken from (Nudelman & Zarivach, 2014).

1.7.1. Mms6 protein and its function

The debate regarding the function of Mms6 -nucleating or shape control protein- is still open (Staniland & Rawlings, 2016). To better understand the role of Mms6 in *M.magneticum AMB-1*, Tanaka et al. performed *mms6* gene knockout experiments, generating a *Δmms6* mutant strain. Although the loss of *mms6* gene did not affect the bacteria growth and the number of crystals, it was observed that crystals in *Δmms6* mutants are: 1) smaller respect to the wild-type, 2) show indefinite shapes instead of the cubo-octaedral structure observed for the wild-type, 3) present a (110) face on the magnetic face surface, characterized by an higher energy and instability that is generally noticed in not matured crystals (Tanaka et al., 2010); (**Figure 14**). Moreover, SDS-PAGE experiments in *Δmms6* strains point out a decrease of Mms5, 7 and Mms13 proteins expression, suggesting that Mms6 could be involved not only in crystal shape and definition processes, but also in other Mms proteins recruitment. These results confirmed that Mms6 regulates crystals formation, as already proposed by Amemiya and further reported by Murat et al. (Amemiya et al., 2007; Lohsse et al., 2014; Murat et al., 2012). Nevertheless, other findings theorise a role for Mms6 in magnetite crystal nucleation (Arakaki et al., 2003; Arakaki et al., 2014; Galloway J.M. et al., 2012). Magnetite (Fe_3O_4), is formed by ferric ($Fe3^+$), and ferrous iron ($Fe2^+$), at the 2:1 stoichiometric ratio. One way of producing magnetite in vitro relies on mixing these two valence irons that are subsequently precipitated by raising the pH (Staniland & Rawlings, 2016). Araki et al. found that by adding Mms6 (20 ug/ml) at room temperature co-precipitation, the products of the reaction were mainly magnetite and an uncontrolled iron oxide precipitate respect to the wild-type crystals (Arakaki et al., 2003). The particles also showed a cuboidal shape, and a narrow size distribution, similar to the crystals observed in the magnetosomes. This experiment was repeated by other researchers, changing some reaction parameters (Amemiya et al., 2007; Bird et al., 2016; Galloway J.M. et al., 2012), and in all the cases it was demonstrated that the Mms6 addition increased the magnetite production. It was also observed that the crystal size is influenced by the protein surface curvature. Indeed when Mms6 is immobilised on the surface the crystals size is much bigger than when the protein is present in micelles (Bird et al., 2016). A

possible explanation provided for this behaviour is that by changing the protein curvature -flat or concave- also the angle of contact between Mms6 and the mineral changes, creating different particle sizes (Tanaka et al., 2011).

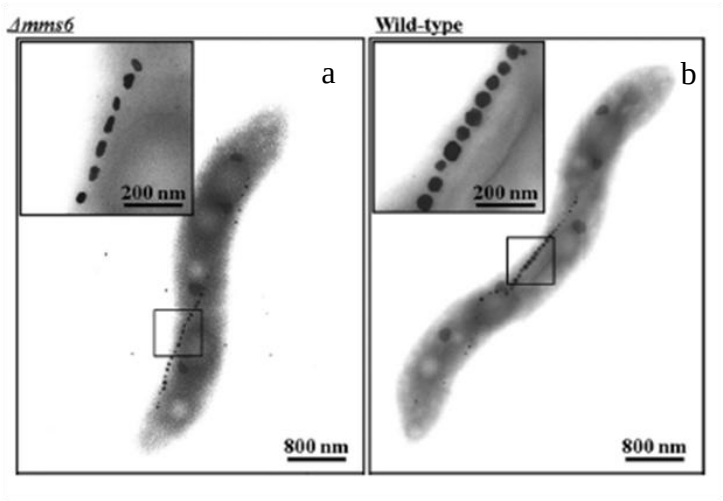

Figure 14. TEM of a) *Δmms6* mutant and b) wild-type *M.magneticum AMB-1* strains.
In a), the loss of *mms6* gene affects crystals size and shape, which appear smaller and of indefinite shape respect to the wild type (b). These results suggest that Mms6 could play a role in crystals formation.
Original picture taken from (Tanaka et al., 2011).

1.7.2. Mms6 iron binding model

Mms6 is an amphiphilic protein, which means that it possess both a hydrophilic (C-terminal) and a hydrophobic (N-terminal) region, so in water Mms6 tends to form micelles, exposing the hydrophilic C-terminal outside and shielding the hydrophobic N-terminal within the core. Mms6 structure investigation by size-exclusion chromography, later confirmed by dynamic scattering experiments, suggest micelle dimensions of 200-400 kDa, formed of 20-40 protein subunits. Moreover, it was found that in presence of iron, the micelles tend to form highly ordered structures, such as discs, presumably interacting with iron (L. Wang, Prozorov, et al., 2012; H. Zhang et al., 2015).

Staniland et al. proposed that Mms6 self-assembles creating proteins rafts on the interior MM, exposing a C-terminal surface, similar to the surface of in vitro

micelles, but with opposite curvature (Staniland & Rawlings, 2016), (**Figure 15**). They noticed that the Mms6 protein without the N-terminal (named C20Mms6) could self-assembly, but fails in controlling the magnetite formation. The Mms6 self-assembly hypothesis was also guided by the observation that the 6 kDa Mms6 protein sequence is rich of glycine-leucine repeated sequence (**Figure 13a**), a feature of self-assembly proteins, while the repeated sequences are missed in the C20Mms6. According to Staniland et al., the adjacent Mms6 molecules self-assemble through a "*knob and hole arrangement*", where hydrophobic residues interlock adjacent Mms6 molecules creating "*regularly packed structure*" (**Figure 15c**). In this way, the acidic C-termini create a negatively-charged surface which binds iron. In addition to that, Staniland et al. studied the magnetite precipitation with or without Mms6 at different pH titrations, finding out that the action of Mms6 below pH 4 is negligible and that Mms6 increases the magnetite production of the 20% in "*ferrous-rich ferric: ferrous ion ratios*", acting as a "*mineral/ferrous ion buffer*". At pH<4, the acidic groups of Mms6 are protonated, a condition that reduces Mms6 iron binding ability, while at pH=7, deprotonation occurs forming negatively charged micelles with negative-charged surface that binds iron, with a more accurate binding activity of ferrous iron (Rawlings et al., 2016; Zhang et al., 2015). All together, Staniland et al. proposed model suggests that: a) Mms6 self-assembles in the internal MM in a regulated way with a "*knob and hole*" mechanism, exposing the negatively charged carboxylate-rich surfaces; b) Mms6 binds iron on such surfaces when pH is near to 7, with a more specific binding activity for ferrous iron; c) it is possible to tune the MNPs size by changing the protein surface curvature.

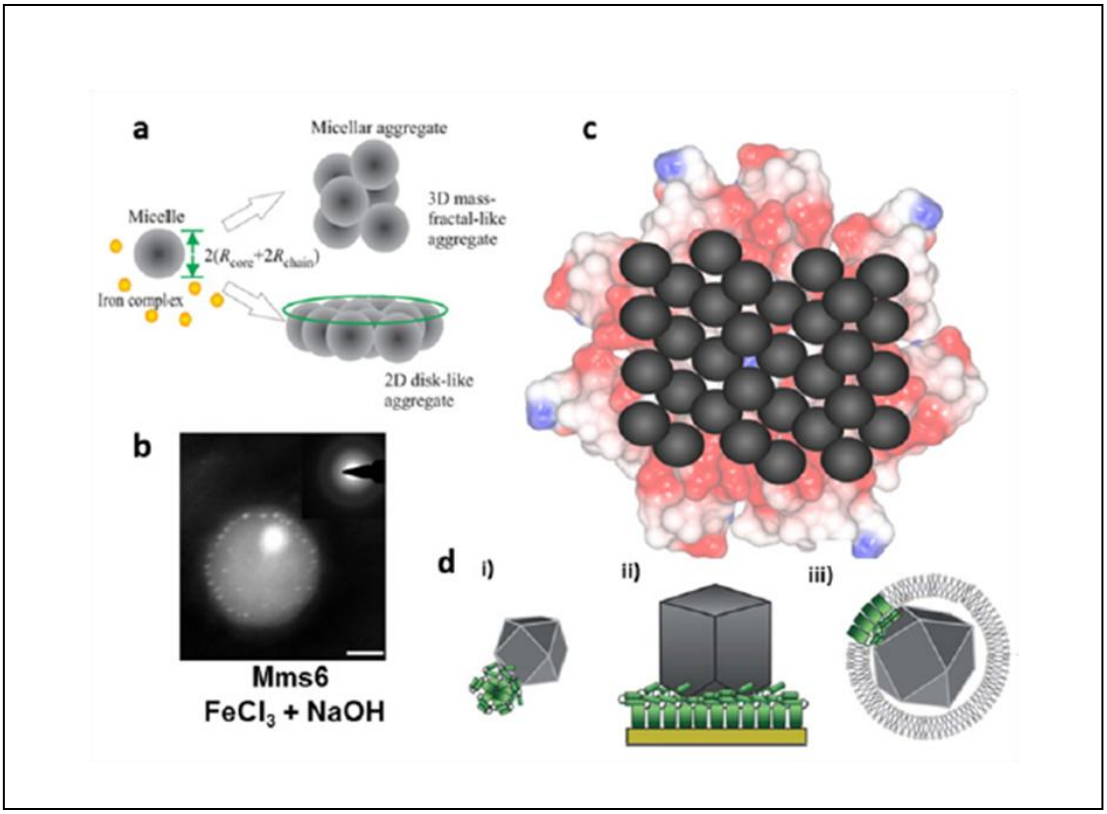

Figure 15. Mms6 self-assembly models.

a) Schematic representation of the Mms6 micellar assembly model (H. Zhang et al., 2015) in (Staniland & Rawlings, 2016). b) iron oxide MNPs (indicated by bright spots) nucleate and precipitate on the surface of Mms6 micelles, scale bar =20 nm (Kashyap et al., 2014) in (Staniland & Rawlings, 2016); c) schematic model illustrating Mms6 self-assembly in negatively charged rafts, containing C-terminal binding sites for regular iron ions binding to nucleate magnetite formation in (Staniland & Rawlings, 2016); d) schematic representation of how the crystal size is influenced by Mms6 protein surface curvature: i) Mms6 is in solution, forming micelles, ii) Mms6 is on a surface, iii) Mms6 is on MM. From (Bird et al., 2016) in (Staniland & Rawlings, 2016).

1.7.3. MmsF protein and its function

MmsF is an integral MM protein (Murat et al., 2012; Nudelman & Zarivach, 2014) encoded by *mmsF* gene, which belongs to the *mms6* gene cluster of MAI (**Figure 16a**). In *M. Magneticum* AMB-1, *mmsF* is located directly downstream to *mms6*, separated from it by only 17 nucleotides. No promoter was identified upstream of *mmsF*, so *mms6* and *mmsF* are supposed to be co-transcribed (Murat et al., 2012).

MmsF predicted structure is formed of three transmembrane spanning (TMS) helices, with the C-terminus located inside the MM, and the N-terminus protruding in the magnetosomes cytoplasm (Murat et al., 2012), (**Figure 16b**). MmsF was firstly discovered as an abundant MM protein in *Magnetospirillum Magneticum MS-1*, but other homologs were also found in other species of MTB. Rawlings et al. identified two homologs of MmsF (amb0957) in *M. magneticum AMB-1*, denoted as *mamF* (amb0953) and *mmxF* (am1026), (**Figure 16c**). TMS helices and loops that connect them are highly conserved in all the proteins studied, as indicated in **Figure 16c**. Studies on MmsF homologs show that even if they share more than 65% of identity with *mmsF*, there is not redundancy between functions of these genes. Indeed, it was demonstrated that the deletion of the *mmsF* gene causes deficient magnetosomes crystallisation that is not recovered by *mamF* and *mmxF* (Rawlings et al., 2016).

When MmsF, MamF and MmxF are in the water, they solubilise and aggregate to protect their hydrophobic region from the aqueous environment (Rawlings et al., 2016). This unusual soluble behaviour was analysed in water by TEM and cryoelectron microscopy, confirming that in presence of water, MmsF and its homologs self-assemble into precise vesicles-like structures, called "*proteinosomes*" by Rawlings et al. In their model, helices participate to protein assembly, while the loop connecting helices 1 and 2 is involved in magnetite formation process. Moreover, MmsF, MamF and MmxF create a protein island inside the MM, directing their acidic termini towards the inner part of magnetosome, so that they can take part in the crystal nucleation. However, despite their homology and their tendency to form ordered vesicles-like structures in water, only MmsF can improve the uniformity and the magnetisation of particles in vitro when added to magnetite precipitation reactions, while MamF and MmxF give origin only to mixed irons. MmsF is also the only protein among the three investigated to share the same "acid acid-acid-X-acid" motif with Mms6, adding weight to the hypothesis that MmsF is involved in magnetite oxides formation. Murat et al., trying to clarify the MmsF function in biomineralization, discovered that *ΔmmsF* mutants show misshapen crystals, carrying severe defects. These findings define a pivotal role for MmsF in biomineralization. Murat et al. also discovered that, when Mms6 is deleted, MamFDC proteins inhibit the action of MmsF. Indeed, MmsF recovers the wild

phenotype in *ΔR3 mutants*, lacking both *mms6* and *mamFDC* clusters, but fails to recreate the wild-type features in *Δmms6c1* mutants, which still contain *mamFDC* genes. These findings suggest that the magnetite synthesis is a complex phenomenon, to which many players take part. To further explore the MmsF role in magnetite formation, Murat et al. created mutants expressing only *mamAB* gene cluster, called miniMAI strain. The miniMAI strain is still able to form magnetosomes chains, even if the magnetosomes are fewer and of smaller dimension compared to the wild-type. In vivo MmsF can ameliorate the phenotype of miniMAI strain, enhancing the magnetite production and the answer to a magnetic field; however, it fails in completely recovering the wild-type phenotype. This behaviour suggests that other MAI regions, such as R6 combined with R14, could orchestrate the biomineralization, that is a result of many complexes, discrete steps (Murat et al., 2012). Overall, *mmsF* functions could be summarised as follow:

1) *mmsF* restores wild-type phenotype in *Δmms6c1* mutants for magnetisation but not for crystals shape (*mms6* indeed is not present);

2) *mmsF* restores wild-type phenotype in ΔR3 mutants;

3) *mmsF* determinates crystals size and shape, as *ΔmmsF* mutants grow smaller nanoparticles with different geometry respect to wild-type and fail to mature in the cubo-octaedral shape.

The complete list of Mam and Mms proteins and their suggested role are summarised in **Table 4**.

.

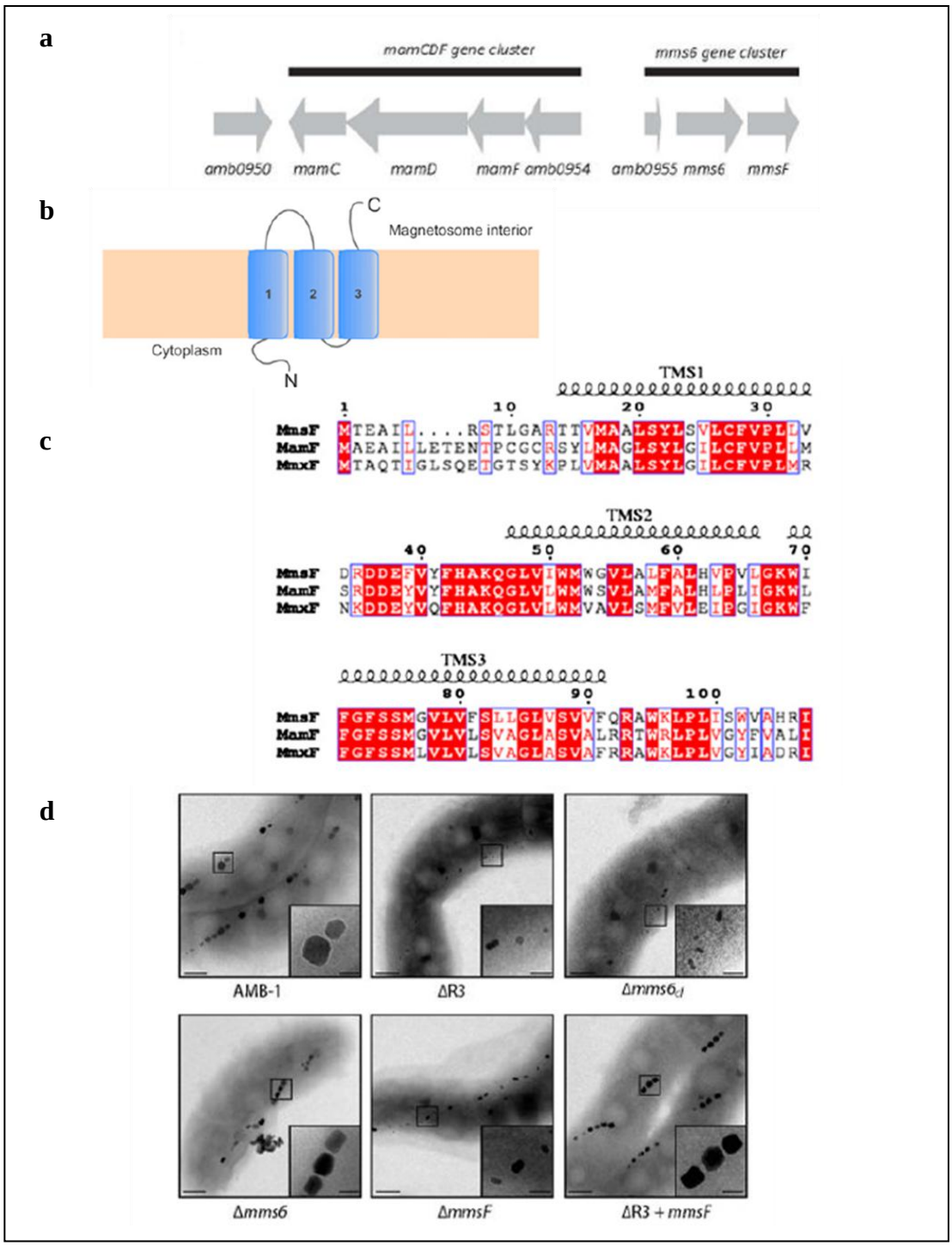
a
mamCDF gene cluster
mms6 gene cluster
amb0950
mamC
mamD
mamF
amb0954
amb0955
mms6
mmsF
b
C
Magnetosome interior
1
2
3
Cytoplasm
N
c
TMS1
TMS2
TMS3
MmsF
MamF
MmxF
d
AMB-1
ΔR3
Δmms6-1
Δmms6
ΔmmsF
ΔR3 + mmsF

Figure 16. MmsF description.

a) Schematic representation of the *mms6* gene cluster to which *mmsF* gene belongs. The genes and ORFs comprised are represented by grey arrows, indicating the orientation of transcription. The gene name, or gene number, is indicated below each gene or ORF. The black lines show the groups of genes identified as gene clusters. b) Schematic representation of the MmsF protein membrane spanning. c) The Sequences of MmsF, MamF, and MmxF were aligned in ESPript. Conserved residues are highlighted in red, similar residue types are shown in blue boxes, and TMS helices are indicated. d) Electron micrographs of wild-type AMB-1, ΔR3, Δ*mms6*cl, Δ*mms6*, Δ*mmsF* mutants and the ΔR3 mutant complemented with *mmsF*. The insets are showing a higher magnification of the region boxed in the micrograph. Scale bars: 100 nm, insets 50 nm. Pictures a) and d) are original images taken from Murat (Murat et al., 2012). Pictures b) and c) are original images taken from (Rawlings et al., 2014).

Protein	#Amino acids	Encoding operon	Suggested role
MamA	217	*mamAB*	Protein sorting
MamB	297	*mamAB*	Membrane invagination, iron transport
MamC	125	*mamGFDC*	Crystal size and shape control
MamD	314	*mamGFDC*	Crystal size and shape control
MamE	772	*mamAB*	Protein sorting, redox control
MamF	111	*mamGFDC*	Crystal size control
MamG	84	*mamGFDC*	Crystal size and shape control
MamH	427	*mamAB*	Iron transport
MamI	76	*mamAB*	Membrane invagination
MamJ	466	*mamAB*	Magnetosome alignment
MamK	359	*mamAB*	Magnetosome alignment
MamL	122	*mamAB*	Membrane invagination
MamM	318	*mamAB*	Iron transport
MamN	437	*mamAB*	pH control
MamO	632	*mamAB*	Crystal nucleation
MamP	269	*mamAB*	Redox control
MamQ	271	*mamAB*	Membrane invagination
MamR	72	*mamAB*	Crystal size and number control
MamS	180	*mamAB*	Crystal size and shape control
MamT	174	*mamAB*	Redox control
MamX	268	*mamXY*	Redox control
MamY	370	*mamXY*	Membrane invagination
MamZ	660	*mamXY*	Iron transport, redox control
FtsZm	323	*mamXY*	Crystal size and shape control, denitrification
Mms6	136	*mms6*	Crystal size and shape control
MmsF	124	*mms6*	Crystal size and shape control

Table 4. List of Mam and Mms proteins and they suggested function.

Table adapted from (Barber-Zucker et al., 2016).

1.8. MSCs in tumour therapy

1.8.1. MSCs distinctive characteristics

Adult mesenchymal stem cells (MSCs), are non-haematopoietic cells described for the first time by Friedenstein et al.(Nancarrow-Lei et al., 2017). MSCs can be detected as an heterogeneous subgroup of stromal stem cells also in adult brain tissue, heart, lung, adipose tissue, umbilical cord, fetal tissue and bone marrow (Norozi et al., 2016).

It was reported that MSCs, in particular the ones isolated from bone marrow, adipose tissue, dental pulp, and other organs of the body, originate from blood vessel wall, and were found in the so-called perivascular "*niche*", that is the microenvironment responsible for the regulation of stem cells fate (da Silva Meirelles et al., 2008). The *niche* provides a plethora of signals to activate and/or repress genes and transcription programs. Accordingly to the stimuli received, stem cells are maintained in a dormant state (undifferentiated), or undertake the self-renewal or the differentiation pathway respectively, entering in different cell cycles, to fulfil the changing tissue demand during the life (Ferraro et al., 2010). From their perivascular location, MSCs can maintain the surrounding tissue, taking part to the blood vessels stabilization, tissue and immune system homeostasis regulation and focal tissue injuries repair (Figure 17) (D. A. Mukhopadhyay, 2017).

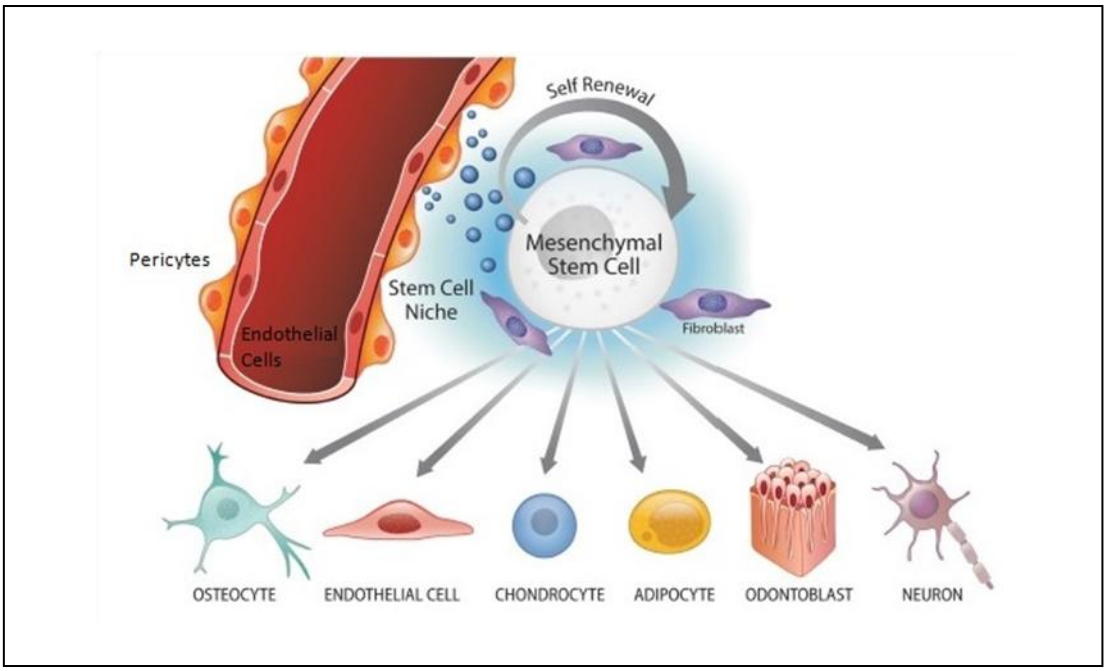

Figure 17. MSCs localise in perivascular *niche*.

From there, MSCs undergo self-renewal and maintain the surrounding cells/tissue. When specific signals are given, they could differentiate into the osteoblastic (osteocytic), endothelial, chondrocytic, adipocytic, odontoblastic, and neural lineages. Original picture taken from (M. Oh & Nör, 2015)

MSCs are defined by the following features (De Becker & Riet, 2016; Norozi, Ahmadzadeh, Shahrabi, et al., 2016):

- they show a fibroblastic morphology and they adhere to plastic when cultivated *in vitro*;
- they have the ability to differentiate in different cell lineage, such as chondrocytes, osteoblasts, adipocytes;
- they are able to self renewal and to support haematopoiesis;
- they must express CD105, CD73 and CD90, and lack expression of CD34, CD45, CD14, CD19, HLA-DR surface molecules.

Among these qualities, MSCs possess also specific characteristics: 1) they are multipotent; 2) they tend to migrate to sites of tissue injury/inflammation; 3) they show immunomodulatory capacities; 4) they could escape immune recognition; 5) even if they do not express naturally MHC class II antigens, they can upregulate the expression of these molecules after being exposed to inflammatory cytokines or during MSCs differentiation (Le Blanc & Ringden, 2005).

All these characteristic, especially the ability to engraft in the site of injury and their multipotency, make MSCs the suitable effectors in a wide variety of clinical fields, such as orthopaedics, where they have been employed for bone repair (Bashir et al., 2014), haematology, where they have been employed to support the engraftment of hematopoietic stem cells (Bashir et al., 2014; De Becker & Van Riet, 2015; Fouillard et al., 2007), or as a deliver in anticancer treatments (Durinikova et al., 2014; Hammer et al., 2015; Park et al., 2015; B. Qiao et al., 2015).

Tumour-homing is a discussed MSCs property. The list of tumours to which MSCs can home specifically comprises gliomas (Nakamizo et al., 2005), breast (Goldstein et al., 2010; Karnoub et al., 2007; Liu et al., 2011), colon (Hung et al., 2005), ovarian (Komarova et al., 2010), and lung carcinomas, among many other primary and metastatic tumours (Loebinger et al., 2009; Xin et al., 2009). However, MSCs tissue migration and homing is a complex process, guided by a multitude of molecules and signals, from which the destiny of the tumour depends.

As stated above, MSCs are characterized by self-renewal and multipotency properties.

Self-renewal refers to the ability to proliferate maintaining the undifferentiated state: the cell divides symmetrically creating two identical copies of itself for long periods of time. Depending on the stem cell, self-renewal is a well-modulated process, involving complex signalling networks. MSCs fate is regulated both by the niche signalling than by the circulation factors, which could enhance MSCs tropism or maintain the cells in their state (He et al., 2009).

Multipotency is defined as the ability of a progenitor cell to differentiate into a limited number of cell types with specific functions. The MSCs plasticity to differentiate in different cell lineages (osteogenic, adipogenic, and chondrogenic), together with their immunomodulatory and anti-inflammatory properties, make of these cells the best candidate for regenerative medicine, for the cancer therapy and for the treatment of autoimmune diseases such as type 1 diabetes (Murphy et al., 2013; Rohban & Pieber, 2017b).

Despite their interesting role in many clinical applications, MSCs origin *in situ* is still uncertain. Recent scientific works by Bruno Péault and others were aimed to disclose MSCs origin, finding out that MSCs originate from two progenitors cells, the pericytes and the adventitial cells (Corselli et al., 2012; Crisan et al., 2012).

These two different cell populations were found associated with the blood vessels, depending on their size. The outside of the small blood vessels, such as capillaries and microvessels, is encircled by pericytes, while largest vessels such as arteries and veins are surrounded by adventitial cells (Rohban & Pieber, 2017a). Pericytes are contractile cells, embedded in the basement membrane, characterized by a prominent nucleus, a poor cytoplasm, and finger-like projections. Through their projecting processes, pericytes wrap around small vessels giving structural integrity to the vessel wall. Moreover, pericytes support the stem cell self-renewal and proliferation and are involved in the tissue regeneration and repair (Birbrair et al., 2014; Kunisaki et al., 2013).

Adventitial cells were found on the *tunica adventitia*, one of the three layers of which all the blood vessels wall, with the exception of capillaries, are formed (the others two are named *tunica intima* and *tunica media*). For a long time, scientists have described the tunica adventitia as an unorganized layer made of fibroblasts and perivascular nerves, enclosed in a collagen-rich connective tissue (Majesky et al., 2011).

Only recently, it was found that the tunica adventitia is far more complex, and it is actively involved in the communication between vascular endothelial cells and smooth muscle cells, in the control of lumen size and in the immune response. The tunica adventitia contains different populations of cells, such as fibroblasts, macrophages, T-cells, B-cells, mast cells, and dendritic cells, which play a role in the vessel homeostasis and repair (Swedenborg et al., 2011).

Recent scientific works by Bruno Péault and others found that actually adventitial cells and pericytes could have other properties in addition to the ones already discovered. These cells, indeed, not only express MSC markers (e.g., CD10, CD13, CD44, CD73, CD90, CD105) but have also the ability to commit to osteogenic, adipogenic and chondrogenic cell lineages. Under inductive conditions in vitro, adventitial cells are able to differentiate into pericyte-like cells, which can then differentiate into mesoderm lineage cells, giving rise in culture to genuine MSC (Corselli et al., 2012; Crisan et al., 2012).

These findings define the pericytes and adventitial cells as the MSCs progenitors and ease the way for a better application of these cells in the regenerative medicine.

1.8.2. MSCs Homing in injury site

The full mechanism by which the MSCs migrate and home to the tissue is still object of study. However, it is accepted that MSCs follow the same process followed by leucocytes, which is described in **Figure 18** and could be sum up in four steps:

1. In the blood stream, the cell contacts the endothelium;
2. G-protein-coupled receptors activate the MSCs cells;
3. an integrin-mediated, activation-dependent arrest happens;
4. the cells transmigrate through endothelium and underlying basement membrane (Butcher, 1996).

Different factors play a distinctive role in MSCs migration and engraftment to the site of injury. Some of them are: the specialized glyoform of CD44, called hematopoietic cell E-/L-selectin ligand (HCELL), the chemokine G-protein coupled receptor, called CXCR4-stromal derived factor-1(SDF-1), and Integrins α4 and β1, which combine to the antigen 4 (VLA-4), determining its interaction with vascular cell adhesion molecule 1 (VCAM-1) (Moll & Ransohoff, 2010; Ruster et al., 2006; Sackstein, 2004; Segers et al., 2006).

In the fourth and last step, MSCs transmigrate through the endothelial cell layer and the underlying basement membrane, composed of collagen and gelatin. These components of the basement membrane are degraded by lytic enzymes called metalloproteinase (MMP). An example of MMP involved in the degradation process is given by MMP-2 and MMP-9, that are two gelatinases participating in the collagen and gelatin degradation (Nagase & Woessner, 1999; Steingen et al., 2008).

To improve the MSCs homing efficiency, the CXCR4 expression has been enhanced both directly- by designed transfection or transduction experiments in which a plasmid was introduced into the cells virally (Bobis-Wozowicz et al., 2011) or not virally (Otani et al., 2009; Wiehe et al., 2013) or indirectly, by using molecules or process that could favour CXCR4 expression. To improve the CXCR4 expression on MSCs membrane, many strategies have been proposed, such as treating the MSCs culture before of the injection with a cocktails of cytokines (Shi et al., 2007) like flt3

ligand stem cell factor (SCF), IL3, IL6 and hepatocyte growing factor (HGF), insulin-like growing factor 1 (IGF-1), tumour necrosis factor α (TNF α), IL 1β, interferon γ (IFN γ).

Recombinant CXCR4 was bound to the cell surface of MSCs also using lipid-PEG (Won et al., 2014). MSCs migration is stimulated by Valproic acid and hypoxia, which increase expression of CXCR4 and MMP-2 in MSCs in culture, while MSCs motility and MMP-2 expression are enhanced by erythropoietin (EPO) and granulocyte colony stimulating factor (G-CSF). MSCs homing efficiency is improved by irradiation and by expression of P-selectin glycoprotein ligand-1 (PSGL-1) and HCELL, two E-selectin ligands that are required for HSC bone marrow homing (Fouillard et al., 2007; Mouiseddine et al., 2007; Ponomaryov et al., 2000). Indeed, the MSCs homing capability was improved when the active site of PSGL-1, called Sialyl Lewis X (SLEX), was introduced into the MSCs cell membrane using biotinylated vesicles (Sarkar et al., 2010). Also, high cell confluence influences MSCs migration behaviour, decreased by TIMP-3 which at high cell concentration inhibits MMPs and lowers cell migration (De Becker et al., 2007).

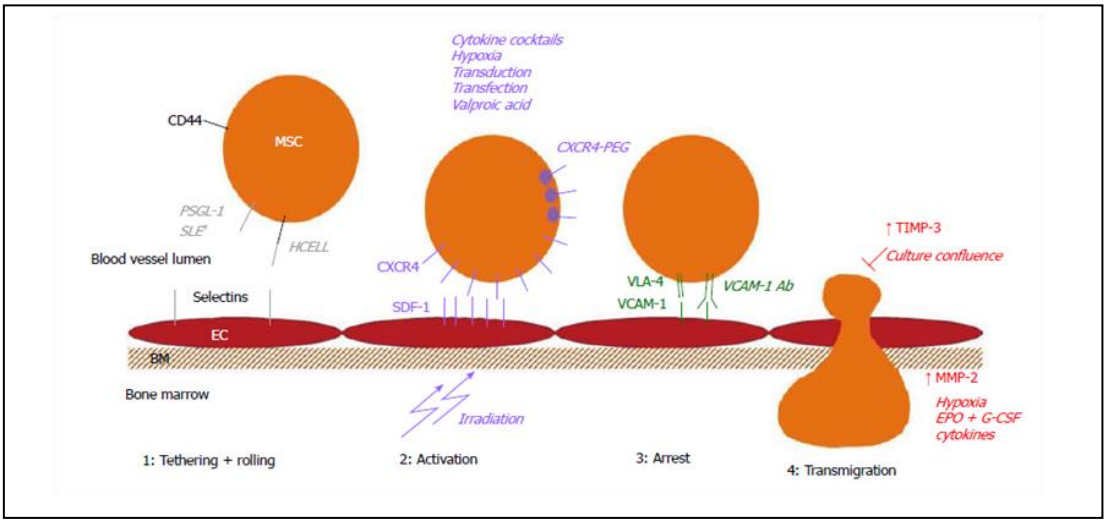

Figure 18. MSC migration to bone marrow.

Four steps describing the MSCs migration and homing to bone marrow (Thethering+rolling, Activation, Arrest, Transmigration) with the main strategies used to enhance MSC homing (Cytokine cocktails, Hypoxia, Transduction, Transfection, Valproic acid, Irradiation, SDF-1 and CXCR4 expression stimulation).

CD: Cluster of differentiation; EC: Endothelial cell; BM: Basement membrane; HCELL: Hematopoietic cell E-/L-selectin ligand; PSGL-1: P-selectin glycoprotein ligand-1; SLEX: Sialyl Lewis X; SDF-1: Stromal cell derived factor 1; VLA-4: Very late antigen 4; VCAM-1: Vascular cell adhesion molecule 1; Ab: Antibody; TIMP:Tissue inhibitor of metalloproteinases; MMP: Matrix metalloproteinase; EPO: Erythropoietin; G-CSF: Granulocyte colony stimulating factor; MSC: Mesenchymal stromal cell. Original picture taken from (De Becker & Riet, 2016).

1.8.3. MSCs clinical administration

MSCs could be clinically applied by two principal routes: systemic administration and local administration. In systemic administration, the cells are injected by intravenous (IV) or intra-arterial injection (IA); in local administration, they are injected by intracoronary injection (IC) or directly in the tissue of interest (De Becker & Riet, 2016). In animal models, MSCs are usually injected into circulation by intravenous injection (IV): this method is considered the safest and repeatable, but the downsides are that cells could be trapped in lungs, not reaching the tumour site immediately. IV injections can be subcutaneous (Reagan & Kaplan, 2011; N. Wang et al., 2009), intratracheal (Xin et al., 2009), through the tail vein (Wang et al., 2009), through the internal carotid artery (Nakamizo et al., 2005), or intraperitoneal (Komarova et al., 2010).

1.8.4. MSCs and their double-edge role in tumour

The natural predisposition of MSCs to reach sites of injury, especially tumour, is today well established (Hong et al., 2014; Loebinger, Kyrtatos, et al., 2009; Mathieu et al., 2012; Menon et al., 2007). However, it is still difficult to define the role that MSCs play in the tumour growth, as it appears dual (**Figure 19**). According to some researches, MSCs favour the tumour growth and spreading, acting as tumour progression factors, while others claim that MSCs have a role in tumour suppression, inhibiting tumour growth by direct/indirect interaction with tumour cells (Norozi et al., 2016). This "double edge" behaviour of MSCs in tumour growth will be discussed below.

1.8.5. MSCs support tumour growth

Solid tumours are composed of two main components: tumour cells and tumour stroma, which comprises tumour vasculature, cells of the immune system,

extracellular matrix (ECM), carcinoma-associated fibroblasts (CAF) and tumour-associated fibroblasts (TAF), that are fibroblastic stroma cells and MSCs (Goel & Mercurio, 2013; Huang et al., 2012; Caplan &Dennis, 2006; Locatelli &Bianchi, 2014). All the components of tumour stroma are actively involved in the ECM signals release. The concern in MSCs application in tumour arises from the fact that MSCs can differentiate in TAFs and CAFs and form the vascular network of the tumour (Dominici et al., 2006; Hong et al., 2014). Furthermore, MSCs seem able to secrete growth factors and to suppress the immune response by inhibiting the proliferation of CD4 and CD8 T-cells while increasing the T-regulatory cells (T-reg) (Lysko et al., 2011; Xiao et al., 2009). In addition to that, MSCs could lead to metastasis by the epithelial-to-mesenchymal transition (EMT) program, which is a process for invasiveness and metastasis of cancer cells associated with a poor clinical prognosis (Erta et al., 2012; Kuai et al., 2012; Norozi, Ahmadzadeh, Shahjahani, et al., 2016). This process is activated by factors like collagen, cytokines, TGF-β, FGF, HGF and epidermal growth factor (EGF), that are also secreted by MSCs (Caplan & Dennis, 2006). In addition to that, MSCs could also inhibit the production of pro-inflammatory cytokines (TNFα and IFN-γ) while increasing the expression of suppressing cytokines as IL-10 (Perron & Dodd, 2012). In damaged sites, activated ECM proteases favour the recruitment of MSCs (Bergfeld & DeClerck, 2010). MSCs can actively interfere with cancer stem cells (CSC), supporting their self-renewal and enhancing their invasive properties. CSC, indeed, produce IL-6, which can support MSCs chemotaxis and homing in primary tumour growth site. (Arango-Rodriguez et al., 2015). Additionally, IL-6 binds to IL6R/gp130 on MSCs, stimulating CXCL7. The molecule CXCL7 binds to the CXCR2 receptor on CSCs, favouring the synthesis of cytokines IL-8, IL-6, CXCL6 and CXCL5, which lead to CSCs self-renewal and invasiveness (Buschmann et al., 2001; Luheshi et al., 2009).

1.8.6. MSCs suppress tumour growth

Despite many studies underline the promoting effect of MSCs on tumour growth and expansion, many others found that MSCs are actively involved in tumour

suppression (**Figure 19**). Indeed, MSCs seem to discourage tumour growth by promoting: angiogenesis inhibition, inflammatory cells infiltration and Wnt and AKT signal suppression, cell cycle arrest and cell apoptosis (Cousin et al., 2009; Dasari, Kaur, et al., 2010; Dasari, Velpula, et al., 2010; Khakoo et al., 2006; Lu et al., 2008; Ohlsson et al., 2003; Olaso et al., 1997; L. Qiao, Xu, Zhao, Zhao, et al., 2008; L. Qiao, Xu, Zhao, Ye, et al., 2008; Rhee et al., 2015). Studeny and al. and Ryu et al. demonstrate that MSCs can synthesise IFN-β, inhibiting the tumour growth (Ryu et al., 2014; Studeny et al., 2004a). When cultured in 3D systems, MSCs express TRAIL, which lead to tumour-cell specific apoptosis (Du et al., 2012; Madrigal et al., 2014). MSCs exert tumour inhibition by increasing p21 expression and favouring caspase 3 pathway, which blocks the cell cycle in phase G0/G1 leading to apoptosis of cancer cells (Lu et al., 2008). MSCs injected into mice bearing non-Hodgkin's lymphoma, increase animals' survival. MSCs were also seen to play an anti-angiogenic role when co-cultured with endothelial cells (Secchiero et al., 2010). The immunocompatibility of MSCs make them a suitable universal donor for allogeneic transplantation (Chiu, 2005).

MSCs can stop tumour cells growth by arresting the cell cycle in G1 phase by expressing factors as CyclinA, CyclinE, CyclinD2, and p27KIP1 (Aggarwal & Pittenger, 2005; Corcione et al., 2006; Cousin et al., 2009; Glennie et al., 2005; Lu et al., 2008; Ramasamy et al., 2007; Sotiropoulou et al., 2006). It was demonstrated that the addition of ADSC-conditioned cell culture medium in cancer cells stimulated necrosis after G1-phase arrest in the absence of apoptosis, and when ADSC was introduced into pancreatic adenocarcinoma, the tumour growth stopped (Lu et al., 2008). In some cases, *in vivo* results do not reflect *in vitro* results: the growth of tumour cells cultivated with MSCs *in vitro* was arrested at the G1 phase, but when mice were injected with MSCs and tumour cells the effect was the opposite, and tumour growth augmented compared to tumour cell alone (Ramasamy et al., 2007; Rhee et al., 2015).

MSCs can regulate the cellular signalling in the tumour. MSCs injected intravenously in a Kaposi's sarcoma model migrated to the tumour and effectively inhibited tumour proliferation through inhibition of AKT (Khakoo et al., 2006), one of the most important players in the tumour migration and invasiveness process.

AKT, together with WNT creates the phosphoinositide 3-kinase (PI3K)/AKT and WNT/β-catenin signalling pathway, involved in the cell survival, proliferation, growth, migration, and metabolism (Engelman et al., 2006).

MSCs can have a pro-inflammatory effect on the tumour. Ohlsson et al. documented that MSCs were able to inhibit rat colon carcinoma by stimulating the infiltration of both granulocytes and macrophages, even if MHC-class I expression was low and MHC class II was absent (Ohlsson et al., 2003).

Some studies found that MSCs are not detrimental when applied to the tumour site, and exploited the MSCs ability of homing to the tumour to deliver pro-apoptotic agents directly to the tumour site. The most employed anti-cancer drugs that MSCs carry are type I interferon (IFNα- and IFN-β), IL-2, IL-12, CXCL1, cytokine deaminase, TRAIL (Komarova et al., 2006; Loebinger, Eddaoudi, et al., 2009; Menon et al., 2009; Nakamizo et al., 2005; Studeny et al., 2002; Studeny et al., 2004b). IL-2overexpressing MSCs were effective against different types of tumour (X. Chen et al., 2008; Nakamura et al., 2004; Stagg et al., 2004), whereas CXCL1 and IL-12, activating both T cells and NK cells, can reduce breast tumour, lung tumour and melanoma (X. Chen et al., 2008; X. C. Chen et al., 2006; Eliopoulos et al., 2008; Gao et al., 2010; Xin et al., 2007). Beside these treatments, the effect of the former drugs could be amplified by using MSCs specifically engineered to express them (Nakamizo et al., 2005; Ren et al., 2008; Studeny et al., 2002; Studeny et al., 2004a). Tumour cells can be specifically targeted by oncolytic viruses- expressing MSCs (Dembinski et al., 2010; Hakkarainen et al., 2007; Komarova et al., 2006; Stoff-Khalili et al., 2007), or by MSCs carrying nanoparticles in drug delivery (L. Li et al., 2011), or again by MSCs converting enzymes in cancer therapies (Hamada et al., 2005; Kucerova et al., 2008a, 2008b; Matuskova et al., 2010; Uchibori et al., 2009; Zischek et al., 2009).

In summary, these contrasting findings on MSCs action on tumour growth and microenvironment, suggest that MSCs regulation in tumour is determined by a complex plethora of factors which take part in the process, such as timing of MSCs injection, type of tumour cells, MSCs origin and degree of differentiation (Norozi, Ahmadzadeh, Shahrabi, et al., 2016). Therefore, caution and evaluation of the specific case are mandatory when working with MSCs.

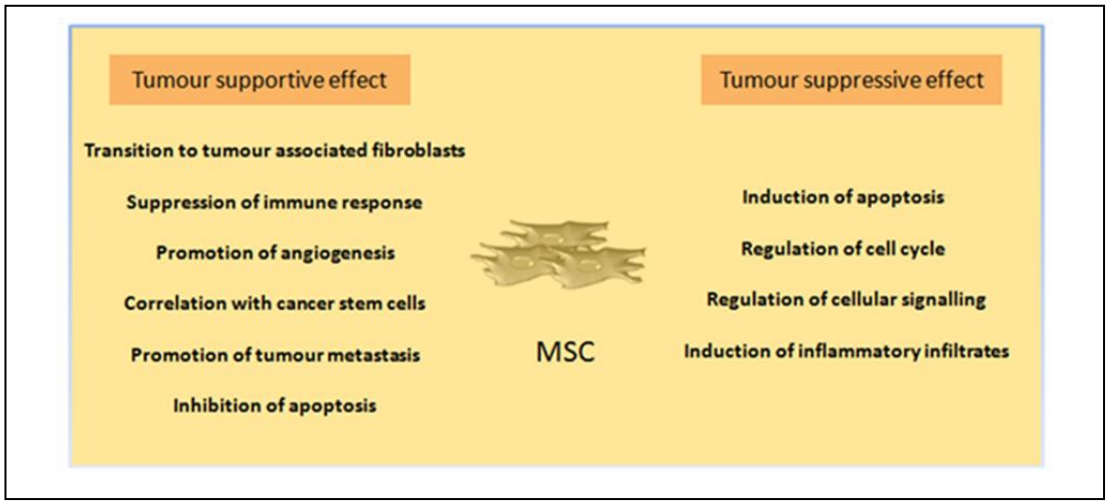

Figure 19. MSC "double edge" behaviour in tumour growth.

1.9. Bacterial magnetosomes in MHT

1.9.1. Magnetosomes show features that are indicated for magnetic hyperthermia experiments

Recently, MTB magnetosomes have attracted scientific interest in the MHT of tumours. MHT treats tumours by the use of MNPs localised in the tumour site that is exposed to the AMF: the MNPs, heated by the AMF, exert an anti-tumour activity (Alphandery et al., 2013). Nowadays, the nanoparticles employed in the clinical application are Superparamagnetic Iron Oxide Nanoparticles (SPIONS), that are chemically synthesised. However, SPIONS do not fulfil all the requirements to be successfully employed in MHT. Indeed, due to their small size, SPIONS are unable to deliver the necessary amount of heat when subjected to an AMF, but form aggregates which cause toxicity *in vivo*. Moreover, they show thermally unstable magnetic moment (Alphandery et al., 2013).

Magnetosomes, on the other hand, show peculiar characteristics that make them, to date, the most feasible nanoparticles for MHT. Their ferrimagnetic behaviour, together with their large size, allow the release of a significant amount of heat when they are subjected to an AMF. In addition to that, magnetosomes can provide a uniform amount of heat in the cell without any agglomeration, due to their arrangement into chains (Alphandery et al., 2013). Magnetosomes can be isolated by MTB by different ways, such as sodium hydroxide, sonication, French press, and a pressure homogenizer to lyse the bacteria cells. After extraction, magnetosomes are subjected to the purification step, lyophilisation and sterilization with gamma rays, and in the end, the suspension of magnetosomes is characterised before therapeutic administration (Alphandery et al., 2013).

1.9.2. Magnetosomes toxicity: are they safe for the body?

In vitro, magnetosomes are not toxic for H22, HL60 and EMT-6 cells at the dose of 9 µl/ml, as well as they are not toxic for mouse fibroblasts at the concentration of 1.3 mg/ml. *In vivo* experiments on mice and rats, reveal that animal death is reached when they are injected intravenously with 480 mg/kg of bacterial magnetosomes for mice and less than 82 mg/kg for rats (Sun J. et al., 2010). However, it was necessary a far lower dose of SPIONS (135 mg/kg) to kill the mice (Liu R-T et al., 2012), suggesting that magnetosomes are less toxic to the body than SPIONS. Organs of rats treated with less than 82 mg/kg were investigated by histological analysis, and no haemorrhage nor inflammation or hyperaemia were found.

Moreover, another point in favour of magnetosomes is that they contain magnetite (Fe_3O_4), a relative insoluble iron oxide, that is unable to trigger any Fenton reaction, which typically occurs when iron ions are dissolved, creating hydroxyl radicals, strong oxidants (Alphandery et al., 2013). On the contrary, magnetosomes have been reported to scavenge ROS (Guo et al., 2012). The toxic effect ascribed to magnetosomes could derive from their nanometric size, which favours their clogging, leading to embolism, blood clot, and cell toxicity (Alphandery et al., 2013). Magnetosomes immunotoxicity could also depend on other biological components, such as nucleic acids and proteins which remain in impure magnetosomes. Despite studies regarding magnetosomes immunotoxicity have been carried out, it is still not clear if magnetosomes contain antigens or pyrogens (Sun J. et al., 2010).

Magnetosomes injected in mice and rats are degraded by lysosomes after 28 days (Liu R-T et al., 2012). In one study, magnetosomes administrated to mice and rats were tracked by fluorescence microscopy (T. Tang et al., 2012), whereas in another study organs of animals injected with magnetosomes were subjected to histological analysis (Liu R-T et al., 2012; Sun et al., 2009). Magnetosomes appear to migrate in liver (Liu R-T et al., 2012; Sun et al., 2009), spleen (Liu R-T et al., 2012), lungs (T. Tang et al., 2012), where they were found located inside lysosomes, partially degraded. In addition to that, the presence of magnetosomes was not detected by the analysis of urine and faeces of mice and rats subjected to intravenous injection of

magnetosomes, suggesting that the magnetosomes have been totally degraded by animals (Sun et al., 2009). However, magnetosomes were detected in faeces of mice after both intra-tumoral and intravenous administration by another study (Alphandery et al., 2011). Understanding how magnetosomes are degraded inside the body is challenging, but the most accredited hypothesis suggests principally two routes: the reticuloendothelial system and urine/faeces (Alphandery et al., 2013). Not many studies have compared magnetosomes and chemically synthesised MNPs body degradation; however, experiments on MNPs degradation inside the body reveal that MNPs are metabolised by organ's parenchyma with metal ions, leaking from the core material up to 6 months after the intravenous injection (Lacava et al., 2004). Although it is still too early to indicate the magnetosomes as the safest SPION, these findings suggest a possible use of magnetosomes as therapeutic agents in MHT.

1.9.3. Physic properties of magnetosomes

Magnetosomes are the nanoparticles which provide the most powerful source of heat when applied in MH (Alphandery et al., 2013). This quality is given by specific features, such as ferrimagnetic behaviour, cubic shape, large shape and thermally stable magnetic moment, that are all factors leading to a high loss per cycle. Loss per cycle is defined as the SAR divided by the frequency of oscillations of the AMF, and it is useful for the comparison of magnetosomes SAR in different AMF. Moreover, it was demonstrated that magnetosome loss per cycle increases by increasing the magnetic field strength (Dutz et al., 2007; Rudolf Hergt et al., 2005; Sun et al., 2009; Timko et al., 2009) and, above 10 mT, magnetosome losses are either equivalent or larger than the losses of chemically synthesised MNPs (Alphandéry et al., 2011; Dutz et al., 2007). Alphandery et al. investigated in which way the magnetosomes should be administrated to led to the higher heat efficiency, if whole AMB-1 MTB, chains of magnetosomes, or single magnetosomes (Alphandery et al., 2011); (**Figure 20**). In an applied magnetic field of 108 kHz and strength of 22 to 88 mT to whole AMB-1 bacteria, they found that the losses per cycle were due to the magnetosomes viscosity and not to the whole bacteria, whose contribute was very low (Alphandéry

et al., 2011). Instead, magnetosomes extracted as a chain or as a single component produced a heat given both by the inversion of magnetosome than by the magnetosome rotation, with an increasing in the magnetic losses. However, the study was not able to define which was the best arrangement -magnetosome or chains of magnetosomes- in MH application, since both of them gave high losses per cycles values.

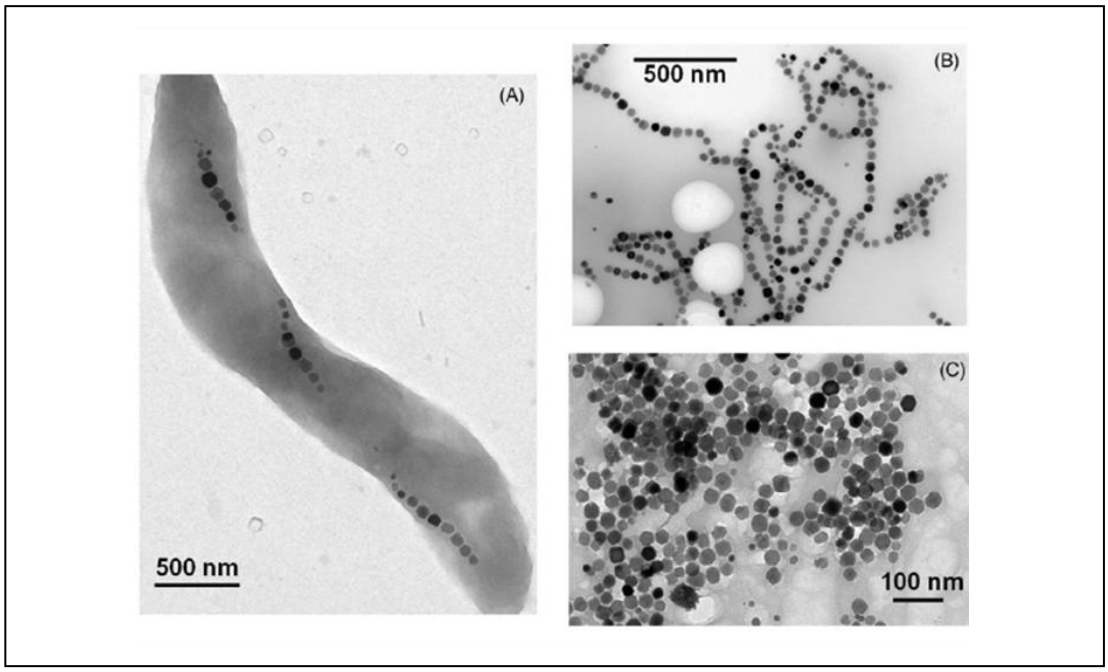

Figure 20. TEM investigation of MTB.

Pictures of whole AMB-1 MTB (A), chains of magnetosomes from AMB-1 MTB (B), and single magnetosomes from AMB-1 MTB (C). Images taken from (Alphandery et al., 2013).

1.9.4. Magnetosomes as anti-tumour treatment

There are only a few studies conducted to determine the magnetosomes effect as anti-tumour treatment. In one study in which MCF-7 tumour cells were mixed together with magnetosomes, 80% of cell population died following AMF application and reaching a temperature of 47 °C. The treatment, which resulted more harsh for the cancer cells respect to the healthy ones, was considered safe also if applied to the healthy tissue. Cell death was directly proportional to the increasing

incubation time, the concentration of magnetosomes, the magnetic field strength and the number of times that the experiment was repeated (Liu R-T et al., 2012). Alphandéry et al. performed an experiment in which whole MTB, chains of magnetosomes, individual magnetosomes, and SPIONS were tested applying a magnetic field strength of 40 mT at a frequency of 198 kHz, in xenografted breast tumours mice. Results revealed that only chains of magnetosomes made the tumour to disappear, also after 30 days from treatment. The temperature reached during the treatment with chains of magnetosomes was 45-46 °C, demonstrating that is the particular arrangement of chains to make magnetosomes efficient in MHT. The chains prevent agglomerations, and the resulting toxic effect, while the heating is distributed more uniformly inside the cell (E. Alphandery et al., 2011). Chains of magnetosomes have a different coating, made of proteins and lipids respect to single magnetosomes, that have only a lipidic coating (E. Alphandery et al., 2012), a feature that is believed responsible for their different z potential[3] (–22mV at pH 7), respect to the one of the individual magnetosomes (+10mV at pH 7) while their alignment into chains give them larger magnetic anisotropy and a faster elimination from the body.

These results were partially contradicted by a study conducted by (Mannucci et al., 2014). In the study it was investigated the effect of chains of magnetosomes extracted from *M. gryphiswaldense* on colon cancer cells HT-29 in HT experiments. The findings revealed that the magnetosomes enter the cells not as chains but as single nanoparticles or short chains. Mannucci et al. described the internalisation of magnetosomes inside the cells as a multistep process, in which: 1) magnetosomes adhere to the cellular membrane, 2) magnetosomes are internalised in vesicles, 3) magnetosomes are carried to the Golgi apparatus, 4) magnetosomes are included in double layer membrane-like vesicles. In this study, it was observed no tumour remission in mice treated, but tumour tissue necrosis both by histology and MRI. The low tumour cell death, compared to other studies in which magnetosomes were successfully employed to kill tumour cells (Alphandery, 2014) was imputed to the

[3] *Zeta potential* is the potential difference between the surface of a solid particle immersed in a conducting liquid and the bulk of the liquid https://en.oxforddictionaries.com/

lower AMF strength and frequency applied, to the different strain of MTB used and to the different tumour model investigated. However, in mice exposed to the treatment, it was observed a temperature increase of 2-3 °C, and it was also found that temperature increased linearly with the increasing of the AMF. Mannucci et al. also proposed a model of MNPs migration, based both on a passive transport carried on by the reticuloendothelial system and by active transport, operated by macrophages, similar to what happen for iron. In addition to that, the success in tracking magnetosomes in living tissue, due to their iron content, also opens more possibilities of magnetosomes employment as negative contrast agents or magnetic tracers.

1.10. Aims

Magnetic Hyperthermia Therapy (MHT) is a promising tumour treatment. However, the MNPs used as a mediator in the treatment until now are still far from optimal (Alphandery et al., 2013). To overcome the use of synthetic MNPs, the research moved toward the use of bacterial magnetosomes found in MTB and characterised by high SAR and a better heat distribution (Alphandery et al., 2013). Still, the concern regarding the use of these bacterial organelles in the human body could cause reluctance in the medical community.

Among all the MTB proteins, Mms6 and MmsF had been suggested as determinant players in iron crystal morphology regulation (Amemiya et al., 2007) (Murat et al., 2012). A new prospect for MHT is provided by MSCs. These cells not only show exceptional qualities of tumour homing, but could also be engineered, making them able to express the required gene and, consequently, the features derived from that gene expression. With these qualities, MSCs become the "Trojan horse of biology", making possible to deliver the engineered MSCs directly inside the tumour.

The goal of this study was to create engineered MSCs, able to express *mms6* and *mmsF* genes, alone or in combination, in the attempt to create MNPs bearing MSCs.

The main aims to prove that were:

1. To transfect MSCs with the MTB genes *mms6* and *mmsF*, alone or in combination;
2. To determine if the expression of *mms6* and *mmsF* genes inside MSCs leads to the production of MNPs, as seen for the MTB;
3. To estabilish if the expression of the *mms6* gene inside MSCs affects MSCs functionality;
4. To determine if the MNPs created inside the *mms6*-expressing MSCs could be responsive to an AMF and to kill tumour cells, *in vitro* and *in vivo*.

2. Materials and Methods

2.1. Materials

2.1.1. List of reagents:

Table 5. Cell culture reagents

Reagents	Company
DMEM (Dulbecco's Modified Eagle Medium)	Life Technologies, UK
FBS (Fetal Bovine Serum)	Life Technologies, UK
Trypsin with 0.25% EDTA (Ethylenediaminetetraacetic acid)	Life Technologies, UK
100x PenStrep (Penicilin/Streptomycin)	Life Technologies, UK
PBS (Phosphate Buffered Saline)	SigmaAldrich, UK
HBSS (Hanks' Balanced Salt Solution)	Sigma Aldrich, UK
OptiMem Reduced Serum Medium	Gibco, UK

Table 6. RNA isolation/DNA synthesis/agarose gel electrophoresis/PCR reactions reagents/Sanger Sequencing

Reagent	Company
Qiazol	Qiagen, UK
Chloroform	SigmaAldrich, UK
Isopropyl alcohol	SigmaAldrich, UK
Ethanol	SigmaAldrich, UK
DNA/RNA-se free water	SigmaAldrich, UK
RNA Denaturating Loading Buffer	New England Biolabs, UK
MOPS (3-(N-morpholino) propanesulfonic acid)	SigmaAldrich, UK
Agarose	SigmaAldrich, UK
Tris-borate-EDTA (TBE) buffer	Thermo Fisher Scientific, UK
RNeasy Mini Kit	Qiagen, UK
DNAse I kit	Qiagen, UK
TopTaq	Qiagen, UK
qScript cDNA Synthesis Kit	Quanta Biosciences/VWR, UK
SYBRStain	Life Technologies, UK
DNA ladder	New England BioLabs, UK
Q5High-Fidelity DNA Polymerase	New England BioLabs, UK
dNTPs	Thermo Fisher Scientific, UK
BigDye Terminator v3.1	Applied Biosystems,UK

Table 7. Gene purification from agarose gel/restriction enzymes digestion/vector dephosphorylation and ligation

Reagent	Company
QIAquick Gel Extraction Kit	Qiagen, UK
EcoRI enzyme	New England Biolabs, UK
NotI enzyme	New England Biolabs, UK
NEBuffer 3.1(10x concentrated)	New England Biolabs, UK
BSA (Bovine serum Albumin)	SigmaAldrich, UK
Rapid DNA ligation kit	Roche, UK

Table 8. Bacteria transformation/plasmid amplification/ plasmid purification

Reagent	Company
Subcloning Efficiency™ DH5α™ Competent Cells	Invitrogen, UK
SOC medium	Invitrogen, UK
Agar	SigmaAldrich, UK
Ampicillin 1000x	SigmaAldrich, UK
LB Broth (Luria-Bertani medium)	SigmaAldrich, UK
Plasmid Maxi Kit	Qiagen, UK
Isopropanol	SigmaAldrich, UK
Ethanol	SigmaAldrich, UK

Table 9. Transfection/TEM/IHC/IF/Flow Cytometry reagents

Reagent	Company
X-tremeGENE HP Transfection Reagent	Roche,UK
3% Glutaraldehyde	SigmaAldrich, UK
1% Osmium tetroxide	SigmaAldrich, UK
Resin	TAAB,UK
Cleaved Caspase-3 antibody (Asp175)-(NEB9661S)	Cell Signaling Technology, UK
Anti-Nuclei Antibody, clone 3E1.3(MAB4383)	Merck Millipore, UK
MOM Blocking reagent	Vector Laboratories, UK
Bond Polymer Refine Detection kit	Leica,UK
Harris Hematoxylin solution	SigmaAldrich, UK
HistoChoice	SigmaAldrich, UK
DPX mounting medium	Fluka,UK
Rabbit anti-osteocalcin antibody (ab13420)	Abcam, UK
Blocking serum (X0907)	DAKO,UK
Alexa Fluor 488-conjugated goat anti-rabbit lgG (green) secondary antibody (A32731)	ThermoFisher Scientific, UK
Antifade Mounting Medium with DAPI (H1200)	Vector Laboratories, UK
Formaldehyde	SigmaAldrich,UK
Anti-Mouse Ig, κ/Negative Control Compensation Particles Set	BD Biosciences,UK

Table 10. MSC osteogenic/chondrogenic/adipogenic differentiation

Reagent	Company
StemPro Osteogenesis Differentiation Kit	Gibco, UK
StemPro Chondrogenesis Differentiation Kit	Gibco, UK
StemPro Adipogenesis Differentiation Kit	Gibco, UK
4% Paraformaldehyde	SigmaAldrich,UK
Alizarin Red	SigmaAldrich,UK
Alcian Blue	Fluka,UK
Oil Red Solution	Sigma Aldrich, UK
Isopropanol	Fisher Scientific, UK

Table 11. *In vitro/in vivo* AMF exposure

Reagent	Company
Pierce LDH Cytotoxicity Assay	ThermoScientific, UK
AlamarBlue Cell Viability Assay	ThermoScientific, UK
CellTracker CM-DiI Red Dye	Molecular Probes, Invitrogen, UK.
CellTracker CM-DiI Green CMFDA Dye	Molecular Probes, Invitrogen, UK.
DMSO	Sigma-Aldrich,UK
Trypan Blue Exclusion Assay	Thermo Fisher Scientific, UK

2.1.2. List of Solutions

Table 12. List and recipes of solutions

Solution	Recipe
Ferric quinate solution (0.01M)	0.27 g of $FeCl_3$ and 0.19 g of quinic acid were added to 100.0 ml of distilled water. The pH of the solution has been adjusted to 6.7 (human cell pH) by adding some drops of NaOH before to autoclave it at 121°C for 15 minutes
3% glutaraldehyde solution	glutaraldehyde diluted in 0.1M sodium cacodylate buffer
Flow cytometry buffer	0.5 % BSA and 0.05 % sodium azide (NaN_3) were dissolved in 1xPBS
CellTrackerTM CM-Dil Red dye stock	50µl of DMSO were added to one vial containing 50µg dried powder, to the final concentration of 1M
CellTracker Green CMFDA dye stock solution	11µl of DMSO were added to one vial of 50 mg CellTracker Green CMFDA Dye dried powder, to the final concentration of 10mM
2% Alizarin Red S solution (pH 4.2)	2 g of Alizarin Red S were dissolved in 100 ml of ddH_2O, mixing and adjusting pH to 4.2 with 0.1% NH_4OH
4% PFA	10 ml of PFA diluted in 30 ml of 1x PBS
3.7% paraformaldehyde for Immunofluorescence	for 100 ml: 10 ml of 10x PBS, 33.4 ml of 11.1% formaldehyde (freshly prepared), 0.6 ml of 30% Triton X-100, 56 ml of distilled water.
Washing Buffer	0.1% Tween 20 in 1x PBS
Alcian Blue staining solution	60 ml of ethanol 100% were mixed with 40 ml acetic acid 100%. Then, 100 mg of Alcian Blue were dissolved in this solution and mixed in magnetic stirrer.
Alcian Blue destaining solution	120 ml of 100% ethanol were mixed with 80 ml of 100% acetic acid
Oil Red O solution	300 mg of Oil Red O powder were dissolved in 100 ml of 99% Isopropanol
Oil Red O solution 3:2	3 parts of Oil Red O solution were diluted in 2 parts of ddH_2O and sterile filtered with a 0.22 µm filter.
60% Isopropanol	60 ml of 100% isopropanol were mixed with 40 ml of ddH_2O.

2.2. Methods

2.2.1. Cell culture media

MG63 Homo sapiens bone osteosarcoma cells and A431 Ecad-GFP expressing human epidermoid carcinoma cell line culture medium: DMEM medium, high glucose, supplemented with 10% FBS and 1% of 100U/ml/100µg/ml Penicillin-Streptomycin (P/S). The complete medium was prepared by adding to 450 ml of DMEM medium 50 ml of FBS and 5 ml of P/S.

MG63 Homo sapiens bone osteosarcoma cells FeQ doped medium: MG63 Homo sapiens bone osteosarcoma cells medium described above with the addition of 3.4 µl/ml of FeQ solution, to a final concentration of 34 µM.

Human Mesenchymal Stem Cells (MSCs) culture standard medium: DMEM medium, high glucose supplemented with 20% of FBS and 1% of 100 U/ml/100µg/ml P/S. The complete medium was prepared adding to 400 ml of DMEM medium 100 ml of FBS and 5 ml of P/S.

Human Mesenchymal Stem Cells (MSCs) FeQ doped medium: Human Mesenchymal Stem Cells (MSCs) culture standard medium with the addition of 3.4 µl/ml of FeQ solution to a final concentration of 34 µM.

MSC osteogenesis differentiation medium: StemPro Osteogenesis Supplement was added to the StemPro Osteocyte/Differentiation Basal Medium, from the StemPro Osteogenesis Differentiation Kit (Gibco).

MSC chondrogenesis differentiation medium: StemPro Chondrogenesis Supplement was added to the StemPro Osteocyte/Differentiation Basal Medium, from the StemPro Chondrogenesis Differentiation Kit (Gibco).

MSC adipogenesis differentiation medium: StemPro Adipocyte Supplement was added to the StemPro Adipocyte Differentiation Basal Medium, from the StemPro Adipogenesis Differentiation Kit (Gibco).

Resuscitation of the cells:

A cryogenic vial containing an aliquot of cells was removed from liquid nitrogen, and thawed in a water bath at 37°C for 2 minutes. The cells were then immediately mixed with 10 ml of complete pre-warmed medium and centrifuged at 177 x g for 5 minutes. The supernatant was discarded, and cells were resuspended in 10 ml of complete medium and seeded in a 75 cm^2 flask. Cells were cultivated in the incubator, at 37 °C with 5% CO_2.

2.2.2. Cell culture

All the cell culture procedures were performed in laminar flow hoods. Cells were cultured in their specific medium and cultured in the incubator, at 37 °C with 5% CO_2.

A431 ecad-GFP expressing human epidermoid carcinoma cell line was kindly provided by Professor Val Brunton, MRC Institute of Genetics & Molecular Medicine, University of Edinburgh.

Human mesenchymal stem cells (MSCs) were kindly provided by B.Péault laboratory, MRC Centre for Regenerative Medicine (CRM), Royal Infirmary, Edinburgh. Cells were isolated from human fetal bone marrow with informed consent from Edinburgh Royal Infirmary, propagated and used at low passage ($p<10$).

2.2.3. Passaging of cells

Cells were passaged when they reached the 80% of confluence (2 times a week). Cells were washed with 4 ml of 1x PBS and then incubated with 1 ml of Trypsin-EDTA 0.25% for 2 minutes in the incubator at 37 °C with 5% CO_2. Cells were then resuspended and collected in 10 ml of complete medium. The cell suspension was then centrifuged at 177 x g for 5 minutes, the supernatant was discarded, and the cell pellet was resuspended in 10 ml of complete medium. Then 2 ml of cell suspension were put into a T75 flask containing 8 ml of complete medium (1:5 ratio).

2.2.4. Cells transfection

MG63 cells and MSCs were transfected with plasmid pcDNA3.1 containing the gene *mms6* and with the plasmid pcDNA4/TO containing the gene *mmsF*, alone or in combination, using the X-tremeGENE HP Transfection Reagent (Roche),

accordingly with the manufacture's protocol. The details about the gene *mms6* and the insertion of the gene *mmsF* into the plasmid pcDNA4/TO can be found in the **appendix 8.1** and in **appendix 8.2** respectively.

A detailed transfection protocol could be found in **appendix 8.3**.Transfection efficiency was estimated around 70% (**appendix 8.4**).

Briefly, cells were grown in T25 flasks. When the cells reached 80% confluence, 6 µl of each plasmid (1000 ng/µl), alone or in combination, were added to a sterile vial (1.5 ml) containing 600 µl of pre-warmed Optimem Medium (Gibco). Then, 18 µl of Transfection Reagent were added to the vial directly in the middle of the medium without touching the vial's walls. The solution was gently mixed and it was left at RT for 20 minutes. In the meanwhile, the medium of the T25 flasks was changed with 6 ml of DMEM 20% FBS without P/S.

After 20 minutes, the mix was spin down for 3 seconds and then it was gently added to the cells in the flask, trying to cover all the flask surface, drop by drop. The flask was gently swirled for 30 seconds and then incubated O/N in incubator. The day after, the medium was changed with fresh medium doped with Ferric Quinate (FeQ) solution (0.01 M, 3.4 µl/ml).

After transfection of cells, drug selection was not used.

The control wild-type cells that were doped with FeQ were not exposed to the transfection reagent.

2.2.5. Storage of cells

The freezing medium was made by adding 1 part of DMSO to nine parts of FBS. $5x10^6$ cells were added to each vial. Cells were stored to -80°C freezer for one day and then transferred to liquid nitrogen for longer storage.

2.3. Molecular Techniques

2.3.1. Isolation of total RNA from cells

RNA was isolated from cells using the standard Qiazol method. Confluent cells were washed with 4 ml of sterile 1x PBS twice. 1 ml of Qiazol was added in each 75 cm^2 flask, gently covering all the surface; the flask was then incubated at RT for 5 minutes. The cells were homogenised by pipetting and transferred in a fresh 1.5 ml DEPC treated microcentrifuge tube. Then 200 µl of chloroform were added to the cells, in the chemical hood. Then, cells were mixed by vortex and incubated at RT for 3 minutes. The cells were subsequently centrifuged at 13,000xg in a bench ultracentrifuge at 4^oC for 20 minutes. In the tube appeared three aqueous phases: a transparent phase, containing the RNA, a white ring, and a pink phase, containing the proteins. Carefully, only the transparent phase was aspirated with a filtered tip and transferred in a fresh DEPC treated microcentrifuge tube. 500 µl of isopropanol were added to the tube, mixing its content by slow inversion for 15 times and then it was incubated at RT for 10 minutes, followed by centrifugation at 13,000xg at 4^oC for 10 minutes. The supernatant was discarded, and the pellet was washed twice adding 500 µl of 75% ethanol, followed by centrifugation at 13,000xg at 4^oC for 10 minutes. The supernatant was discarded and the excess of ethanol was removed by a 200 µl filtered tip. The pellet was air-dried at RT for 10 minutes. Then, the pellet was resuspended in 30 µl of RNAse free water and then it was kept on ice. RNA yield and purity were investigated by spectrophotometry. RNA was stored at -80^oC for future use.

2.3.2. RNA yield and purity determination by spectrophotometry

Yield and purity of RNA samples were determined using a NanoDrop spectrophotometer (Labtech, UK). The absorbance was measured at wavelength 260,

280 and 230 nm. The absorbance ratio of RNA samples at 260/280nm of ~2.0 and absorbance ratio at 260/230nm in a range of 2.0 - 2.2 were considered as highly pure.

2.3.3. RNA integrity assessment

RNA integrity was assessed by electrophoresis on denaturing agarose gel. Briefly, 5 µg of RNA were dissolved in 2x RNA Denaturing Loading Buffer and incubated at 65 ^{o}C for 5 minutes. For denaturing agarose gel preparation, 0.5 g of agarose were added to 36 ml of ddH_2O, and the solution was microwaved for 2-3 minutes, to dissolve the agarose. Then, 14ml of MOPS Running Buffer were added to the agarose under the fume hood together with 1µl of 10,000x concentrated SyberSafe, to visualise the RNA under the ultra-violet (UV) image analyser. The gel was left at RT to cool down. Electrophoresis was performed in 1x MOPS Buffer using a horizontal gel electrophoresis system (Bio-Rad). An example of RNA stability test is in a**ppendix 8.5,** showing the two main bands of RNA: 28S rRNA and 18S rRNA. RNA was stored at -80^{o}C for future use.

2.3.4. cDNA synthesis and DNAse I treatment

cDNA was synthesised by reverse-transcribing 1µg of RNA. The genomic DNA contamination was removed by incubating 1µg of RNA with 1 µl of DNAse I and 1µl of 10x DNAse I buffer for 15 minutes at room temperature (RT). DNAse I activity was inactivated by adding 1µl of 200 µM EDTA followed by samples incubation at 65 ºC for 10 min. cDNA was synthesised following qScript™cDNA Synthesis Kit (Quanta Biosciences) protocol: 1µg of RNA was added to 1µl of qScript Reverse Transcriptase enzyme and 4 µl of 5x qScript Reaction Mix (which contained random oligo-dT), and then water was added up to 20 µl of final total volume. The reaction was vortexed gently and then centrifuged for 10 seconds to collect contents.
Then, the reaction was incubated in a thermal cycler (Tetrad2 DNA Engine, Bio-Rad) programmed as follows:

- 1 cycle: 22ºC, 5 min
- 1 cycle: 42ºC, 30 min
- 1 cycle: 85ºC, 5 min
- 4ºC hold

Then, 1/10th of the reaction (2 µl) were used for RT-PCR amplification. Samples of cDNA were stored in -20 ºC.

2.3.5. Reverse Transcription Polymerase Chain Reaction (RT-PCR)

The nucleotide sequences of the primers used in this study were designed using Primer3 software. Primers were bought from Sigma Aldrich. Amplification of fragment was performed in a thermal cycler (Tetrad2 DNA Engine, Bio-Rad).

RT-PCR was prepared according to the protocol provided by Quiagen:

- 12.5 µl of TopTaq Buffer (2x),
- 2.5 µl of TopTaq Dye (10x),
- 2 µl of cDNA,
- 1µl of primer Forward (10µM),
- 1µl of primer Reverse (10µM),
- 6 µl of RNAse free water.

The PCR reaction was conducted as follows:

- Initial Denaturation Temperature: 95 ºC - 3 min
- Denaturation Temperature: 95 ºC - 30sec
- Annealing Temperature: 55-62 ºC - 30-45 sec } 35 cycles
- Extension Temperature: 72 ºC - 1 min
- Final Extension Temperature: 72 ºC - 1 min
- Hold: 4 ºC - ∞

The human Glyceroaldehyde-3-Phosphate Dehydrogenase (GAPDH) was chosen as housekeeping gene. To determine the *mmsF* gene expression in the MG63 cells, two couples of primers were designed using Primer3 software, named *MmsF*A and *MmsF*B. Both of them matched the theoretical requirements to detect the *mmsF* gene expression in MG63 cells, so it was chosen to work with both the couples of primers to determine the best one to detect the *mmsF* expression in cells. Primers sequences are shown in **appendix 8.6**.

2.3.6. DNA agarose gel electrophoresis

The PCR amplified products were resolved in 2% agarose gel. Briefly, 2 g of agarose were mixed with 100 ml of 0.5x TBE, and dissolved using microwave. Then, 10,000x diluted SyberSafe stain (Invitrogen) was added to the gel to visualise the DNA under UV image analyser. The gel was cooled at RT, and then 12-20 µl of the sample were loaded into the gel and run in running buffer made of 0.5xTBE in horizontal gel electrophoresis system (Bio-Rad) at a constant voltage of 110V for 40-50 min. The molecular weight (MW) of the PCR product was determined by loading 1 µl of DNA ladder onto the gel (100bp DNA Ladder, New England BioLabs). Then, the gel was exposed to UV light to image the DNA bands. Gene expression was normalised using GAPDH as housekeeping gene.

2.4. Physical techniques

2.4.1. Transmission Electron Microscopy (TEM) samples preparation

$1x10^6$ cells were resuspended in 1ml of cell culture medium. The cells were centrifuged at 200xg for 5 minutes, and the pellet was resuspended in 50µl of cell culture medium and transferred to a 1,5 ml microcentrifuge tube. Then, 1% agarose solution was prepared by dissolving in a glass beaker 0,5 g of agarose powder in 50 ml of 1x PBS. The solution was put in microwave at 800 W for 3 minutes, checking every 30 seconds that the solution did not flow out of the beacker. In the meantime, the bottom of a PCR tube (volume 0.5 ml) was cut with scissors and it was put upside down with the lid closed in an ice bucket. The 1% agarose solution was left to cool down for 30 seconds at room temperature; then cell pellet was carefully resuspended in 100 µl of agarose solution avoiding air bubbles. The cell solution was immediately transferred to the PCR tube with the cut bottom.

The cell solution was left to solidify for 10 minutes, then with the help of a pipette tip, the solidified cell sample was transferred in a 5 ml bijoux filled with 3% glutaraldehyde solution, under the chemical hood.

The samples were then processed in the Electron Microscopy facility (Western General Hospital), Edinburgh. Briefly, samples were included in resin according to the following procedure: incubation in 1% Osmium tetroxide overnight at 4 °C, followed by samples dehydratation with increasing concentration of Ethanol (10%, 50%, absolute ethanol). Then, samples were incubated with propylene oxide for 20 minutes at RT twice and then incubated with propylene oxide/resin mix (50/50) for 1 hour. Samples were then included in resin (TAAB) for 2 hours at room temperature and then incubated in the same resin for 24 hours at 60°C.

Ultrathin sections, 60 nm thick, were cut on a Leica EM UC7 Ultratome and picked up on copper grids. The grids were stained with uranyl acetate and lead citrate and

viewed on a Jeol 1200EX2 transmission electron microscope. The digital images were viewed with a Deben AMT XR41 camera system.

ImageJ analysis of TEM pictures

TEM pictures of *mms6*-pcDNA3.1 transfected MSCs at day 0, 15 and 21 were analysed using a custom-made plugin of the ImageJ software. Ten TEM pictures were analysed for each time-point. For each picture, it was determined the total number of vesicles filled with the electron-dense content, then their average at each time point was calculated using Excel software. It was also calculated, for each analysed cell, the percentage of electron-dense filling of vesicles; then the average was calculated using Excel software. Statistical analysis and graphs were performed using GraphPad Prism (Prism 5.0, USA).

2.4.2. SQUID (Superconducting Quantum Interference Device) samples preparation

SQUID magnetometer is an instrument which measures the total magnetic moment of a sample, including all atomic and molecular magnetic contributions. To perform SQUID measurements, cells were centrifuged at 5000 x g for 5 minutes, the supernatant was removed, and the pellet was washed with 1 ml of 1x PBS and centrifuged again at 5000 x g for 5 minutes. The supernatant was discarded and the pellet was transferred in a non-magnetic plastic capsule inside a 1.5 ml microcentrifuge tube sealed with parafilm. The pellet was desiccated at 60 °C for 30 minutes in a vacuum-pump centrifuge (RVC 2-18, CHRIST). The parafilm that sealed each Eppendorf was punctured to avoid sample damage by vacuum. The sample material was weighed using a Sartorius Micro M3P balance to derive mass-specific values. Then, the capsule was closed and inserted in a plastic straw inside the SQUID magnetometer, following the protocol described in the **appendix 8.7**. Magnetisation data were taken at temperatures $5\,K < T < 350\,K$, using a liquid-He-cooled variable-temperature insert installed in the commercial SQUID-magnetometer apparatus (MPMS, Quantum Design Inc., San Diego, USA). For MG63 cells, two

different measurement modes were applied. In the first mode, the temperature-dependent magnetisation was determined in a small, fixed field ($\mu 0H = 0.01T$) between body temperature, $T = 310\,K$, and $T = 5\,K$. In the second mode, it was determined the field dependence of the magnetisation at body temperature in magnetic fields up to $\mu 0H = 7T$. MSCs were analysed only in the first mode.

The measurements were performed at varying temperatures moving the samples through a pick-up coil system connected to the SQUID via a flux transformer in a constant magnetic field, generated by a superconducting coil. The diamagnetic contribution of the pure-protein component to magnetisation given by controls sample of transfected cells grown in non-iron containing media was subtracted from the measured properties of the other sample materials, to obtain the magnetisation component originating from the nanoparticles.

The SQUID measurements on MG63 cells were kindly carried out by Dr. Marc Uhlarz in Dresden High Magnetic Field Laboratory (HLD-EMFL), Helmholtz-Zentrum Dresden-Rossendorf (Germany), while the SQUID measurements on MSCs were performed at King's Building, in Edinburgh (Scotland).

2.4.3. Hyperthermia samples preparation

The cellular hyperthermia was kindly measured by Dr Franca Albertini's group, Magnetic Materials Group IMEM-CNR in Parma, Italy.
The cells were investigated using the magnetic hyperthermia device from NanoScale Biomagnetics, DM1 and DM2 applicators (0-300G, up to 430kHz) for colloidal solutions and cell cultures.
The cells were firstly collected in 1,5 Eppendorf tubes and then washed twice with 1x PBS. Following cells centrifugation at 5000 x g for 5 minutes, a pellet formed and the supernatant was removed. The cell material was dried at room temperature for 12 hours and then preserved in -80 °C freezer until shipment.
In Parma, the cells were then resuspended in 0.2 ml of distilled water in a vial connected to a thermocouple whose ends were in contact with the cell solution. The

vial was put in a calorimeter totally isolated from the external environment. Around the calorimeter, there was a coil which generated an AMF. When the system reached the thermal equilibrium, the magnetic field was switched on, and only the temperature variation due to the magnetic component of the cells was measured, making possible to determine which gene was responsible for the cells magnetisation. Results were analysed using Origin Software.

2.4.4. AFM (Atomic Force Microscopy) and MFM (Magnetic Force Microscopy) experiments

AFM (Atomic Force Microscopy) and MFM (Magnetic Force Microscopy) measurements were kindly performed by Dr. Alek Dediu research group, Consiglio Nazionale delle Ricerche (CNR), Bologna, Italy.

AFM/MFM Samples Preparation

For the AFM/MFM investigations, paraffin blocks of cells used for TEM measurements were cut on a Leica EM UC7 Ultratome in slices of a thickness of 80 nm, and put on circular glass coverslips used as support. Each section was put on a different glass coverslip for AFM-MFM imaging, considering 4 sections for each sample. Slices were fixed on glass coverslips with a drop of water and they were left to dry at room temperature, then the glass coverslips were put into a 24 wells plate, considering one glass for each well. Then, the plates were sent to Bologna for AFM/MFM measurement.

AFM (Atomic Force Microscopy) experiments

Semi-contact mode AFM was performed at ambient conditions using the AFM device *Stand-Alone SMENA AFM, (NT-MDT)*. The AFM was equipped with a SFC050 head mounting silicon probes with a guaranteed curvature radius of < 10 nm and resonance frequencies of 190 – 330 kHz *(NSG series probes, NT-MDT)*. Image resolution was 512 x 512 pixels.

MFM (Magnetic Force Microscopy) experiments

Magnetic Force Microscopy was performed on a Bruker Multimode 8 AFM (Bruker Nano Surface) equipped with a Nanoscope V Controller, a JV type scanner and magnetic probes NT-MDT. The microscope was operated in double-pass lift mode with lift heights ranging from 30 to 600 nm. The images shown were acquired at 512 x 512 pixel resolution. The noise-level corresponding to *ad-hoc* non-magnetic samples was also evaluated around 0.1-0.3 degrees, hence at least one order of magnitude less than the signal measured on magnetic samples.

2.5. MSCs functionality assessment

2.5.1. Immunofluorescent flow cytometry staining of MSCs

A suspension of 1×10^6 MSCs was stained with APC-conjugated CD34, VioBlue-conjugated CD45, PE-conjugated CD73, PE-c
onjugated Vio770 CD90 and FITC-conjugated CD105. Experiments were performed using BD FACSARIA II (BD Biosciences), and results were analysed by BD FACS Diva Software version 6.1.3 (BD Biosciences). The complete list of antibodies could be found in **appendix 8.8**. The experiments were repeated in triplicate.

Optimisation of fluorescence compensation settings for multicolour flow cytometric analyses

The fluorescence spillover from fluorochrome-conjugated antibodies was compensated using Compbeads (BD Biosciences). Briefly, 5 µl of each prediluted antibody stock to be tested were incubated with 60 µl of CompBeads Anti-Mouse Ig, κ particles and 60 µl of CompBeads Negative Control for 30 minutes at RT in the dark. Then, 200 µl of 1x PBS were added to each tube and pelleted by centrifugation at 200xg for 10 minutes. The supernatant was aspirated with a Pasteur pipette, and the bead pellet was resuspended adding 200 µl of 1x PBS in each tube, and mixed thoroughly. Samples were then analysed by flow cytometry.

Flow Cytometry fluorescent antibody staining

1×10^6 MSCs were resuspended in 100 µl of flow cytometry buffer and incubated for 10 minutes in the dark at 4°C with 5 µl of each antibody: APC-conjugated CD34, VioBlue-conjugated CD45, PE-conjugated CD73, PE-conjugated Vio770 CD90 and FITC-conjugated CD105. Then, cells were washed by adding 2 ml of flow cytometry buffer and centrifuged at 300xg for 10 minutes. The supernatant was aspirated completely, and cells were resuspended in 200 µl of 1xPBS and then analysed by flow cytometry.

2.6. MSCs differentiation experiments

2.6.1. Osteogenesis

Wild-type and *mms6*-expressing MSCs were differentiated in cell culture medium for osteogenesis for 10 or 21 days, using StemPro Osteogenesis Differentiation Kit (Gibco). Cells not induced in osteogenic medium were considered as a negative control (*0 Day*).

The differentiation experiments were performed in the absence of FeQ doping.

To perform the osteogenic differentiation, cells were seeded in 3 different 24 wells plates for each cell group, at a density of $2x10^4$ cells/well cultured in standard culture medium. After 48 hours, at confluence, cells grown in one plate for each group were considered as time point *0 Day*, the medium was removed, cells were washed twice with 1x PBS and fixed in 4% PFA for 30 minutes at RT in the fume hood. After fixation, cells were washed twice with 1 ml of ddH_2O/well and stained with 2% Alizarin Red S solution (pH 4.2) for 30 minutes. The cells were then washed three times with 1ml of ddH_2O/well and observed under light microscope and photographed at 100X magnification.

In cells considered as time point *10 Days and 21 Days*, the standard culture medium was removed, cells were washed once with 1x PBS and it was added 1 ml/well of pre-warmed MSCs osteogenesis differentiation medium. Cells were then cultured in the incubator at 37 °C, 5% CO_2, and were refeeded every 3 days. After 10 and 21 days, the MSCs osteogenesis differentiation medium was removed, cells were washed twice with 1 ml of 1xPBS and fixed in 4% PFA for 30 minutes at RT in fume hood. After fixation, cells were washed twice with 1 ml of ddH_2O /well and stained with 2% Alizarin Red S solution (pH4.2) for 30 minutes. The cells were then washed three times with 1ml of ddH_2O/well and observed under light microscope and photographed at 100X magnification.

2.6.2. Immunofluorescent Osteocalcin staining

To perform the Immunofluorescent staining (IF), MSCs (passage<10) were seeded on coverslips in 3 different 24 wells plates for each cell group, at a density of $2x10^4$ cells/well, cultured in the standard medium, at 37°C and 5% CO_2. The cells were then induced for osteogenesis and, after 10 or 21 days of incubation with the differentiation medium, cells were subjected to IF.

The medium was aspirated, then cells were washed three times with 1 ml of 1x PBS and fixed with 1 ml of 4% PFA diluted in 1x PBS for 15 min at RT. The fixative was aspirated, and cells were rinsed three times in 1x PBS for 5 min each and permeabilized in 0.1% Triton X-100 in 1x PBS for 10 min and washed three times in 1x PBS before blocking in normal goat serum (20% in 0.1% BSA-PBS) for 60 min at RT. The blocking solution was then aspirated and cells were incubated with rabbit anti-human osteocalcin IgG (AbD Serotec 7060-1515; 1:40 in 0.1% BSA-PBS) overnight at 4°C, followed by three washings in 1x PBS and incubation with Alexa-Fluor 488-conjugated goat anti-rabbit IgG diluted 1:100 in 0.1% BSA-PBS for 1hour at RT in the dark. Coverslips were washed three times with 1x PBS then incubated in DAPI solution (1:5000 in distilled water) for 10 minutes at RT and imaged using a Fluorescent Microscope (Nikon E800). Experiments were performed in triplicate and repeated three times.

2.6.3. Chondrogenesis

Wild-type and *mms6*-expressing MSCs were differentiated in cell culture medium for chondrogenesis for 21 days using StemPro Chondrogenesis Differentiation Kit (Gibco). Cells not induced in chondrogenic media were considered as a negative control *(0 Day)*.

To perform the chondrogenic differentiation, cells were seeded in 2 different 24 wells plates for each cell group, at a density of $2*10^4$ cells/ well in standard culture medium. After 48 hours, when the cells reached the confluence, cells grown in one plate for each group were considered as time point *0 Day*, medium was removed and

cells were washed twice with 1X PBS, then fixed in 4% PFA for 30 minutes at RT in a fume hood, washed twice with ddH_2O, and stained with Alcian Blue staining solution, as explained below.

In cells considered as time point *21 Days*, the medium was removed, and it was added 1 ml/well of pre-warmed chondrogenic differentiation medium in the dark. The cells were then cultured in the incubator, at 37°C and 5% CO_2 until day 21. Culture were refed every 3 days.

After 21 days, the cartilage spheroids were well visible. The differentiation medium was removed, and spheroids were carefully washed with 1x PBS twice, paying attention to do not aspirate them, and then they were fixed in 4% PFA for 30 minutes at RT. Then, the fixative was removed and spheroids were washed twice with ddH_2O. Immediately before use, the required amount of Alcian Blue staining solution was filtered through a 0.22 µm syringe filter equipped with a PES-membrane. The ddH_2O was carefully aspirated, and 2 ml of filtered Alcian Blue staining solution were added in each well. Then, spheroids were incubated in the dark for 45 minutes at RT. At the end of the incubation time, the Alcian Blue staining solution was carefully aspirated and the cartilage spheroids were washed with 1 ml of Alcian Blue destaining solution for 10 min, for three times. The destaining solution was removed and spheroids were covered with 1 ml of 1x PBS. The intense dark blue cartilage spheroids were then pictured using an IPhone 6 camera.

2.6.4. Adipogenesis

Wild-type and *mms6*-expressing MSCs were differentiated in cell culture medium for adipogenesis for 10 or 21 days using *StemPro Adipogenesis Differentiation Kit* (Gibco). Cells not induced in the adipogenic medium were considered as a negative control (*0 Day*).

To perform the adipogenic differentiation, cells were seeded in 3 different 24 wells plates for each cell group, at a density of $2x10^4$ cells/well in standard culture

medium. After 48 hours, when the cells reached the confluence, cells grown in one plate for each group were considered as time point *0 Day*, medium was removed from the wells and cells were washed twice with 1x PBS, then fixed in 4% PFA and stained with Oil Red O solution, as explained below.

In cells considered as time point *10 Days* or *21 Days*, the medium was removed and it was added 1 ml/well of pre-warmed complete Adipogenesis differentiation medium in the dark. The cells were then put in the incubator, at 37°C and 5% CO_2 for the required time. Culture were refed every 3 days. After 10 and 21 days of incubation with the complete differentiation media, the medium was removed and plates were carefully washed twice with 1 ml of 1x PBS, to not disrupt the cells monolayer. The cells were fixated in 4% PFA under the chemical hood, then they were incubated for 1 hour at 37°C, paying attention to do not perturb the lipids droplets. After fixation, cells were washed twice with 1ml of 1x PBS, then incubated with 1 ml of 60% isopropanol for 1 minute. Then, the isopropanol was disposed and the cells were let dry under the chemical hood. At this point, it was added the Oil Red O solution diluted 3:2 in distilled water for 20 minutes. When the incubation time passed, cells were washed with 1x PBS for three times and imaged immediately at light microscope at 200x magnification. Cells were pictured using a coloured camera (Micropublisher camera, QIMAGING). The pictures of cells incubated with complete differentiation media for 10 and 21 days were compared to the *0 Day* plates.

2.6.5. Cell proliferation assessment by Incucyte ZOOM System Software

Incucyte ZOOM System Software was used to study the cell proliferation by both qualitative and quantitative analysis. Cell proliferation was qualitatively monitored by pictures, and quantitatively assessed as the percentage rate of MSCs plate coverage, in a real-time quantitative live-cell analysis.

To perform the cell proliferation study, MSCs cells (passage<10) were seeded in 3 different 24 wells plates for each cell group, at a density of $2x10^4$ cells/well in standard culture medium. The cells were seeded in each plate according to the following layout:

- Lane 1- Wild-type MSCs
- Lane 2- Wild-type MSCs in FeQ doped medium for 21 days
- Lane 3 - *mms6*-expressing MSCs (21 days post transfection, cultured in FeQ doped medium)

After 1 hour from seeding, the cells were moved from cell culture incubator in the Incucyte machine incubator, where the proliferation monitoring started. Cells were refed every 3 days. Experiments were performed in triplicate and repeated three times.

2.7. *In vitro* AMF exposure

2.7.1. Media used in the experiments

- Standard medium: DMEM supplemented with 20% FBS + Penicillin/streptomycin (100 U/ml/100µg/ml), without FeQ.
- Exposure medium: DMEM supplemented with 10% FBS, without Penicillin streptomycin and without FeQ.

2.7.2. *mms6*-expressing MSCs monolayers creation and cell exposure procedures

MSCs seeding in Petri dishes for cell monolayer arrangements

Wild-type MSCs and *mms6*-expressing MSCs were seeded in sterile 35 mm Petri dishes at the density of $3x10^5$ cells each Petri dish, using 2 ml of standard medium. Cells were incubated at 37°C, 5% CO_2 overnight. The following day, the standard medium was changed with the exposure medium, immediately before the AMF exposure.

AMF exposure of cell monolayers:

Six sterile 35 mm Petri dishes, each containing a single monolayer of *mms6*-expressing MSCs, were created as explained above. Then, three Petri dishes were exposed one by one to an AMF of 565.3 kHz frequency for 1 hour, in the magneTherm device, using 40°C recirculating water from water bath, while the other three Petri dishes were inserted in the magneTherm system under the same conditions, but with AMF switched off, as a control. After exposure, unless otherwise specified, Petri dishes were incubated overnight in the incubator at 37°C and 5% CO_2. The same procedure was repeated to test the AMF effect on Plain MSCs.

Bright field microscopy investigation of the effect of the exposure for one hour to an AMF of 565.3 kHz frequency on Plain MSCs and *mms6*-expressing MSCs, arranged in a monolayer.

Wild-type MSCs and *mms6*-expressing MSCs, grown in a monolayer arrangement as previously explained, exposed and not exposed to AMF, were imaged in bright field microscopy at 40x magnification with an inverted microscope.

2.7.3. MSCs seeding in tubes for 3D cell pellets arrangements

Creation of 3D pellets composed only of MSCs cells

To create 3D pellets of *mms6*-expressing MSCs, cells were seeded in 35 mm Petri dishes at the concentration of $3x10^5$ cells for each Petri dish and cultivated in the incubator at 37°C and 5% CO_2 in standard medium, until confluence. From each Petri dish, a 3D pellet was created as follows: the cells were trypsinized and resuspended in 150 µl of the standard medium, in a 15 ml sterile plastic tube. The cells were then centrifuged at 113xg for 2 minutes, to create a pellet, and incubated overnight in the incubator at 37°C, 5% CO_2 before AMF exposure.

Creation of 3D co-cultures of *mms6*-expressing MSCs and cancer cells pellets

Two types of 3D co-cultures cell pellets were created, one composed of *mms6*-expressing MSCs mixed with MG63 cells and one composed of *mms6*-expressing MSCs mixed with A431 ecad-GFP expressing cells respectively. To create a 3D co-culture composed of *mms6*-expressing MSCs and MG63 cells, at **1:2 ratio**, $2x10^5$ *mms6*-expressing MSCs and $4x10^5$ MG63 cells were mixed and resuspended in 200µl of medium; to create the **1:4 ratio**, $1.2x10^5$ *mms6*-expressing MSCs and $4.8x10^5$ MG63 cells were mixed and resuspended in 200µl of medium. To create a 3D co-culture composed of *mms6*-expressing MSCs and A431 ecad-GFP expressing cells, at **1:2 ratio,** $2x10^5$ *mms6*-expressing MSCs and $4x10^5$ A431 ecad-GFP expressing cells were mixed and resuspended in 200 µl of medium. The cells were

then centrifuged at 113xg for 2 minutes, to create a pellet, and incubated overnight in the incubator at 37°C, 5% CO_2 before AMF exposure.

2.7.4. Description of the assays used in the experiments: Pierce LDH Cytotoxicity Assay, AlamarBlue Cell Viability Assay, Trypan Blue Exclusion Assay.

Pierce LDH Cytotoxicity Assay description

The kit quantifies lactate dehydrogenase (LDH), an enzyme involved in the energy production, found in cell cytosol. In glycolysis, LDH enzyme converts pyruvate to lactate via reduction of NAD^+ to NADH, while inside the liver LDH performs the opposite reaction in the Cori cycle. When cells are damaged, and their plasma membrane breaks, LDH is released in the medium. The kit used in the experiments exploits the reaction between a diaphorase (an enzyme that catalyses the reduction of various dyes) and the NADH formed by LDH reaction. The NADH is used by the diaphorase to reduce a tetrazolium salt to a red formazan product. In this way, it is possible to quantify the extracellular LDH presence, which is directly proportional to the formazan production. To measure the LDH release, cell culture media is transferred in a fresh microplate with the addition of the kit reagents. Following an incubation time of 30 minutes at RT, the reaction is stopped, and the LDH activity is determined by spectrophotometric absorbance at 490 nm.

Pierce LDH Cytotoxicity Assay experimental procedure

After the exposure, the AMF exposed and the unexposed controls cells were immediately seeded in a 96 wells sterile plastic plate at the concentration of $5.5x10^3$ cells/well, in triplicate, considering three wells for the Maximum LDH activity (Lysis buffer) and three wells for the Spontaneous LDH activity (water), as suggested by manufacture's protocol. Then, the cells were incubated overnight in the incubator at 37°C, 5% CO_2. The day after, the Lysis buffer (10 µl each well) was added to the three wells considered for the Maximum LDH activity, while water (10 µl each well) was added in the three wells considered for the Spontaneous LDH

activity. The plates were then incubated in the incubator for 45 minutes. After that, 50 µl of medium taken from each well were transferred in a fresh 96 well plate, flat bottom. Then, 50 µl of Reaction Mixture were added to each well, and the plate was incubated at RT for 30 minutes in the dark. At the end of the incubation time, 50 µl of Stop Solution were added to each well, and the solution absorbance was immediately read at the plate reader (FLUOstar Omega, BMG LABTECH).

The percentage of cytotoxicity was calculated according to the formula suggested by the protocol:

$$\%\ \text{Cytotoxicity} = \frac{\text{Exposed LDH activity} - \text{Spontaneous LDH activity}}{\text{Maximum LDH activity} - \text{Spontaneous LDH activity}} * 100$$

2.7.5. Cell viability investigation by AlamarBlue Cell Viability Assay

AlamarBlue Cell Viability Assay description

Cytosol of viable and healthy cells is a reducing environment. The kit employed for these experiments relies on the reduction capacity that living cells have. *AlamarBlue Cell Viability Assay* contains *resazurin*, which is a cell permeable, non-fluorescent and non-toxic blue dye. *Resazurin* enters inside the cells, and it is reduced by the viable ones in *resorufin*, a red fluorescent dye, that can be monitored on a plate reader or a fluorescence spectrophotometer. Comparing the fluorescence of two or more cell populations, it is possible to establish which one is the more viable.

AlamarBlue Cell Viability Assay experimental procedure

After the exposure, Alamar Blue reagent was added to the cells medium in the proportion of $1/10^{th}$ of cell medium volume. Then, the cells were incubated in the incubator at 37°C, 5% CO_2. Medium fluorescence was read after 3 hours of incubation with Alamar Blue reagent in the plate reader (FLUOstar Omega, BMG LABTECH) by excitation at 544 nm and emission at 590 nm. Results are presented

both as relative fluorescence units (RFU) than as the percentage of cell viability, against controls considered as 100% viable. This percentage was calculated according to (Zachari et al., 2014; Duzgunes, 2003):

$$\%\text{Viability} = \frac{\text{RFU(exposed)} - \text{RFU(negative ctr)}}{\text{RFU(not exposed)} - \text{RFU (negative ctr)}} * 100$$

Negative controls are represented by exposure medium without cells and with the addition of 10% Alamar Blue reagent.

2.7.6. Cell death determination by *Trypan Blue Exclusion Assay*

Trypan Blue Exclusion Assay description

Trypan Blue solution is routinely employed to count the cells in the haemocytometer during subculturing and in experiments that require an accurate determination of the cell viability using bright field microscopy. Trypan Blue dye is excluded from viable cells, which possess a selective membrane. Dead cells, instead, are permeable to the dye and do uptake it. Observing the cells in bright field microscopy, it is possible to differentiate the dead cells, which appear blue, from the living cells, which remain translucent.

Trypan Blue Exclusion Assay experimental procedure

To count the viable cells number by Trypan Blue Exclusion Assay, 100 µl of 0.4% Trypan Blue Solution were added to 100 µl of cells suspension (1:1 dilution) and incubated at RT for 5 minutes. Then, 10 µl of the suspension were loaded into a haemocytometer. Blue stained cells and the number of total cells were counted using bright field microscopy, at 100x magnification.

Percentage of living cells were calculated as:

$$\%\ viable\ cells = 1 - \left(\frac{\text{number of blue cells}}{\text{number of total cells}}\right) \times 100$$

2.7.7. Description of the MSCs staining procedures with CellTracker CM-DiI Red

CellTracker CM-DiI Red description

CellTracker CM-DiI Red is a nontoxic red fluorescent dye employed for cell tracking that could be viewed in fluorescent microscopy. It is a nonspecific lipophilic compound that labels the plasma membrane of cells in culture. This dye is well retained by the cell, allowing for multigenerational tracking of cellular movements. The *CellTracker CM-DiI Red* excitation/emission spectra (553/570 nm maxima) do not overlap with green fluorescent dyes and proteins.

MSCs staining with CellTracker CM-DiI Red

The *CellTracker CM-DiI Red* dye stock solution was reconstituted at the concentration of 1 mg/ml according to manufacturer's protocol, by adding 50µl of DMSO to one vial containing 50µg of dried powder, to the final concentration of 1M. For the *mms6*-expressing MSCs labelling, cells were cultivated in standard medium supplemented with FeQ 3.4µl/ml in a T75 cell culture flask. When cells reached confluence, the exhausted medium was removed, and the cells were rinsed with 5 ml of HBSS. Next, 30 µL of the *CellTracker CM-DiI Red* dye stock solution were added in 10 ml of HBSS inside a sterile plastic tube and the solution was added to the cells in the flask, in the dark. The cells were then incubated in the incubator at 37^{o}C and 5% CO_2 for 5 minutes followed by 15 minutes of incubation in ice, in the dark. Then, the solution was removed, and the cells were washed with 4 ml of HBSS. The cells were trypsinized and resuspended in 10 ml of HBSS in a sterile 15 ml plastic tube. Then, the cells were centrifuged at 177xg for 5 minutes. Supernatant was discarded and cells were counted.

2.7.8. Description of the MG63 cells staining procedures with CellTracker Green CMFDA Dye

CellTracker Green CMFDA Dye description

CellTracker Green CMFDA (5-chloromethylfluorescein diacetate) is a green, stable, nontoxic fluorescent dye used for cell tracking. As for *CellTracker CM-DiI*, this dye passes through cell membrane, it is well retained by cells and it is passed to the next generation of daughter cells. *CellTracker Green CMFDA* dye fluorescence lasts for at least 72 hours and its green excitation/emission spectra (492/517 nm maxima) does not overlap with GFP (green fluorescent protein) and RFP (red fluorescent protein) excitation/emission spectra.

CellTracker Green CMFDA Dye MG63 staining experimental procedure

The *CellTracker Green CMFDA Dye* stock solution was reconstituted at the concentration of 10 mM according to manufacturer's protocols by adding 11µl of DMSO to one vial containing 50 mg *CellTracker Green CMFDA Dye* dried powder.

For the MG63 cells labelling, cells were cultivated in standard medium in a T75 cell culture flask. When cells reached confluence, the exhausted medium was removed and the cells were rinsed with 5 ml of HBSS. Next, 10 µL of the *CellTracker™ Green CMFDA Dye* stock solution were added in 10 ml of HBSS in a sterile plastic tube, and the solution was added to the cells in the flask, in the dark. The cells were then incubated in incubator at 37°C, 5% CO_2 for 30 minutes. At the end of the incubation time, the staining solution was removed and cells were rinsed with 4 ml of HBSS after the labelling. The cells were harvested by trypsinization, resuspended in 10 ml of HBSS in a sterile 15 ml plastic tube and then centrifuged at 177xg for 5 minutes. The supernatant was discarded, and cells were counted in an haemocytometer.

2.7.9. Description of the experimental procedures used for AMF exposure of *mms6*-expressing MSCs cultivated in a monolayer

The effect of one hour 565.3 kHz AMF on *mms6*-expressing MSCs arranged in a monolayer. Determination of cell cytotoxicity by *LDH cytotoxicity assay*

The effect of AMF exposure at 565.3 kHz on *mms6*-expressing MSCs was established by the *Pierce LDH Cytotoxicity Assay Kit*. In these experiments, the cells were grown in monolayers in Petri dishes, as explained in section 2.7.2. Three Petri dishes were exposed to AMF at 565.3 kHz frequency for 1 hour, in the magneTherm system, using 40 °C recirculating water from the water bath, while three Petri dishes were inserted in the magneTherm system under the same conditions, but with AMF switched off, as a control. The controls and the exposed cells were tripsinised immediately after the exposure and seeded in a 96 wells plate at the concentration of $5.5x10^3$ cells/well, in triplicate. The cells were incubated O/N in the incubator. The following day, the *Pierce LDH Cytotoxicity Assay* was carried out as explained in section 2.7.4.

The effect of one hour 565.3 kHz AMF on *mms6*-expressing MSCs arranged in a monolayer. Determination of cell viability by *AlamarBlue Cell Viability Assay*.

The effect of one hour of AMF exposure at 565.3 kHz on *mms6*-expressing MSCs viability was established by the *AlamarBlue Cell Viability Assay*. In these experiments, the cells were grown in a monolayer in Petri dishes, as explained in section 2.7.2. Three Petri dishes were exposed to AMF at 565.3 kHz frequency for 1 hour, in the magneTherm system, using 40°C recirculating water from the water bath, while three Petri dishes were inserted in the magneTherm system under the same conditions, but with the AMF switched off, as a control.

After the exposure, the Petri dishes were put in the incubator. The next day, the cell viability was assessed by *AlamarBlue Cell Viability Assay* as suggested by manufacture's protocol, as explained in section 2.7.5, and fluorescence intensity was read after 3h of incubation with AlamarBlue reagent.

2.7.10. Description of the experimental procedures used for AMF exposure of 3D cultures:

The effect of one hour 565.3 kHz AMF on 3D cultures of *mms6*-expressing MSCs. Treatment was repeated twice and followed by cell death assessment by *Trypan Blue Exclusion Assay*.

Six tubes containing 3D pellets of *mms6*-expressing MSCs were created as explained in section 2.7.3. Then, three tubes were exposed one by one to AMF of 565.3 kHz frequency for 1 hour, in the magneTherm system, using 40 °C recirculating water from water bath, while the other three tubes were inserted in the magneTherm system under the same conditions, but with AMF switched off, as a control. After exposure, tubes were incubated overnight in the incubator at 37°C and 5% CO_2. In this experiment, due to the 3D arrangement of cells that formed a thick pellet, it was chosen to duplicate the AMF exposure, so the following day, the exposed tubes were exposed again at 565.3 kHz for 1 hour (double exposure). Cell viability was assessed by *Trypan Blue Exclusion Assay*, as explained in section 2.7.6.

The effect of one hour 565.3 kHz AMF on 3D cultures of *mms6*-expressing MSCs and MG63 cells. Treatment was repeated three times and followed by cell viability assessment by *Trypan Blue Exclusion Assay*.

The formation of 3D pellets was obtained by co-culturing *mms6*-expressing MSCs and MG63 cells in 15 ml tubes, at 1:2 and at 1:4 ratio, as explained in section 2.7.3. For each ratio, six tubes were made, three were inserted one by one in the magneTherm system and exposed to an AMF at 565.3 kHz frequency for one hour, while the other three tubes were inserted in the magneTherm system under the same conditions, but with the AMF switched off, as a control. After the exposure, the tubes were put in incubator at 37°C and 5% CO_2. The following day, the tubes that had been exposed the previous day to the AMF, were exposed again twice, for one hour at the same 565.3 kHz frequency, with a 2 hours pause between each exposure. The cells of each tube were then counted by *Trypan Blue Exclusion Assay*, as explained in section 2.7.6.

The effect of one hour 565.3 kHz AMF on 3D co-cultures of *mms6*-expressing MSCs and A431 ecad-GFP expressing cells. Treatment was repeated three times and followed by *AlamarBlue Cell Viability Assay.*

The formation of 3D pellets was obtained by co-culturing *mms6*-expressing MSCs and A431 ecad-GFP expressing cells in 15 ml tubes, as explained in section 2.7.3. For these experiments, the chosen ratio was 1:2, counting $2x10^5$ *mms6*-expressing MSCs, stained by *CellTracker CM-Dil Red*, and $4x10^5$ A431 ecad-GFP expressing cells. For each experiment, three pellets were exposed one by one to AMF at the frequency of 565.3 kHz for 1 hour, while three pellets were kept in the machine under the same conditions but not exposed at AMF, serving as controls. The following day, the exposed pellets were exposed again twice, for one hour at the same 565.3 kHz frequency, with a 2 hours pause between each exposure. Then the cells were seeded in triplicate in a 96 multiwells plate at a density of $5.5\ x10^3$ cells/well in 100 µl of exposure medium and incubated overnight in the incubator at 37°C and 5% CO_2. The following day, *AlamarBlue Cell Viability Assay* was performed as described in section 2.7.5, using 10 µl of Alamar Blue reagent per well, as indicated by the manufacture's protocol.

2.7.11. Fluorescent microscopy on 3D co-cultures of *CellTracker CM-DiI Red* stained *mms6*-expressing MSCs and *CellTracker Green CMFDA Dye* stained MG63 cells, at 1:2 ratio.

mms6-expressing MSCs were stained with *CellTracker CM-DiI Red*, while MG63 cells were stained with *CellTracker Green CMFDA Dye*, as explained in sections 2.7.7 and 2.7.8. The two cell populations were then mixed in plastic sterile tubes (15 ml each) at the ratio of 2:1, counting $4x10^5$ MG63 green stained cells and $2x10^5$ CM-DiI Red stained 21 days *mms6*-expressing MSCs. The cells were then centrifuged at 177xg for 2 minutes, forming pellets. Three pellets were exposed to AMF for 1 hour, in the magneTherm system at 565.3 kHz frequency, using 40 °C recirculating water from the water bath, while the other three pellets were placed in the magneTherm system in the same conditions, but with the AMF switched off, as a control. Then, pellets were incubated at 37°C, 5% CO_2. The day after, the exposed pellets were exposed again twice, with a pause of 2 hours between the two exposures. Then the cells (control and exposed) were seeded in quadruplicate in 24 wells plate ($2 x10^4$ cells/well). The next day, the nuclei of the cells were stained with DAPI, by adding 25 µl of *VECTASHIELD mounting medium with DAPI* on cells. Cells were covered with a glass coverslip, and then they were immediately imaged by fluorescence microscopy, at 100x magnification. The pictures were analysed using ImageJ software, and for each picture, the number of green cells (MG63 cells) and the number of blue nuclei, corresponding to the total number of cells, was counted.

2.7.12. MagneTherm system device description

The AMF was applied using the *magneTherm* system device from Nanotherics, a commercial device designed to study magnetic fluid and nanoparticles hyperthermia (**Figure 21**). In this work, the device was used to investigate the AMF effects on the MNPs created inside the MSCs by *mms6* gene expression, 21 days post transfection.

The physical principle that underlies the *magneTherm system* device function is that a current applied through a conductor determines the creation of a circular magnetic field around it, as described by Ampere's law:

$$B = \frac{\mu_0 I}{2\pi r}$$

where B is the magnetic field, μ_0 the permeability of the free space, I is the current in the wire, and r the radius from the wire.

If the conductor is a coil (as for the *magneTherm system*), the magnetic field strength is enhanced, and a strong field is created at the centre of the coil, where all the magnetic field generated by each turn of the coil pass. The physical concept that drives the experiments is that MNPs subjected to an AC magnetic field:

- lose energy as a consequence of their magnetisation reversal process, producing heat;
- tend to vibrate, causing the cell membrane breaking.

The *magneTherm* system device was used in this case to determine if MNPs expressed by *mms6*-expressing MSCs could support MH when an AMF is applied. For all the experiments it was used the 17-turning coil provided with the instrument, with the capacitor array type B6.2. The oscilloscope Volts/Div was set at 50 mV, the DC power supply voltage was set at 23.1 V and the AMF frequency chosen was 565.3 kHz. The device was integrated with a water jacket to keep the cells at a constant temperature of 37°C. In all the experiments performed, the Petri dishes and the tubes in which the cells were seeded were inserted in the magneTherm device one by one and not all in stack, to have the same magnetic field strength among all the samples.

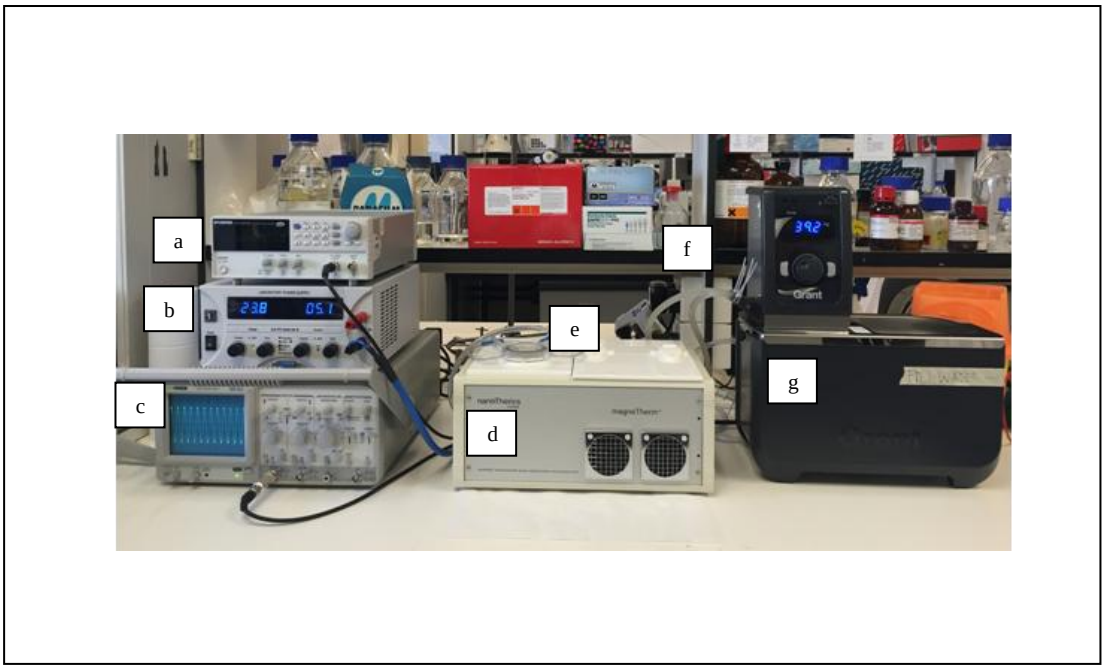

Figure 21. ***Nanotherics magneTherm*** **system device used in the experiments.**

Components of the system are: a) Function Generator, b) DC Power Supply, c) Oscilloscope, d) magneTherm system, e) Water jacket, f) Cooling water connecting tubes, g) Waterbath.

2.8. In vivo AMF exposure

2.8.1. Delivery of an AMF by magneTherm device: experiment layout

"All experiments were carried out in accordance with the United Kingdom Animal Scientific Procedures Act (1986) and UK Home Office regulations under project licence number (PPL No.) 70/7926.
All the implantation and the culling were undertaken by Morwenna Muir".

16 female CD-1 nude mice, two-months old, were implanted subcutaneously bilaterally, with $1x10^6$ A431 Ecad-GFP cells per implant, diluted in 0.1ml of HBSS.

Tumours were measured twice weekly by plastic callipers (Camlab, UK) and animals were weighed daily post-intracardiac injection. The volume of mice tumours was calculated as an ideal ellipsoid following the formula:

0.5 x lenght of tumour x square of tumour breadth

Tumours were randomised before to start, and 4 groups of 4 mice each were created by grouping tumours of the same volume together, so that the total volume of each group was the same as each other.

Then, groups of mice were treated as follow:

Group A - A431 Ecad-GFP cells s/c + Anaesthesia Only

Group B - A431 Ecad-GFP cells s/c + magneTherm treatment, 565.3kHz Daily, x 3 days

Group C - A431 Ecad-GFP cells s/c + red *mms6*-expressing MSCs + Anaesthesia Only

Group D - A431 Ecad-GFP cells s/c + red *mms6*-expressing MSCs + magneTherm treatment, 565.3kHz Daily, x 3 days

One week later, Group C and Group D were intracardiac injected with $1x10^6$ red *mms6*-expressing MSCs. Animals were culled after the final magneTherm treatment

(treatment am, cull pm). On cull, tumours were split and stored in HBSS, formal saline and snap frozen; liver, lung and spleen were removed and halved and half stored in formal saline for immunohistochemistry investigation, half snap frozen for fluorescent microscopy imaging.

Due to the busy laboratory schedule, Group A and B were implanted one week later than Group C and D.

2.8.2. Description of AMF treatment by magneTherm device

The MagneTherm water bath was set to 40^{o}C to keep the instrument coil at the same temperature during all the treatment, as suggested by the manufacture. Mice exposed to magneTherm were anesthetised by isofluorane, their eyes were cover with Lacrilube (Allergan) to avoid eyes drying, and then they were positioned on a ruler with the face mask on to provide anesthetisation during all the duration of the treatment. The ruler was carefully inlaid through the magneTherm to allow a rectal probe to be inserted with the help of soft paraffin on. The ruler was then pushed back into the magneTherm machine so that the tumours were centrally placed and the reading on the ruler was kept in consideration to ensure that further treatments were all placed the same. magneTherm was plug in and frequency was set at 565.3 kHz following the protocol described in the **appendix 8.9**. Mice were treated in the magneTherm for 30 minutes. The mice skin temperature was read every 5 minutes respectively by an infrared thermometer gun, while mice core temperature was read by a rectal thermocouple. At the end of the treatment, the ruler was slightly moved through the magneTherm to allow rectal probe or thermocouple wire to be removed, then back through the magneTherm to remove the mouse. At the end of the AMF treatment, mice were placed into the recovery box and monitored until their full recovery from the treatment.

2.8.3. RNA extraction from mice tissues

RNA was extracted from mice organs and tumours using the RNeasy Mini Kit (Quiagen) and following the manufacture's instructions. Briefly, the tissue samples from the animals were disrupted, and the lysate was homogenised in Buffer RLT and centrifuged for 3 minutes at full speed. Then, the supernatant was carefully removed by pipetting and transferred into a new microcentrifuge tube. A volume of 70% ethanol was added to the cleared lysate, and mixed immediately by pipetting. The samples were transferred to an RNeasy spin column placed in a 2 ml collection tube and centrifuged for 15 seconds at 8000xg. The flow-through was discarded. Then, 700 µl Buffer RW1 were added to the RNeasy spin column and samples were centrifuged for 15 seconds at 8000xg to wash the spin column membrane. The flow-through was discarded. Then, 500 µl Buffer RPE were added to the RNeasy spin column, and samples were centrifuged for 15 seconds at 8000xg to wash the spin column membrane. The flow-through was discarded. This step was repeated twice. The RNeasy spin column was placed in a new 1.5 ml collection tube and 30–50 µl RNase-free water were added directly to the spin column membrane. Samples were centrifuged for 1 min at 8000xg to elute the RNA. Yield and purity of RNA samples were determined using a NanoDrop spectrophotometer and cDNA was synthesised to perform the RT-PCR, as previously explained.

2.8.4. Prussian Blue staining

For each mouse, sections of liver, spleen, lung and tumours were stained with PBR solution. Sections were washed in water and then incubated in the PBR solution for 20 minutes. Then, sections were washed well in running water and counterstained with 1% neutral red. Then, section were washed again in running water, cleared and mounted. Ferric iron was blue and nuclei were stained in red. Sections were imaged in bright field at 400x magnification, in NanoZoomer Digital Slide Scanner (Hamamatsu), using NanoZoomer Digital Pathology software (Hamamatsu) and considering 5 fields for each section.

2.8.5. Fluorescent microscopy

Following mice sacrifice, spleen, liver, lung and tumours were retrieved and snap frozen, to be subsequently sectioned at 5 µm thickness at the cryostat. Cell nuclei were stained with DAPI (Vectashield) and then sections were imaged by fluorescence microscopy at 200x magnification (Zeiss Axioskop 2).

2.8.6. Cells Fixable Viability Dye eFluor 450 staining

Tumour tissues were analysed for dead cells by *Fixable Viability Dye eFluor® 450* (ThermoFisher). The dye was thawed at room temperature for 10 minutes, then diluted 1:1000 in 1X PBS (20 µl of dye were diluted in 20 ml of 1x PBS). Fresh tumours tissues were cut into small pieces by scalpel and immediately placed in a 24 wells sterile plate. Tumour tissues were washed twice with 1 ml of 1x PBS, then they were covered with 2 ml of diluted Fixable Viability Dye eFluor® 450 and incubated on ice in the dark for 30 minutes. After incubation, the dye was removed from each well, and tumour tissues were washed with 1x PBS twice. To avoid samples drying, 2 ml of 1x PBS were added to each well. Tumour tissues were kept on ice in the dark and immediately imaged at Multiphoton microscope. Image analysis was carried out using Imaris software (8.0.1).

2.8.7. Multiphoton Imaging setup

After mice culling, slices of fresh tumours were analysed for dead cells by *Fixable Viability Dye eFluor 450* (ThermoFisher) and for the red MSCs presence (Group C and Group D).

Briefly, a picoEmerald (APE) laser provided both a tunable pump laser (720–990 nm, 7 ps, 80 MHz repetition rate) and a spatially overlapped second beam termed the Stokes laser (1064 nm, 5–6 ps and 80 MHz repetition rate). The laser was inserted into an Olympus FV1000 microscope coupled to an Olympus

XLPL25XWMP N.A. 1.05 objective lens using a short-pass 690 nm dichroic mirror (Olympus). GFP protein fluorescence detection: two-photon fluorescence signals were filtered using the following series of filters: FF520-Di02, FF483/639-Di01 and ET525/50m. CellTracker CM-DiI Dye red fluorescence detection: two-photon fluorescence signals were filtered using FF520-Di02, FF757-Di01 and FF01-609/181. Fixable Viability Dye eFluor signals were filtered using FF520-Di02, FF483/639-Di01 and FF01-466/40. The pump laser was tuned to 860 nm and used 50 mW power as measured at the objective, whilst the Stokes laser used 20 mW power as measured at the objective.

2.8.8. Immunohistochemistry (IHC) of paraffin embedded sections

Following mouse sacrifice, the organs were washed extensively in 1xPBS, collected in HBSS and then fixed in 4% formaldehyde for 24 hours at RT. They were then washed three times in 1xPBS before sending to the Division of Pathology Histology services laboratories for processing and paraffin embedding. 4µm sections were cut from the paraffin blocks and put on positive charged glass slides. IHC staining was performed on an automated Leica Bond III stainer using Bond Polymer Refine Detection kit (Leica). Slides were subjected to dewaxing, epitope retrieval and then antibody staining processes. The following protocols for Caspase 3 and E3.1 were followed.

For Caspase3 antibody staining, the sections were incubated with the primary antibody diluted 1:100 for 1 hour, followed by three washes in BOND wash. The sections were then incubated with Post Primary antibody solution to enhance antibody penetration for 8 minutes, followed by a further three washes in BOND wash. Ready to use Dako EnVision-HRP labelled anti-rabbit labelled polymer (Dako) secondary antibody was then applied for 30 minutes at RT, followed by three washes in BOND wash before adding two washes of Mixed DAB Refine solution-substrate chromogen, 3.3'- diaminobenzidine (DAB) to allow visualization of the complex with a brown precipitate. The sections were washed three times in deionised water and counterstained using Harris Hematoxylin solution for 5 minutes, followed by deionised water wash, BOND wash and one final deionised water wash.

For E3.1 antibody staining, the sections were incubated with MOM Blocking reagent (*Mouse on Mouse*, Vector Laboratories) for 60 minutes, followed by three washes in BOND wash. The Blocking Reagent is used to block any non-specific binding of mouse antibodies.

Slides were then incubated with primary antibody diluted 1:500 for 15 minutes, followed by three washes in BOND wash. The sections were then incubated with anti Mouse IgG-HRP secondary antibody (SigmaAldrich) diluted 1:300 for 15 minutes, followed by three washes in BOND wash before adding Mixed DAB Refine Solution to visualise. Then, a further 3 washes in deionised water were applied after DAB incubation.

The sections were then counterstained with Harris Hematoxylin solution for 5 minutes, followed by deionised water wash, BOND wash and final deionised water wash.

All IHC Slides were then dehydrated and cleared in graded alcohols and Xylene as follows: 50% ethanol for 30 sec, 80% ethanol for 2 mins, 2x 100% ethanol for 2 min and 2x Xylene for 5min. Sections were then mounted in a DPX mounting medium.

2.8.9. Haematoxylin and Eosin (H/E) staining of paraffin embedded sections

Sections were washed in distilled water, dewaxed in xylene and rehydrated in increasing concentration of ethanol (100%- 80%- 50% ethanol, 2 minutes each). Then, sections were washed in running water for 2 minutes and stained with ready-made Harris Haematoxylin (Shandon) for 4 minutes, transferred to a dish of Scott's tap water substitute (SigmaAldrich) until the tissue sections turned blue, then washed in running water and stained with EosinY solution (Shandon) for 5 minutes. Slides were washed in running water, dehydrated and cleared in graded alcohols, and mounted in a DPX mounting medium.

2.8.10. Statistical Analysis

The results were analysed using Excel software and GraphPad Prism (Prism 5.0, USA).

Statistical analysis of TEM pictures and flow cytometry results was performed using one-way ANOVA, followed by post hoc Tukey test between groups when a statistical difference was found. A value of $p < 0.05$ was considered statistically significant.

Proliferation statistical analysis was performed using two-way ANOVA test, followed by Bonferroni post test to perform multiple pairwise comparisons when the two-way ANOVA confirmed statistical significance. A value of $p<0.05$ was considered statistically significant.

For the *in vitro* AMF exposure results, statistic analysis was carried out using Student's t-test to compare the two cell populations -exposed and not exposed- to AMF. A value of $p < 0.05$ was considered statistically significant.

Statistical analysis on tumours volume and growth was carried out using two-ways ANOVA. A value of $p < 0.05$ was considered statistically significant.

Statistical analysis on red MSCs inside the tumours of exposed and not exposed mice was calculated using Student's t-test to compare the two cell populations -exposed and not exposed- to AMF. A p-value that was equal or less than 0.01 was considered statistically significant.

For Caspase-3 stained tumour cells, five different regions of each tumour were considered, and the percentage of caspase-3 stained cells on the total cell nuclei was determined. Statistical analysis was performed using one-way ANOVA. A value of $p < 0.05$ was considered statistically significant.

3. Expression of MTB genes *mms6* and *mmsF*, alone or in combination, in human osteosarcoma MG63 cells. Study of the created intracytoplasmic structures by TEM, SQUID and Hyperthermia.

3.1. Introduction

In this chapter, it was determined whether the MTB genes *mms6* and *mmsF* could be expressed or co-expressed in human osteosarcoma MG63 cells. It was also investigated if the expression of these genes in human cells leads to the creation of vesicles similar to magnetosomes, as for MTB. To ascertain that, the human osteosarcoma MG63 cells were transfected with plasmids pcDNA 3.1 containing the *mms6* gene, the plasmid pcDNA 4/TO containing the *mmsF* gene, and co-transfected with both of them. The cells were then cultured in a ferric quinate (FeQ) doped medium (3.4 µl FeQ/ml), following the same protocol for the culture of MTB, to provide non-magnetic iron necessary to create magnetosomes. The expression of the MTB genes in MG63 cells was determined at the transcript level by RT-PCR. The creation of intracytoplasmic structures, due to the translation of the *mms6*, *mmsF* and *mms6+mmsF* genes respectively into *Mms6*, *MmsF* and *Mms6+MmsF* proteins, was assessed by *Transmission Electron Microscopy* (TEM). The magnetic properties of the created structures were evaluated by *Superconducting Quantum Interference Device* (SQUID). The response of the created intracytoplasmic structures to an AMF was studied by *Hyperthermia* measurements.

3.2. Aims

The hypothesis of the presented study was that it is possible to express MTB genes *mms6* and *mmsF*, alone or in combination, in human osteosarcoma MG63 cells.

The goal of the study was to confirm the former hypothesis and to evaluate the intracytoplasmic particles formed by the MTB genes expression inside the cells, according to different techniques:

1. The *mms6* and *mmsF* gene expression, alone or in combination, inside the MG63 cells, was assessed by ***Reverse Transcription Polymerase Chain Reaction*** **(RT-PCR)**.
2. The morphology of the intracytoplasmic particles created in the MG63 cells by *mms6* and *mmsF* gene expression, alone or in combination, was analysed by ***Transmission Electron Microscopy*** **(TEM).**
3. The magnetisation of MG63 cells expressing *mms6* and *mmsF* genes, alone or in combination**,** was analysed by ***Superconducting Quantum Interference Device*** **(SQUID).**
4. It was determined if the intracytoplasmic particles created inside the MG63 cells by *mms6* and *mmsF* gene expression, alone or in combination, could produce an HT response following application of AMF by **Hyperthermia** experiments.

3.3. *mms6*, *mmsF* and *mms6+mmsF* co-expression in MG63 cells assessment by RT-PCR

MG63 cells were transfected with plasmids pcDNA 3.1 containing the *mms6* gene, with plasmid pcDNA4/TO containing the *mmsF* gene, and co-transfected with both of them and cultured in a FeQ doped medium (34 μM). Ten days after the transfection, RNA was extracted from transfected MG63 cells, and cDNA was synthesised. The expression of these genes in MG63 transfected cells was evaluated by RT-PCR. Wild-type MG63 cells cultured for 10 days in a FeQ doped medium (34 μM) were considered as a control.

mms6, *mmsF* and *mms6+mmsF* co-expression were normalized to the housekeeping gene GAPDH. To test the *mmsF* gene expression in MG63 cells, it was chosen to design two different pairs of primers, named *MmsF*A and *MmFB*, to obtain two different amplicons length of 122 bp for *MmsF*A and 205 bp for *MmsF*B respectively.

The RT-PCR results show the expression of both genes, *mms6* and *mmsF*, in the MG63 cell line, confirming the validity of the transfection (**Figure 22**). *mms6* gene was present in *mms6*-pcDNA 3.1 transfected and in *mms6*-pcDNA3.1+*mmsF*-pcDNA4/TO co-transfected MG63, as indicated by the band of 108 bp present in wells 2 and 3, while it was absent in the control cells (well 1). Both the couples of primers designed to test the *mmsF* gene expression inside the MG63 cells worked. *MmsF* was present in *mmsF*-pcDNA4/TO transfected and in *mms6*-pcDNA3.1+*mmsF*-pcDNA4/TO co-transfected MG63, as indicated respectively by the expected band of 122 bp for the couple of primers *MmsF*A (wells 5 and 6), and by the expected band of 205 bp for the couple of primers *MmsF*B (wells 8 and 9), while it was absent in the wild-type (control) cells (wells 4 and 7). The mixes Mms6, MmsFA, MmsFB and GAPDH, containing all the reagents for RT-PCR except the cDNA, were considered as a negative control for RT-PCR reaction. The light band in the *MmsF*A mix (negative control-well 15), shows a light contamination in the couple of primers *MmsF*A: for this reason the couple of primers *MmsF*A was

discarded and the couple of primers MmsFB was kept for the subsequent experiments and called for simplicity *MmsF*. As a control, the GAPDH expression levels were found to be constant for all the samples (wells 10-13), as shown by the expected band of 210 bp, indicating that the gel lanes have been evenly loaded with sample material. Except the mix *MmsF*A, all the negative controls show no bands, indicating no contamination in the RT- PCR mixes (wells 14, 16, 17).

The co-transfection of MG63 cells with *mms6*-pcDNA 3.1 and *mmsF*-pcDNA4/TO resulted in less expression of each transcript than the single transfections alone, as indicated by the lighter bands (wells 3,6,9).

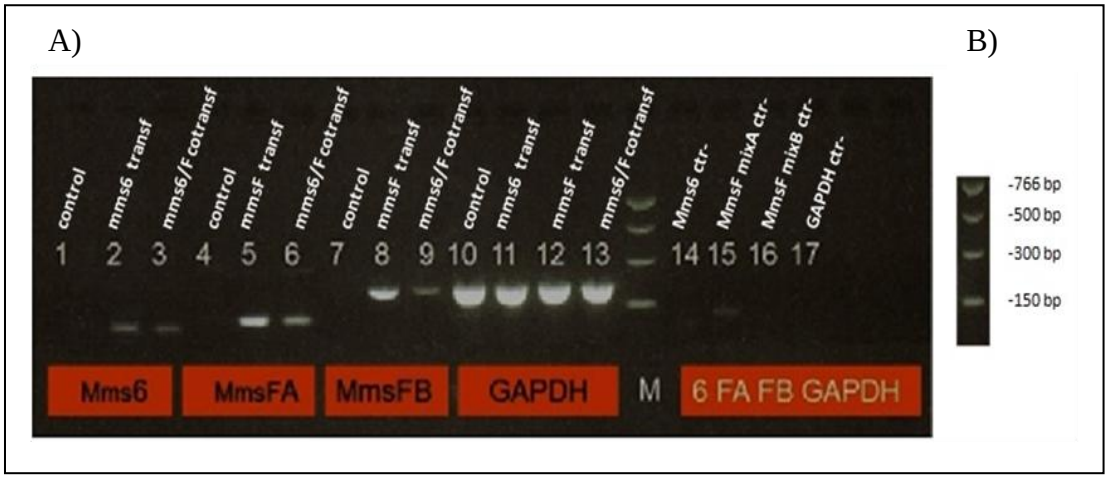

Figure 22 Representative image for RT-PCR reaction for *mms6* and *mmsF* genes expression in MG63 cells.

A) Mix Mms6: 1) Control cells; 2) *mms6*-pcDNA3.1 transfected cells; 3) *mms6*-pcDNA3.1+*mmsF*-pcDNA4/TO co-transfected cells. Mix MmsFA: 4) Control cells; 5) *mmsF*-pcDNA4/TO transfected cells; 6) *mms6*-pcDNA3.1+*mmsF*-pcDNA4/TO co-transfected cells. Mix MmsFB: 7) Control cells; 8) *mmsF*-pcDNA4/TO transfected cells; 9) *mms6*-pcDNA3.1+ *mmsF*-pcDNA4/TO co-transfected cells. Mix GAPDH: 10) Control cells; 11) *mms6*-pcDNA3.1 transfected cells; 12) *mmsF*-pcDNA4/TO transfected cells; 13) *mms6*-pcDNA3.1+*mmsF*-pcDNA4/TO co-transfected cells. M=marker. 14) Mms6 mix negative control; 15) MmsF mixA negative control; 16) MmsF mixB negative control; 17) GAPDH mix negative control. B) 766 bp NEB marker used in the gel electrophoresis.

3.4. Analysis of the intracytoplasmic particles formation in *mms6*-pcDNA3.1, *mmsF* pcDNA/4TO and *mms6*-pcDNA3.1+ *mmsF* pcDNA/4TO co-transfected MG63 cells using *Transmission Electron Microscopy* (TEM)

Having confirmed by RT-PCR that MTB genes *mms6*, *mmsF* and *mms6*+*mmsF* are expressed in MG63 transfected cells, the effect of these genes product on the inner morphology of MG63 cells was investigated by TEM. This technique was employed to determine if these genes, alone or in combination, can create in MG63 cells the magnetosomes observed in MTB. *mms6*-pcDNA3.1, *mmsF*-pcDNA/4TO and *mms6*-pcDNA3.1+*mmsF*-pcDNA/4TO co-transfected MG63 cells were cultured in medium doped with FeQ (34 μM) for 10 days after transfection. Wild-type MG63 cells cultured in medium doped with FeQ (34 μM) for 10 days were considered as a control.

From TEM investigation, it could be noticed that the cytoplasm of the wild-type cells incubated only with FeQ solution appears clear, without the presence of inner vesicles or intracytoplasmic particles (**Figure 24 a-c**).

However, two different kinds of structures were identified in the cytoplasm of MG63 cells expressing the gene *mms6*, *mmsF* or both of them:

1) vesicles containing dispersed content, with the tendency to form clusters (**Figure 24 e, i**);

2) vesicles containing electron dense material, present in *mms6*, *mmsF* and *mms6*+*mmsF* expressing MG63 cells (**Figure 24 f, h, n**).

The vesicles size varies from 300 nm to more than 1 μm, and at higher magnification they appear filled with groups of clustered granules, with a diameter smaller than 100 nm. It is not clear if the larger nanoparticles are aggregates of the smaller particles.

Electron-dense structures were found in most, but not all mms6/F expressing cells, which agrees with the fact that not all cells will be transfected (Figure 23).

No differences were noticed between vesicles formed by the gene *mms6*, *mmsF* or both of them: the size of the granules embedded in the membrane is comparable for both the genes. The electron dense structures observed in the transfected cells, did not show visible difference among the different transfections: the vesicles content seems to be neatly separated and completely different from the ordered cubooctahedral magnetosome crystals seen in MTB (**Figure 24 f**).

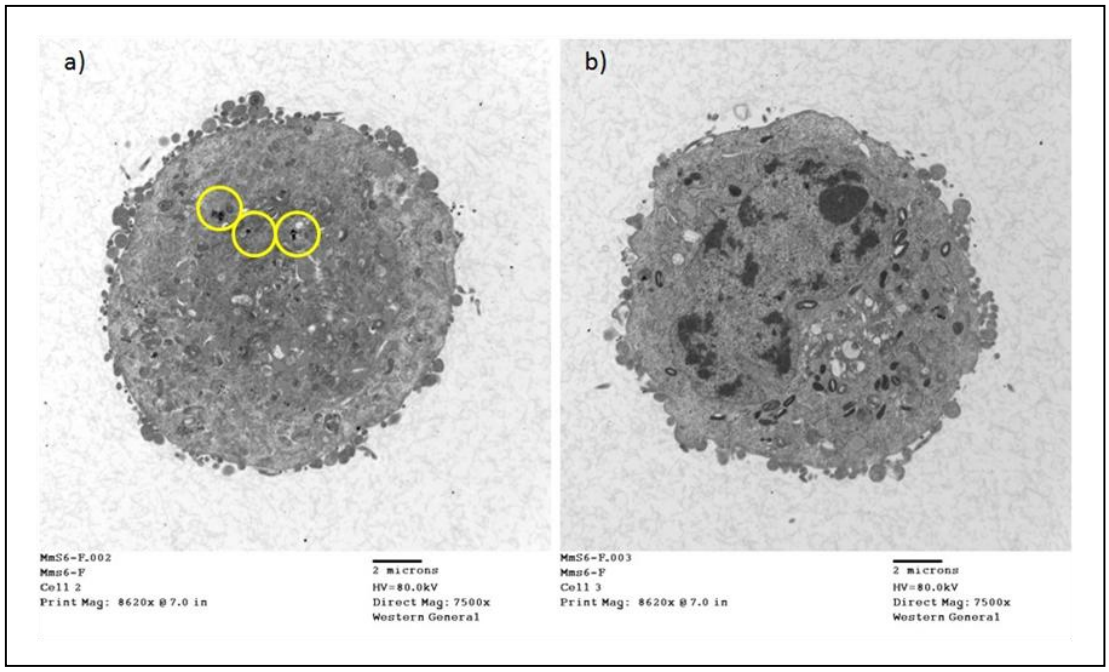

Figure 23. TEM investigation of Mms6/F transfected MG63 cells.

Not all MG63 cells co-transfected with *mms6*-pcDNA3.1+*mmsF*-pcDNA/4TO showed electron-dense structures. In some cases, only a few structures were found in cells, pointed by yellow circles (a), and in other cases almost none (b). Scale bar is 2 µm.

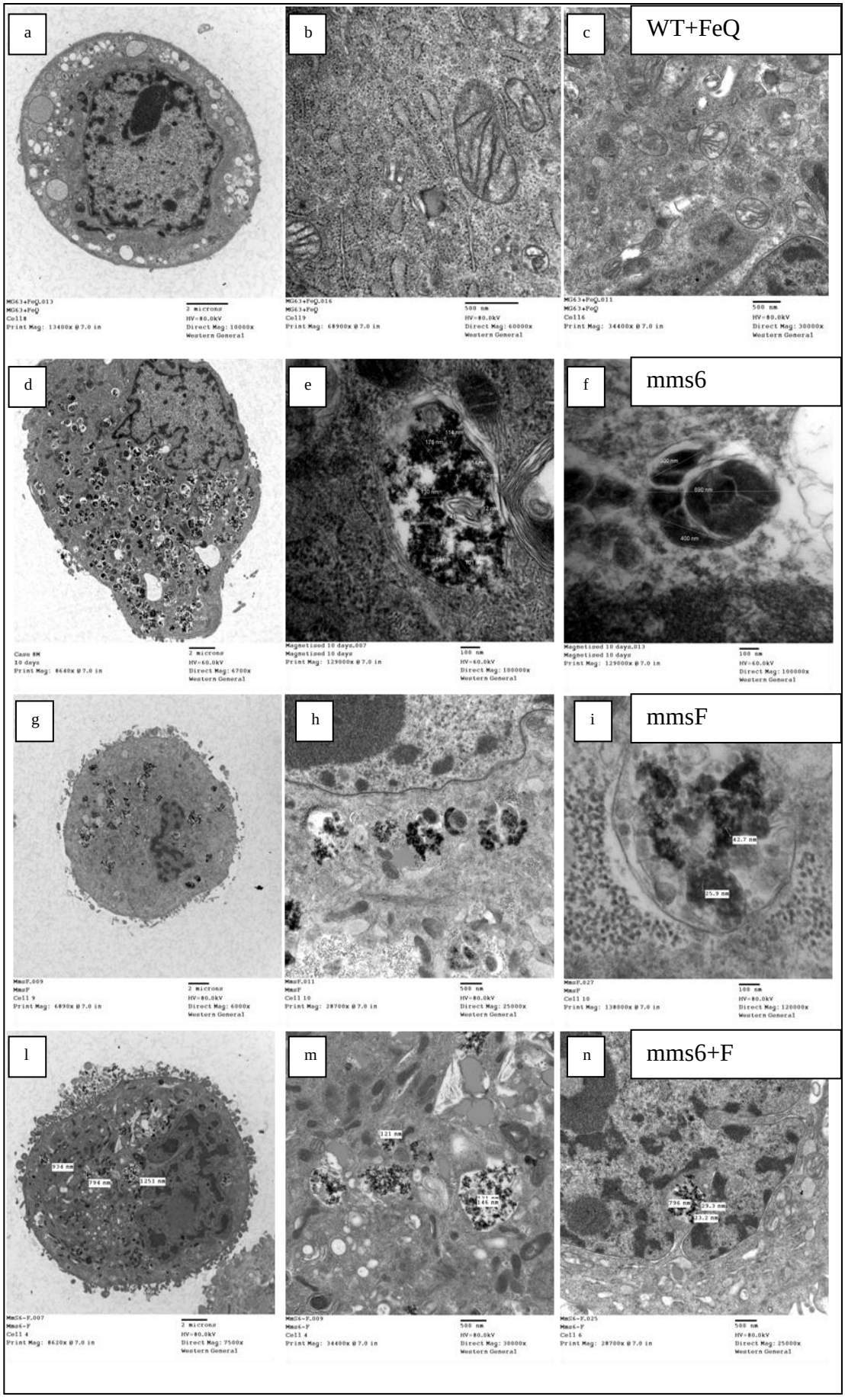
a
b
c
WT+FeQ
d
e
f
mms6
g
h
i
mmsF
l
m
n
mms6+F

Figure 24. TEM investigation of MG63 cells.

a-c) MG63 cells incubated with FeQ (34 µM FeQ) for 10 days, single cell and cytoplasm. The black area of the nucleus contains densely packed DNAd-f) *mms6*-pcDNA3.1 transfected MG63, single cells and cytoplasm. g-i) *mmsF*-pcDNA/4TO transfected MG63, single cells and cytoplasm. l-n) *mms6*-pcDNA3.1+ *mmsF*-pcDNA/4TO co-transfected MG63, single cells and cytoplasm. Scale bars are: 2 µm for figures a, d, g, l; 500 nm for figures b, c, h, m, n and 100 nm for figures e, f, i.

3.5. SQUID measurements on *mms6*-pcDNA3.1, *mms*F-pcDNA/4TO and *mms6*-pcDNA3.1 + *mmsF* pcDNA/4TO co-transfected MG63 cells.

The magnetisation of *mms6*-pcDNA3.1, *mmsF*-pcDNA/4TO and *mms6*-pcDNA3.1+ *mmsF* pcDNA/4TO co-transfected MG63 cells was analysed by *Superconducting Quantum Interference Device* magnetometer (SQUID). In these experiments it was measured the magnetisation of $10x10^6$ MG63 cells for each sample, 10 days after the transfection, incubated with FeQ (3.4 µl FeQ/ml). Wild-type MG63 cells incubated with FeQ (3.4 µl FeQ/ml) for 10 days were considered as a control. The $FeCl_3$ powder used in the FeQ solution was firstly investigated alone under the same conditions used later for the other samples, resulting non-magnetic (**Figure 25**).It was measured the $FeCl_3$ powder and not the FeQ solution as the SQUID used in this experiment could measure only dry samples.

The samples magnetisation was first investigated in a temperature-dependent experiment (**Figure 26**, **panel a**). The resulting plot shows a lower branch and an upper branch, both of them equal approximately at 20 K. Firstly, the samples were cooled down to the lowest temperature (5K), so that the nanoparticles were randomly oriented. Then, at 5K, a very low field was applied (100 Oersted, or in other measurement 100 millitesla) and the recording started. The samples were then heated very slowly up to 320 K, (lower branch of the curve). The temperature raising makes the nanoparticles more mobile, so they tend to orient themselves in the field, increasing the magnetisation of the sample. However, above a certain temperature (here 20 K), the Brownian motion brings so much disorder that the nanoparticles start to move randomly and they disorient again, causing the magnetisation decreasing. In the upper branch of the curve, samples were cooled down again. In the beginning, the magnetisation matched very well with that of the heating curve, but a little above 20 K the magnetisation increased, where the heating curve dropped. *MmsF*-pcDNA/4TO transfected MG63 cells showed the higher magnetisation ($10.5*10^{-5}$ emu) while *mms6*-pcDNA3.1 transfected MG63 cells showed only a magnetisation of $7*10^{-5}$ emu and *mms6*-pcDNA3.1+ *MmsF*-pcDNA/4TO co-

transfected MG63 showed a very poor magnetisation ($2.2*10^{-5}$ emu), very similar to that registered for the negative controls ($2.6*10^{-5}$emu).

The magnetisation of the samples was then measured in a magnetic field dependent experiment at the fixed temperature of 310 K, corresponding to 36.85 °C, the human body temperature (**Figure 26, panel b**). Due to the cost of the experiment, in terms of money and time, it was chosen to investigate, for this second part of the experiment, only the *mms6*-pcDNA3.1 transfected MG63 cells and the *mmsF*-pcDNA/4TO transfected MG63, which showed the higher magnetisation, considering the MG63 cells incubated with FeQ solution for 10 days as a control. The magnetic field was varied up to 7T, maintaining constant the temperature at 310K. The obtained magnetisation curve, although "square-shaped", describes a superparamagnetic behaviour. No hysteresis was detected, therefore it can be excluded that the samples are ferrimagnetic.

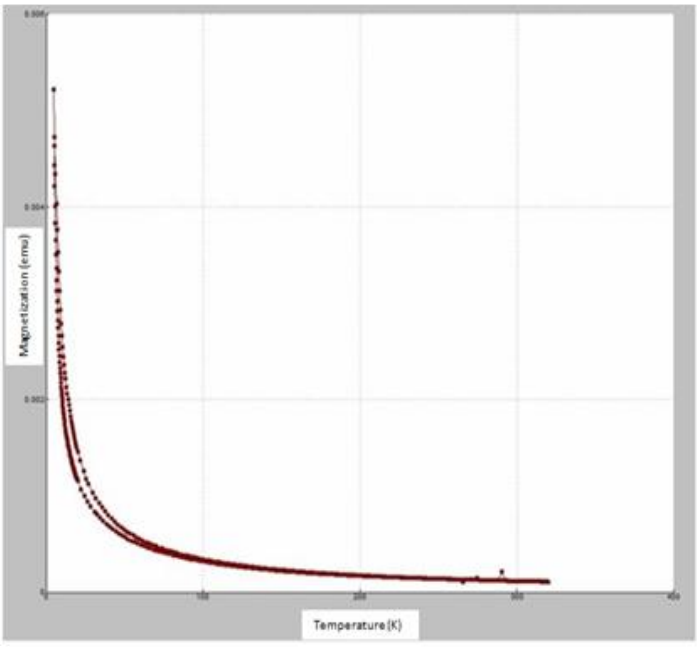

Figure 25. SQUID measurement of $FeCl_3$ powder.

Powder was bought from Sigma Aldrich (product number 157740) and shows a paramagnetic behaviour. No ferrimagnetism has been recorded.

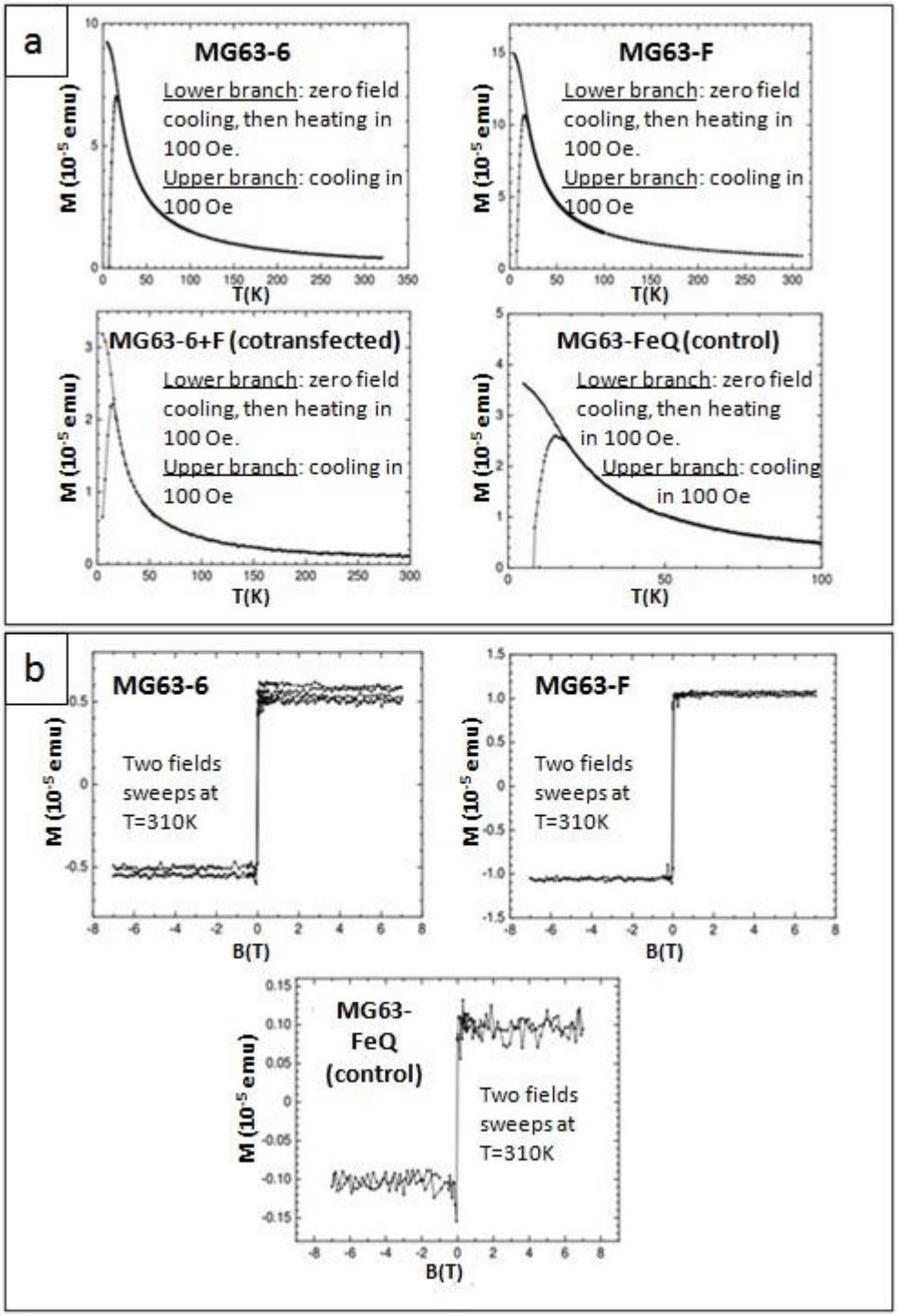
a
MG63-6
Lower branch: zero field cooling, then heating in 100 Oe.
Upper branch: cooling in 100 Oe
M (10-5 emu)
T(K)
MG63-F
Lower branch: zero field cooling, then heating in 100 Oe.
Upper branch: cooling in 100 Oe
M (10-5 emu)
T(K)
MG63-6+F (cotransfected)
Lower branch: zero field cooling, then heating in 100 Oe.
Upper branch: cooling in 100 Oe
M (10-5 emu)
T(K)
MG63-FeQ (control)
Lower branch: zero field cooling, then heating in 100 Oe.
Upper branch: cooling in 100 Oe
M (10-5 emu)
T(K)
b
MG63-6
Two fields sweeps at T=310K
M (10-5 emu)
B(T)
MG63-F
Two fields sweeps at T=310K
M (10-5 emu)
B(T)
MG63-FeQ (control)
Two fields sweeps at T=310K
M (10-5 emu)
B(T)

Figure 26. SQUID measurement of MG63 cells.

Panel a: representative picture of SQUID measurements on *mms6*-pcDNA3.1, *mmsF*-pcDNA/4TO and *mms6*-pcDNA3.1+ *mmsF* pcDNA/4TO co-transfected MG63 cells, incubated with FeQ (3.4 µl FeQ/ml) for 10 days. Lower branch: zero field cooling, then the samples were heated in 100 Oe. Upper branch: samples were then cooled again in 100 Oe. MG63 cells cultured in a medium doped with FeQ (3.4 µl FeQ/ml) for 10 days were used as a control.

Panel b: Representative picture of field-dependent curves at fixed temperature (310 K, equal to 36.85 ºC) on *mms6*-pcDNA3.1 and *mms*F-pcDNA/4TO transfected MG63 cells, incubated with FeQ (3.4 µl FeQ/ml) for 10 days. No hysteresis loop around (0,0) point was noticed, so the samples show superparamagnetism. MG63 cells cultured in a medium doped with FeQ (3.4 µl FeQ/ml) for 10 days were used as a control.

3.6. Hyperthermia measurements on *mms6*-pcDNA3.1, *mmsF*-pcDNA/4TO and *mms6*-pcDNA3.1+ *mmsF* pcDNA/4TO co-transfected MG63 cells.

It was investigated if the transfection of MG63 cells with *mms6*-pcDNA3.1 and *mmsF*-pcDNA/4TO plasmids, alone or in combination, results in intracytoplasmic structures that produce HT response following application of AMF. For this reason, the transfected MG63 cells, 10 days after transfection and cultured in the presence of FeQ (3.4 µl FeQ/ml), were subjected to HT experiments. Wild-type (Plain) MG63 and wild-type (Plain) MG63 cultured in the presence of FeQ (3.4 µl FeQ/ml) for 10 days were considered as negative controls. Samples were investigated under a magnetic field of 250 Oe and 429 kHz, using $18*10^6$ MG63 cells for each sample. The temperature values were recorded for 20 minutes from the beginning of the measurements (**Figure 27**).

In the first 300 seconds, samples temperature raised of 0.1 °C for all the transfected cells, which seem to have all the same magnetic behaviour. However, increasing the magnetic exposure time, it was noticed a different behaviour for each gene: after 1000 seconds of exposure to the magnetic field, *mmsF* was the gene which conferred the higher magnetisation to the MG63 cells, showing a temperature rising of 1.1 °C compared with *mms6* (+0.8°C) and *mms6*+*mmsF* genes (+0.7°C). Surprisingly, MG63 transfected with both the plasmids were the less magnetised cells, indicating that the co-transfection of MG63 cells with both the genes, does not lead to a summative effect of the single magnetisations. MG63 Plain and MG63+FeQ, both negative controls, showed no rising in temperature.

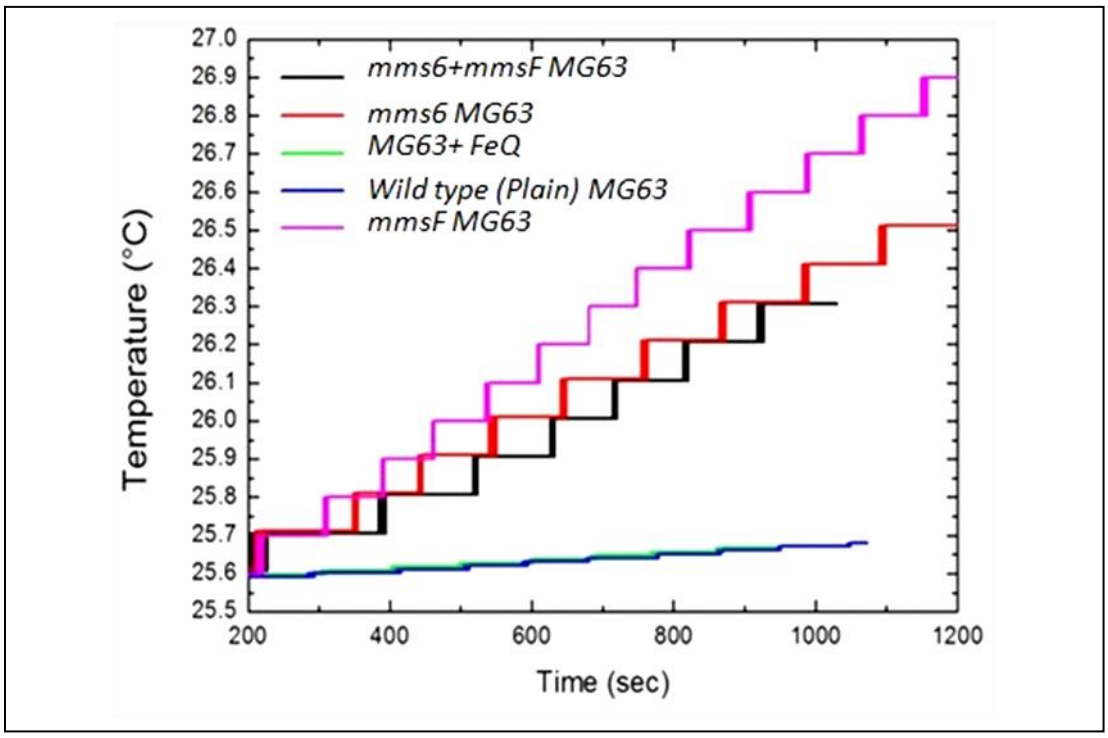

Figure 27. Hyperthermia on MG63 cells.

Effect of AMF on the temperature of mms6-pcDNA3.1, mmsF-pcDNA/4TO and mms6-pcDNA3.1+ mmsF pcDNA/4TO co-transfected MG63 cells.

Cells were cultivated in a FeQ doped medium (3.4 µl FeQ/ml) for 10 days after transfection and then investigated under a magnetic field of 250 Oe and 429 kHz in a time of 1200 seconds. A number of $18*10^6$ cells was considered for each sample. Wild-type (Plain) MG63 and wild-type (Plain) MG63 cultured in the presence of FeQ (3.4 µl FeQ/ml) for 10 days were considered as negative controls.

3.7. Discussion

The RT-PCR results indicate that the MTB genes *mms6* and *mmsF* could be successfully expressed or co-expressed in the MG63 cells and that their translation into proteins leads to the creation of electro-dense structures, which are visible at TEM.

When transfected MG63 cells were observed at TEM, it was noticed the presence of two different types of vesicles, respectively filled with dispersed and electron dense content. The latter ones bear resemblance to magnetosomes, but without their characteristic geometrical shape. The most probable inner-membrane typology these vesicles resemble are endosomes (**appendix 8.10**), possibly transformed by genes *mms6* and *mmsF* in structures able to accept FeQ solution and to convert it in iron-like crystals. TEM images of transfected cells reflect what found elsewhere (Zurkiya et al., 2008). Zurkiya et al. studied the effects of the expression of the MTB gene MagA, involved with iron transport, into the monoclonal cell line 2B5, derived from the human cell line 293FT and which expresses the *magA* gene under the control of the doxycycline-inducible promoter.

The 2B5 cell line was induced and incubated with 200 μM Fe for 4 days, then imaged at TEM. Electron micrographs revealed the presence of vesicles very similar to endosomes, filled with particles and with the typical compartmentalization of the multivesicular bodies of the cellular degradation pathway. The particles were present also outside the vesicles, which were found individually or grouped and not aligned into chains, as seen for magnetosomes. As stated by Zurkiya et al., the lack of organization of the vesicles into a chain-like structure could be due to the lack of the presence of the other MTB genes involved in the chains organization process.

Overall, TEM pictures from Zurkiya show cells with the same characteristics observed also in the MTB gene expressing cells of this study, adding weight to the findings.

There was no difference in the vesicles appearances between the different groups of transfected cells.

The investigation of the magnetism of transfected MG63 cells assessed by SQUID reveals a superparamagnetic behaviour, demonstrating that the expression of the MTB genes *mms6*, *mmsF* in MG63 cells create magnetic electro-dense structures, similar to the MTB observed magnetosomes. The registered SQUID magnetization was of the order of 10^{-5} emu, which is consistent with the measurements performed on natural MTB magnetosmes (Schüler, 2006)

The Hyperthermia experiments conducted to evaluate the response to an AMF field of the intracytoplasmic structures created by *mms6* and *mmsF* gene expression inside MG63 cells, alone or in combination, shown only a mild temperature rising for transfected cells compared to the negative controls. The observed rising of temperature is very far from the one normally observed in magnetic HT (HT is achieved when the temperature is $\geq$42 °C), therefore it is difficult to define this behaviour a real "*hyperthermia response*" of the transfected MG63 cells to an applied AMF. The SQUID and the HT experiments would have benefited from a positive control of synthetic MNPs, i.e. SPIONS. This could have helped in defining the magnetic behaviour of the magnetic electron-dense structures observed in the transfected cells, comparing their response to the magnetic field with the chemical synthesised MNPs.

4. Evaluation of the effect of the transfection on MSCs stemness, proliferation and pluripotency. Expression of MTB genes *mms6* and *mmsF*, alone or in combination, in human MSCs and study of the created intracellular structures by TEM, SQUID, Hyperthermia, AFM/MFM .

4.1. Introduction

The results obtained expressing the genes *mms6*, *mmsF* and co-expressing both of them in the MG63 cells show that it is possible to transfect a human cancer cell line with MTB genes, and that these genes are able to create magnetic structures inside the cells.

However, the final aim of the research was to create magnetic human MSCs, so the subsequent step of the research was to transfect human fetal bone marrow derived MSCs with plasmid pcDNA 3.1 containing *mms6* gene, with the plasmid pcDNA4/TO containing *mmsF* gene, and co-transfect MSCs with both the plasmids.

To determine if the transfection of MSCs with *mms6*-pcDNA3.1 plasmid does lead to any detrimental effect on the cells, a number of experiments were carried out to determine if, after 21 days from transfection, the MSCs could still be considered stem cells and so could be employed in MHT medical experiments.

Flow cytometry experiments and differentiation experiments were respectively carried out to confirm MSCs stemness and their ability to differentiate into the osteogenic, chondrogenic and adipogenic lineage. *Incucyte ZOOM System* was used to assess that MSCs proliferation is unchanged after transfection. Wild-type MSCs cultivated for 21 days in normal medium conditions and MSCs cultivated for 21 days in medium doped with FeQ (3.4 μM) were considered as controls.

The expression of the *mms6*, *mmsF* and *mms6+mmsF* genes in MSCs was determined at transcript level by RT-PCR. The creation of magnetic structures, due to the translation of the genes into proteins, was assessed by TEM. The magnetism of the created structures was evaluated by *Superconducting Quantum Interference Device* (SQUID), *Hyperthermia* and *Atomic Force Microscopy* (AFM)/ *Magnetic Force Microscopy* (MFM) measurements.

4.2. Aims

The aim of this chapter was to demonstrate the hypothesis that the transfection with plasmid *mms6*-pcDNA3.1 could be performed on MSCs without any adverse effect on MSCs stemness, proliferation and ability to differentiate into the osteogenic, chondrogenic ad adipogenic lineage.

The effects of the transfection on MSCs were investigated up to 21 days post-transfection, to determine if the MSCs properties remain unaltered, also after several days from transfection.

Then, it was demonstrated that it is possible to express MTB genes *mms6* and *mmsF*, alone or in combination, in human MSCs.

The transfected MSCs were subjected to different experiments:

1. The MTB *mms6* and *mmsF* gene expression, alone or in combination, inside the MSCs, was confirmed by ***Reverse Transcription Polymerase Chain Reaction*** **(RT-PCR)**.
2. The morphology of the intracytoplasmic particles created in the MSCs by MTB *mms6* and *mmsF* gene expression, alone or in combination, was analysed by ***Transmission Electron Microscopy*** **(TEM)**.
3. The magnetisation of MSCs expressing MTB *mms6* and *mmsF* genes, alone or in combination, was analysed by ***Superconducting Quantum Interference Device*** **(SQUID)**.
4. It was analysed if the intracytoplasmic particles created in the MSCs by MTB *mms6* and *mmsF* gene expression, alone or in combination, could produce an HT response following application of AMF by ***Hyperthermia*** experiments.

4.3. Results

4.3.1. Flow cytometry on MSCs

Flow cytometry was used to evaluate if MSCs are still able to express the typical mesenchymal stem cell surface markers 21 days after the transfection. All the cells analysed were at low passage (passage<10). Cell surface markers for undifferentiated MSCs are: ecto-5-prime-nucleotidase CD73, Thy1-antigen CD90, CD105 or endoglin; while negative markers for MSC are hematopoietic progenitor cell antigen CD34 and CD45 (common leukocyte antigen).

It was counted the percentage of *mms6*-pcDNA3.1 transfected MSCs expressing the surface markers CD34, CD45, CD73, CD90 and CD105, 21 days after the transfection and after being cultivated in medium doped with FeQ solution (34 µM). Wild-type MSCs cultivated for 21 days in normal medium (Plain cells) and Wild-type MSCs cultivated in medium doped with FeQ solution (34 µM) for 21 days were used as controls.

Figure 28,Figure 29 and Figure 30 show a representative picture of flow cytometry experiments and Figure **31** illustrates the percentage of positive cells for the investigated surface markers.

Results show that 21 days after *mms6*-pcDNA3.1 plasmid transfection, MSCs are positive for CD73, CD90, CD105 (>95%) and negative for CD34 (<5%). In particular, there is no difference between the groups of cells in the average of the percentage of positive cells for surface markers CD34, CD73,CD90 and CD105, while the percentage of CD45 positive cells for MSCs transfected with *mms6*-pcDNA3.1 plasmid for 21 days is slightly higher than 5% (7.6%). All the groups are statistically different for marker CD45 (p values <0.0001).

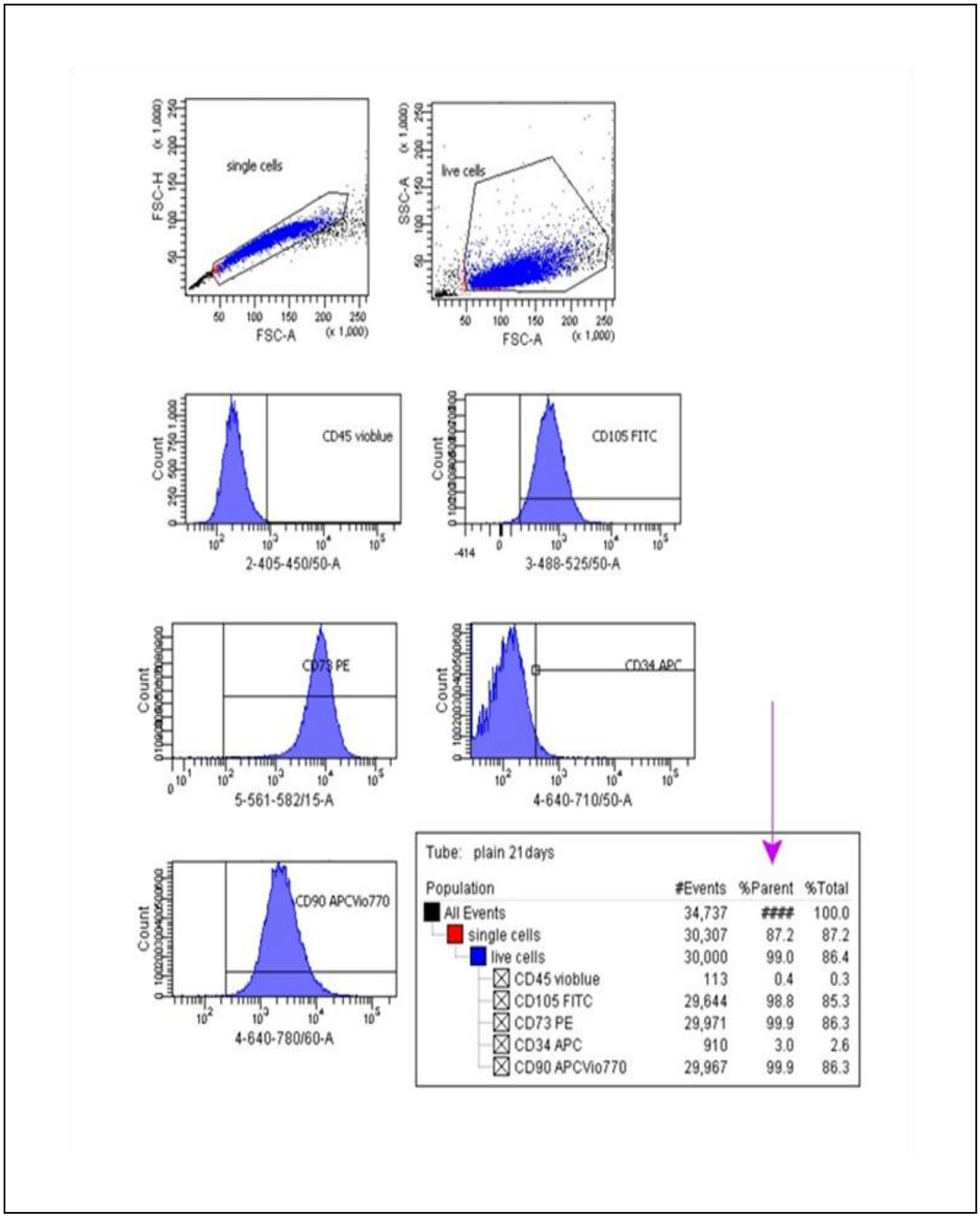

Figure 28. Representative image for flow cytometry experiment for wild-type MSCs cultured for 21 days in standard medium (Plain cells).

Percentage of positive cells for CD34, CD45, CD73, CD90 and CD105 markers are indicated by the purple arrow in the panel.

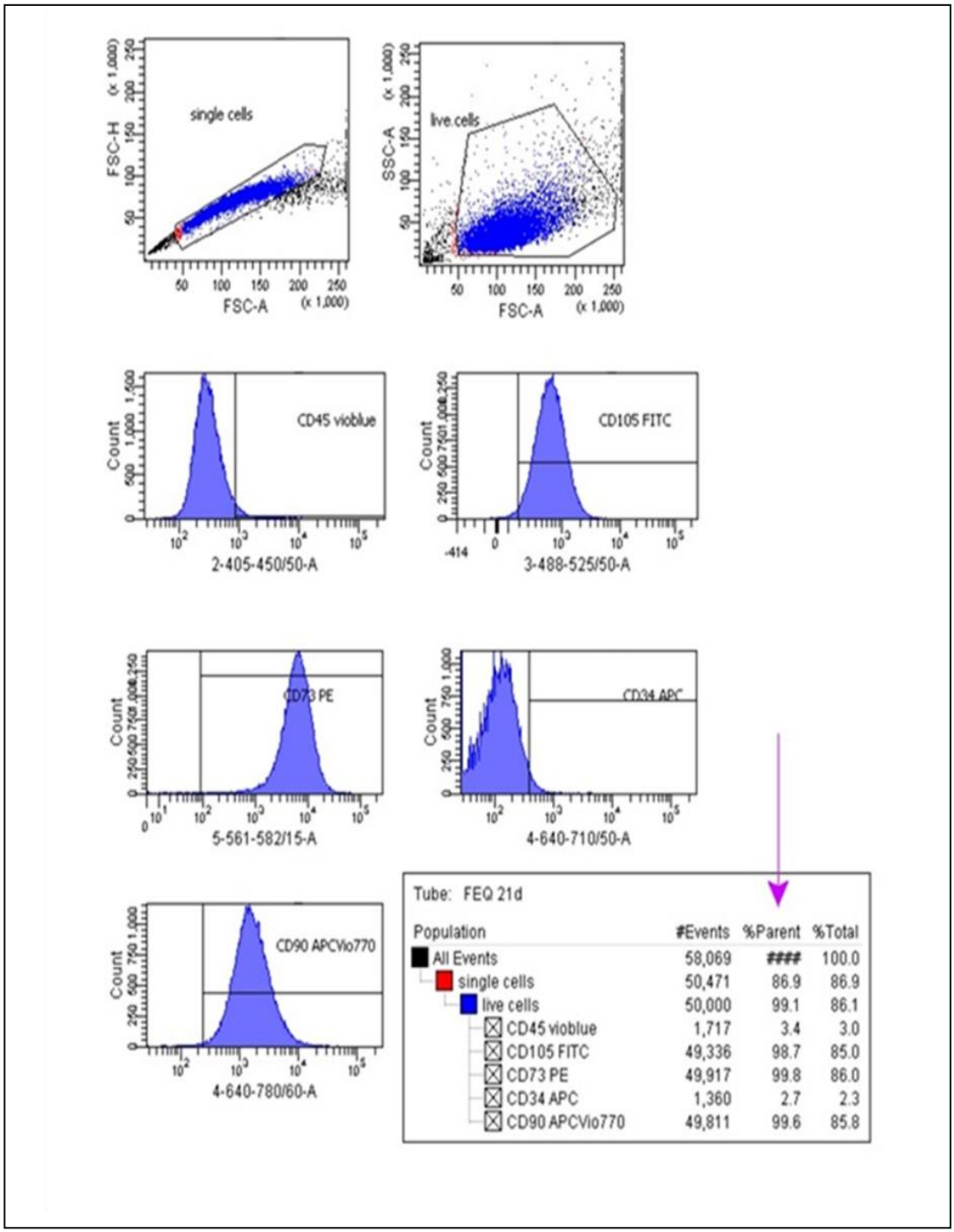

Figure 29. Representative image for flow cytometry experiment for MSCs cultured in medium doped with FeQ (3.4 µl FeQ/ml) for 21 days.

Percentage of positive cells for markers CD34, CD45, CD73, CD90 and CD105 are indicated by the purple arrow in the panel.

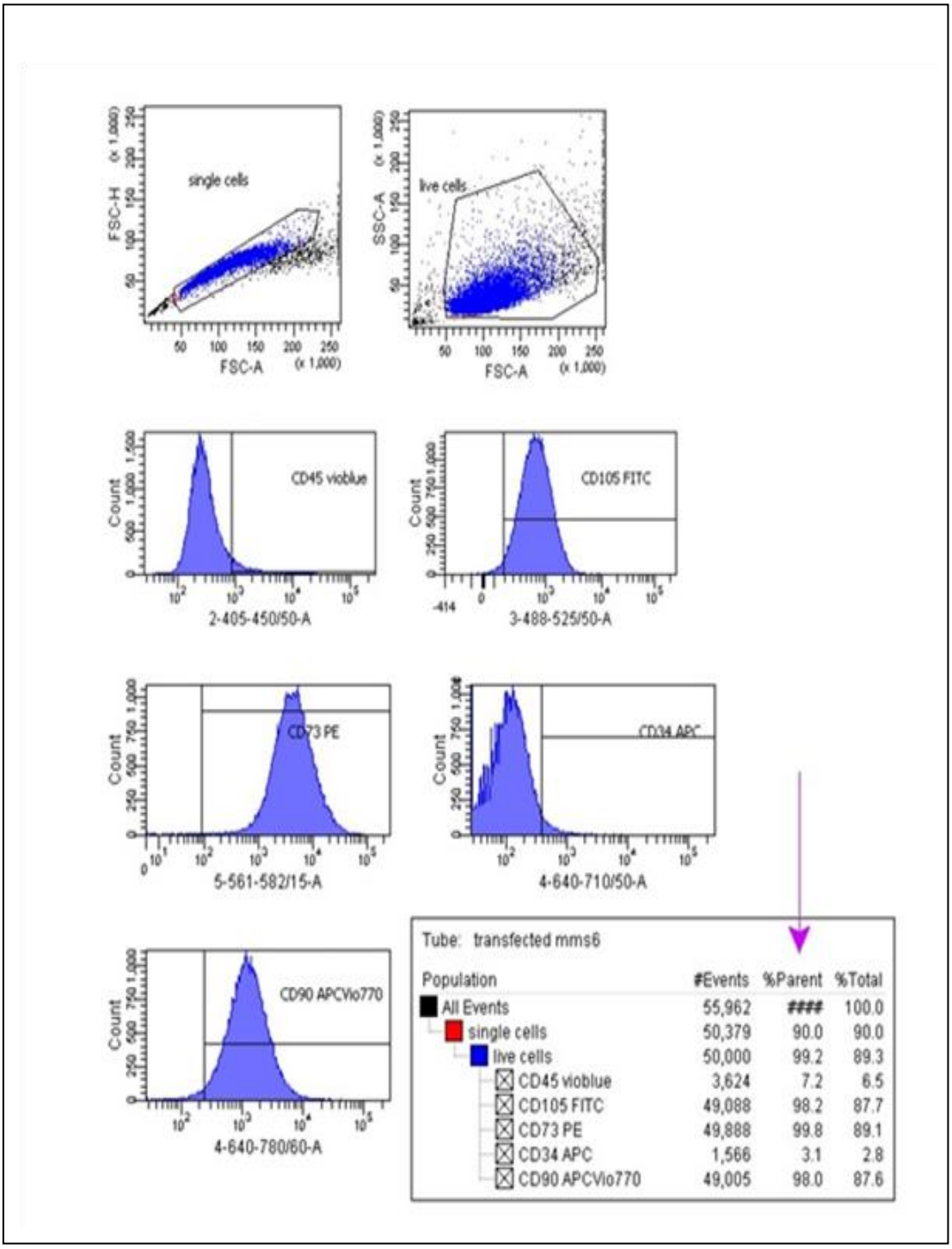

Figure 30. Representative image for flow cytometry experiment for 21 days *mms6*-pcDNA3.1 transfected MSCs.

Percentage of positive cells for markers CD34, CD45, CD73, CD90 and CD105 are indicated by the purple arrow in the panel.

a)

	Wild type MSCs cultured in standard medium for 21 days (Plain)	MSCs cultivated in medium doped with FeQ for 21 days	21 days *mms6*-pcDNA3.1 transfected MSCs
CD34	3.1±0.1	2.9±0.3	3.2±0.2
CD45	0.3±0.1	3.8±0.3	7.6±0.4
CD73	99.9±0.1	99.8±0.1	99.8±0.1
CD90	99.9±0.1	99.6±0.1	98.1±0.1
CD105	98.8±0.1	98.7±0.1	98.3±0.1

b)

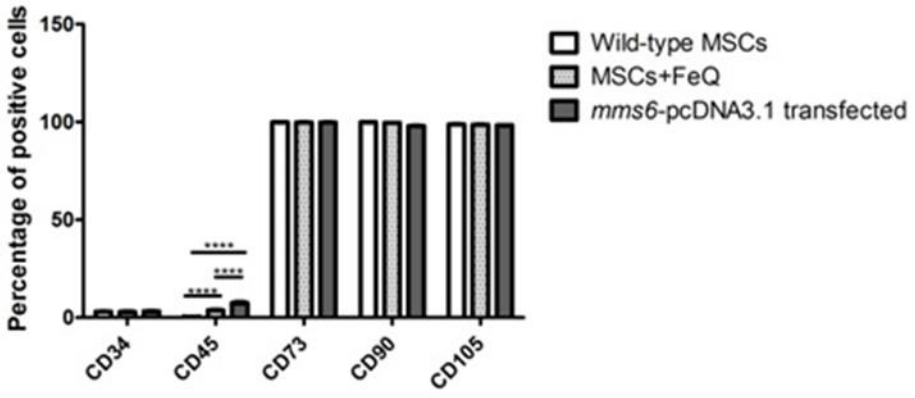

Figure 31. Flow cytometry analysis on MSCs.

a)Table and b) graph of percentages of positive cells for CD34, CD45, CD73, CD90 and CD105 markers in wild-type MSCs cultured for 21 days (Plain), MSCs cultured in medium doped with FeQ solution (3.4 µl FeQ/ml) for 21 days and 21 days *mms6*-pcDNA3.1 transfected MSCs, cultured in medium doped with FeQ solution (3.4 µl FeQ/ml). Values were obtained by flow cytometry analysis. All the cells are negative for CD34 and CD45 (positive cells <5%), while only 21 days *mms6*-pcDNA3.1 transfected MSCs are slightly positive for CD45 (positive cells >5%). All the groups of cells are statistically different for CD45 marker. All the cells are positive for CD73, CD90 and CD105 markers (cell percentage> 95%). Results are shown ± standard deviation. Statistically significant results are indicated by asterisks.

4.3.2. MSCs proliferation analysis

Cells proliferation was another parameter taken into consideration to determine if the transfection of MSCs with *mms6*-pcDNA 3.1 plasmid could affect the health and the function of the transfected cells. Three different groups of cells were considered: wild-type MSCs cultured in standard medium for 21 days (Plain), wild-type MSCs cultivated in medium doped with FeQ solution (34 μM) for 21 days and 21 days *mms6*-pcDNA3.1 MSCs transfected cultivated in medium doped with FeQ solution (34 μM) for 21 days.

The experiment was carried on for a period longer than 6 days. **Figure 33** shows that at day number 5 (corresponding to time point 120 hours) all the cell groups reached >90% confluence and after this time point it was almost impossible to notice any difference in the cells plate coverage by visual inspection only. The *mms6*-pcDNA3.1 transfected MSCs seemed to adhere to the plate surface in a smaller number than the other two groups at investigation time point 0, corresponding to 2 hours after the cells seeding (**Figure 32**, time 0). However, in the pictures taken later, the transfected cells covered the plate surface in the same way than the other two groups (**Figure 32**, day 2).

The quantitative analysis of the cells plate coverage reveals that there is no difference in cell proliferation of the three groups until day 3 and 4, where it was noticed a statistical difference ($p<0.01$) between *mms6*-pcDNA3.1 transfected MSCs and MSCs grown in the medium doped with FeQ for 21 days (**Figure 34a**). However, the fact that no statistical difference was observed between wild-type and *mms6*-pcDNA3.1 transfected MSCs, indicates that the transfection does not affect the proliferation of transfected MSCs significantly. No statistical difference was noticed at day 5 and 6, when the plate coverage is more than 95% for all the groups.

The results indicate that the MSCs proliferation, 21 days after transfection, is not affected immediately after the cells seeding, but instead 3-4 days later, and only if compared to MSCs grown in the medium doped with FeQ for 21 days. Moreover, even if this data is not statistically relevant, it was observed that in some cases the transfected cells require more hours to fully cover the plate, compared to the other

two groups (Transfected MSCs reach >95% of confluence on day 6, one day later than the other two groups). **Figure 34b** shows a representative picture of the cell proliferation curve created directly by the instrument from the collected data.

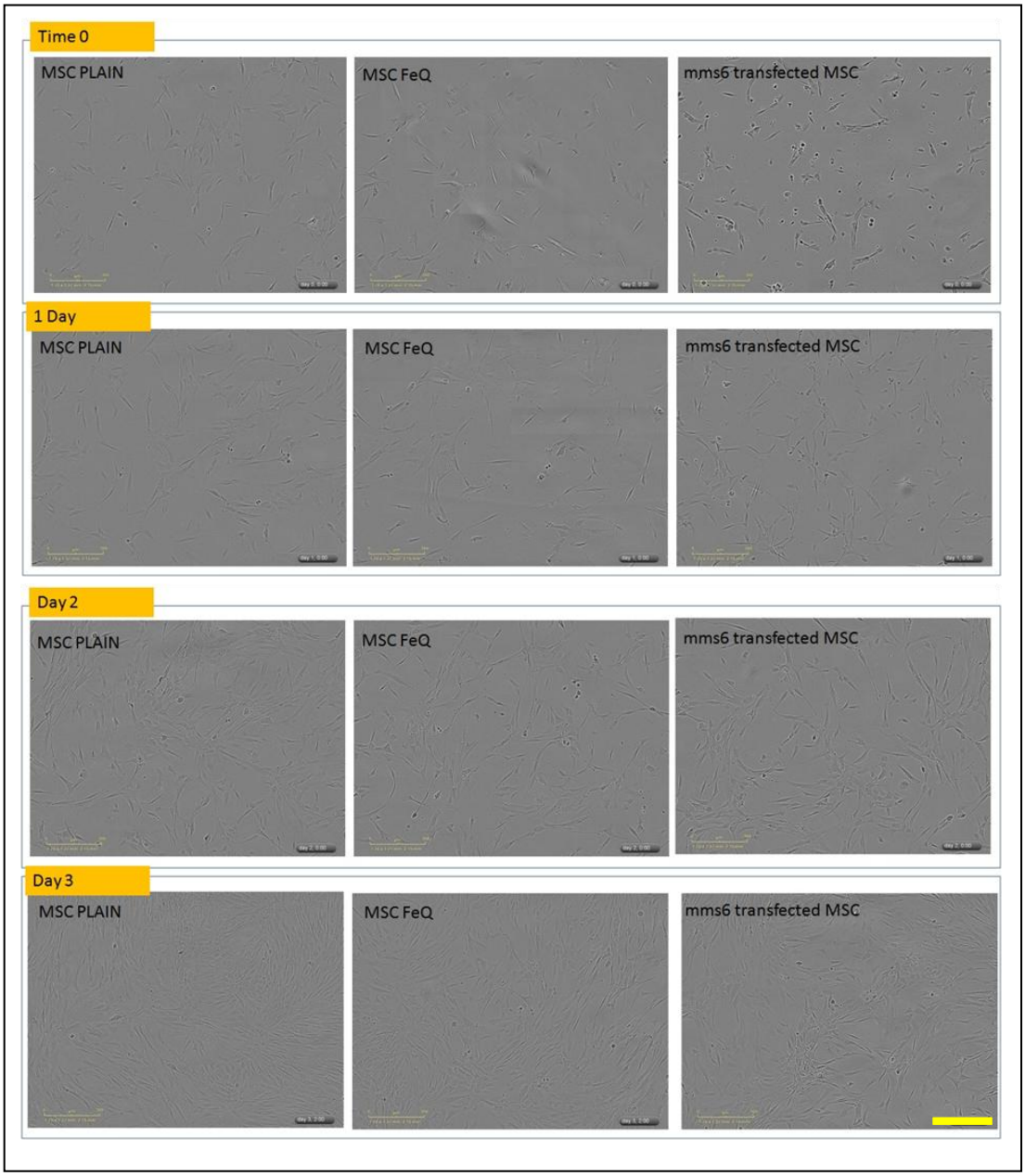

Figure 32. Representative image of qualitative analysis of MSCs proliferation.

The cells investigated were wild-type MSCs cultivated in standard condition for 21 days (Plain), MSCs incubated with FeQ doped medium for 21 days and 21 days *mms6*-pcDNA 3.1 MSCs transfected incubated with FeQ doped medium for 21 days. Cells were imaged at different time points (day 0-3). Pictures were taken using Incucyte ZOOM System device, scale bar=300µm.

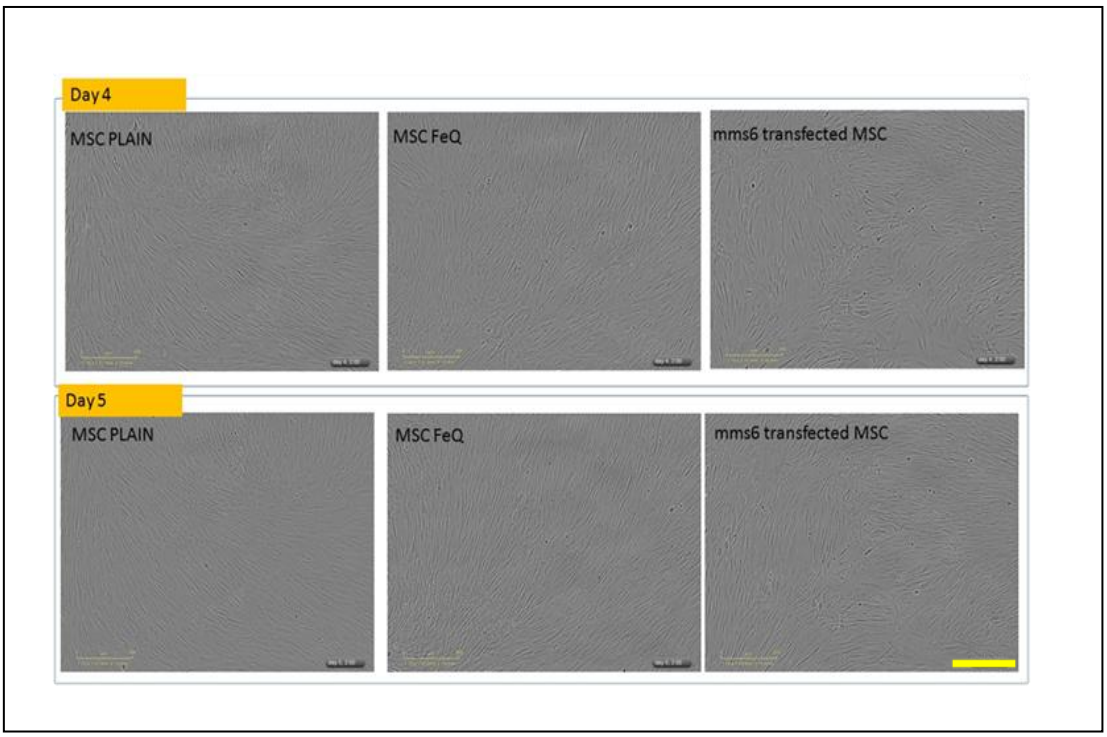

Figure 33. Representative image of qualitative analysis of MSCs proliferation.

The cells investigated were wild-type MSCs cultivated in standard condition for 21 days (Plain), MSCs incubated with FeQ doped medium for 21 days and 21 days *mms6*-pcDNA 3.1 MSCs transfected incubated with FeQ doped medium for 21 days. Cells were imaged at different time points (day 4-5). Pictures were taken using Incucyte ZOOM System device, scale bar=300µm.

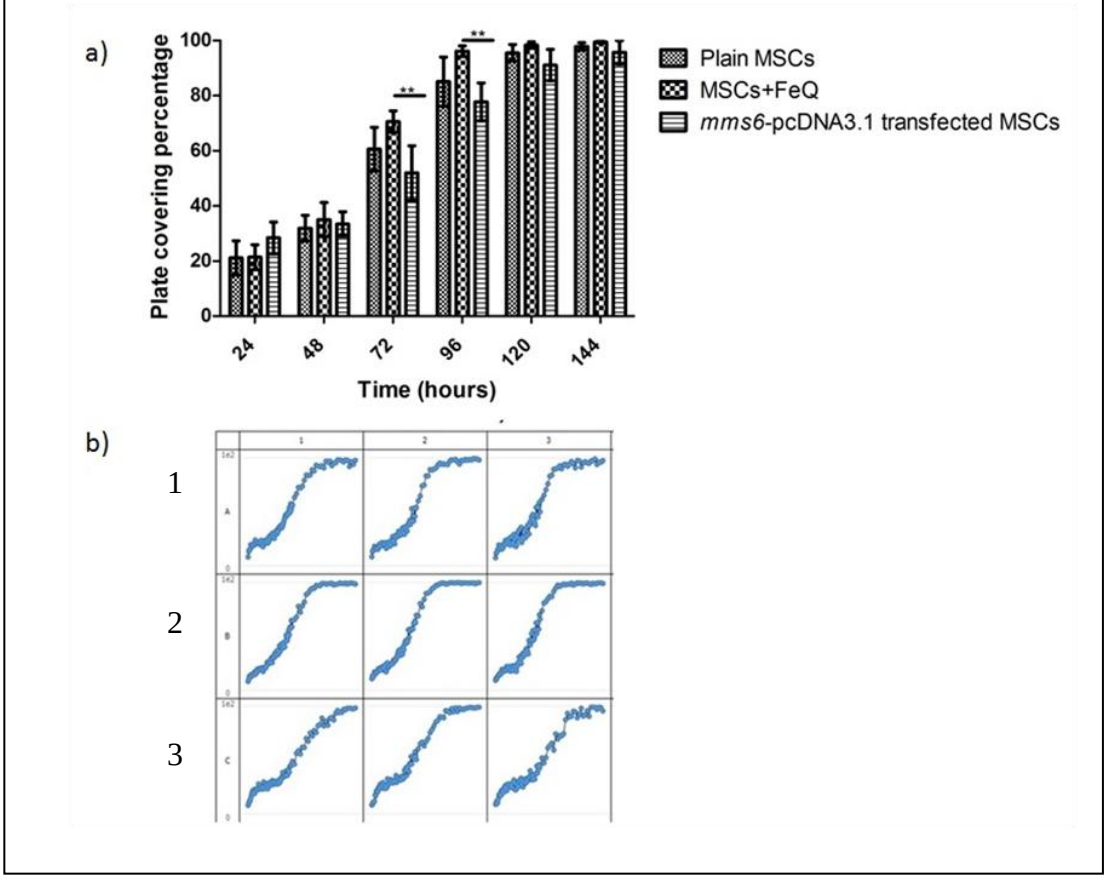

Figure 34. ***Incucyte ZOOM System*** **cell proliferation analysis.**

a) Quantitative evaluation of proliferation rate (expressed as plate coverage percentage average) of wild-type MSCs cultivated in standard condition for 21 days, MSCs incubated with FeQ doped medium (3.4 µl/ml) for 21 days, and 21 days *mms6*-pcDNA3.1 transfected MSCs incubated with FeQ doped medium (3.4 µl/ml). Cell proliferation was monitored for a time longer than 6 days. Results are shown as proliferation rate average with standard deviation bars. Statistically significant results are indicated by asterisks.

b) Representative picture of *Incucyte ZOOM System* cell proliferation curve of wild-type MSCs cultivated in standard condition for 21 days (1), MSCs incubated with FeQ for 21 days (2) and 21 days *mms6*-pcDNA 3.1 transfected MSCs incubated with FeQ for 21 days (3) over an incubation period longer than 6 days.

4.3.3. Differentiation of MSCs

To evaluate if the transfection could cause any adverse effect on MSCs pluripotency, *in vitro* functional differentiation experiments were carried out on wild-type MSCs and *mms6*-pcDNA3.1 transfected MSCs. Both the cells groups were differentiated into the osteogenic, chondrogenic and adipogenic lineage using the appropriate medium for each lineage. The results were then compared, using the wild-type MSCs as a positive control.

4.3.4. Osteogenic Differentiation

Wild-type and *mms6*-pcDNA3.1 transfected MSCs were incubated with osteogenic differentiation medium for 0, 10 and 21 days. After 3 weeks of incubation with the osteogenic differentiation medium, the successful differentiation of MSCs in osteoblasts was confirmed by free calcium deposits stained by the Alizarin Red dye (**Figure 35**). No difference was observed between the wild-type MSCs and the *mms6*-pcDNA3.1 transfected MSCs.

MSCs incubated with osteogenic differentiation medium for 10 and 21 days were also investigated for osteocalcin (OCN) expression by immunofluorescence (**Figure 36**). OCN is a protein secreted merely by osteoblasts and plays a role in bone mineralization and calcium ions homeostasis. For this reason, OCN is employed as a biochemical marker in bone formation. From **Figure 36** it is possible to appreciate that OCN production is already detectable after 10 days of cells incubation with osteogenic medium, as indicated by green fluorescence. Negative controls are shown in **appendix 8.12**.

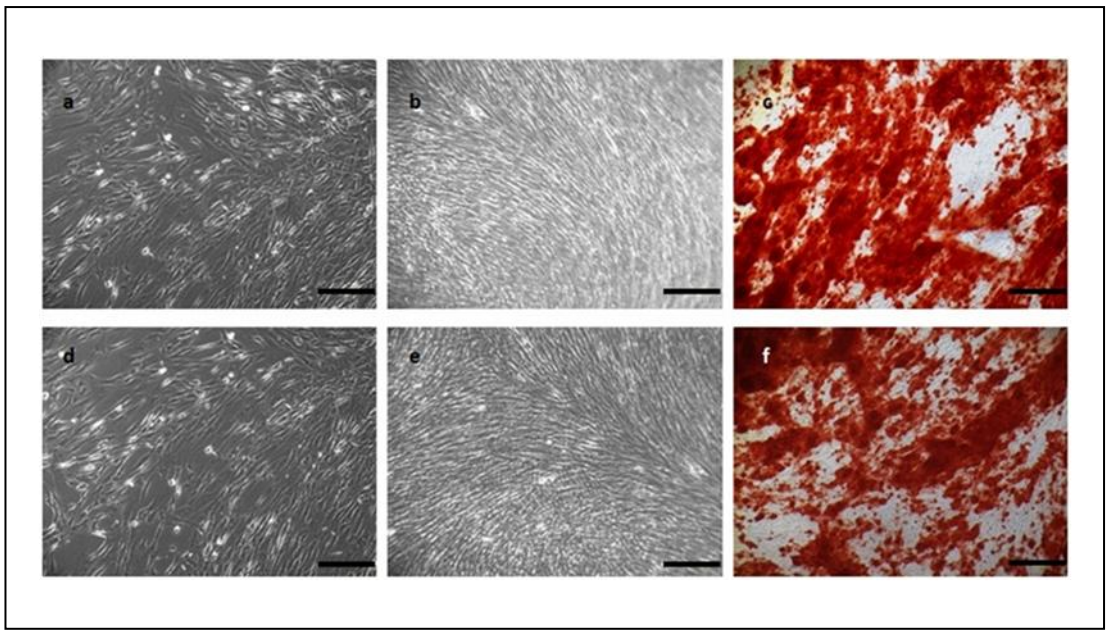

Figure 35. Representative pictures of Alizarin Red staining.

a-c) Wild-type MSCs incubated with osteogenic differentiation medium for 0, 10 and 21 days. d-f) *mms6*-pcDNA3.1 transfected MSCs incubated with osteogenic differentiation medium for 0 days, 10 days and 21 days. Scale bar is 100 µm, 100x magnification.

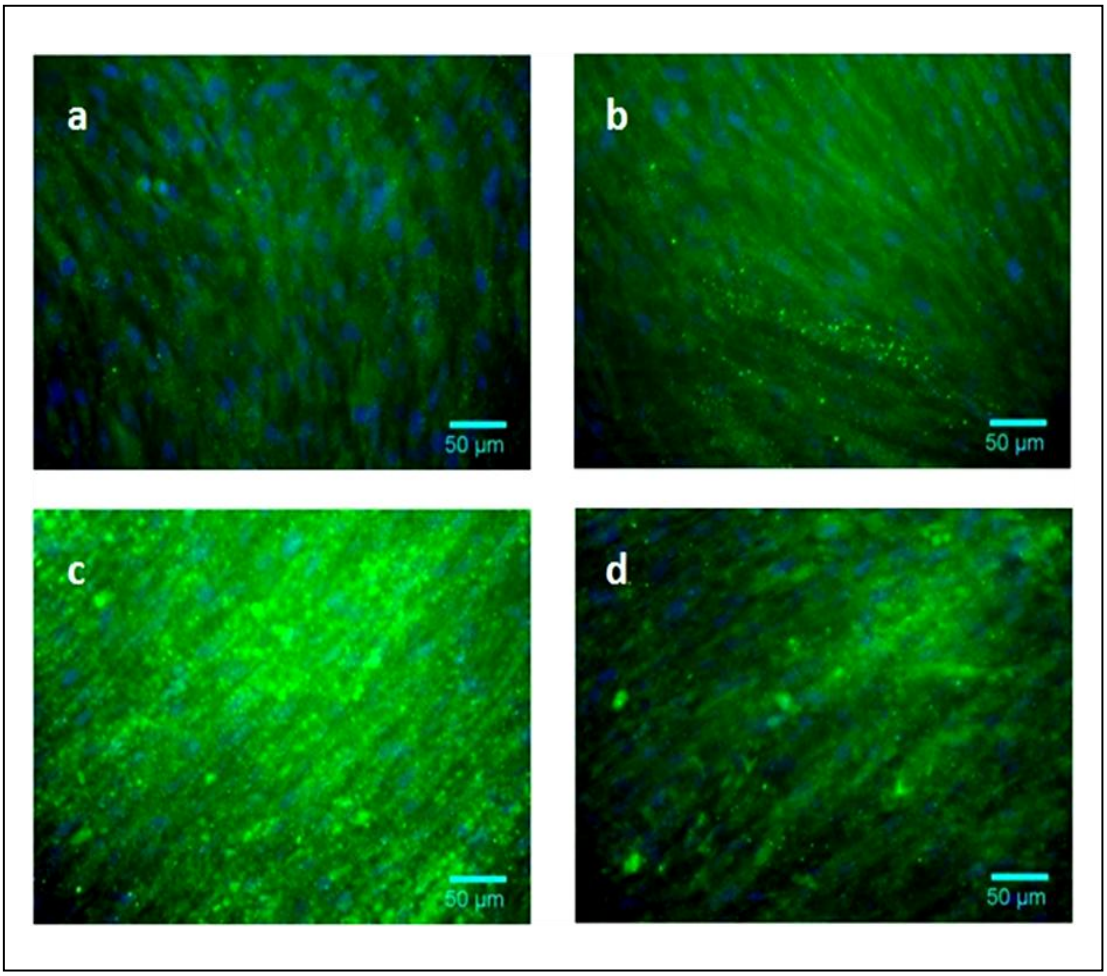

Figure 36. Representative images of indirect immunofluorescence.

OCN antibody staining in wild-type and *mms6*-pcDNA3.1 transfected MSCs followed by Alexa Fluor 488-conjugated goat anti-rabbit lgG (green) secondary antibody. a) wild-type MSCs after 10 days of incubation with the osteogenic medium; b) *mms6*-pcDNA3.1 transfected MSCs after 10 days of incubation with the osteogenic medium; c) wild-type MSCs after 21 days of incubation with the osteogenic medium d) *mms6*-pcDNA3.1 transfected MSCs after 21 days of incubation with the osteogenic medium. DAPI was used to stain the cell nuclei (blue). Images were taken using the confocal microscope. Scale bar is 50 µm.

4.3.5. Chondrogenic Differentiation

Wild-type and *mms6*-pcDNA3.1 transfected MSCs were incubated with chondrogenic differentiation medium for 21 days. At day 21, the cells layers of both the cells groups were observed to shrink and to completely detach from the plate bottom, creating spheroids. Cells were then fixed in formalin 10% and stained with Alcian Blue to reveal any presence of aggrecan (**Figure 37**). Both the cells types showed the presence of aggrecan, indicating the correct differentiation into the chondrogenic lineage. No difference was observed between the wild-type MSCs and the *mms6*-pcDNA3.1 transfected MSCs.

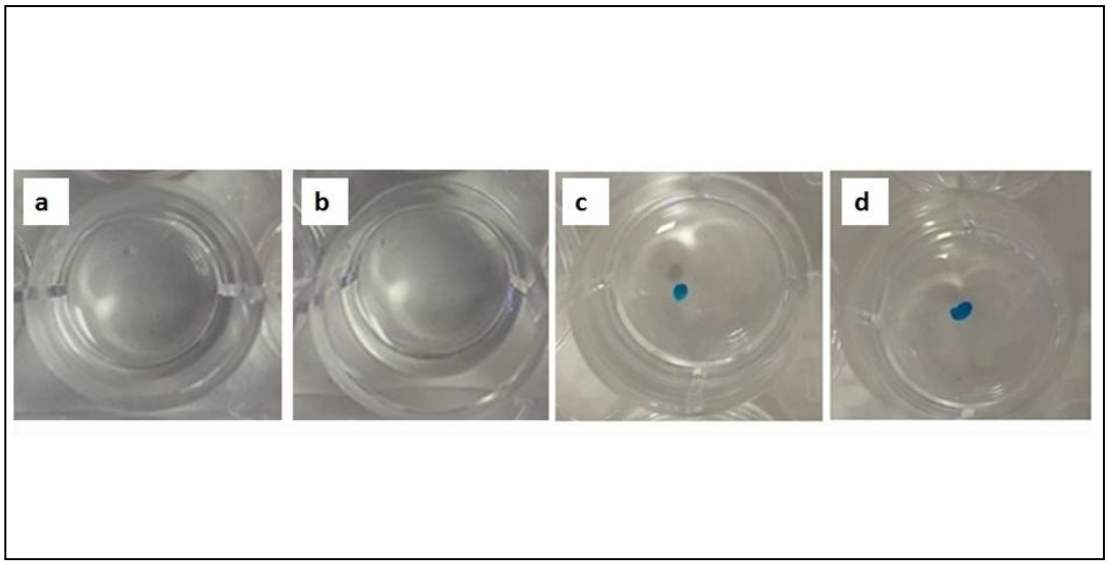

Figure 37. Representative pictures of Alcian Blue staining.

a) Wild-type MSCs and b) *mms6*-pcDNA3.1 transfected MSCs at day zero. c) Wild-type MSCs and d) *mms6*-pcDNA3.1 transfected MSCs incubated with chondrogenesis differentiation medium for 21 days. After the staining, the plates were immediately pictured using a digital camera.

4.3.6. Adipogenic Differentiation

Wild-type and *mms6*-pcDNA3.1 transfected MSCs were incubated with adipogenic differentiation medium for 0, 10 and 21 days. At each time point, cells were fixed in 4% paraformaldehyde and stained by Oil Red O. Pictures of cells were taken in light microscopy and photographed at 200x magnification in bright field, using a coloured camera (**Figure 38**). Wild-type MSCs grown in standard medium served as negative controls: no changes in morphology were noticed, and cells were negative for Oil Red O staining. In both the cell types induced for adipogenesis, at day 10, it was possible to appreciate the formation of lipid droplets, which became more evident at day 21, stained in bright red by Oil Red O. The lipid droplets size of wild-type MSCs appeared bigger than the *mms6*-pcDNA3.1 transfected, which showed an higher amount of tiny intracellular lipid vesicles. Overall these results confirm that wild-type MSCs and *mms6*-pcDNA3.1 transfected MSCs could both differentiate into adipocytes.

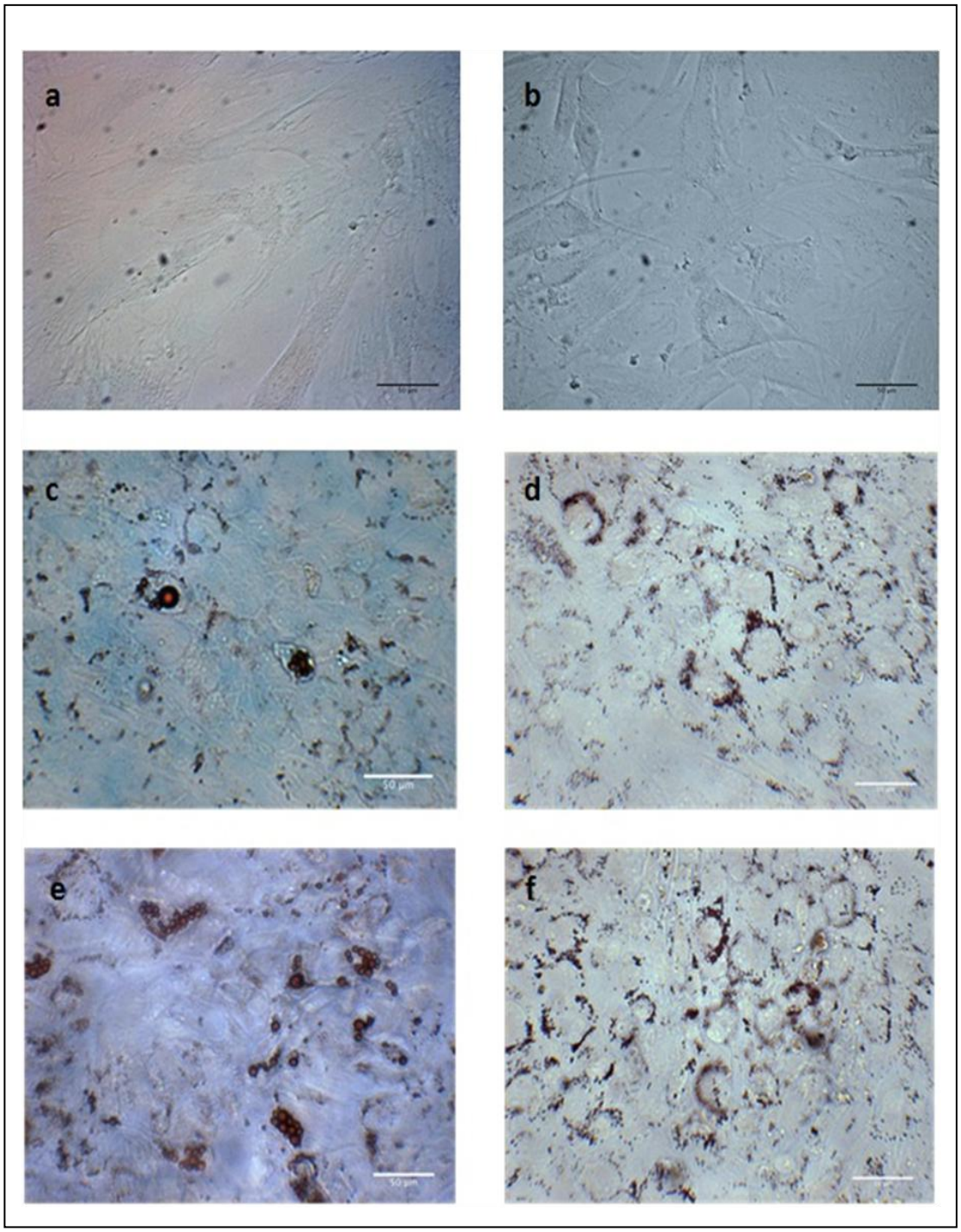

Figure 38. Representative pictures of Oil Red O staining.

a) Wild-type MSCs not induced in the adipogenesis differentiation medium (day 0); b) *mms6*-pcDNA3.1 transfected MSCs not induced in the adipogenesis differentiation medium (day 0); c) wild-type MSCs incubated with the adipogenesis differentiation medium for 10 days; d) *mms6*-pcDNA3.1 transfected MSCs incubated with the adipogenesis differentiation medium for 10 days. e) wild-type MSCs incubated with the adipogenesis differentiation medium for 21 days, f) *mms6*-pcDNA3.1 transfected MSCs incubated with the adipogenesis differentiation medium for 21 days. After staining, the plates were immediately imaged at 200x in bright field, using a coloured camera. Scale bar is 50 µm.

4.4. *mms6*, *mmsF* and *mms6+mmsF* co-expression in MSCs assessment by RT-PCR

It was determined whether *mms6*, *mmsF* and *mms6+mmsF* genes could be expressed in MSCs. MSCs were transfected with plasmids *mms6*-pcDNA 3.1, *mmsF* -pcDNA 4/TO, and co-transfected with both of them. Then, the transfected MSCs were incubated for ten days in a FeQ doped medium (34 µM). Wild-type MSCs and wild-type MSCs cultured for 10 days in a FeQ doped medium (34 µM) were considered as control.

Ten days after the transfection, RNA was extracted from MSCs and cDNA was synthesised. The transfection and expression of these genes were evaluated by RT-PCR experiments, which confirmed the *mms6*, *mmsF* and *mms6+mmsF* genes expression in transfected MSCs (**Figure 39**). *mms6*-pcDNA 3.1 and *mms6*-pcDNA3.1+ *mmsF*-pcDNA4/TO co-transfected MSCs express the *mms6* gene, as indicated by the band of 108 bp (wells 3 and 5), while the wild-type MSCs, the wild-type MSCs cultured in medium doped with the FeQ solution and the MSCs transfected only with *mmsF*-pcDNA4/TO do not express it (wells 1, 2, 4).

The gene *mmsF* was present in *mmsF*-pcDNA4/TO transfected and in *mms6*-pcDNA3.1+ *mmsF*-pcDNA4/TO co-transfected MSCs (wells 9 and 10), as indicated by the expected band of 205 bp for the pairs of primers *MmsF*B, called for simplicity MmsF, while the wild-type MSCs, the wild-type MSCs cultured in medium doped with the FeQ solution and the MSCs transfected only with *mms6*-pcDNA3.1 do not express it (wells 6-8). The bands present at the bottom of the gel are due to primer dimer amplification and do not compromise the quality of the experiment.

The *mms6*, *mmsF* and *mms6+mmsF* co-expression was normalized to the housekeeping gene GAPDH. The GAPDH expression levels were found to be constant for all the samples (wells 13-17), as shown by the expected band of 94 bp, indicating that the gel lanes have been evenly loaded with sample material.

Mixes *Mms6*, *MmsF and GAPDH* (wells 11,12,18) containing all the reagents for RT-PCR except the cDNA, were considered as negative controls for the RT-PCR reaction and showed no bands, indicating no contamination in the RT- PCR mixes.

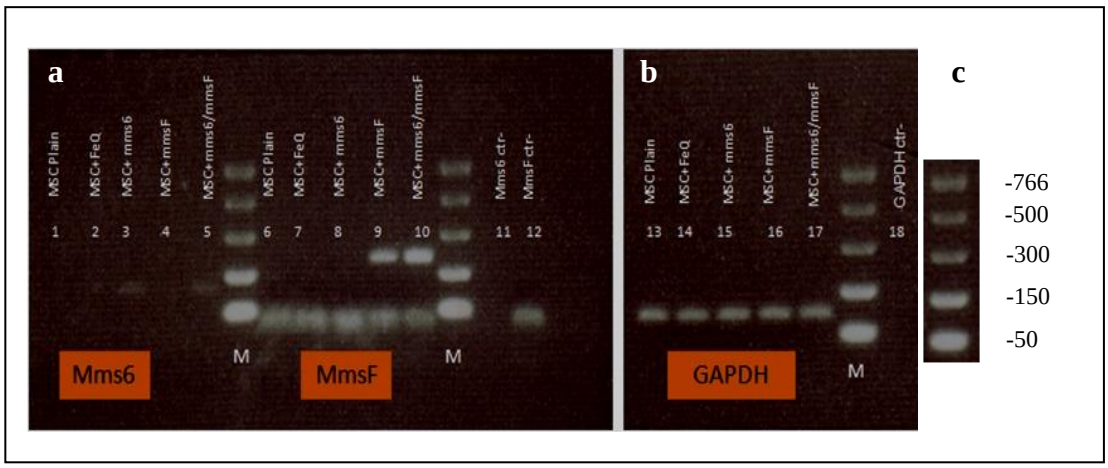

Figure 39. RT-PCR on MSCs.

a) Representative image for expression of *mms6*, *mmsF* and *mms6+mmsF* genes in MSCs. *mms6* gene expression was investigated for: 1) Wild-type (Plain) MSCs, 2) MSCs incubated with FeQ (34 µM) for 10 days, 3) *mms6*-pcDNA3.1 10 days transfected MSCs, 4) *mmsF*-pcDNA/4TO 10 days transfected MSCs, 5) *mms6*-pcDNA3.1+ *mmsF*-pcDNA/4TO 10 days transfected MSCs. *mmsF* gene expression was investigated for: 6) Wild-type (Plain) MSCs, 7) MSCs incubated with FeQ (34 µM) for 10 days, 8) *mms6*-pcDNA3.1 10 days transfected MSCs, 9) *mmsF*-pcDNA/4TO 10 days transfected MSCs, 10) *mms6*-pcDNA3.1+*mmsF*-pcDNA/4TO 10 days transfected MSCs. 11) Mms6 mix (negative control), 12) MmsF mix (negative control).

b) GAPDH gene expression was investigated for: 13) Wild-type (Plain) MSCs, 14) MSCs incubated with FeQ (34 µM) for 10 days, 15) *mms6*-pcDNA3.1 10 days transfected MSCs, 16) *mmsF*-pcDNA/4TO 10 days transfected MSCs, 17) *mms6*-pcDNA3.1+*mmsF*-pcDNA/4TO 10 days transfected MSCs. 18) GAPDH mix (negative control). M= marker.

c) 766 bp NEB marker used in the gel electrophoresis.

4.5. Analysis of the intracytoplasmic structures formed in *mms6*-pcDNA3.1, *mmsF*-pcDNA/4TO and *mms6*-pcDNA3.1+ *mmsF*-pcDNA/4TO co-transfected MSCs using Transmission Electron Microscopy (TEM)

After having established that genes *mms6*, *mmsF* and *mms6*+*mmsF* were expressed respectively in *mms6*-pcDNA3.1, *mmsF*-pcDNA/4TO and *mms6*-pcDNA3.1+ *mmsF*-pcDNA/4TO co-transfected MSCs, it was determined how the effect of these genes expression influenced the internal morphology of the MSCs using TEM. This technique was used to investigate if these genes are able, alone or in combination, to create in human MSCs the same vesicles observed for *mms6*, *mmsF* and *mms6*+*mmsF* expressing MG63 cells.

mms6-pcDNA 3.1, *mmsF*-pcDNA 4/TO and *mms6*-pcDNA 3.1+ *mmsF*-pcDNA4/TO co-transfected MSCs were analysed at TEM after 10,15 and 21 days from transfection. The pictures were compared with the ones obtained for MSCs cultured in medium doped with FeQ (3.4 µl FeQ/ml) after 10 days, 15 days and 21 days of incubation with the solution, considered as controls.

TEM pictures of MSCs cultured in medium doped with FeQ (34 µM) after 10 days, 15 days and 21 days of incubation with the solution show a time-dependant increasing amount of vesicles containing disperse material, probably the FeQ solution (**Figure 40**).

MSCs expressing MTB genes show vesicles filled with both dispersed (**Figure 41c**, **Figure 41f**, **Figure 42h**, **Figure 42 i**, **Figure 43c**) and electro-dense material (**Figure 41e, Figure 41h**, **Figure 42f**, **Figure 43i**). The vesicles diameter could reach more than 1 µm in length (**Figure 42 f**) and each of them could encase more sub-vesicles filled within electron-dense content (**Figure 41c**, **Figure 41e**, **Figure 41h**, **Figure 42e-f, Figure 43b**). No difference was noticed between the structures created in the *mms6*-pcDNA3.1 and the *mmsF*-pcDNA/4TO transfected MSCs. All the observed

vesicles are filled with the same electron-dense material and show similar shape and size. *mms6*-pcDNA3.1+*mmsF*-pcDNA/4TO co-transfected MSCs vesicles, however, are less numerous in the cells and poorly filled (**Figure 43 h-i**).

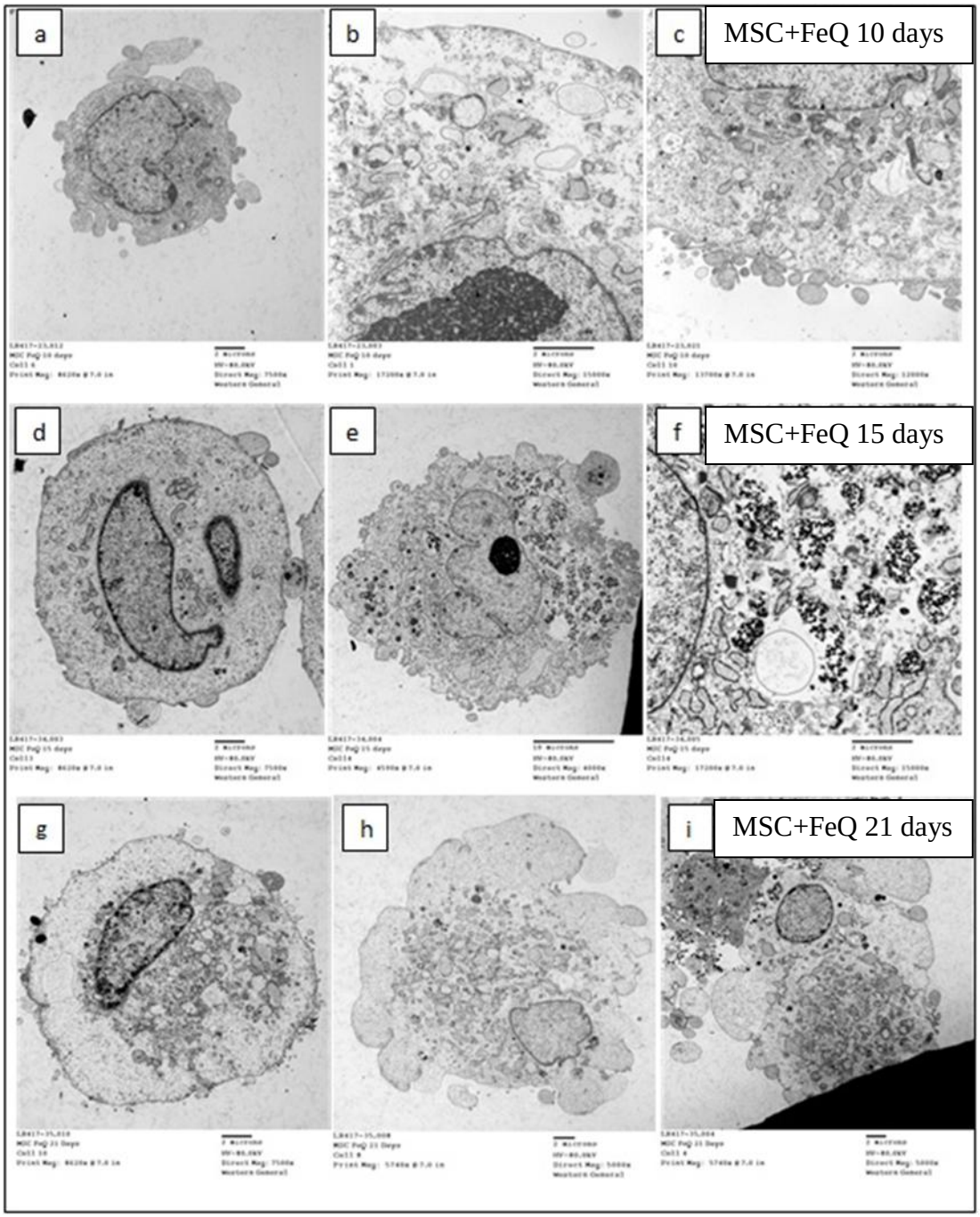

Figure 40. TEM pictures of MSCs cultured in medium doped with FeQ.

Representative TEM pictures of MSCs doped with FeQ (34 µM) after 10 days, 15 days and 21 days of incubation with the solution.

a-c) 10 days of incubation with the solution: single cell and particulars of the cytoplasm; d-f) 15 days of incubation with the solution: single cell and particulars of the cytoplasm; g-i) 21 days of incubation with the solution.

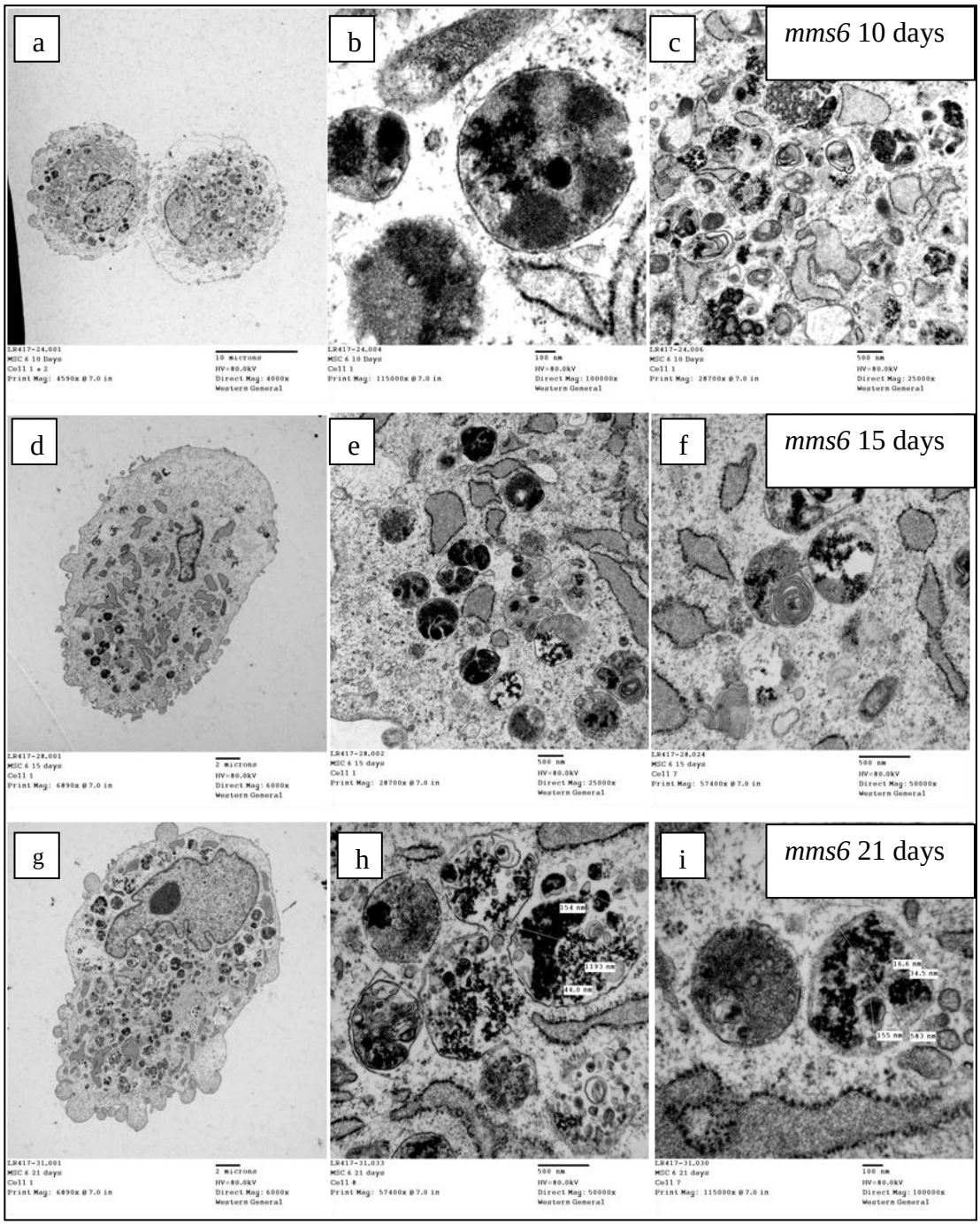

Figure 41. TEM pictures of *mms6*-expressing MSCs.

Representative TEM pictures of *mms6*-expressing MSCs cultured in medium doped with FeQ 10 days, 15 days and 21 days after the transfection.

a-c) 10 days after the transfection: single cell and particulars of the cytoplasm; d-f) 15 days after the transfection: single cell and particulars of the cytoplasm; g-i) 21 days after the transfection: single cell and particulars of the cytoplasm. Scale bars: a) = 10 µm; b) and i) =100 nm; c), e), f), h) =500 nm; d) and g) =2 µm.

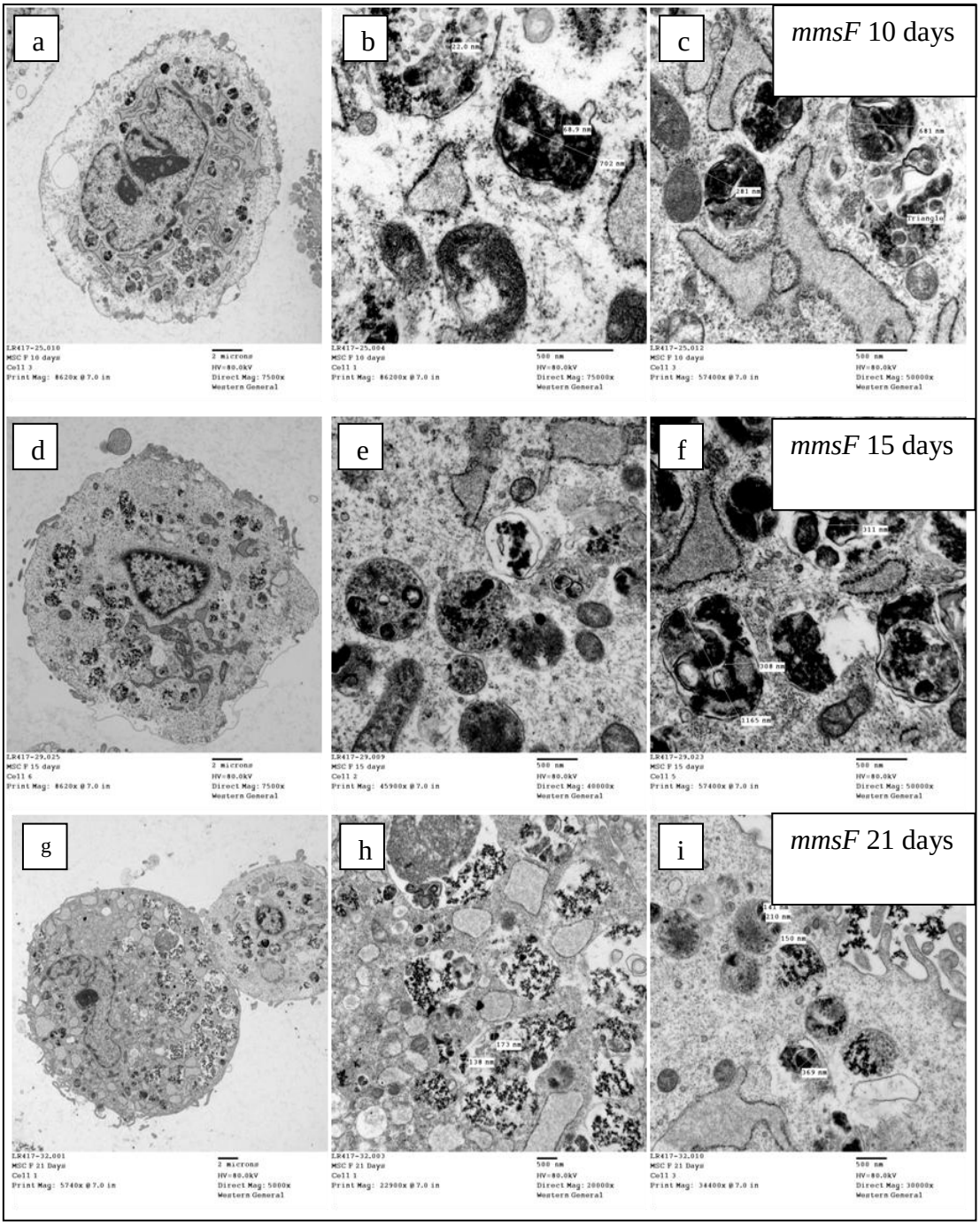

Figure 42. TEM pictures of *mmsF*-expressing MSCs.

Representative TEM pictures of *mmsF*-expressing MSCs cultured in medium doped with FeQ 10 days, 15 days and 21 days after the transfection.

a-c) 10 days after the transfection: single cell and particulars of the cytoplasm; d-f) 15 days after the transfection: single cell and particulars of the cytoplasm; g-i) 21 days after the transfection: single cell and particulars of the cytoplasm. Scale bars are: a), d), g) =2 µm; b), c), e), f), h), i)= 500 nm.

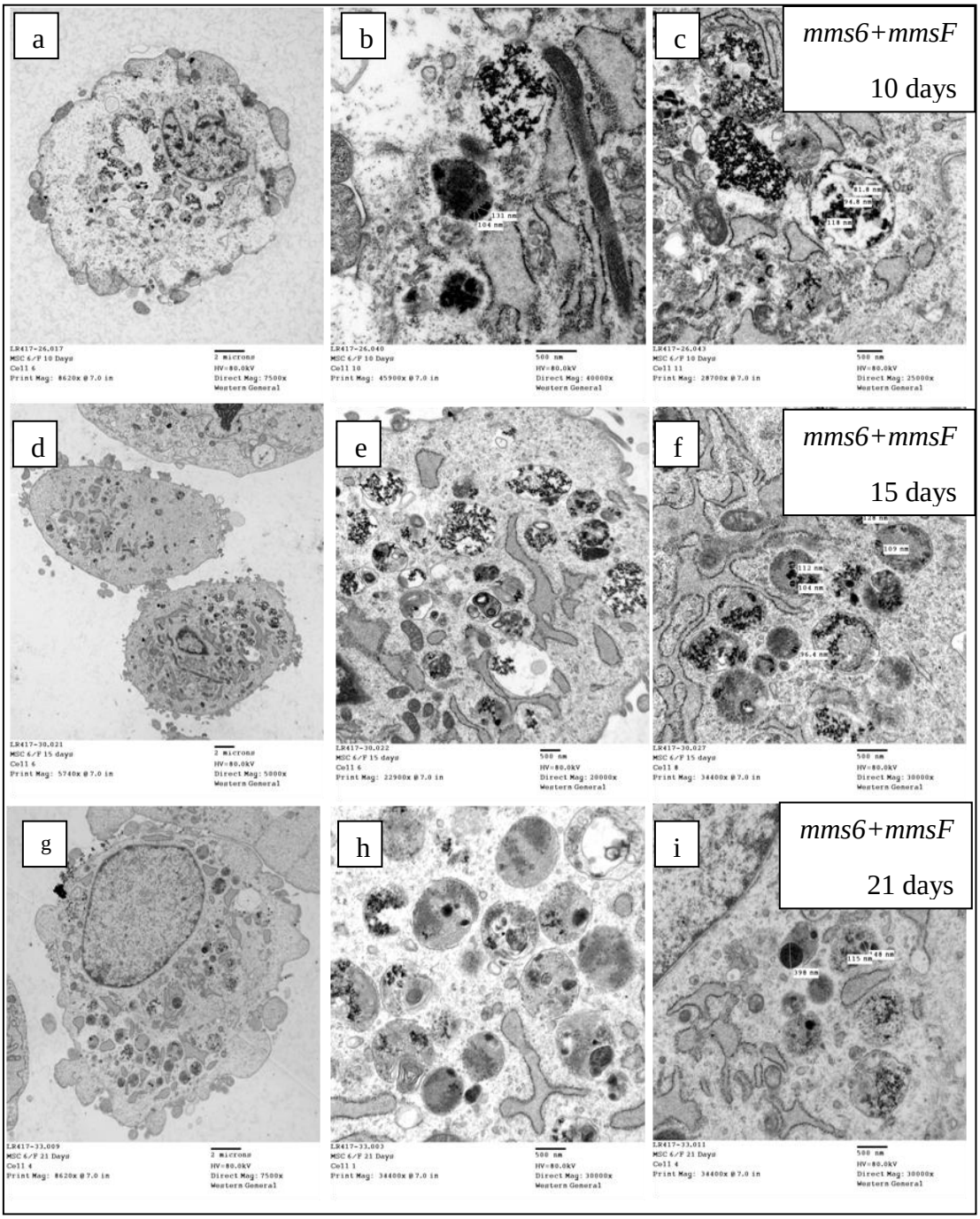

Figure 43. TEM pictures of *mms6+mmsF* expressing MSCs.

Representative TEM pictures of *mms6+mmsF* expressing MSCs cultured in medium doped with FeQ 10 days, 15 days and 21 days after the co-transfection.

a-c) 10 days after the co-transfection: single cell and particulars of the cytoplasm; d-f) 15 days after the co-transfection: single cells and particulars of the cytoplasm; g-i) 21 days after the co-transfection: single cell and particulars of the cytoplasm. Scale bars are: a), d), g)= 2 µm; b), c), e), f), h), i)= 500 nm.

4.6. SQUID measurements on *mms6*-pcDNA3.1, *mmsF*-pcDNA/4TO and *mms6*-pcDNA3.1+*mmsF* pcDNA/4TO co-transfected MSCs

The magnetisation of transfected MSCs was analysed by *Superconducting Quantum Interference Device* magnetometer (SQUID). The samples analysed were *mms6*-pcDNA3.1, *mmsF*-pcDNA/4TO and *mms6*-pcDNA3.1+*mmsF* pcDNA/4TO co-transfected MSCs, 10 days after transfection and incubated with FeQ (34 μM), considering $10x10^6$ cells for each sample. MSCs incubated with FeQ (34 μM) for 10 days were used as a control.

The time point chosen to analyse the MSCs (10 days) was the same chosen for the MG63 cells, to detect any consistency between the magnetic behaviour of the two cell types.

The samples magnetisation was investigated in a temperature-dependent experiment (**Figure 44**). The lower branch and the upper branch of the graphs are equal approximately at 20 K. In order to obtain a random orientation of the nanoparticles, samples were cooled down to 5K and then it was applied a very low field (100 Oersted, corresponding to 100 millitesla), beginning the magnetic recording. The samples were then heated very slowly up to 320 K, (lower branch of the curve). The magnetisation of the sample follows the temperature rising until 20 K. Above this temperature, magnetisation decreases, as previously seen for MG63 cells. As the temperature of samples was lowered again (upper branch of the curve), it was observed that both the magnetisation curve and the heating curve were aligned but then, around 20 K, the magnetisation of samples increases, while the heating curve decreases, according to the typical behaviour of superparamagnetic nanoparticles: the nanoparticles are oriented in the field, and lowering the temperature only makes the order stronger.

The most magnetised cells appear to be *mms6*-pcDNA3.1 transfected MSCs, with a magnetisation near to $6*10^{-5}$ emu, followed by *mmsF*-pcDNA/4TO transfected MSCs ($5*10^{-5}$ emu) and by *mms6*-pcDNA3.1+ *mmsF*-pcDNA/4TO co-transfected MSCs

($2.8*10^{-5}$ emu). A very low magnetisation was found for MSCs incubated with FeQ ($3.1*10^{-6}$ emu).

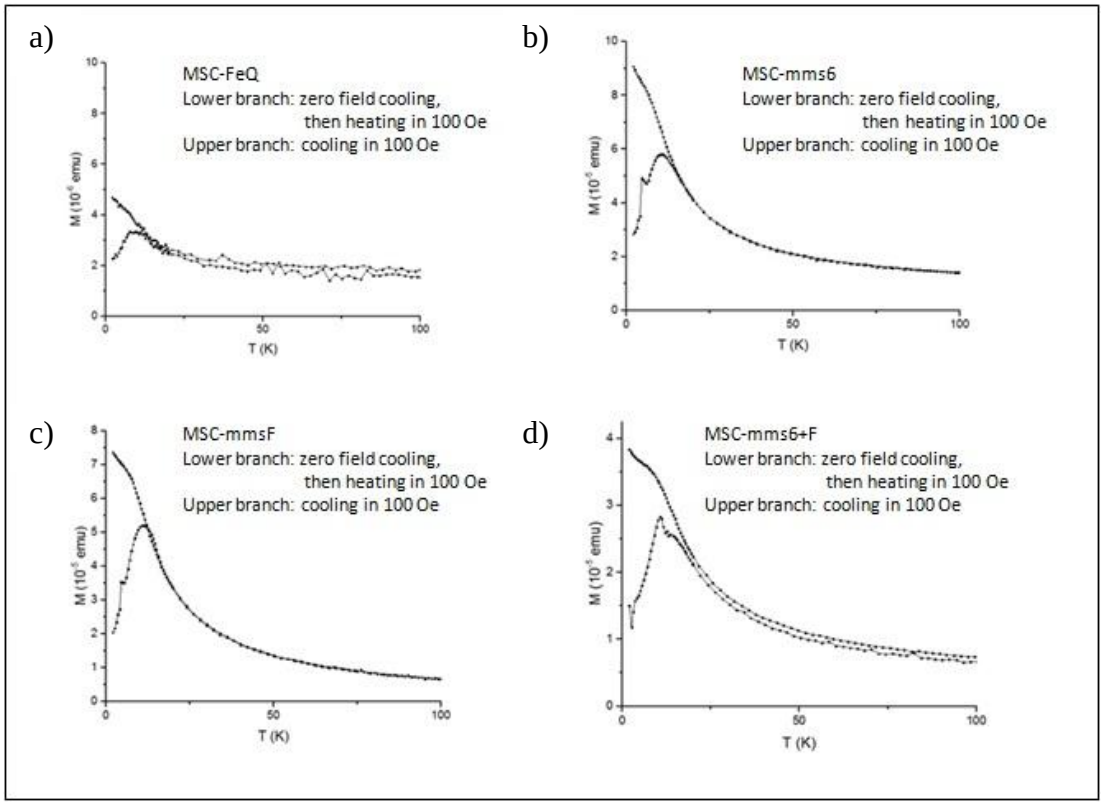

Figure 44. Representative SQUID measurement of MSCs.

a) MSCs incubated with FeQ (3.4 µl FeQ/ml) for 10 days; b) *mms6*-pcDNA3.1, c) *mmsF*-pcDNA/4TO and d) *mms6*-pcDNA3.1+ *mmsF* pcDNA/4TO co-transfected MSCs, all incubated with FeQ (34 µM) for 10 days. Lower branch: zero field cooling, then the samples were heated in 100 Oe. Upper branch: samples were then cooled again in 100 Oe.

4.7. Hyperthermia measurements on intracytoplasmic vesicles created within *mms6*-pcDNA3.1, *mmsF*-pcDNA/4TO and *mms6*-pcDNA3.1+*mmsF*-pcDNA/4TO co-transfected MSCs

The magnetism of the intracytoplasmic vesicles created within MSCs transfected with plasmids *mms6*-pcDNA3.1, *mmsF*-pcDNA/4TO and *mms6*-pcDNA3.1+ *mmsF*-pcDNA/4TO, 10 days after transfection, and incubated in medium doped with FeQ solution (34 μM) was investigated by HT experiments. Wild-type MSCs cultured in standard medium for 10 days and wild-type MSCs incubated in medium doped with FeQ solution (34 μM) for 10 days were considered as controls. Samples were investigated under a magnetic field of 250 Oe and 429 kHz, using $4.5x10^6$ cells for each sample. The rising of temperature was investigated until 750 seconds after the beginning of the experiment (**Figure 45**).

It was noticed a modest temperature rising in the transfected MSCs. In the first 150 seconds, samples temperature raises of 0.1 °C for all the transfected cells, which seem to have all the same magnetic behaviour. Increasing the magnetic exposure time, the higher temperature rising was determined in this case by the *mms6* gene, which leads to a cell temperature rising of +0.3 °C after 7 minutes, +0.5 °C after 8.5 minutes and up to +0.6 °C after 10 minutes, proving to be the most magnetising gene. Results show that MSCs co-expressing both the *mms6*+*mmsF* genes are slightly more magnetised than *mmsF* expressing MSCs, but both the cell types show a temperature rising of less than +0.4 °C after 10 minutes from the exposure to the AMF. Controls kept a constant temperature for all the treatment.

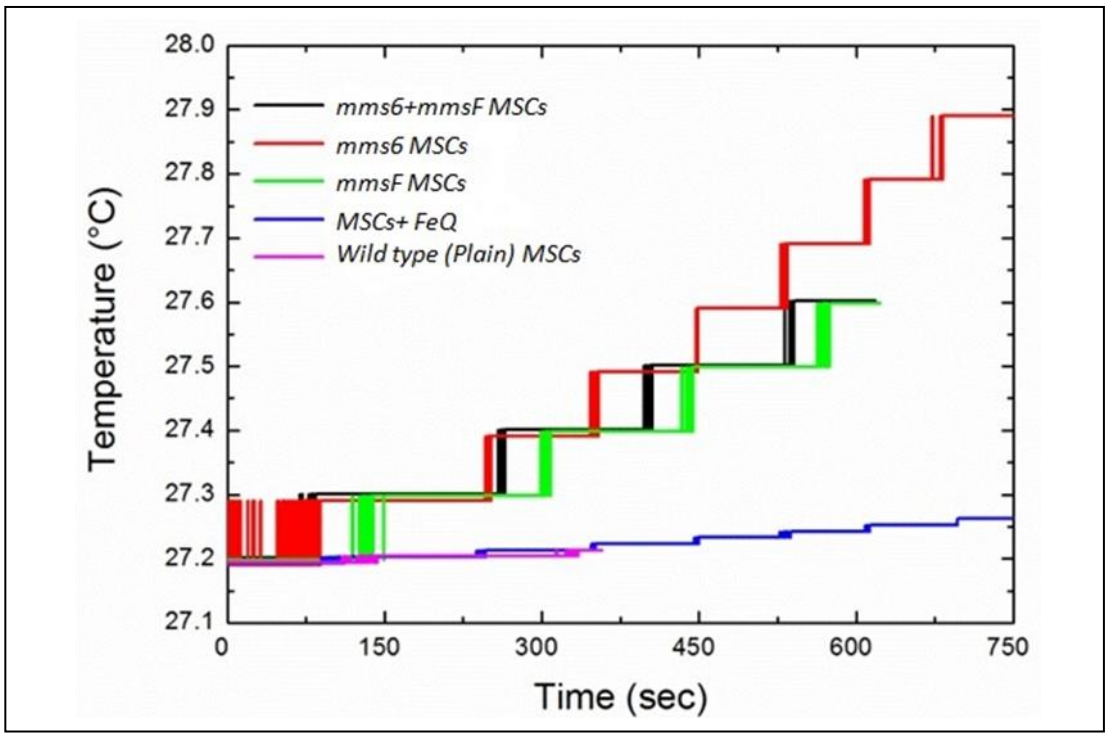

Figure 45. Representative picture of hyperthermia measurements on MSCs.

Cells investigated were *mms6*-pcDNA3.1, *mmsF*-pcDNA/4TO and *mms6*-pcDNA3.1+*mmsF*-pcDNA/4TO co-transfected MSCs in a magnetic field of 250 Oe and 429 kHz in a time of 750 seconds. Wild-type MSCs and Wild-type MSCs incubated with FeQ (34 µM) for 10 days served as controls.

4.8. Transmission Electron Microscopy (TEM) analysis of the intracytoplasmic structures formed within *mms6*-pcDNA3.1 transfected MSCs

Both the SQUID and the hyperthermia measurements confirmed that *mms6* is the gene which confers the higher magnetisation to MSCs, and TEM pictures indicated that *mms6* is also responsible for the creation of magnetic vesicles filled with electron-dense material inside the *mms6*-expressing MSCs.

Following these findings, it was necessary to understand if the passing of time after transfection could influence the number of vesicles created inside the *mms6*-pcDNA3.1 transfected MSCs as well as the percentage of electron-dense content found in each cell.

The expression of *mms6* gene in *mms6*-pcDNA3.1 transfected MSCs was confirmed by RT-PCR experiments at the different time points taken in consideration for TEM vesicles analysis (**Figure 46**). *mms6* genes is expressed in MSCs after 10, 15 and 21 days from transfection, as indicated by the band of 108 bp present in wells 5-7, while it was absent in the wild-type MSCs and in the wild-type MSCs incubated with medium doped with FeQ solution for 10,15 and 21 days (wells 1-4). GAPDH expression levels were found to be constant for all the samples, as shown by the expected band of 94 bp (wells 8-14), indicating that the gel lanes have been evenly loaded with sample material.

Mms6 and GAPDH mixes without cDNA (wells 15 and 16) served as negative controls and show no bands, indicating no contamination in the RT- PCR mixes.

The results of the ImageJ analysis of TEM pictures of *mms6*-pcDNA transfected MSCs at 10, 15 and 21 days are shown in a time-dependent graph (**Figure 47**, **Panel A**). The average of the number of vesicles formed by the *mms6* gene at day 21 respect to day 15 is statistically significant ($p<0.05$).

For each vesicle, it was also calculated the percentage of electron-dense filling respect to the vescicle area, then the average was calculated, considering 10 pictures for each time point. The results are shown in a time-dependent graph (**Figure 47**, **Panel B**), where the percentage of electron-dense material created at day 15 and at day 21 respect to day 10 was found statistically different ($p<0.05$).

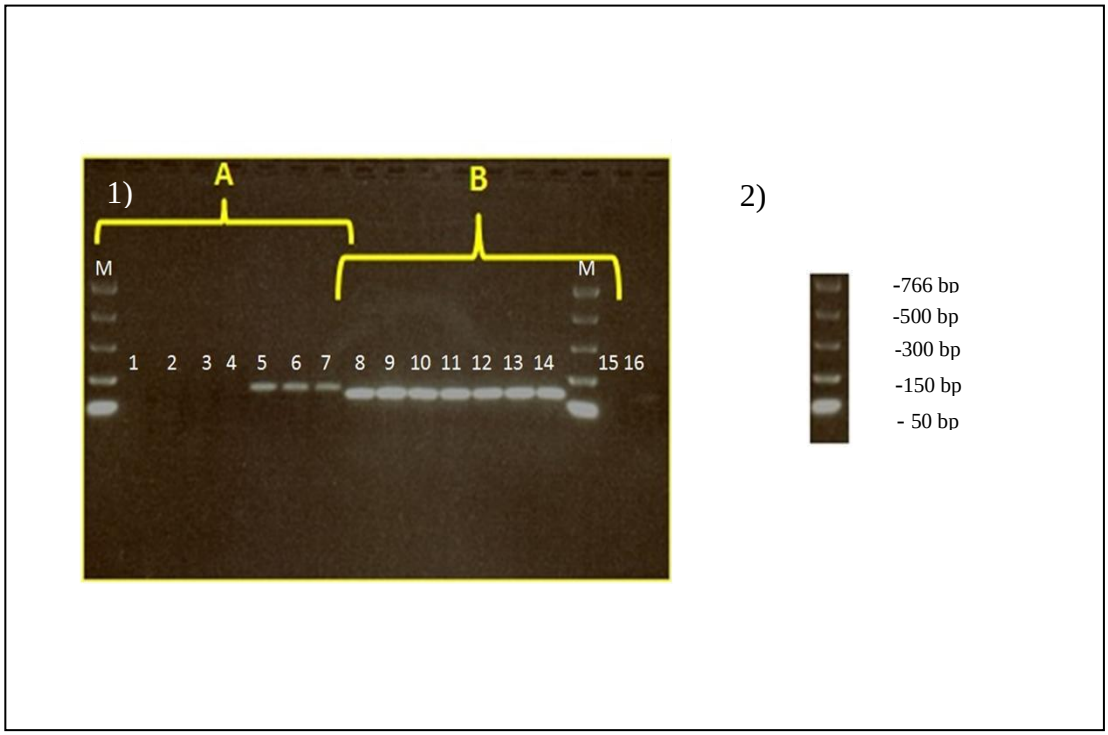

Figure 46. ***mms6*** **expression in MSCs at different time points.**

1. A) Mms6 mix: 1) Wild-type MSCs, 2) MSCs incubated with FeQ for 10 days, 3) MSCs incubated with FeQ for 15 days, 4) MSCs incubated with FeQ for 21 days, 5) 10 days *mms6*-pcDNA3.1 transfected MSCs, 6) 15 days *mms6*-pcDNA3.1 transfected MSCs, 7) 21 days *mms6*-pcDNA3.1 transfected MSCs. B) GAPDH mix: 8) Wild-type MSCs, 9) MSCs incubated with FeQ for 10 days, 10) MSCs incubated with FeQ for 15 days, 11) MSCs incubated with FeQ for 21 days, 12) 10 days *mms6*-pcDNA3.1 transfected MSCs, 13) 15 days *mms6*-pcDNA3.1 transfected MSCs, 14) 21 days *mms6*-pcDNA3.1 transfected MSCs. 15) Mms6 mix (negative control), 16) GAPDH mix (negative control). M= marker.

2. 766 bp NEB marker used in the gel electrophoresis.

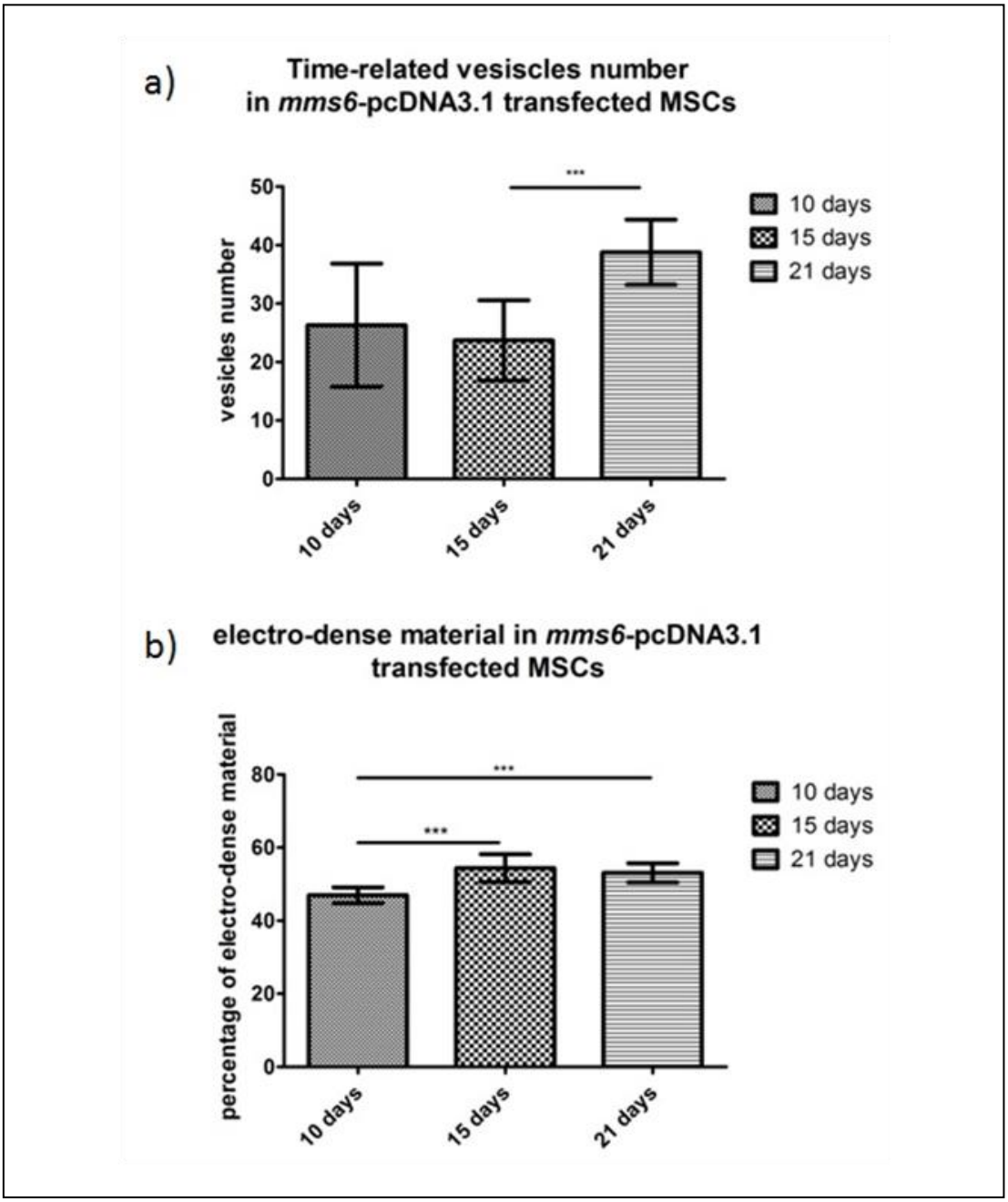

Figure 47. Analysis of vesicles investigated at TEM.

Panel a. Average of the vesicles number at different time points (10, 15 and 21 days) after MSCs transfection with *mms6*-pcDNA3.1 plasmid. Panel b: Average of the percentage of electron-dense material found in vesicles at different time points (10, 15 and 21 days) after MSCs transfection with *mms6*-pcDNA3.1 plasmid. Results are indicated as average with standard deviation error bars. One-way ANOVA test was used for statistical significance, followed by post hoc Tukey test between groups when a statstical difference was found; a value of $p<0.05$ was considered statistically significant; n=10. Asterisks indicate statistical significance.

4.9. Magnetic Force Microscopy (MFM) on *mms6*-pcDNA3.1 transfected MSCs

SQUID measurements revealed that *mms6* is the gene able to confer the highest magnetism to MSCs. To have a further confirmation of the *mms6*-pcDNA3.1 transfected MSCs magnetism, these cells were investigated by Magnetic Force Microscopy (MFM) after 10, 15 or 21 days from the transfection with *mms6*-pcDNA3.1 plasmid, to understand if the prolongation of the incubation time with the FeQ solution after the transfection could influence MSCs magnetism.

MFM was used in these experiments to detect the presence of superparamagnetic nanoparticles created in *mms6*-pcDNA3.1 transfected MSCs by the expression of MTB *mms6* gene in the MSCs. The surface of the samples was investigated by AFM in semi-contact mode, to detect any roughness corresponding to nanoparticles aggregates, which were then subjected to MFM measurement to determine their magnetisation.

The experiments were performed using a magnetic probe in dynamic lift mode to detect the presence of nanoparticles in the presence of a weak external magnetic field (a few hundreds of Gauss). The observed magnetisation was very weak for 10 days *mms6*-pcDNA3.1 transfected MSCs (**Figure 48**), while it was observed a stronger magnetisation after 15 and 21 days respectively from transfection of MSCs with *mms6*-pcDNA3.1 (**Figure 49** and **Figure 50**), indicating a time-dependent magnetisation process.

In Figure 48, corresponding to 10 days *mms6*-pcDNA3.1 transfected MSCs, it was detected a small magnetic signal, pointed by arrow (**Figure 48 b**, and magnification of the signal in **Figure 48 d**). In **Figure 49**, where the 15 days *mms6*-pcDNA3.1 transfected MSCs were analysed, the magnetism increases (**Figure 49 d**). In **Figure 50**, negative and positive signal contrasts are detected in correspondence of intracellular aggregates of 21 days *mms6*-pcDNA3.1 transfected MSCs, resulting in fraction/few degrees phase shifts, hence clearly detectable in the setup. It should be noticed that the magnitude of the cantilever deflection *versus* the tip-sample distance

follows the attenuation law typically observed when the lift distance is brought far from the Van Der Waals regime (Schreiber et al., 2008), hence confirming that it was observed genuine magnetic contrast. Control AMF/MFM studies are shown in **appendix 8.11**.

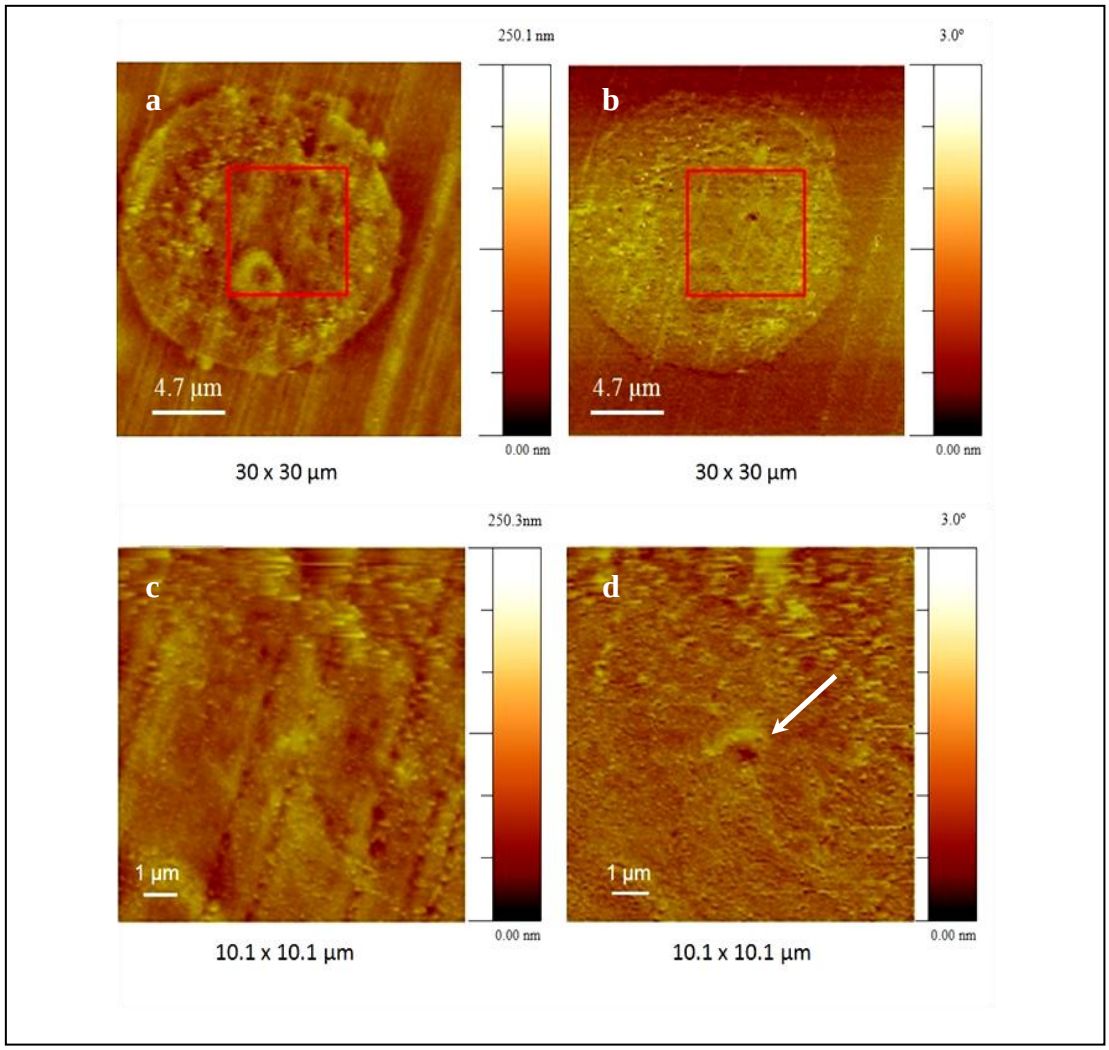

Figure 48. AFM/MFM of 10 days *mms6*-pcDNA3.1 transfected MSCs.

Topographic AFM image obtained in semicontact mode (a) and its corresponding MFM phase image (b). c) magnification of semicontact mode, d) magnification of MFM phase. At this stage is possible to detect few magnetic intracellular aggregates (indicated by the arrow). Scale bars are indicated in pictures.

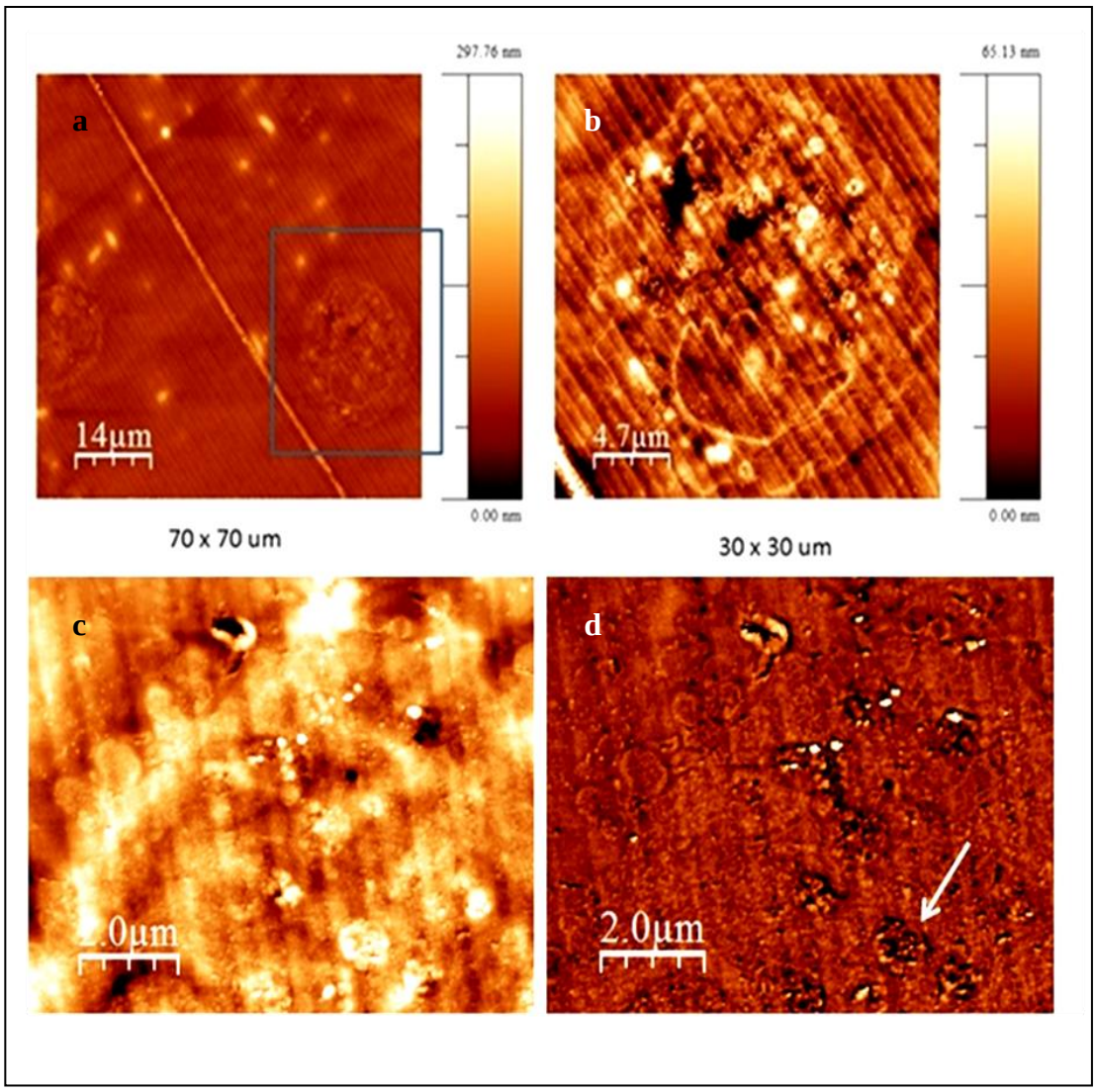

Figure 49. AFM/MFM of 15 days *mms6*-pcDNA3.1 transfected MSCs.

Topographic AFM image obtained in semi-contact mode (a, b, c) and its corresponding MFM phase image (d), z scales: c) magnification of semi-contact mode (0 - 120 nm); d) (-3.0 to +2.5 degrees) at 100 nm lift distance. The magnetic intracellular aggregates are indicated by the arrow. Scale bars are indicated in pictures.

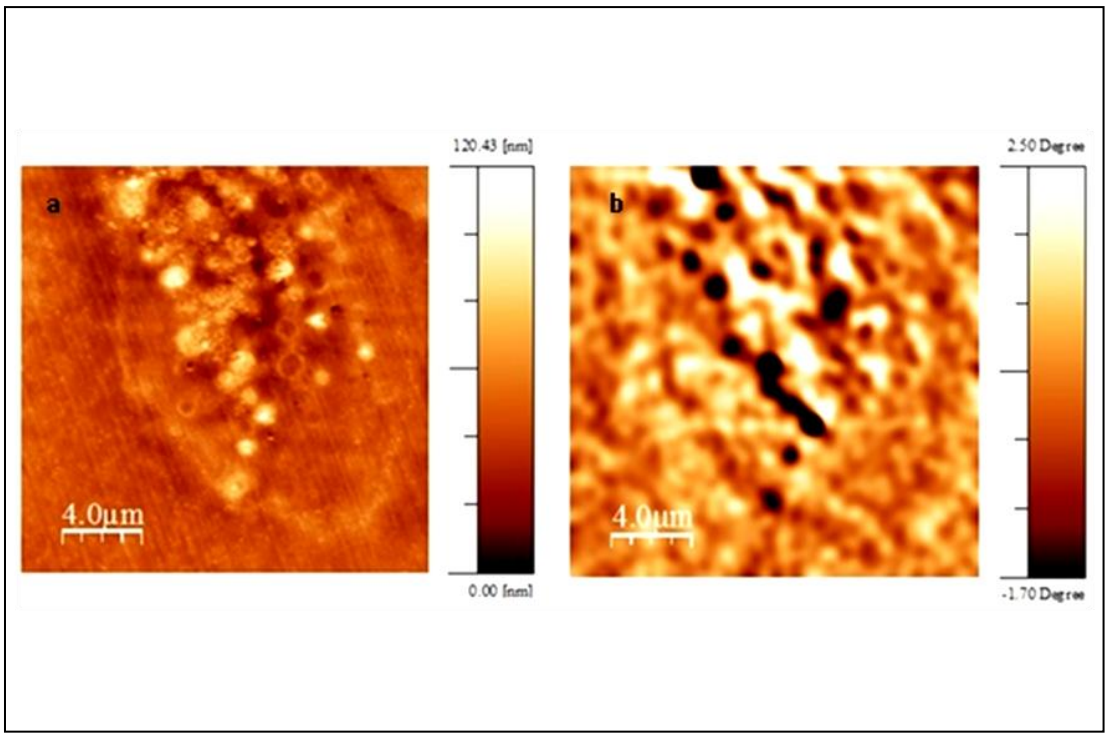

Figure 50. AFM/MFM of 21 days *mms6*-pcDNA3.1 transfected MSCs.

Topographic AFM image obtained in semi-contact mode (a) and its corresponding MFM phase image (b), obtained at 30 nm lift distance. Positive and negative signal contrast corresponding to intracellular aggregates. Scale bars are indicated in pictures.

4.10. Discussion

In this chapter, it was determined if:

1. the transfection of MSCs with *mms6*-pcDNA3.1 could cause any detrimental effect on the cells by investigating MSCs stemness, MSCs proliferation and MSCs pluripotency 21 days post transfection;
2. it is possible to express MTB genes *mms6* and *mmsF*, alone or in combination, in human MSCs and if the genes expression inside the human MSCs creates magnetic structures.

Regarding the point 1, flow cytometry experiments revealed that the MSCs stemness remains unchanged before and after transfection, except for the marker CD45, whose presence was found slightly higher in 21 days transfected MSCs.

Also the study of the MSCs proliferation, that was investigated either qualitatively than quantitatively by the device *Incucyte ZOOM System*, revealed no remarkable differences between the three groups of MSCs analysed.

MSC multipotency was tested by inducing the wild-type and the transfected MSCs in the osteogenic, chondrogenic and adipogenic lineage. After 21 days from differentiation induction, both the cell types were able to differentiate into the different cell lineages, as suggested by staining procedures of the typical differentiation markers for each lineage.

Taken together these evidence show that 21 days post transfection with *mms6*-pcDNA3.1 plasmid, the MSCs nature is unaffected by the expression of the bacterial genes.

Gross differentiation defects were not detected, however, scientific evidence suggest that MSCs labelled with SPIONS show an impaired chondrogenesis and osteogenesis (Y. C. Chen et al., 2010; Kostura et al., 2004). It would be useful to compare the transfected cells with the wild-type ones, analysing the expression of the major genes involved in the three considered differentiation pathway by qPCR. Another way to determine if the transfection could affect MSCs stemness and differentiation

ability could be to find the transcriptional differences among transfected and wild-type cells by RNA deep sequencing (RNAseq), a technique which is used to find differences in levels of expression and structure of RNA (Goldman & Domschke, 2014; Roson-Burgo et al., 2014).

Although in this work the genome or the transcriptome of the transfected cells were not deeply analysed, there are previous studies by Goldhawk et al. which show that it is possible to transfect mouse and human cancer cell lines with *magA*, a MTB putative iron transporter gene, without affecting cells viability or proliferation. (Goldhawk et al., 2009; Sengupta et al., 2014). The viability of transfected cells and their capacity for active transport of iron were assessed by MTT assay and by measuring ATP content respectively. As *magA* is a gene which seems to share a lot of traits in common with *mms6* -one above all the capacity to confer to the transfected cells the ability to become magnetic- these findings are encouraging also for the application of *mms6* in human cells.

Regarding point 2, RT-PCR experiments confirmed the expression of MTB genes *mms6* and *mmsF*, alone or in combination, inside MSCs, validating the transfection success.

TEM investigations revealed the presence of two types of intracytoplasmic vesicles, respectively inside wild-type MSCs cultured in FeQ doped medium and in the *mms6*-pcDNA3.1, *mmsF*-pcDNA/4TO and *mms6*-pcDNA3.1+ *mmsF*-pcDNA/4TO co-transfected MSCs. While the former contain disperse material (**Figure 40f**), the latter ones are filled with electron-dense content, indicating that FeQ solution uptake occurs in all the cells, but only the transfected ones can modify the FeQ solution in dense granules (**Figure 41e**, **Figure 41f**, **Figure 42b**). The observed vesicles are similar to the MG63 cells ones, and their shape resembles endosomes or lysosomes, as previously observed for the MG63 cells. The vesicles create spherical, multilamellar and multivesicular structures with the passing of time (**Figure 41f**), a process occurring when the intracellular vesicles age. These features, together with the lacking of tubules and the close-packed luminal vesicles, are typical of late

endosomes and lysosomes (**appendix 8.10**). The ImageJ analysis of the intracytoplasmic vesicles imaged at TEM of *mms6* expressing MSCs reveals that the number of the detected vesicles increases at day 21, while the percentage of electron dense material inside the vesicles increases at day 15 respect to day 10 to remain constant at day 21.

SQUID analysis reveals that both MSCs and MG63 transfected cells show the same power of magnetisation (10^{-5}), indicating a consistency in the magnetic behaviour after being transfected with the MTB genes. In MSCs, the higher magnetisation was registered for *mms6*-pcDNA3.1 transfected MSCs.

The response of the intracytoplasmic vesicles of the transfected MSCs to an applied AMF was studied with the Hyperthermia experiments. The measured rising of temperature for MSCs is very far from the one normally observed in MHT (≥42 °C) but it was noticed a mild temperature rising for transfected cells respect to the negative controls. The temperature rising observed for the transfected MSCs is in line with that registered for the MG63 transfected cells. However, for the MSCs, the temperature increasing is slightly lower than the cancer cell line. This behaviour could be due to the fact that the number of MSCs analysed by the hyperthermia experiment were less than the number of MG63 employed for the same experiment ($4.5*10^6$ MSCs against $18*10^6$ MG63 cells). The higher temperature rising in MSCs was registered for *mms6* expressing MSCs.

The magnetism of *mms6*-pcDNA3.1 transfected MSCs was also confirmed by AFM/MFM measurements. MFM technique can detect the magnetic interaction between a probe and superparamagnetic nanoparticles in ambient condition. The superparamagnetic nanoparticles buried in a cell tissue cause weak cantilever deflection when a magnetic probe is brought close to the surface. MFM detects local phase shift of the cantilever oscillations as the tip scans across the sample, at a lift distance that is pre-determined to maximise such deflection; hence the detection of a non-zero signal is a signature of magnetic clusters/particles at the surface.

It should be underlined that positive or negative phase variations detected within the intracellular medium, associated with the presence of superparamagnetic

particles/aggregates, are usually very small (less than a few degrees). Indeed, isolated 20-200 nm large clusters of magnetic nanoparticles have shown the resulting net magnetisation corresponding to weak superparamagnetic signal contrast (less than 1 degree phase variations when a magnetic field of few hundred Gauss is applied) (Schreiber et al., 2008). In the experiments, it was registered a genuine magnetic contrast, that was higher for 21 days *mms6*-pcDNA3.1 transfected MSCs. The increasing magnetism revealed at day 21 could depend on the higher number of vesicles found inside the 21 days transfected MSCs, together with the higher percentage of electro-dense material that the cells show at this time point, as revealed by the ImageJ analysis.

Although the mechanism by which *mms6*, as a single gene, is able to provide the human cells with magnetic properties is still obscure, there are some specific properties of the Mms6 protein which could justify its ability to confer such fascinating properties to the cells.

Mms6 was described as a protein able to bind iron and generate uniform magnetic crystals (Prozorov et al., 2007), with a high affinity for iron ions and bearing negative charges which give to the protein the peculiar ability to self-assemble and which make it a key regulator of crystal size and morphology (Amemiya et al., 2007; Arakaki et al., 2010; Arakaki et al., 2014).

Moreover, Mms6 is not the only protein able to confer magnetic properties to mammalian cells. As previously said, the expression of the gene MagA into mammalian cells was found able to increase the iron retention and to create magnetic structures inside mouse and human cancer cells, as well as in human embryonal kidney cell line. The magnetic structures generated by MagA in the cells generated contrast at MRI of 11T, making it a reporter gene for MRI applications (Goldhawk et al., 2009; Sengupta et al., 2014; Zurkiya et al., 2008). These evidence support the idea that a single gene could be sufficient to impart magnetic properties to mammalian cells.

Overall, it could be inferred from these experiments that:

- *mms6* gene could be expressed in MSCs;

- *mms6* is responsible for the creation of intracytoplasmic vesicles in MSCs, which contain magnetic material;
- the *mms6*-pcDNA3.1 transfected MSCs magnetism increases with the passing of time and reaches the higher value at day 21, which is the longest observed time in this experiment.

Taken together, this findings suggest that *mms6* expressed alone in MSCs gives the higher magnetisation to the cells and does not affect cells stemness, proliferation and differentiation ability..

5. *In vitro* application of an AMF of 565.3 kHz on cell cultures arranged in monolayers or in 3D models.

5.1. Introduction

In this chapter it was assessed whether the MNPs created inside the 21 days *mms6*-expressing MSCs, called for simplicity *mms6*-expressing MSCs, could support an AMF of 565.3 kHz frequency *in vitro*, and if the effects of this interaction could induce MSCs cytotoxicity or death.

The effects of the exposure were studied firstly on *mms6*-expressing MSCs monolayers and secondly on 3D cell population models. In the first case, the effect of the AMF exposure on cell viability was investigated by AlamarBlue Cell Viability Assay, whereas the cytotoxicity was assessed by Pierce LDH Cytotoxicity Assay. In the case of 3D cell population models, cell death was determined by Trypan Blue Exclusion Dye.

Afterwards, in the attempt to create an *in vitro* model of an *in vivo* situation, in which MSCs are injected inside a tumour tissue and then subjected to an AMF application, 3D models of mixed population of *mms6*-expressing MSCs and tumour cell lines MG63 cells and A431 ecad-GFP expressing squamous carcinoma cells were created and subsequently exposed to an AMF of 565.3 kHz frequency. The effects of the AMF on cell viability were studied using AlamarBlue Cell Viability Assay and Trypan Blue Exclusion Dye. In the case of 3D mixed population of *mms6*-expressing MSCs and MG63 cells, Trypan Blue Exclusion Dye results were also supported by fluorescent microscopy pictures analysis. In the case of the 3D mixed population of *mms6*-expressing MSCs and A431 ecad-GFP expressing cells, the green fluorescence blur of GFP protein expressed by A431 ecad-GFP expressing cells made impossible to obtain quality fluorescent pictures to support the cell viability results, therefore they have been omitted from the chapter.

Each test was repeated in three independent experiments. For each experiment, a different flask of transfected cells, 21 days from transfection, was used. This was done to test if different batches of transfected cells were able to react in the same way to the AMF.

5.2. Aims

The hypothesis underlying the presented study was that MNPs created inside the *mms6*-expressing MSCs could support a MH effect when exposed to an AMF of 565.3 kHz frequency, which could induce MSCs cytotoxicity or death *in vitro* either when they are arranged in a monolayer or 3D models. It was also hypothesised that, in the case of co-culture of *mms6*-expressing MSCs with cancer cells, the interaction of MNPs with the AMF is sufficient to induce the death of the neighbouring cancer cells.

The effects of the interaction of the MNPs created inside the *mms6*-expressing MSCs with the AMF of 565.3 kHz frequency were studied investigating cell viability, cell cytotoxicity and cell death, using different assays:

- In the case of *mms6*-expressing MSCs cell monolayers, cell viability was investigated by AlamarBlue Cell Viability Assay and cells cytotoxicity was assessed by Pierce LDH Cytotoxicity Assay.
- In the case of *mms6*-expressing MSCs arranged in 3D models, cell death was determined by Trypan Blue Exclusion Dye.
- In the case of 3D co-cultures of *mms6*-expressing MSCs and MG63 cells, cell death was assessed by Trypan Blue Exclusion Dye and results were supported by fluorescent microscopy pictures.
- In the case of 3D mixed populations of *mms6*-expressing MSCs and A431 ecad-GFP expressing cells, cell viability was determined by AlamarBlue Cell Viability Assay.

5.3. Results

5.3.1. The effect of one hour 565.3 kHz AMF on *mms6*-expressing MSCs arranged in a monolayer. Determination of cell cytotoxicity by *LDH Cytotoxicity Assay*

mms6-expressing MSCs seeded in Petri dishes in a monolayer were exposed at 565.3 kHz frequency for one hour, followed by *Pierce LDH Cytotoxicity Assay*. This frequency was chosen as it appeared the most effective, among the frequencies investigated, to determine cell death (**appendix 8.13**).

The results of the experiments are illustrated in **Figure 51**, where the percentage of LDH cytotoxicity registered for the exposed cells is 44.4±1.9%, while for controls is 5.5±0.8%. The results are statistically significant ($p<0,0001$) and reveal that one hour exposure to an AMF of 565.3 kHz frequency leads to a cytotoxic effect on the *mms6*-expressing exposed MSCs, when arranged in a monolayer.

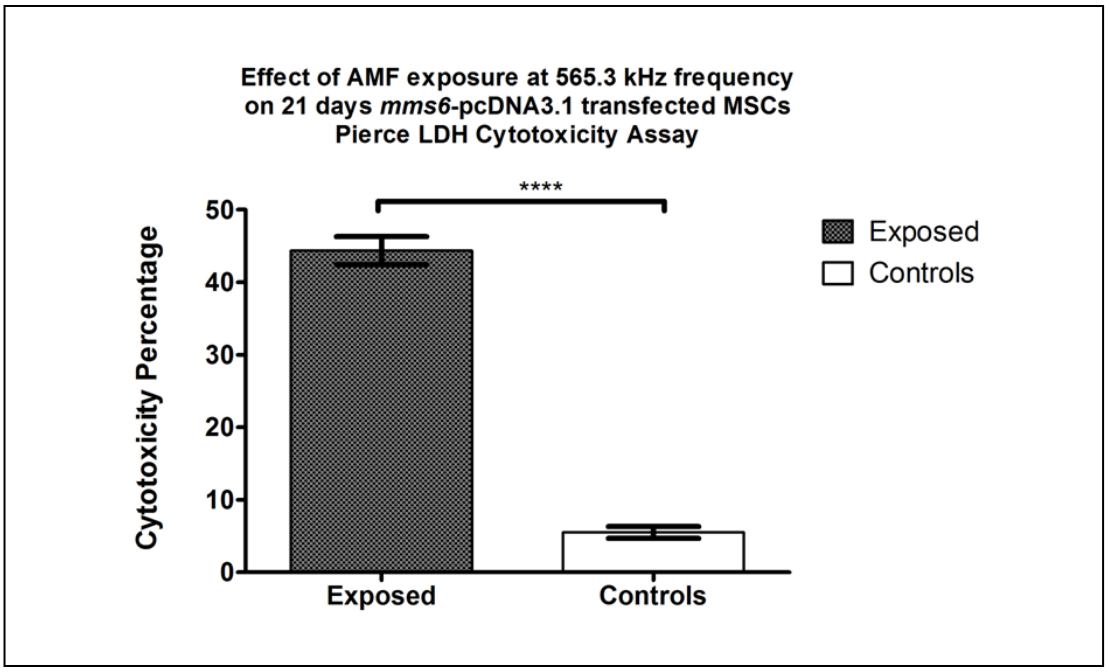

Figure 51. Cell cytotoxicity evaluation by Pierce LDH Cytotoxicity Assay.

mms6-expressing MSCs were exposed at 565.3 kHz for one hour (grey column) or not exposed (controls-white column). Average of cytotoxicity of three independent experiments with standard deviation error bars, $p<0.0001$.

5.3.2. The effect of one hour 565.3 kHz AMF on *mms6*-expressing MSCs, arranged in a monolayer. Determination of cell viability by *AlamarBlue Cell Viability Assay*.

mms6-expressing MSCs seeded in Petri dishes in a monolayer were exposed at 565.3 kHz frequency for one hour, followed by cells viability determination by AlamarBlue Cell Viability Assay (**Figure 52**).

In **Figure 52a**, Alamar Blue fluorescence intensity average of cells exposed to AMF is 51928±2716, against mean fluorescence intensity of 76060±1352 for unexposed ones (controls). The results are statistically significant ($p<0.001$). Cell viability percentage of exposed cells was calculated as a ratio between exposed and controls cells, and it is shown in **Figure 52b**, considering controls as 100% viable. Results reveal that the viability of exposed cells is 68.27±4.78% of that of controls.

As a control, also wild-type MSCs were seeded in Petri dishes in a monolayer and then they were exposed at 565.3 kHz frequency for one hour, followed by cells viability determination by AlamarBlue Cell Viability Assay (**Figure 53**). The wild-type MSCs were not doped with FeQ. Alamar Blue fluorescence intensity average of wild-type cells exposed to AMF is 61453±907, against mean fluorescence intensity of 62350±1778 for unexposed ones (controls). The results reveal that wild-type MSCs viability does not change after AMF exposure (exposed wild-type cells viability is 98.56±4.27% of that of controls; $p>0.05$%).

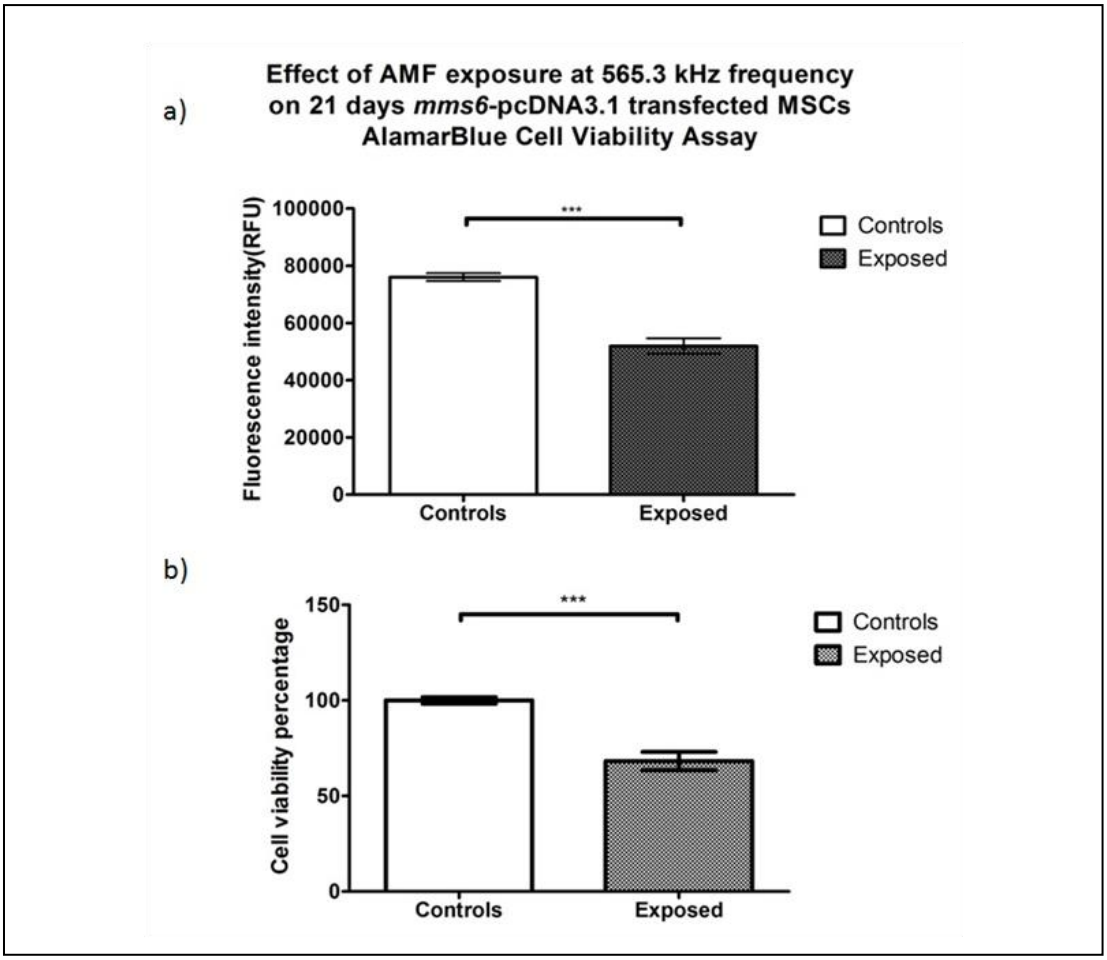

Figure 52. Cell viability evaluation by AlamarBlue Cell Viability Assay.

mms6-expressing MSCs were exposed at 565.3 kHz for one hour (grey column) or not exposed (controls-white column). a) Average of fluorescence intensity of three independent experiments with standard deviation error bar, $p<0.001$. b) Average of three independent experiments of cell viability percentage of exposed cells against controls with standard deviation error bar, $p<0.001$

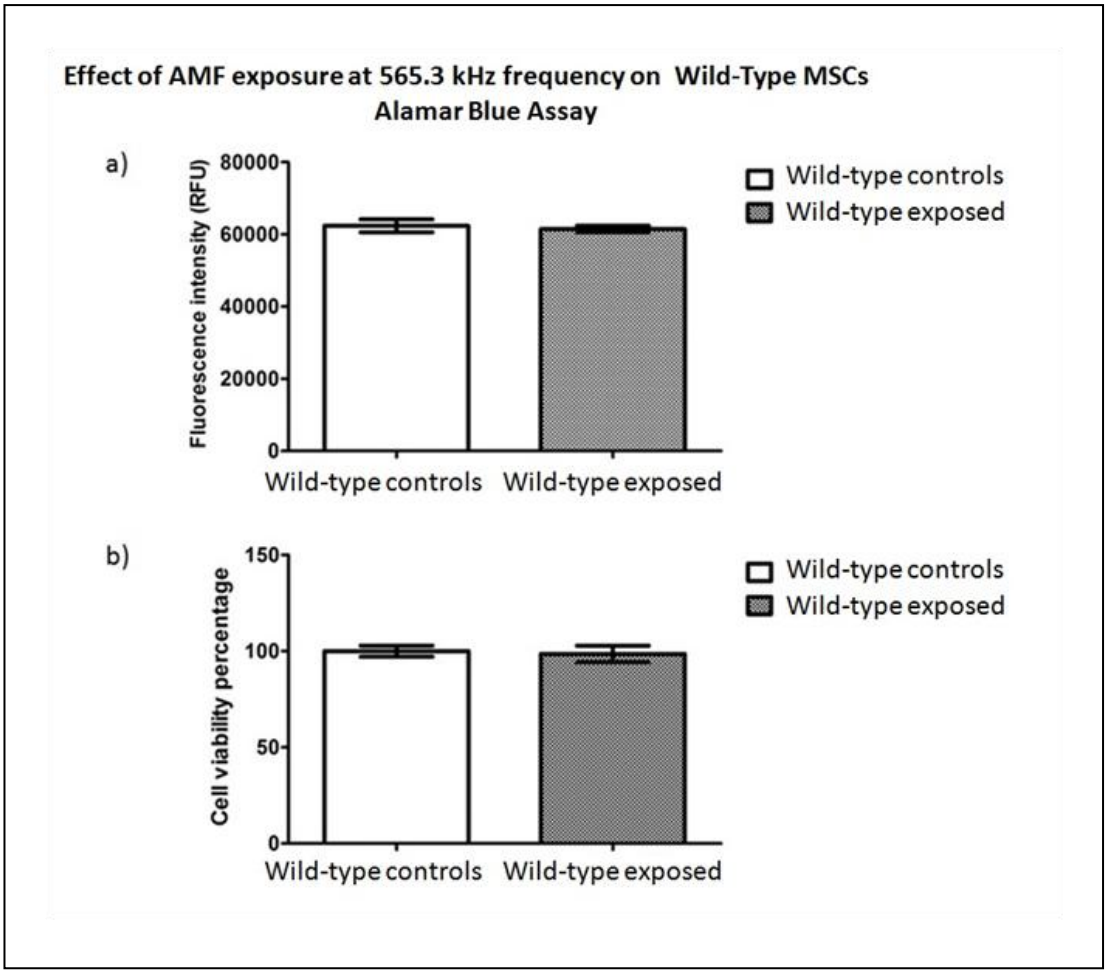

Figure 53. Cell viability evaluation by AlamarBlue Cell Viability Assay.

Wild-type MSCs were exposed at 565.3 kHz for one hour (grey column) or not exposed (controls-white column). The wild-type MSCs were not doped with FeQ. a) Average of fluorescence intensity of three independent experiments with standard deviation error bar. b) Average of three independent experiments of cell viability percentage of exposed cells against controls with standard deviation error bar. The data are not statistically significant.

5.3.3. Bright field microscopy investigation of the effect of the exposure for one hour to an AMF of 565.3 kHz frequency on Plain MSCs and *mms6*-expressing MSCs, arranged in a monolayer.

The effect of AMF exposure at 565.3 kHz frequency on monolayers of *mms6*-expressing MSCs was also investigated by bright field microscopy (**Figure 54** and **Figure 55**). The cells taken in consideration were respectively:

- Wild-type MSCs, exposed at 565.3 kHz frequency for one hour;
- Wild-type MSCs, unexposed;
- *mms6*-expressing MSCs, exposed at 565.3 kHz frequency for one hour;
- *mms6*-expressing MSCs, unexposed.

Bright field pictures indicate, by visual inspection, no differences between exposed and unexposed Plain MSCs arrangement (**Figure 54a, b**). *mms6*-expressing MSCs subjected to AMF treatment agglomerated in bunches, where dark spherical structures were observed (**Figure 55a-f**), while the unexposed *mms6*-expressing MSCs showed a regular pattern (**Figure 55g**). Moreover, in some points of the Petri dish, the entire layer of *mms6*-expressing MSCs subjected to AMF exposure detached from the plate bottom, leaving spots of the Petri dish completely uncovered from the cell monolayer (**Figure 55a-f**). This could be interpreted as a possible cellular sufferance caused by the AMF exposure.

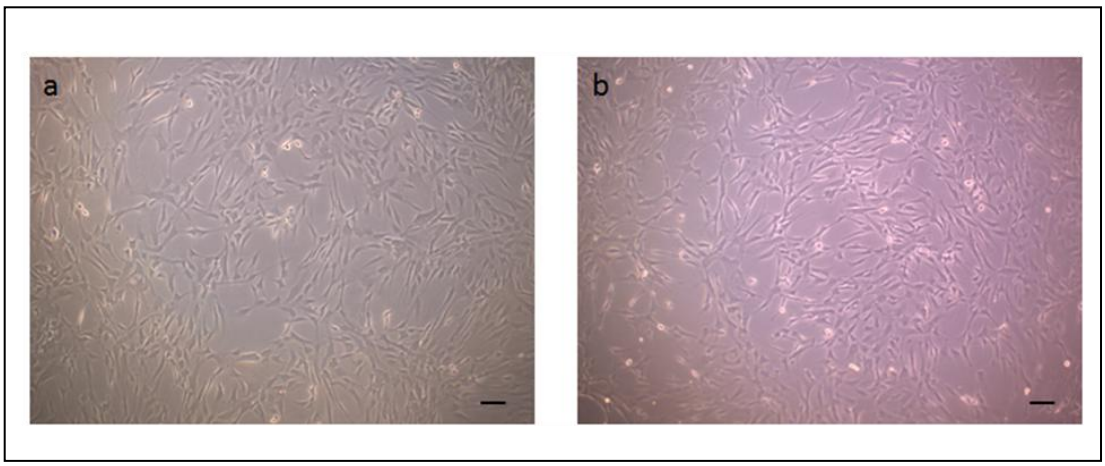

Figure 54. Bright field microscopy of wild-type MSCs.

a) Cells exposed to an AMF of a frequency of 565.3 kHz for one hour; b) Cells unexposed to the AMF (controls). The wild-type MSCs were not doped with FeQ. Scale bar is 100µm.

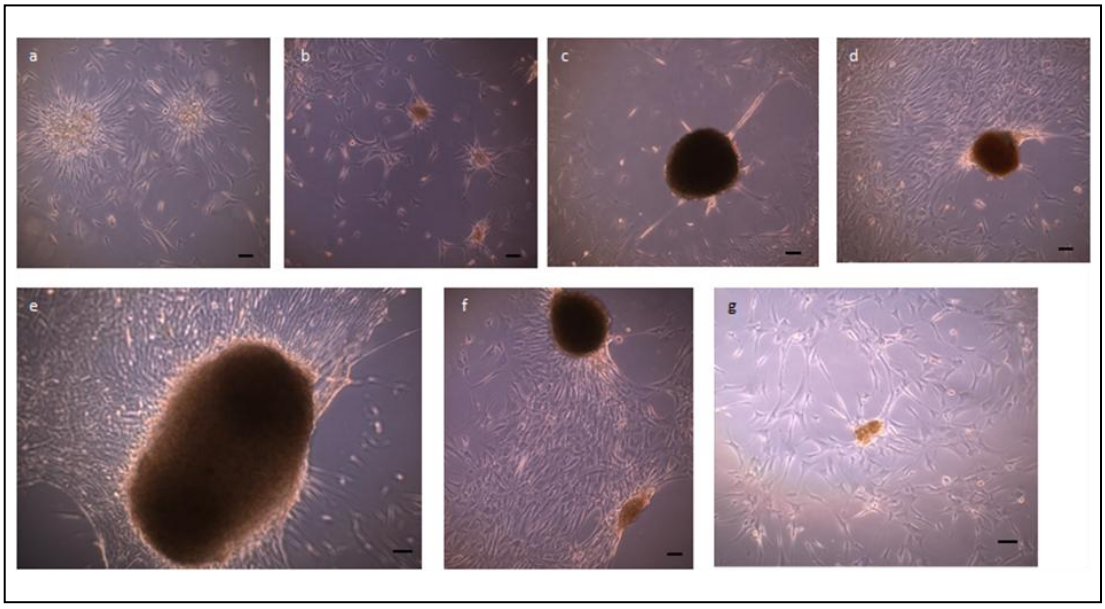

Figure 55. Bright field microscopy of *mms6*-expressing MSCs.

a-f) Pictures of different Petri dishes containing *mms6*-expressing MSCs, arranged in a monolayer, exposed at 565.3 kHz for one hour and g) unexposed. It is possible to notice the tendency of the cells to accumulate in distinct points of the Petri dish, leaving around empty spots, where the layer of cells detaches from the Petri dish bottom (e, f). This behaviour was not observed for *mms6*-expressing MSCs unexposed to AMF, which show a regular pattern of distribution and fewer nanoparticles accumulation (g). Scale bar =100µm.

5.3.4. The effect of one hour 565.3 kHz AMF on 3D cultures of *mms6*-expressing MSCs. Treatment was repeated twice and followed by cell viability assessment by *Trypan Blue Exclusion Assay*.

It was evaluated if an AMF of 565.3 kHz frequency applied on 3D cultures of *mms6*-expressing MSCs for one hour can cause cell death, investigated by Trypan Blue assay. In this experiment, due to the 3D arrangement of cells forming thick pellets, it was chosen to duplicate the AMF exposure, so the day after the first exposure, 3D cell pellets were exposed again at 565.3 kHz for 1 hour (double exposure).

Trypan Blue assay shows a cell death percentage in 41.0 ± 9.5% of cell population exposed to AMF, while unexposed (controls) cells show a cell death percentage of 9.3± 2.6 % (**Figure 56**). The results are statistically significant ($p<0.01$).

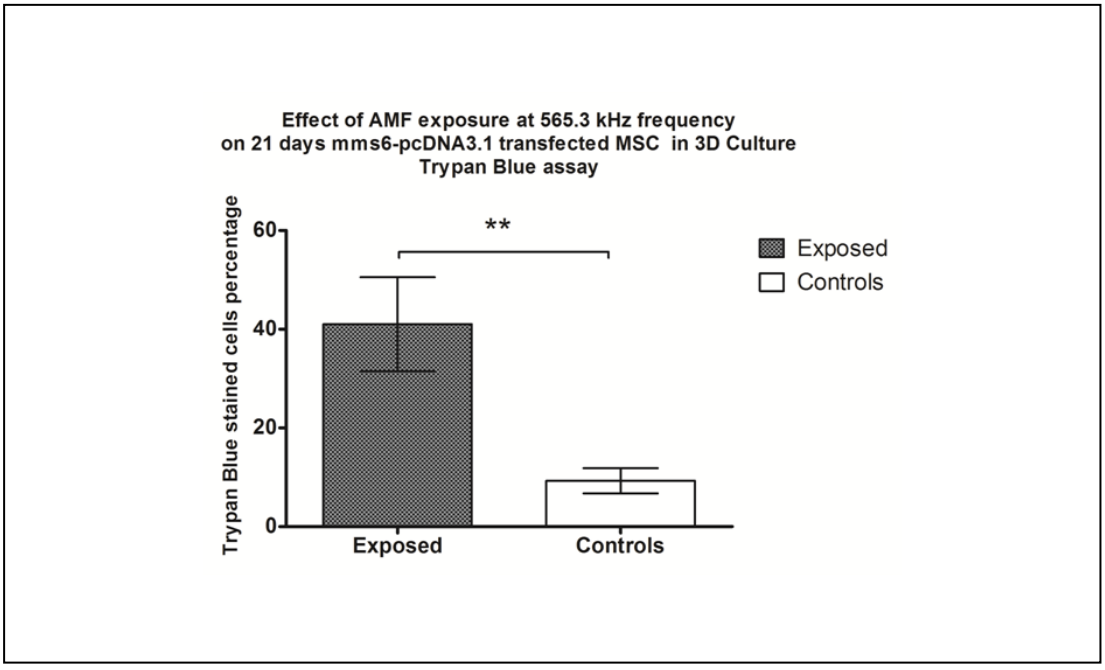

Figure 56. Cell death evaluation by Trypan Blue assay.

In vitro 3D cultures of *mms6*-expressing MSCs were exposed at 565.3 kHz for one hour twice (grey column) or not exposed (controls-white column). Average of Trypan Blue cells staining of three independent experiments with standard deviation error bars, $p<0.01$.

5.3.5. The effect of one hour 565.3 kHz AMF on 3D co-cultures of *mms6*-expressing MSCs and MG63 cells. Treatment was repeated three times and followed by cell viability assessment by *Trypan Blue Exclusion Assay.*

The aim of this experiment was to investigate the effect of an AMF of 565.3 kHz frequency on 3D co-cultures composed of *mms6*-expressing MSCs and MG63 cells, at 1:2 and 1:4 ratio. In total, the 3D mixed cell populations were exposed for one hour at 565.3 kHz frequency three times in two days.

Trypan Blue assay showed a cell death percentage for ratio **1:2** respectively of 39.8±3.7% for exposed cells and of 11.7±2.1% for control cells (**Figure 57a**). For ratio **1:4**, exposed cells showed a death percentage of 43.5±4.0%, while for the controls it was 8.9±2.9% (**Figure 57b**). For both the studied ratios, exposed cells and controls cells are statistically different ($p<0.001$), but it was found no statistical difference between the cell death values of the two ratios ($p>0.05$).

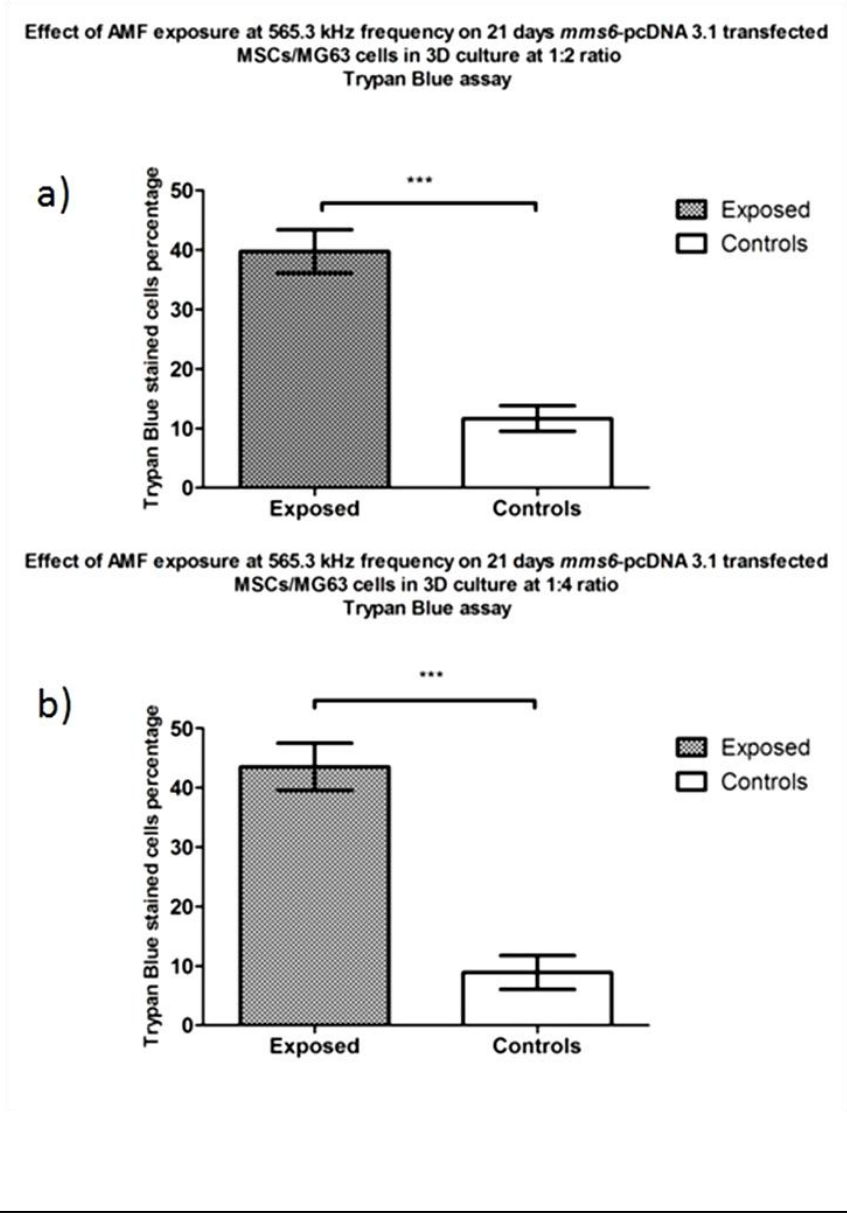

Figure 57. Cell death evaluation by *Trypan Blue Exclusion Assay*.

In vitro 3D cultures of *mms6*-expressing MSCs and MG63 cells were exposed at 565.3 kHz for one hour three times in two days (grey column) or not exposed (controls-white column). Two different MSCs/MG63 ratio were considered, 1:2 (a) and 1:4 (b). Average of Trypan Blue cells staining of three independent experiments with standard deviation error bars, $p<0.001$.

5.3.6. The effect of one hour 565.3 kHz AMF on 3D co-cultures of *mms6*-expressing MSCs + A431 ecad-GFP expressing cells. Treatment was repeated three times and followed by *AlamarBlue Cell Viability Assay.*

In this experiment it was determined the effect of AMF exposure of 565.3 kHz frequency, on 3D co-cultures of *mms6*-expressing MSCs and A431 ecad-GFP expressing cells. In total, the 3D mixed cell populations were exposed for one hour at 565.3 kHz frequency three times in two days. For these experiments, the chosen working ratio MSCs/A431 ecad-GFP expressing cells was 1:2. Cell viability was determined by AlamarBlue Cell Viability Assay (**Figure 58**). In **Figure 58a**, Alamar Blue fluorescence intensity average of cells exposed to AMF is 6664±1104, against mean fluorescence intensity of 14725±2120 for controls. The results are statistically significant ($p<0.05$). Cell viability percentage of exposed cells was calculated as a ratio between exposed and controls cells and it is shown in **Figure 58b**, considering controls as 100% viable. Results reveal that the viability of exposed cells is 45.26±20.75% of that of controls unexposed cells.

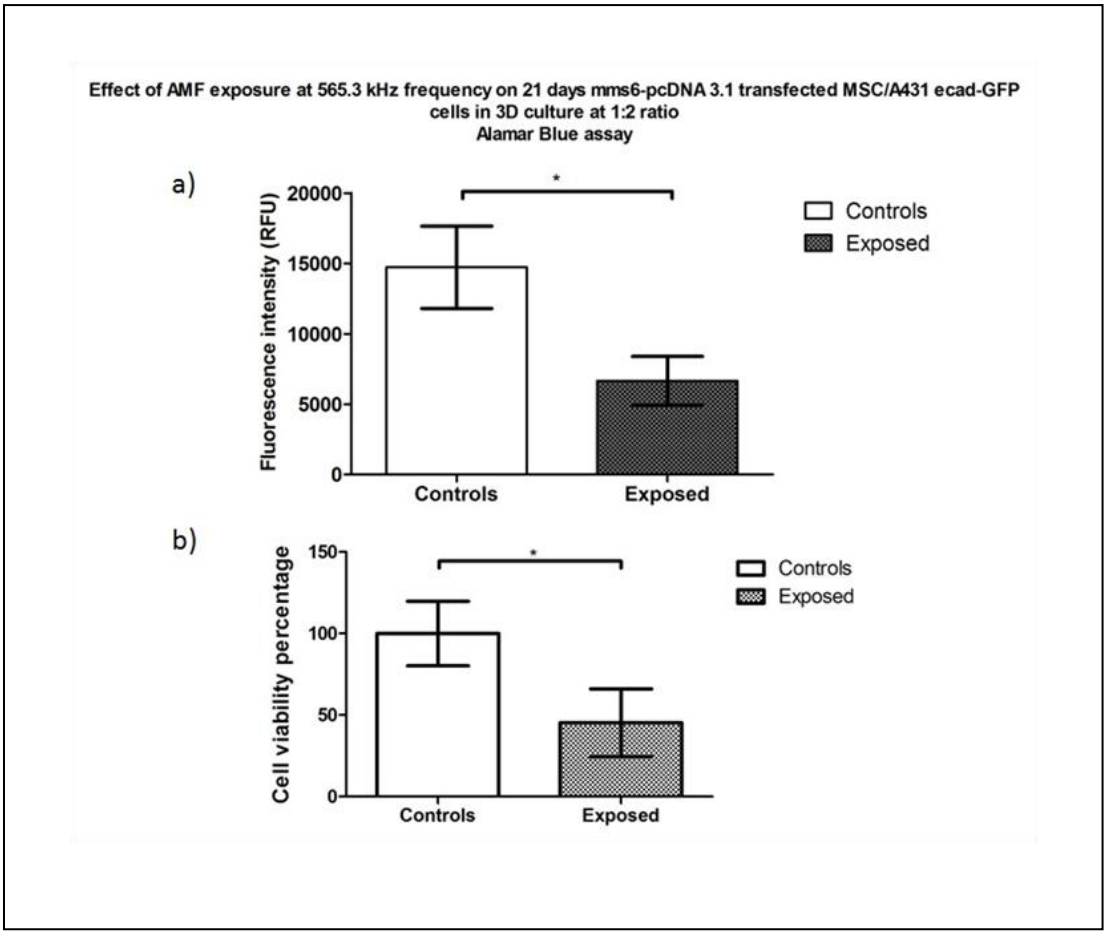

Figure 58. Cell viability evaluation by AlamarBlue Cell Viability Assay.

3D co-cultures of *mms6*-expressing MSCs/A431 ecad-GFP expressing cells, at ratio 1:2, were exposed three times for one hour at 565.3 kHz frequency (grey column) or not exposed (controls, white column).

a) Average of fluorescence intensity of three independent experiments with standard deviation error bar, $p<0.01$. b) Average of cell viability percentage of exposed cells against controls of three independent experiments with standard deviation error bar, $p<0.05$

5.3.7. Fluorescent microscopy on 3D co-cultures of *CellTracker CM-DiI Red* stained *mms6*-expressing MSCs and *CellTracker Green CMFDA Dye* stained MG63 cells at 1:2 ratio.

To support the results obtained by the Trypan Blue Exclusion Assay, the effects of the AMF exposure of 565.3 kHz on 3D cell populations created by co-culturing *mms6*-expressing MSCs and MG63 cells in tubes, at 1:2 ratio, were investigated also by fluorescent microscopy (**Figure 59**). To distinguish the cells in fluorescent microscopy, red MSCs were stained with CellTracker Red CM-DiI Dye and green MG63 cells were stained with CellTracker CM-DiI Green CMFDA Dye, and all the cells nuclei were DAPI stained, as explained in the Materials and Methods section. 3D co-cultures were exposed for one hour at 565.3 kHz frequency three times in two days and compared with not exposed co-cultures (controls).

From the visual inspection of fluorescent microscopy pictures (**Figure 59)** it is possible to notice that the number of AMF exposed cells (**Figure 59, panel c and d**) appear reduced respect to the number of not exposed cells(**Figure 59, panel a and b**). Also, the green cells (cancer cells) appear to be less in AMF exposed cells **(Figure 59, panel c and d)** respect to the not exposed ones (**Figure 59, panel a and b**).

It was also determined:

- The number of the total cells in the exposed tubes compared to the total cells in control tubes (**Figure 60**);
- The ratio of MG63 cells/total cells in the exposed tubes, compared to unexposed controls (**Figure 61**).
- The number of MG63 cells in exposed tubes, compared to the number of MG63 cells in control tubes (**Figure 62**).

Due to the sparse cytoplasmic distribution of red staining, it was difficult to precisely count the MSCs, so for this reason it was preferred to do not include the MSCs counting in the results.

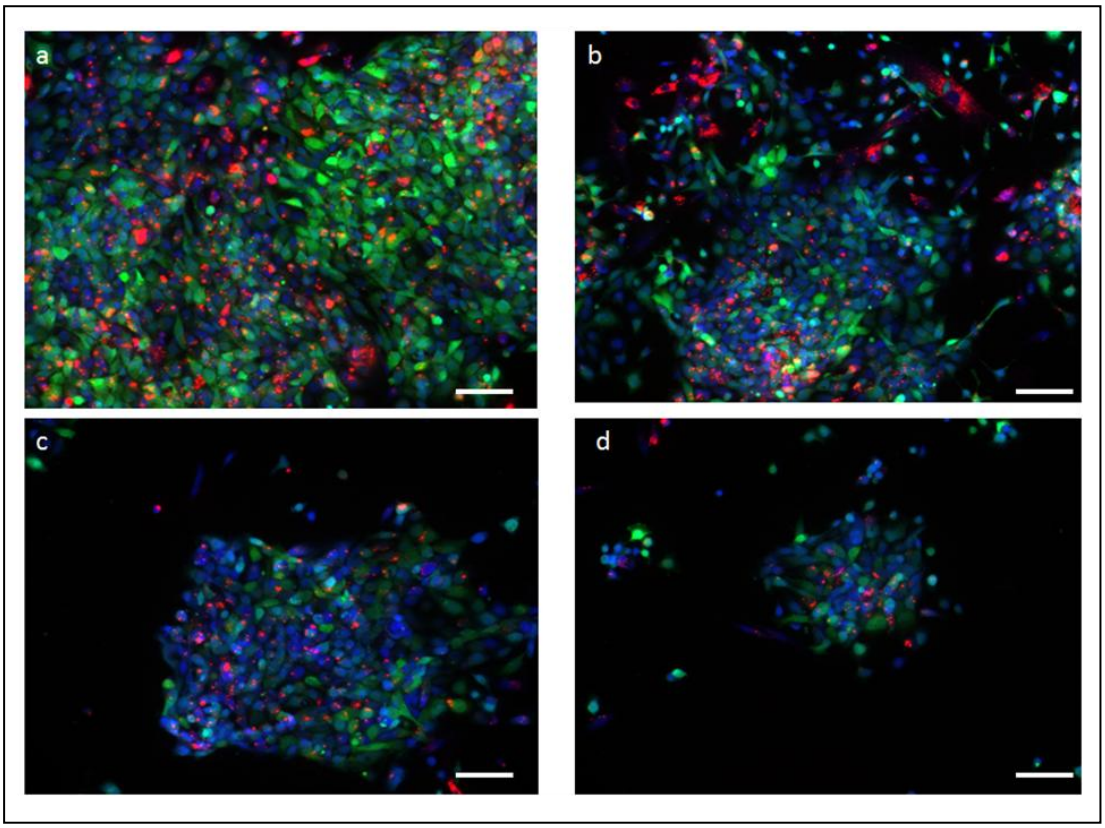

Figure 59. Representative fluorescence pictures of co-cultures of *mms6*-expressing MSCs and MG63 cells.

a, b) cells not exposed to AMF; c, d) cells seeded in Petri dishes following 565.3 kHz exposure of one hour repeated three times. Not exposed cells (a, b) are visually more in number than exposed cells (c, d). Less green cells (cancer cells) are observed in AMF exposed cells (c,d) compared to not exposed cells (a,b).Scale bar=50 µm

The results indicate that:

a) the average of the total nuclei (*mms6*-expressing MSCs + MG63 cells) of the AMF exposed cells is reduced by 60% compared to controls (average of 306±177 total nuclei in the AMF exposed cells against 757± 207 total nuclei counted in controls- **Figure 60**).

b) The ratio of MG63 cells/total cells in the AMF exposed cells is fundamentally unchanged by the treatment (0,58±0.08 in the AMF exposed tubes against 0,60±0.14 in the controls), as indicated in **Figure 61**.

c) The number of MG63 cells counted in the AMF exposed cells is reduced by 63% respect to controls (167± 76 in the AMF exposed tubes against 454± 139 in controls - **Figure 62**).

Results a) and c) are statistically significant ($p<0.05$). The result b) is not statistically significant ($p>0.05$).

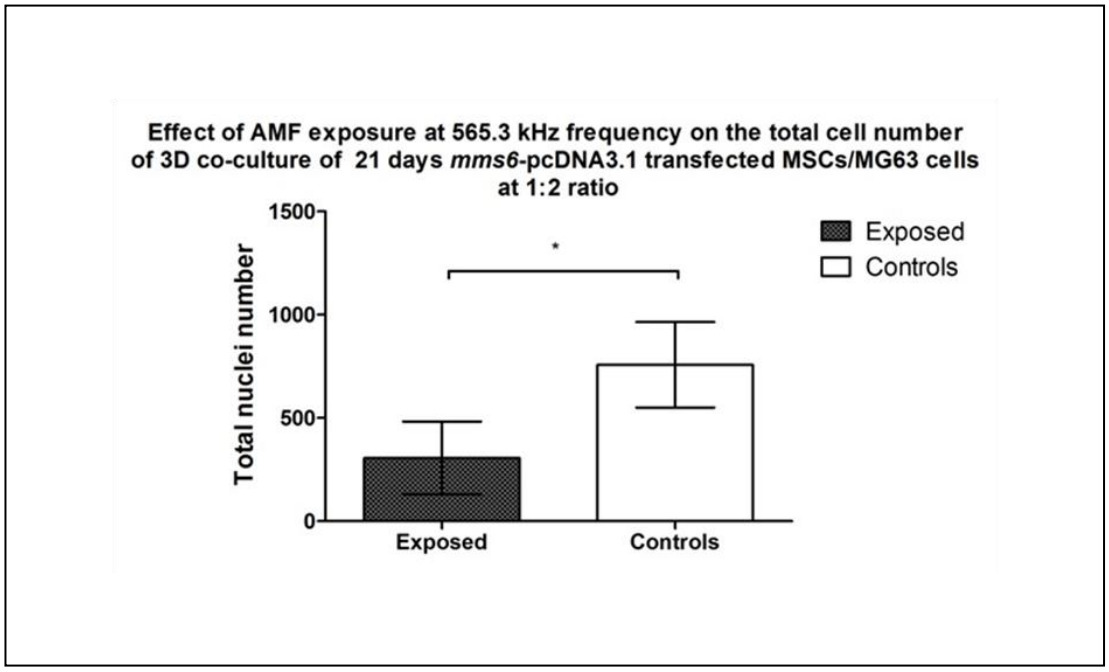

Figure 60. Effect of AMF on the total cell nuclei number.

3D co-cultures of *mms6*-expressing MSCs/MG63 cells at 1:2 ratio were exposed at 565.3 kHz frequency (grey column) or not exposed (controls, white column). Cells were seeded in quadruplicate and experiments were repeated 3 times. Statistical analysis was carried out using Student-t test. Results are shown with standard deviation error bars, $p<0.05$.

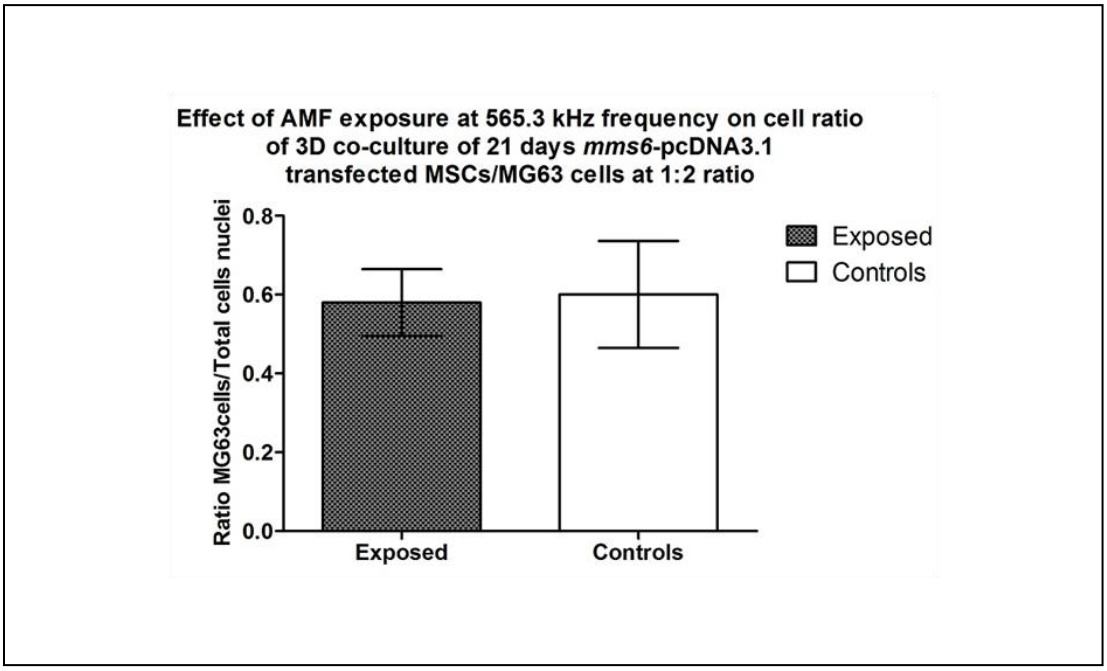

Figure 61. Effect of AMF on the ratio MG63/total cell nuclei.

3D co-cultures of *mms6*-expressing MSCs/MG63 cells at 1:2 ratio were exposed at 565.3 kHz frequency (grey column) or not exposed (controls, white column). Cells were seeded in quadruplicate and experiments were repeated 3 times. Statistical analysis was carried out using Student-t test. Results are shown with standard deviation error bars, $p>0.05$.

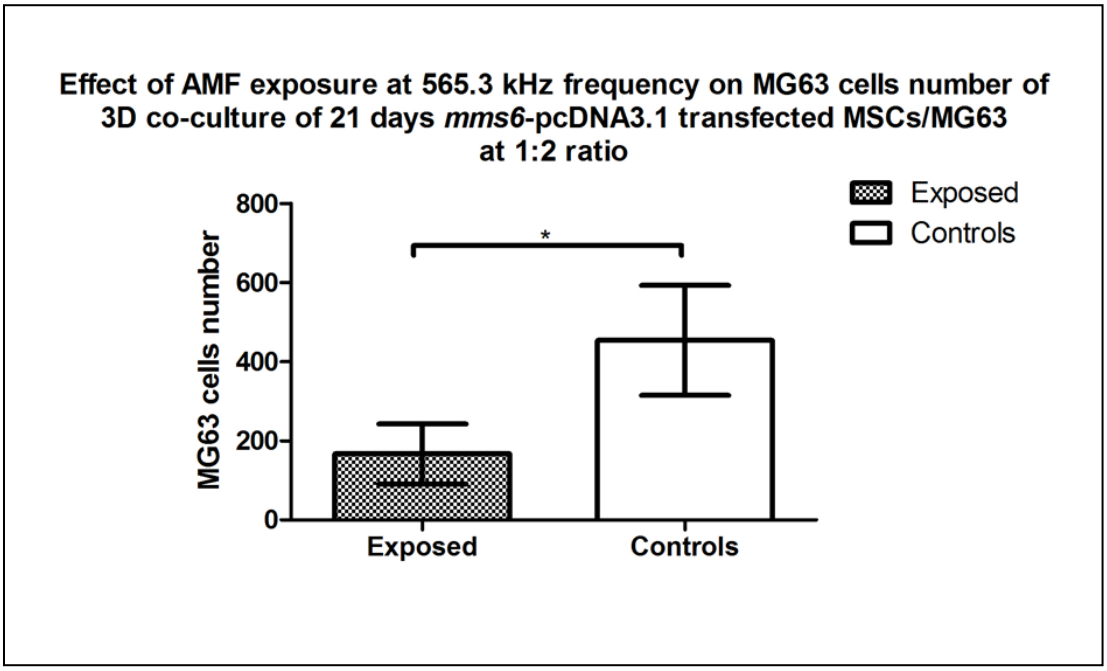

Figure 62. Effect of AMF on MG63 cells number.

3D co-cultures of *mms6*-expressing MSCs/MG63 cells at 1:2 ratio were exposed at 565.3 kHz frequency (grey column) or not exposed (controls, white column). Cells were seeded in quadruplicate and experiments were repeated 3 times. Statistical analysis was carried out using Student-t test. Results are shown with standard deviation error bars, $p<0.05$.

5.4. Discussion

In this chapter, experiments were aimed to evaluate, *in vitro*, the effects of an AMF exposure applied firstly on single layers of *mms6*-expressing MSCs, and then on 3D systems created by *mms6*-expressing MSCs alone or co-cultured with cancer cells (MG63 and A431 ecad-GFP expressing cells respectively).

As declared by Rabin, the nanoparticles retained inside a single cell are not sufficient to create the HT killing effect; however, it could be reached if the nanoparticles are present in an area of at least 1.1 mm diameter, either inside or outside the intracellular environment (Rabin, 2002). It is believed that nanoparticles, singularly or concentrated inside vesicles, deliver heat and cause cell damages, membrane breaking, apoptosis (J. Zhang et al., 2011) and cell necrosis (Asin et al., 2012). The effects of an AMF on MNPs loaded exposed cells have been investigated in previous studies by viability assays and LDH assay, as LDH is an indicator of loss of membrane integrity, of cell necrosis (Chan et al., 2013) and it is extremely sensitive to determine the completely lysed cells (Attar & Haghpanahi, 2016; Quinto et al., 2015; Yan et al., 2014; J. Zhang et al., 2011). In this study, cell viability and cell death were determined by Alamar Blue assay and by Trypan Blue assay, while the loss of cell membrane integrity for single layers of *mms6*-expressing MSCs exposed to AMF was evaluated by LDH assay.

The results of experiments performed on monolayers of *mms6*-expressing MSCs exposed for one hour at 565.3 kHz show that the AMF exposure causes cytotoxicity for the 44.4 ±1.9%, of the cells, while only 5.5±0.8%. of controls show cytotoxicity. Moreover, cell viability in exposed cells is also reduced by one-third (32%), respect to the unexposed controls. The correlation between the loss of viability and the higher LDH values registered for the exposed cells suggests that AMF exposure leads to cell death.

When monolayers of plain MSCs, respectively exposed for one hour at 565.3 kHz and not exposed, were investigated in bright microscopy, no difference was noticed between the two groups, suggesting that AMF exposure does not influence the arrangement of monolayers of plain MSCs. However, when *mms6*-expressing MSCs

were investigated in bright field microscopy after AMF exposure, a weak cell attachment was noticed. The major caveat to interpreting results is that control wild-type MSCs should have been doped with FeQ for 21 days to make them the appropriate control for the *mms6*-expressing cells.

The poor cell attachment in cells exposed to AMF was reported by Quinto et al. and Yan et al. (Quinto et al., 2015; Yan et al., 2014). Quinto et al. observed a reduction in cell attachment in HeLa cells incubated with Doxorubicin (DOX)-loaded SPIOs and exposed to an AMF of 23.77 kA/m, 355 kHz. The cell death percentage registered was higher than 50%. Yan et al. observed an absent or poor cell attachment in hepatocarcinoma cells treated with Fe_2O_3 nanoparticles and irradiated with an AMF frequency of 200 kHz. In this case, they reported a maximum apoptosis very near to the 70% of the whole cell population.

These two studies support the hypothesis that the AMF exposure causes cell detachment and cell death, as observed in this work. However, a caveat is that Quinto et al. used Doxorubicin, which complicated the interpretation and comparison of results.

When the *mms6*-expressing MSCs were exposed twice for one hour at 565.3 kHz frequency in 3D models, the cell death occurred in 41.0 ± 9.5% of the cell population, a percentage very near to the cytotoxicity observed by LDH assay in *mms6*-expressing MSCs arranged in a monolayer and exposed to AMF (44.4 ±1.9%).

When 3D co-culture of *mms6*-expressing MSCs+MG63 cells seeded at 1:2 and 1:4 ratio were exposed at 565.3 kHz frequency for one hour, and the exposure was repeated 3 times in two days, the rate of cell death was, respectively, near to 40% for 1:2 ratio, and near to 44% for the 1:4 ratio. These results indicate that in both the cases, the extent of cell death is greater than that of the percentage of *mms6*-expressing MSCs present in each experiment (respectively 33% for ratio 1:2 and 20% for ratio 1:4), so also MG63 cells adjacent to MSCs were killed by the AMF application.

Fluorescence microscopy analysis of 3D co-cultures of MG63 cells and *mms6*-expressing MSCs supports these results, revealing that the total number of exposed

cells is reduced by the 60% respect to the not exposed ones. Moreover, the ratio between MG63 cells and total cells number is not influenced by the treatment, suggesting that the exposure killed both the cell populations. This result is confirmed by the analysis of the number of MG63 cells alone in exposed and controls 3D co-cultures. The MG63 cells are reduced in number by 60% after the AMF exposure, validating the previous results. The highest number of dead cells observed in fluorescence microscopy, compared with the lower one indicated by *in vitro* assays, could be determined by the stress of the seeding procedure. Indeed, the cells arranged in 3D co-cultures were seeded in the multiwells plates in single layers to make possible the observation at the microscope, so the manipulation of the cells could have influenced their viability.

These results obtained for 3D cell mixing are confirmed by co-culturing the *mms6*-MSCs with A431 ecad-GFP cell at the rate of 1:2, where exposed cell viability is reduced by more than 50% respect to the controls, suggesting again that the AMF treatment also affects cancer cells, in addition to MSCs.

The results of these experiments have been compared to previous studies, which investigated cells loaded with nanoparticles and exposed to AMF of various frequencies. Oh et al. reduce cell viability of more than 70% in breast cancer cells loaded with Doxorubucin (anti-cancer agent) conjugated with $CoFe_2O_4$ nanoparticles, following the application of AMF amplitude of 30 kA/mat at fixed frequency of 307 kHz for 25 min (Y. Oh et al., 2017). De Escalona et al. killed around 50% of cells loaded with magnetic solid lipid nanoparticles made of iron oxide cores and exposed for one hour to a magnetic field with a frequency of 250 kHz and an intensity of 4 kA/m (Munoz de Escalona et al., 2016). Quinto et al. used doxorubicin loaded SPIOs with a phospholipid-polyethylene glycol (PEG) coating, to kill around 64% of cells following AMF treatment (23.77 kA/m, 355 kHz) at a magnetic field for 1 hour (Quinto et al., 2015). Yan et al. irradiated Hepatocarcinoma SMMC-7721 cells with AMF (200 kHz, 4 kW, output current 300 A) for one hour and obtain apoptosis in around 70% of cell population, while inhibiting cell proliferation in more than 80% of population in cells loaded with 8 g/L ferrofluid containing Fe_2O_3 nanoparticles (Yan et al., 2014).

The percentage of dead cells obtained in previous studies is more extensive than the one obtained here, however the above studies used chemical MNPs, while the aim of this study was to create MNPs self-expressing MSCs using an exogenous bacterial gene, and so the results achieved in this research are quite promising, even if they could be improved.

A comparison between the results of this work and the literature findings is shown in Table 13.

Autors	**AMF frequency applied**	**Cells**	**MNPs used**	**Reduction in cell viability**
Oh et al., 2017	307 kHz, 25 minutes	breast cancer cells	Doxorubucin conjugated with $CoFe_2O_4$	70%
De Escalona et al., 2016	250 kHz, 1 hour	human HT29 colon adenocarcinoma cells	iron oxide solid lipid nanoparticles	~50%
Quinto et al., 2015	355 kHz, 1 hour	HeLa cells	doxorubicin SPIOs PEG coated	~64%
Yan et al., 2014	200kHz, 1 hour	Hepatocarcinoma SMMC-7721 cells	ferrofluid Fe_2O_3 nanoparticles	80% cell proliferation inhibition
My Study	565.3 kHz, one hour	monolayers of *mms6*-expressing MSCs	None	32%
	565.3 kHz, one hour, exposed twice	3D models of *mms6*-expressing MSCs	None	~40%
	565.3 kHz for one hour, repeated 3 times in two days	3D co-culture of *mms6*-expressing MSCs+MG63 cells at 1:2 ratio	None	~ 40%
		3D co-culture of *mms6*-expressing MSCs+MG63 cells at 1:4 ratio	None	~ 44%
		3D co-culture of *mms6*-expressing MSCs+A431 ecad-GFP cells at 1:2 ratio	None	>50%

Table 13. Comparison between the results of this study and the literature findings.

Literature findings report a percentage of dead cells respect to the whole population higher than the one obtained in this study. However, the cited studies used chemical MNPs, while in this scientific work were used MSCs able to *de novo* synthesise MNPs, using the *mms6* bacterial gene. For this reason, the percentage of dead cells achieved in this research is quite promising, even if it could be ameliorated.

6. *In vivo* application of an AMF of 565.3 kHz on mice bearing tumours injected with *mms6* expressing- MSCs

6.1. Introduction

After having investigated the effects of 565.3 kHz AMF applications *in vitro*, respectively on both single layer/3D cultures of 21 days *mms6*-expressing MSCs and on mixed populations of the former cells co-cultured with MG63 and A431 Ecad-GFP cells, it was determined if the AMF application to tumours loaded with 21 days *mms6*-expressing MSCs causes tumour necrosis. To distinguish the 21 days *mms6*-expressing MSCs population from the tumour cells, MSCs were labelled with red *CellTracker CM-DiI Dye* reagent, and named for simplicity "red *mms6*-expressing MSCs". To ascertain if tumours loaded with red *mms6*-expressing MSCs undergo necrosis after AMF application, it was chosen to work on CD-1 nude mice implanted subcutaneously bilaterally with A431 Ecad-GFP cells. Red *mms6*-expressing MSCs were intracardiac injected into mice seven days after being injected with cancer cells. The experiment was then carried on following the modality explained in the Materials and Methods section.

6.2. Aims

The aims of the experiment were:

1. to determine the distribution within major organs (spleen, liver and lungs) of red *mms6*-expressing MSCs following intracardiac injection and establish whether red *mms6*-expressing MSCs reach sites of tumour growth *in vivo*.

2. to provide proof of principle that the application of an AMF to tumours loaded with red *mms6*-expressing MSCs causes tumour cell death.

The presence and distribution of red *mms6*-expressing MSCs in the mice body was assessed by RT-PCR, Prussian Blue and fluorescence microscopy.
The effects of the exposure on the tumours were evaluated by measuring the tumour size and volume. Tumour tissue was retrieved following sacrifice of the mice for assessment of red *mms6*-expressing MSCs, tumour cells death and non-tumour tissue response.

Red *mms6*-expressing MSCs infiltration was investigated by Multiphoton microscopy imaging. The effect of AMF on tumour viability was investigated by the uptake of the cell *Fixable Viability Dye eFluor 450* followed by Multiphoton microscopy imaging, by activated caspase 3 expression and by H/E stained sections histomorphology. Non-tumour tissue response was determined by activated caspase 3 expression and by H/E stained sections histomorphology of adjacent non-tumor tissues.

6.3. Results

6.3.1. Application of an AMF of 565.3 kHz for 30 minutes to mice bearing xenografts following intracardiac injection of red *mms6*-expressing MSCs is not dangerous for mice.

AMF studies were carried out on four experimental groups of CD-1 nude mice implanted subcutaneously bilaterally with A431 ecad-GFP expressing squamous carcinoma cells seven days previously. Each group consisted of 4 mice, treated as follow:

Group A - A431 Ecad-GFP cells s/c + Anaesthesia Only

Group B - A431 Ecad-GFP cells s/c + magneTherm treatment, 565.3kHz Daily, x 3 days

Group C - A431 Ecad-GFP cells s/c + red *mms6*-expressing MSCs + Anaesthesia Only

Group D - A431 Ecad-GFP cells s/c + red *mms6*-expressing MSCs + magneTherm treatment, 565.3kHz Daily, x 3 days

Experimental details are explained in the Materials and Methods section 2.8. Mice were anaesthetized during all the duration of the treatment. Mice skin temperature was monitored by infrared thermometer gun while mice core body temperature was monitored by rectal thermometer each minute (**Figure 64**). The mice tolerated the treatment well, and there was no increase in temperature on the skin surface or core body temperature of mice exposed to the AMF **(Figure 65**).

A schematic time-line of the experimental steps is shown in **Figure 63**.

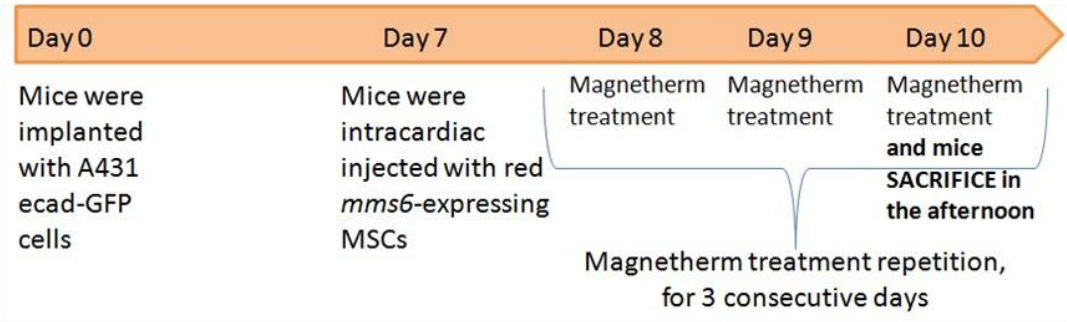

Figure 63. A schematic time-line of all the experimental steps.

Mice were implanted with A431 ecad-GFP cells (day 0), and seven days later were intracardiac injected with red *mms6*-expressing MSCs (day 7). Then, the day after the MSCs injection (day 8), mice were exposed to the Magnetherm treatment, 30 minutes at day, for three consecutive days. The last day of treatment (day 10), mice were sacrificed in the afternoon.

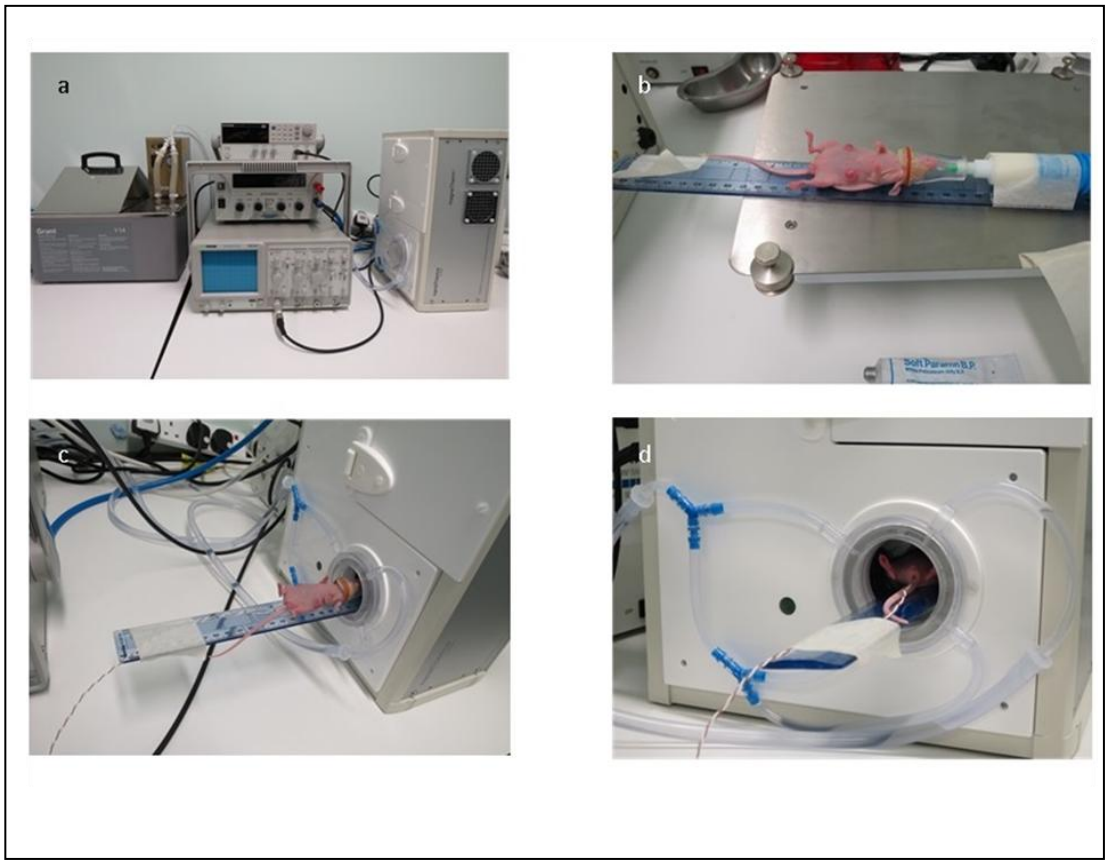

Figure 64. Mice exposed to magneTherm AMF.

a) magneTherm setup, with magneTherm system turned in an upright position, to fit the mouse inside the device. b) Mouse on the ruler, with the anaesthesia mask on. c) The mouse is inserted into the MagneTherm system. d) Particular of the mouse inside the MagneTherm device with the rectal thermocouple to monitor mouse's core body temperature.

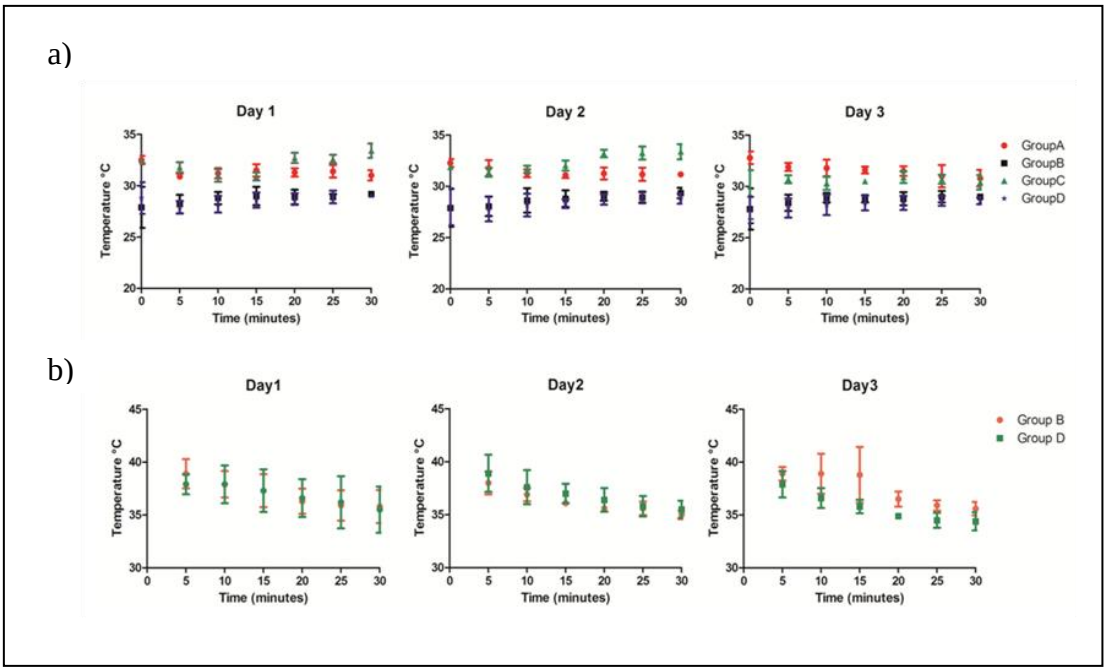

Figure 65. Mice skin and core body temperature measurements.

Mice were exposed (Group B and Group D) or not exposed (Group A and Group C) to an AMF of 565.3 kHz for 30 minutes.

a) Mouse skin temperature, monitored by infrared thermometer gun for all the groups;

b) Mouse core body temperature, monitored by rectal thermometer in the exposed mice. All the values are shown as mean± SD.

6.3.2. Red *mms6*-expressing MSCs home to sites of tumour growth following intracardiac injection

To determine if red *mms6*-expressing MSCs could reach the site of tumour growth and their distribution within major organs (spleen, liver and lungs) when intracardiac injected into CD-1 nude mice, the distribution of the cells was assessed by Prussian Blue staining, fluorescence microscopy, RT-PCR and immunohistochemistry.

As red *mms6*-expressing MSCs were engineered to produce and bear iron nanoparticles, Prussian Blue staining was used to detect the presence of iron in all the tissue investigated (liver, lungs, spleen and tumour xenografts) of mice injected with red *mms6*-expressing MSCs (**Figure 66** and **Figure 67**). Iron, stained in blue, was detected in tumours and in all the mice organs.

However, as iron could be naturally present in tissues, fluorescent microscopy was used to confirm the presence of red *mms6*-expressing MSCs in the tumour xenografts and in lungs, liver and spleen, although quantification was difficult due to the relative weakness of the *CM-DiI Dye* reagent labelling and to the auto fluorescence of the tissue (**Figure 68**). Red *mms6*-expressing MSCs were detected in all the organs and in the tumour xenografts (indicated by white circles), where A431 Ecad-GFP cells were identified by green fluorescence, as they expressed GFP. The expression of *mms6* gene in the tumour xenografts and in lungs, liver and spleen was also confirmed by RT-PCR using primers for the *mms6* gene expression (**Figure 69**), revealing the presence of the gene in all the tissues investigated.

As red *mms6*-expressing MSCs origin is human, the presence of these cells in mice organs was also confirmed by immunohistochemistry, using Anti-human Nuclei Antibody Clone 3E1.3 (**Figure 70**). This experiment was not performed on tumours due to the limited quantity of the material at disposition. Positive control for Antibody Clone 3E1.3 staining is shown in **appendix 8.14**.

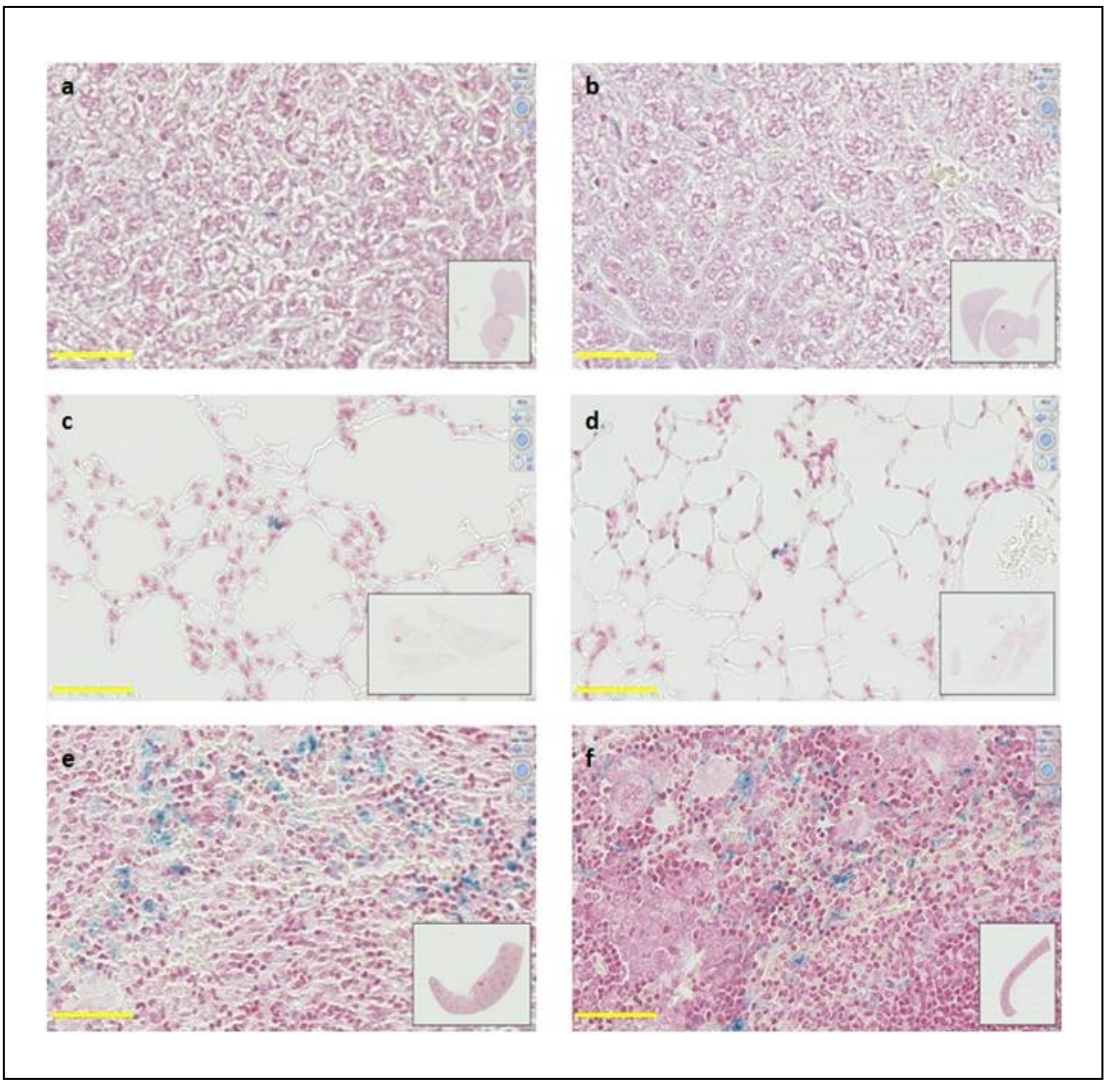

Figure 66. Representative picture of Prussian Blue on Group C and Group D.

a), c) e): liver, lung and spleen of group C (injected with red *mms6*-MSCs and not exposed to AMF). b), d), f): liver, lung and spleen of Group D (injected with red *mms6*-MSCs and exposed to AMF). Inset, lower magnification of organs. Scale bar = 50 µm.

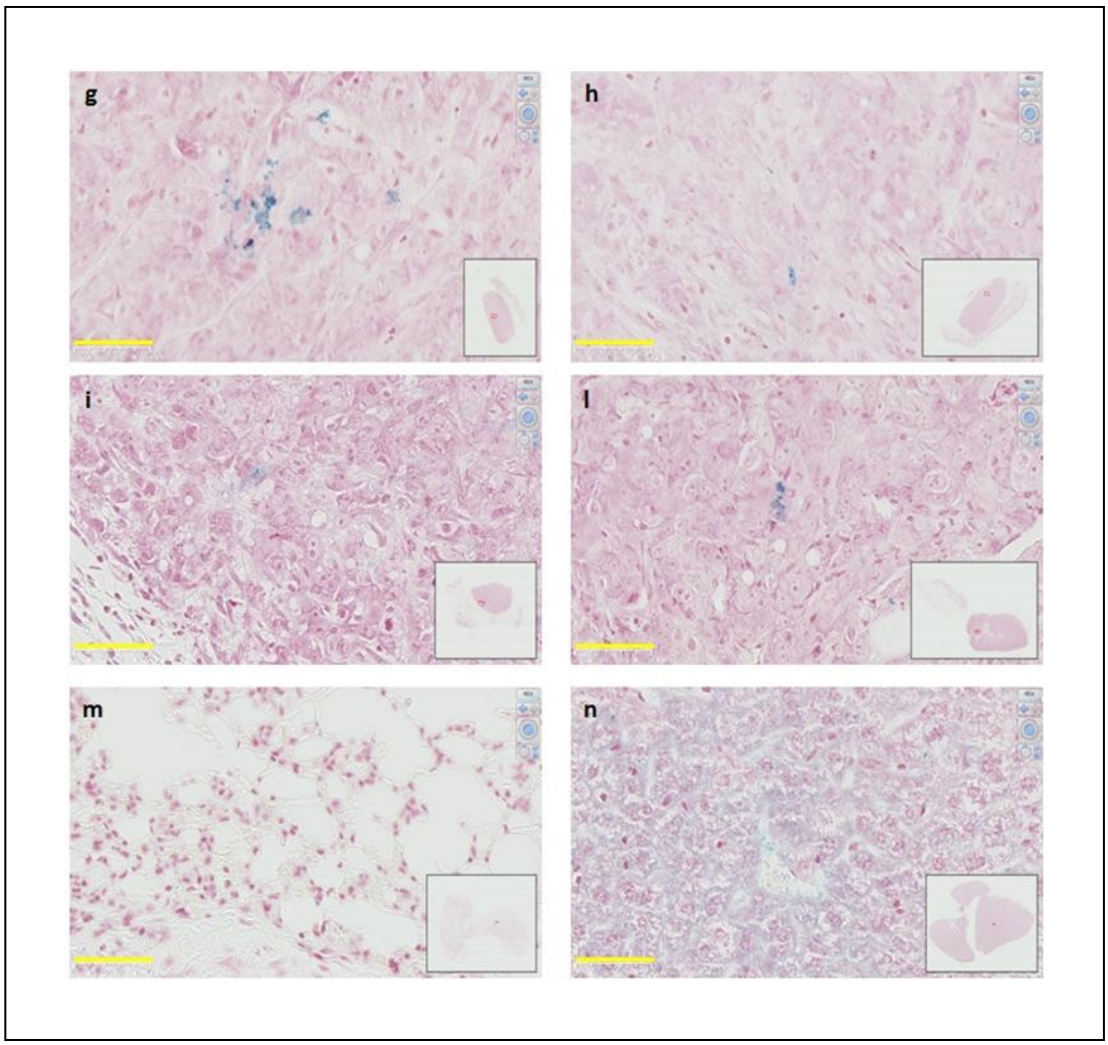

Figure 67. Representative picture of Prussian Blue staining on Group C and Group D.

g), i): tumour right and tumour left of group C (injected with red *mms6*-MSCs and not exposed to AMF). h), l): tumour right and tumour left of group D (injected with red *mms6*-MSCs and exposed to AMF). m): negative control (lung of mouse not injected with MSC; n) positive control (liver which is naturally rich of ferritin and so it is stained with Prussian Blue). Inset, lower magnification of organs. Scale bar= 50 μm.

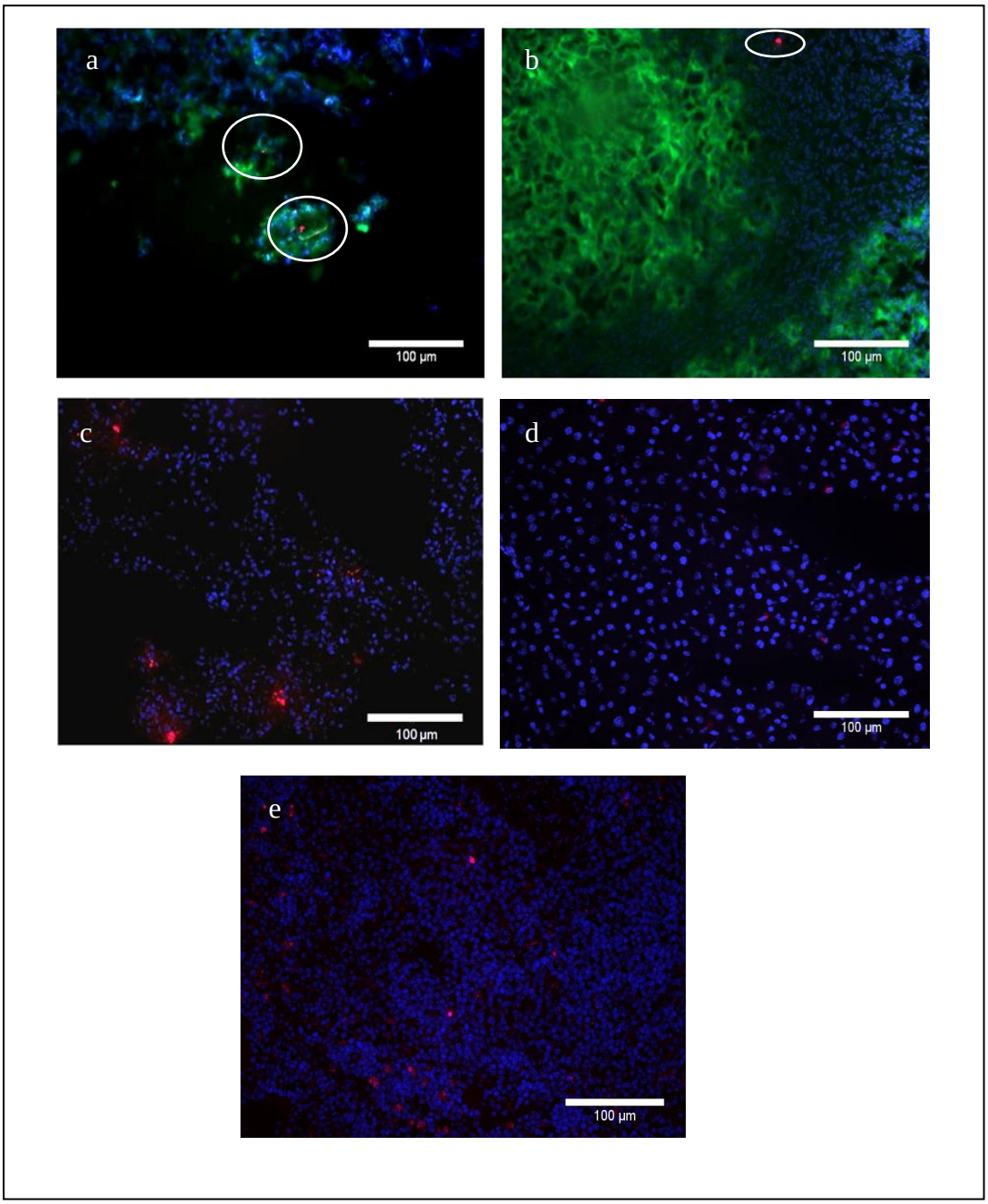

Figure 68. Representative pictures of frozen mice tissues sections imaged at fluorescence microscope in mice injected with red *mms6*-expressing MSCs.

Cancer cells are green, as they express GFP, while cell nuclei were DAPI stained and so are blue. White circles indicate red *mms6*-MSCs. a) Tumour left; b) Tumour right; c) lung; d) liver; e) spleen. Magnification 200x, scale bar 100 µm.

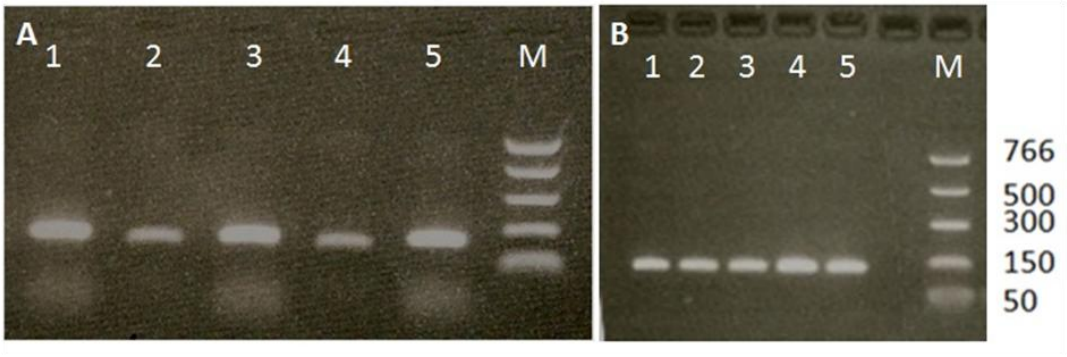

Figure 69. Representative picture of *mms6* expression in mice organs and tumours.

A) *mms6* expression in: lung (lane1), tumour right (lane2), spleen (lane3), tumour left (lane4), liver (lane5). B) eEF2 (mouse housekeeping gene) expression in the same organs with the same order used in gel A. M= NEB marker with bp indicated.

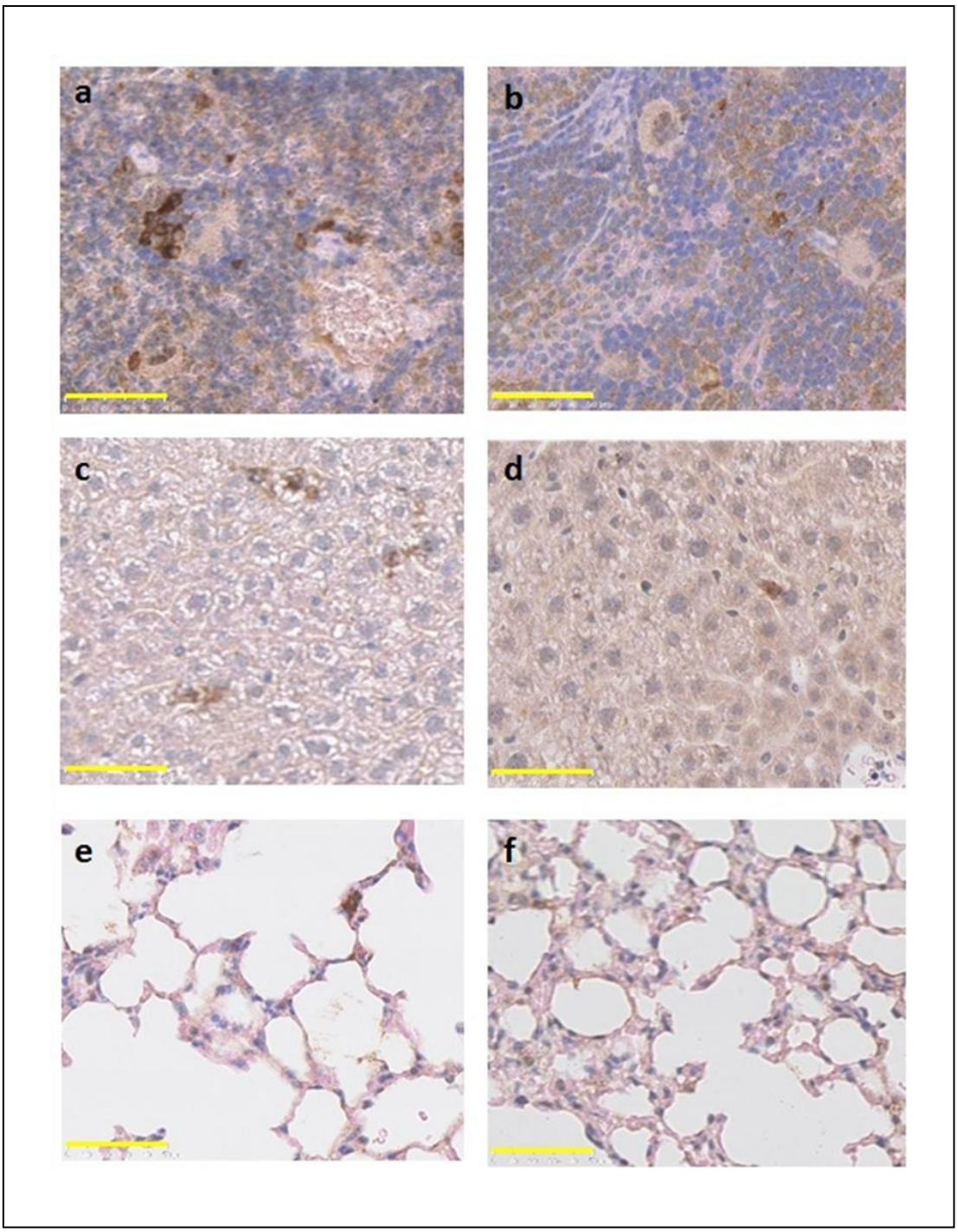

Figure 70. Representation of Anti-human Nuclei Antibody Clone 3E1.3 staining in mice major organs.

a) spleen of Group C; b) spleen of Group D; c) liver of Group C; d) liver of Group D; e) lung of Group C; f) lung of Group D. Scale bar= 50µm.

6.3.3. Tumour size and volume do not reduce after the application of an AMF of 565.3 kHz to mice bearing xenografts following intracardiac injection of 21 days red *mms6*-expressing MSCs.

Tumour size and volumes were measured for each group at different time points: 6 days before the AMF/sham treatment (-6), 2 days before the AMF/sham treatment (-2), and after 2 days from the AMF/sham treatment (2).

Due to the busy schedule of the animal house technical staff, the mice groups have not been implanted with cancer cells all at the same time, but Group A and Group B were implanted a week after than Group C and Group D. This could explain the discrepancy between the starting size of tumours, as shown in **Figure 71**, where Group A and Group B have a starting tumour volume that is bigger than Group C and Group D, despite the number of the injected cancer cells was supposed to be the same ($1x10^6$ per implant).

Tumours volume measurements reveal that there is no difference between Group C (injected with red *mms6*-expressing MSCs but not exposed to AMF) and Group D (injected with red *mms6*-expressing MSCs and exposed to AMF) mice either before or after application of AMF ($p>0.05$), (**Figure 71a**). Statistical differences were found at day 2 between Group A and Group C and Group D respectively ($p<0.05$), and between Group B and Group C and Group D respectively ($p<0.001$).Tumour growth was not measured at day 0 for all the tumours, and so it was chosen to represent it in the graph with the value "1" (**Figure 71b**). Although the growth rate of tumours in Group D mice appeared to be decreased in comparison to those of Group A and B (without red *mms6*-expressing MSCs injection) this is not statistically significant (**Figure 71b**) ($p>0.05$).

Tumour tissue was immediately collected after sacrifice of the mice for assessment of (1) red *mms6*-expressing MSCs, (2) tumour cell death and (3) non-tumour tissue response:

1. red *mms6*-expressing MSCs infiltration into the tumour environment was confirmed by Multiphoton microscopy in control group (Group C, unexposed) and compared to that of the AMF exposed group (Group D), (**Figure 72**). There was wide variation in the number of red *mms6*-expressing MSCs per unit area in the tumours of the exposed and unexposed group (mean 51 range 7-95 vs mean 46, range 14-73 respectively); this was not statistically significant ($p>0.05$).

2. The *effect* of AMF on tumour viability was assessed by the uptake of the *Fixable Viability Dye eFluor 450* followed by Multiphoton microscopy, by haematoxylin and eosin (H/E) staining and by activated Capsase-3 staining.

   The results obtained using *Fixable Viability Dye eFluor 450* reagent visually indicated a cell death of around 50% (**appendix 8.15**) which however does not coincide with the visual assessment of haematoxylin and eosin (H/E) stained sections of the exposed tumour which showed much less in the way of tumour cell death/necrosis (**Figure 73**). Very limited necrotic regions were detected. Indeed, the degree of tumour necrosis in the AMF exposed mice (Group D) group was considerably less than that expected to be of clinical significance for standard chemo/radiotherapy (> 90% tumour necrosis).

   To determine whether AMF caused cell tumour apoptosis, tumours were subjected to immunohistochemistry for Caspase-3 expression. Caspase-3 is a protein which plays a critical role in apoptosis, responsible for the cleavage of other important proteins. The antibody has a cytoplasmic and perinuclear localisation in apoptotic cells (**Figure 74**). Results indicate a wide variation of Capsase-3 stained cells in the tumours of the groups and no statistical difference between groups was found (percentage of caspase 3 activated stained nuclei is 16.7 ±11.8 for Group A, 12.8 ±9.4 for Group B, 7.2 ± 3.7 Group C, 10.1 ± 5.9 Group D, $p>0.05$; data not shown).

3. Histological assessment of adjacent non-tumour tissue showed no histopathological abnormality. The tissue investigated appeared healthy and

activated Caspase-3 was not detected (**Figure 75**). Positive control for Caspase-3 staining is shown in **appendix 8.14**.

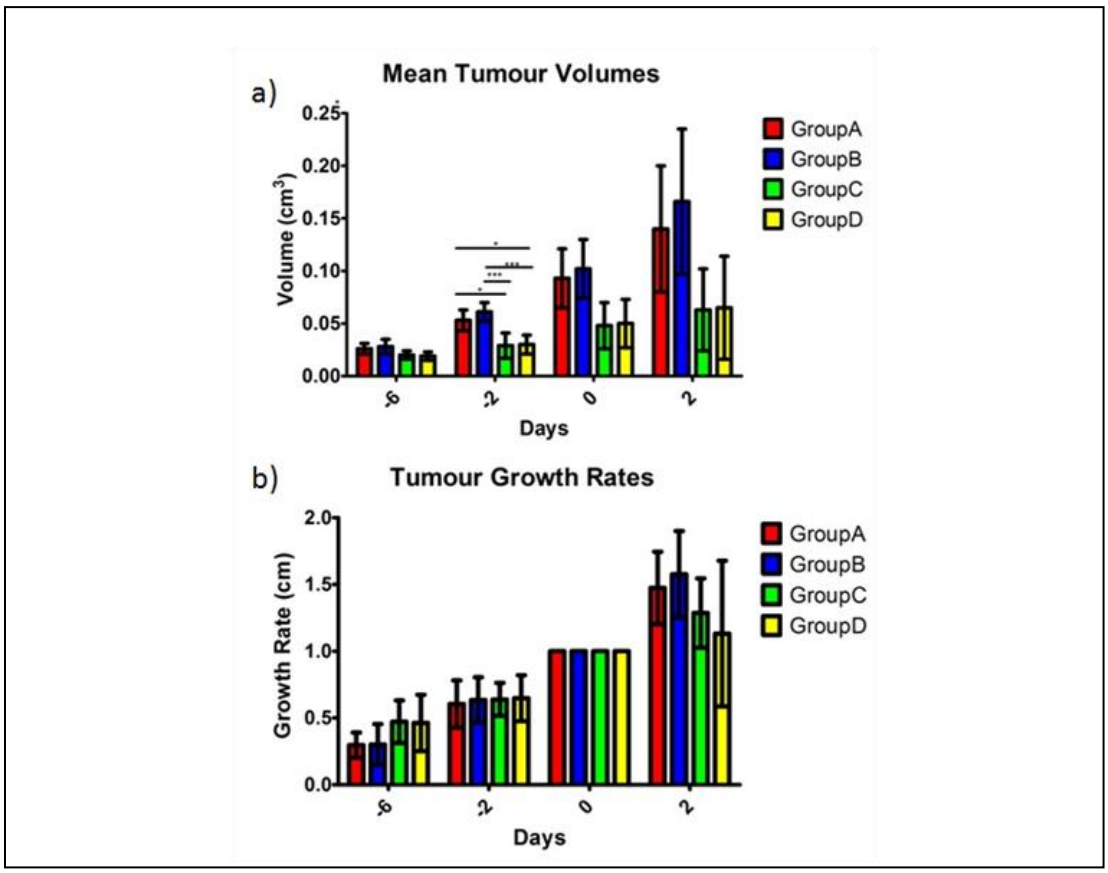

Figure 71. Tumours volume and growth measurements.

Tumours volumes (panel a) and tumours growth (panel b) of Groups A, B, C, D. Results are shown as mean± SD. Statistically significant results are indicated by asterisks.

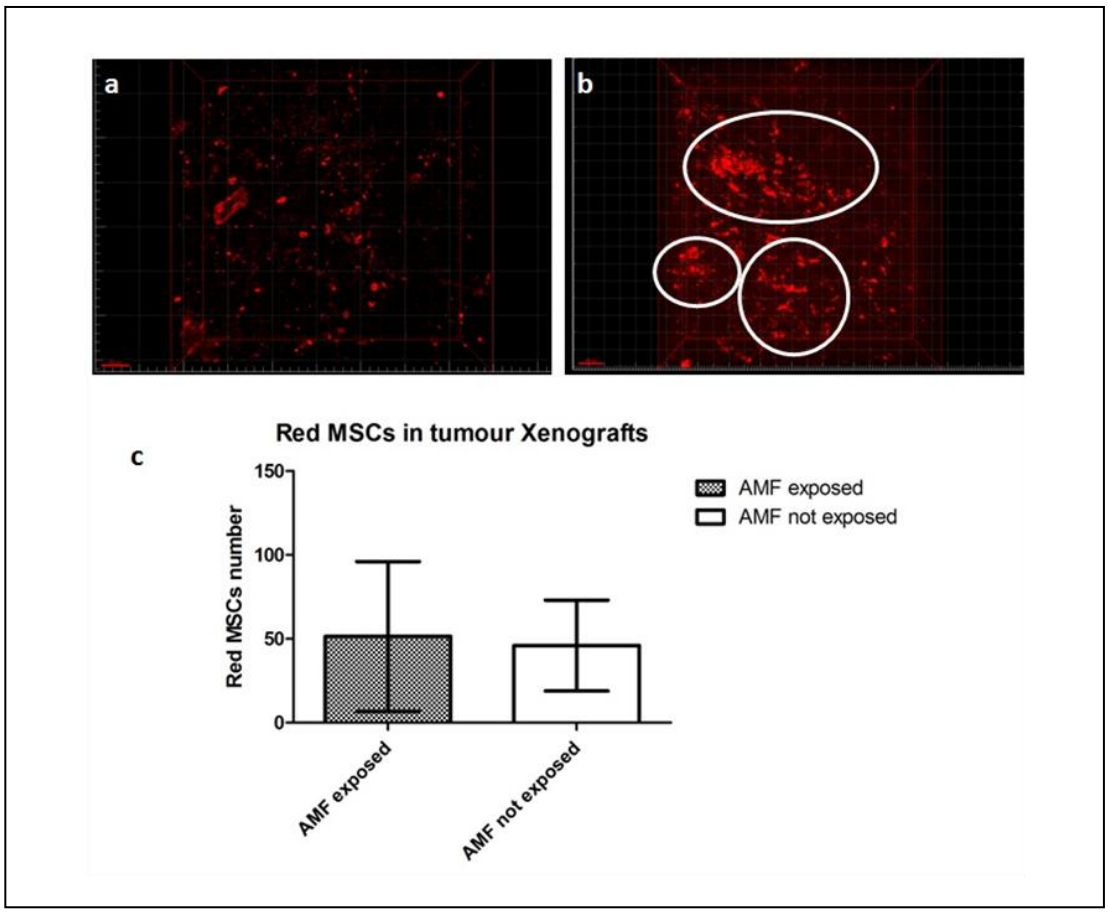

Figure 72. *mms6*-expressing MSCs tumour homing investigation by Multiphoton z-stack.

a-b) Representation of Multiphoton z-stack pictures showing red *mms6*-expressing MSCs in the tumour site. a) not exposed mouse (Group C). b) exposed mouse (Group D). White circles indicate regions where the red stain was more concentrated. Red scale bar=50 μm.

c) red *mms6*-expressing MSCs average number in the tumour xenografts of exposed and not exposed mice. Results are shown as mean± SD.

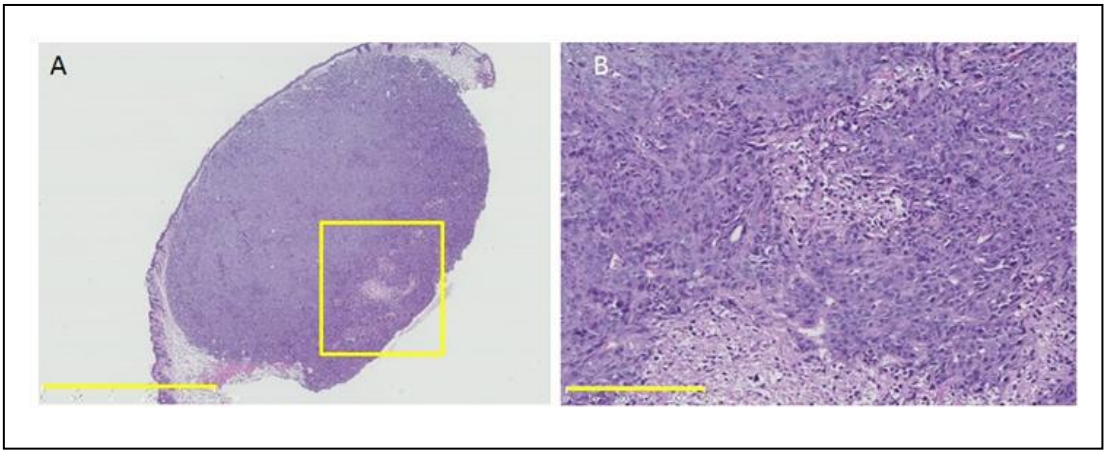

Figure 73. Representation of H/E stained sections of an AMF exposed tumour.

The exposed tumour shows limited cell necrosis (yellow square). A) 1.25 x magnification, scale bar= 2.5 mm; B) Particular of the area of necrosis, 10x magnification, scale bar=250 µm.

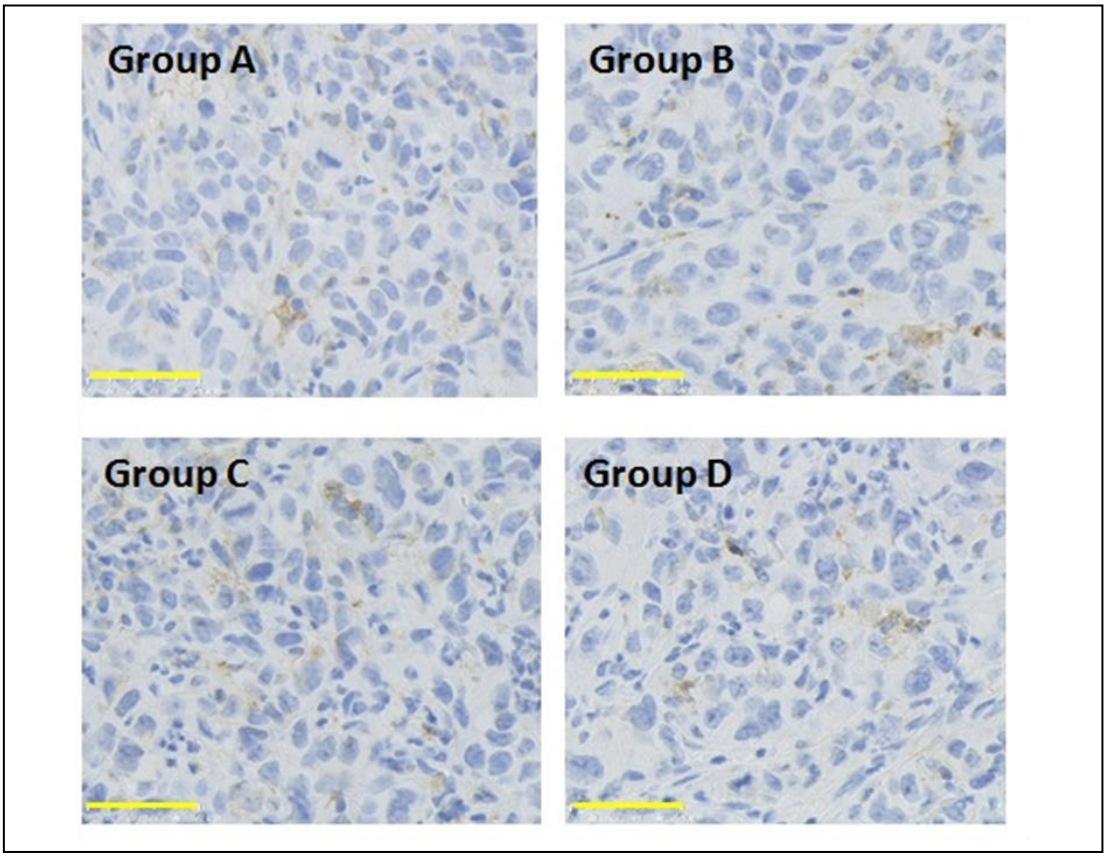

Figure 74. Representative picture of Caspase 3 activated staining for all the groups investigated.

Capsase-3 antibody stains the apoptotic cells in brown, localising in the cytoplasm and in the perinuclear region of the cells. No statistical differences were observed between the number of apoptotic cells in the four groups.Scale bar=50µm.

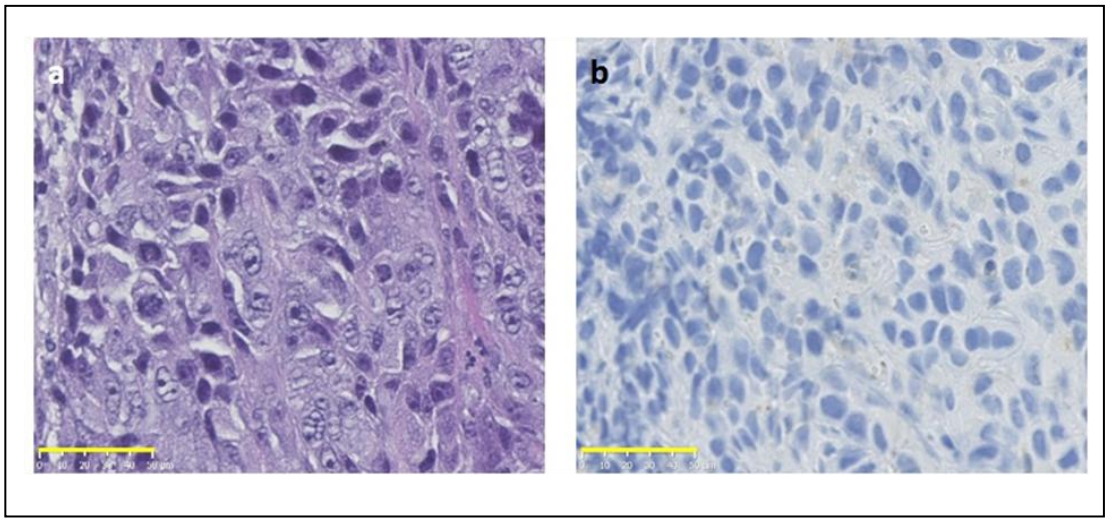

Figure 75. Representative picture of a) H/E staining and b) activated Caspase 3 staining of adjacent non-tumour tissue.

Scale bar=50µm

6.4. Discussion

In this chapter it was investigated if :

- red *mms6*-expressing MSCs injected intracardiac in mice reach the site of tumour growth and if they are distributed in other major organs such as spleen, liver and lungs.
- red *mms6*-expressing MSCs in the tumour growth site could induce tumour cells death when the tumour is exposed to AMF of a frequency of 565.3 kHz, 30 minutes a day for three consecutive days.

MSCs have tumour-targeting properties, both in mouse (Khakoo et al., 2006; R. F. Pereira et al., 1998) than in human (Le Blanc et al., 2004; Koc et al., 2000). In this study Prussian Blue, RT-PCR, fluorescence microscopy and Multiphoton microscopy imaging could suggest the presence of MSCs in mice tumours, however, there is no evidence of homing or targeting of the MSCs to the tumour, as the accumulation of MSCs in the tumours may be due to the leaky vasculature of the tumour.

RT-PCR of Group A and B tissue was not included in the study design, but it would have been a good negative control.

Besides, it was observed the MSCs tendency to randomly accumulate in spleen, liver and lungs. The non-specific migration of MSCs to other organs than tumours was already reported in previous studies, where MSCs cells were shown to localise to the lung (Pereira et al., 1998; Devine et al., 2003; Kucerova et al., 2007; Fischer et al., 2009), spleen (R. F. Pereira et al., 1998), liver (Devine et al., 2003; Gao et al., 2001), or in all of them (Duan et al., 2009; Allers et al., 2004; Chin et al., 2003; Detante et al., 2009; Kraitchman et al., 2005). The MSCs clearance from organs was studied by Studeny et al., who investigated the route of cell delivery of bone marrow-derived MSCs injected into the tail vein of nude mice bearing human A375SM melanoma cells growing in the lungs (Studeny et al., 2002). In his study, Studeny et al. showed that MSCs localise in lung parenchyma and tumour nodules one day after their

intravenous administration, to clear from lung after eight days from the injection, concluding that it is the tumour microenvironment and not the lungs to provide the right conditions for the survival and proliferation of MSCs cells. In my study, *due to a strict time schedule*, the MSCs localisation in organs was monitored only until the fourth day, making impossible to determine if the accumulation of MSCs in lungs stops after eight days. Moreover, it is worth to observe that the mice selected for the study are immune suppressed, which makes easier for MSCs to reach the organs without an active immune system (Eggenhofer et al., 2012).

Next, it was examined if red *mms6*-expressing MSCs localised in the tumour site can kill cancer cells following AMF exposure. Tumours size and volume measurements showed no difference between the control and the AMF exposed group. Although this is not relevant for the experiment, it should be notice that group A and B tumours volume appears bigger than volume of groups C and D, due to the fact that mice of the two couples of groups were injected with cancer cells at two separate times, determining the observed variation among the couples of groups. Indeed, it is possible that the cells injected in Group A and Group B -injected one week later than Group C and Group D-were more in number than the ones injected in GroupC and GroupD, due to human error in cell counting/cell injection or simply due to the experimental variability. This could explain why the differences between averages of the tumour volumes between Group A and Group C and Group D respectively and between the Group B and Group C and Group D respectively were found statistically significant.

However, this discrepancy did not affect the overall outcome of the experiment, which showed no effect of AMF on tumour growth and volume. There is a number of possible reasons for the lack of tumour growth/reduction in AMF exposed mice, as:

- the mice sacrifice occurred the same day of the last exposure, making it difficult to fully evaluate if any effect was really produced from AMF exposure on tumours.

- the number of the injected red *mms6*-expressing MSCs able to reach the tumour site was too low to really lead to an appreciable necrosis effect when tumours were exposed to AMF.
- the *mms6* gene is too low expressed in MSCs to determine enough Mms6 protein to create MNPs able to create an appreciable effect when reacting to AMF.

In tumour, cancer cells death investigated by *Fixable Viability Dye eFluor 450* revealed an high percentage of dead cells (near to 50%), in disagreement with the visual assessment of H/E stained sections. This discrepancy could be explained by the Multiphoton instrument high sensitivity for fluorescence (Schuh et al., 2016) and by the difficulty to completely separate the blue wavelength emission of dead cells from the green fluorescence background given by the tissue, due to the GFP expressed by cancer cells. These interferences have probably lead to a higher estimation of the dead cells number than the one that actually was. Multiphoton excitation microscopy had also been employed to investigate the effect of the AMF on MSCs. This technique was used to see if AMF is able, *in vivo*, to effectively excite the magnetic nanoparticles produced inside the MSCs by *mms6* gene, causing the destruction of MSCs. The pictures analysed by Multiphoton instrument software showed red fluorescence, indicating that some MSCs could still be viable after the AMF treatment or, more likely, that the AMF exposure determined the death of MSCs, causing the rupture of cell membrane and the consequent leakage of the red dye. In this scenario, the red florescence would identify cellular debris and not living cells. Due to an unequal distribution of the red dye in the cell cytoplasm, it is challenging to determine if the MSCs are still viable or not. It is interesting to notice that the red fluorescence was more concentrated in some areas of the tumour tissue, suggesting the hypothesis that MSCs could be able to reach the tumours possibly because of their leaky vasculature, creating niches of cells in the tumour site (**Figure 72B**). Although there are conflicting findings about the real effect of MSCs on tumour growth (Rhee et al., 2015), where some study support the thesis that MSCs could enhance the tumours growth (G. C. Li et al., 2016; Momin et al., 2010), while other suggest a tumour growth inhibitory effect (Beckermann et al., 2008), one hypothesis that could be done is that the presence of niches of MSCs in tumour site

could act as tumour suppressor, with the MSCs occupying the place of cancer cells. More studies are necessary to assess the effect of AMF on MSCs and to entirely understand its consequences in terms of membrane rupture and cell death.

7. General Discussion and Future Perspectives

In MHT, stem cells are considered promising candidates for MNPs delivery, due to their tumour homing capability, they ability to mediate immunosuppression upon transplantation, and their anti-inflammatory properties (Durinikova et al., 2014). However, stem cells display a limited phagocytosis, which proves challenging to load this type of cells with external magnetic nanoparticles (Kim et al., 2010). In addition to that, the so far used MNPs are often chemicals, their uptake in MSCs population is not homogenous and they are diluted with cell divisions. All these issues represent challenges that need to be overcome to exploit MSCs potential in MHT. The goal of this research was to create MSCs able to self-express MNPs by genetically modifying them with MTB genes *mms6* and *mmsF*, alone or in combination.

- In Chapter 3 and Chapter 4 it was demonstrated that *mms6* and *mmsF* genes could be expressed both in MG63 cell line and in MSCs, and the magnetism of the cells was proven by different physical techniques. It was also established that gene *mms6* confers the higher magnetisation to MSCs in comparison to *mmsF* alone and to *mms6+mmsF* genes together. A better understanding of the response of the electron-dense structures created inside the transfected cells to AMF could have been obtained by using a positive control for the SQUID and the HT experiments, for example by loading the cells with synthetic MNPs, such as SPIONS.

Quantification of the amount of iron in cells could have been determined by mass spectrometry, an analytical technique that measures the mass of different molecules within a sample. It works by ionizing the chemical species and sorting the ions based on their mass-to-charge ratio; the mass spectrum indicates the masses within a sample (Glish & Vachet, 2003). In literature, mass spectrometry has been widely used to quantify the SPIONS amount in cells (Nold et al., 2017; Shi et al., 2009; White et al., 2015).

- In Chapter 4 it was also assessed that the expression of *mms6* gene inside MSCs does not change cell stemness, proliferation and capability to differentiate into the osteogenic, chondrogenic and adipogenic lineage after 21 days from transfection. It should be stated that all the differentiation experiments were performed in absence of FeQ doping. It could have been useful to repeat the same experiments also in the

presence of FeQ solution, to determine if the FeQ presence could have affected the MSCs differentiation properties. Indeed, there are scientific works suggesting that SPIONS impairs chondrogenesis and osteogenesis in human MSCs. It was observed that human MSCs treated with Amine-surface-modified SPIONS show lower expression levels of osteogenic lineage marker genes RUNX2, osteocalcin, and type I collagen, inhibiting chondrogenesis and osteogenesis (Chang et al., 2012). These results collimate with previous research findings on inhibitory effect of ferumoxide on chondrogenesis and osteogenesis (Farrell et al., 2008; Kostura et al., 2004) and ferucarbotran on osteogenic differentiation in human MSCs (Y. C. Chen et al., 2010)

- In Chapter 5 an AMF of 565.3 kHz frequency was applied to monolayers and 3D models of *mms6*-expressing MSCs. Cell viability is reduced by one-third when MSCs are exposed in monolayers, while when MSCs are arranged in 3D models cell death interested the 40% of the population. Registered cell death was 40% when MSCs were co-cultured with MG63 cancer cells and 50% when co-cultured with A431-ecad GFP expressing cells. Such results suggest a promising responsiveness *in vitro* of MNPs expressing MSCs to AMF which leads to cell death.

A caveat to interpreting results is that the control wild-type MSCs should have been doped with FeQ for 21 days to make them the appropriate control for the *mms6*-expressing cells.

Apoptosis, also defined as programmed cell death, is a very interesting and relevant response of cells to HT, which affects many of the cell components, ranging from the membrane to the nucleus. Typical apoptosis hallmarks are: cell shrinkage, membrane blebbing, mitochondrial alteration, metabolic changes, nuclear condensation and genomic DNA fragmentation, activated caspases, and the eventual engulfment of the cell by phagosomes. Apoptosis is different from necrosis as it does not involve the inflammatory response, and it is limited to individual cells *in vivo* (Cosentino & Garcia-Saez, 2014; S. Mukhopadhyay et al., 2014) .

If more time were available, the apoptotic process could be investigated also in this study. Nowadays there are so many techniques available to determine if a cell

undergoes apoptosis, that providing a complete list of them would require an entire chapter: for this reason only some of them will be reported.

- The plasma membrane changes could be investigated using AnnexinV, followed by fluorescence, confocal microscopy or, together with propidium iodide, by FACS (Gu et al., 2017).
- The mitochondrial integrity could be stained with MitoTrackerRed, Rhodamine 123, JC1 or TMRE followed by confocal microscopy or FACS (Gorojod et al., 2017).
- The metabolic changes could be investigated taking into account the variation of Ca^{2+}concentration (fura-2, fluo-3, fluo-4) (Giorgi et al., 2015), or the intracellular acidification (SNARF-1, acetoxymethyl ester) (Lucien et al., 2014).
- Proteases activation could be studied by FACS or by fluorescent microscopy analysis of cleavage of fluorogenic substrates (PhiPhiLux), Western-blot or FACS analysis of Caspases-3 and PARP-1, since PARP-1 is cleaved by activated caspase 3 (Li Wang et al., 2013).
- Chromatine condensation could be studied by Hoescht 33342 and propidium iodide, since Hoescht 33342 penetrates all cells and healthy cells exclude propidium iodide (DiBartolomeis & Moné, 2003);
- DNA fragmentation could be investigated by TUNEL (terminal deoxynucleotidyl transferase mediated dUTP nick end labeling) analysis followed by microscopy or by FACS (Kim & Lee, 2014).
- Apoptosis related genes expression could be studied by Real-Time PCR and gene microarray analysis (Kamiya et al., 2012).

Since the Heat Shock Proteins (HSPs) like HSP70, HSP72 and HSP90 play a paramount role in the cellular heat stress response, (Sauvage et al., 2017; Sekihara et al., 2013), the effect of the Hyperthermia on cells could have been investigated also by studying the HSPs expression before and after the AMF application. Some of the techniques measuring the HSPs induction at the intercellular level are qRT-PCR, SDS-PAGE, Western Blot, immunofluorescence and enzyme-linked immunosorbent

assay (ELISA), as seen elsewhere (Bhayani et al., 2013; Jang et al., 2017; M. Moros et al., 2015; R. Yang et al., 2015).

• In Chapter 6, an AMF of 565.3 kHz frequency was applied *in vivo*, on mice bearing tumour xenografts intracardiac injected with *mms6*-expressing MSCs. *mms6*-expressing MSCs were detected in tumours xenografts and mice major organs (spleen, liver, lungs). However, in exposed mice, it was not noticed any statistically significant reduction in tumour volume or growth, neither the tumour cells apoptosis/necrosis in exposed mice was different from the unexposed ones.

Overall, this study demonstrates that it is possible to successfully express MTB genes in MSCs, creating magnetic and AMF responsive MSCs, without an adverse effect on critical cell functions. However, if *mms6*-expressing MSCs could be killed by AFM exposure *in vitro*, also causing the death of the adjacent cancer cells, the same effects was not noticed *in vivo*, where no tumour reduction was observed. This could be due to several limitations:

- The number of *mms6*-expressing MSCs able to reach the tumour *in vivo* was too small to give an appreciable response to AMF, able to kill a sufficient number of cancer cells and so to successfully reduce the tumour volume/growth.
- The way that *mms6*-expressing MSCs react to the AMF could depend on cell arrangement. It is possible that cells are more responsive to AMF when directly exposed to AMF as cell monolayer/3D model, than when they are in a complex system as the animal body.
- Due to the limited time, it was not possible to repeat the *in vivo* experimental part. A repetition of the experiment could have helped to improve experimental settings, such as frequency and exposure time applied.

The use of magnetized MSCs could offer enormous advantages in the field of regenerative medicine and for the *in vivo* cell tracking.

The MSCs properties to "home" toward tumours and the site of injury without rousing the immune system response boosted their use for cancer-specific gene delivery and tissue regeneration (Corsten & Shah, 2008; C. Tang et al., 2010). As a consequence, it is of paramount importance to accurately localize MSCs and to ensure their survival after MSCs targeting to the site of interest.

Magnetic Resonance Imaging (MRI) is the imaging techniques commonly used for *in vivo* cellular imaging as it offers a good resolution with high anatomic background contrast, without ionizing radiation but with the need of a contrast agent (C. Tang et al., 2010). SPIONS are the most commonly used contrast agents in MRI. However, exocytosis and SPIONS dilution during MSCs cell replications lead to a decrease of the magnetic signals with the passing of time, making difficult to track the MSCs in the body and to determine their biodistribution and fate in stem cell-based regenerative therapies (Amado et al., 2005).

The use of self-expressing magnetic gene MSCs could be an appealing strategy for the creation of magnetic MSCs, as it was shown that MRI system could magnetically guide the stem cells to the tissue of interest and then followed their fate in real-time. (Connell et al., 2015).

Moreover, the stable expressing magnetic gene MSCs, able to *de novo* synthesise intracellular MNPs, could avoid the nanoparticles dilution with the cell divisions, and so the fading of the magnetic signal with the passing of time (Elfick et al., 2017). The magnetic gene could function as a reporter gene, which generates contrast depending on cell viability, survival and localization, providing useful information (S. M. Pereira et al., 2015).

Another advantage of using magnetic MSCs for regeneration therapies is their retention in the injury site when a magnet is applied. Scientific evidences prove that the application of an external static magnetic field could enhance the engraftment and retention of magnetic MSCs in the target site, due to the magnetic interactions

between the magnetized cells and the magnetic field, which stimulates the expression of integrins and adhesion factors (Nakamae et al., 2010; Schäfer et al., 2010). With the application of a static magnetic field, SPION-labelled MSCs are better retained into cartilage degeneration sites, fibrocartilages (meniscus), muscles, and bones, which are body districts characterized by limited regenerative capacity and which are poorly targeted by systemic/local MSCs administration (L. H. A. Silva et al., 2017).

In addition to that, the creation of magnetic MSCs offers a tremendous advantage to the magnetic force assisted engineering, as it makes possible to actuate MSCs from distance. This has helped studies of mechanical conditioning bioreactor culture of MSCs (Dobson et al., 2006) and intermittent mechanical activation for long-term bone cells growth (Cartmell et al., 2002).

Magnetic MSCs could find application also in the magnetic manipulation of the biological systems, as they could be driven by an external magnetic force to create an ordered arrangement of cells (*cell-patterning*) or tailored 3D tissues, made of the required shape and size (*magnetic-manufacturing*) (Horie et al., 2017).

This study could be interpreted as a proof of concept experiment regarding *mms6* expression into human MSCs and, regardless results obtained are encouraging, a lot of work is still needed to improve *mms6* expression into MSCs, to enhance the MNPs production and to maximise the MSCs delivery to the tumour.

The use of a specific *Mms6*-antibody, which was not sold by any company at the moment of the research, would have greatly improved the study. The *Mms6*-antibody could have been used in immuno-staining essays (immunohistochemistry, flow cytometry, Western Blotting) and in confocal microscopy investigations to determine the Mms6 protein expression in the transfected cells at different time points from the transfection.

Next experiments will be finalised to the optimisation of *mms6* gene expression in MSCs, using new genome editing techniques, as CRISPR (clustered regularly interspaced short palindromic repeat)-Cas9(CRISPR-associated nuclease 9) system which could be utilised for sequence-specific integration of *mms6* gene in MSCs genome. This technology relies on a synthetic sequence-specific nuclease which,

once transfected into cell, is able to recognise the target genomic site and to create a double-strand DNA break (DSB) at the site (Ding et al., 2016; Jinek et al., 2012; Voytas, 2013; Zhang et al., 2014). The DSB will trigger the repair system which is ubiquitous in all the cells, and it is normally an error-prone non-homologous end-joining pathway, which creates small deletion at the site, causing gene knockout. If the gene of interest (*mms6*), is modified to contain homology to the flanking sequence, it could be integrated into the DSB by homology-directed repair using the donor DNA as a template. This technique has already been utilised in both mouse and human neural stem cells to knock-in epitope tags and fluorescent reporters (Bressan et al., 2017). Using this method, it would be possible to integrate the gene *mms6* into MSCs genome in a more accurate and elegant way than transfection, obtaining a better gene expression and so stimulating more protein production (Ding et al., 2016).

In addition to intracardiac injection, MSCs could reach the tumour by different delivery routes: subcutaneous injection, intravenous injection and intratumoral injection. Seo et al. observed that MSCs, which in their experiment expressed modified interleukin-12, gave the strong tumour-specific T-cell responses, together with anti-metastatic effects and inhibition of solid tumour growth when intratumoral injected (Seo et al., 2011). The intratumoral injection could be applied in future experiments as an alternative delivery route to intracardiac one.

In conclusion, the presented study, although it does not lead to an efficient reduction of tumour volume/growth *in vivo*, contributed to our knowledge on the creation of magnetic human MSCs for their potential application in MHT cancer treatment.

8. Appendices

8.1. mms6 gene description

The *Magnetospirillum magneticum* AMB-1 *mms6* DNA bacterial sequence was codon optimized for mammalian expression and a Kozak sequence added then synthesised. The optimized sequence was synthesised by MRGene GmbH (Germany) and cloned in their proprietary vector with SacI and KpnI restriction sites. The synthetic *mms6* gene was cloned into a pcDNA3.1 expression vector (ThermoFisher Scientific) at BamH1 and EcoRI restriction sites and transfected into human fetal bone marrow derived MSCs with X-tremeGENE HP.

Sanger sequencing data confirmed 100% identity of the DNA sequence of the initial synthetic *mms6* gene inserted within the pcDNA3.1 vector used for transfection (Ref.*mms6*) and the gene expressed after 10, 15 and 21 days of transfection (**Figure 76**). The Sanger sequencing data was obtained as per the following protocol.

Sequencing samples were set up using a reaction volume of 0.5 µl BigDye Terminator v3.1 (Applied Biosystems). The buffers and primers and PCR products were mixed as following: 1.31 µl (x5) buffer, 1µl primer (5µM), 5.19 µl ddH_2O, 2 µl of DNA (per reaction). The samples were run on a peltier thermal cycler with an annealing temperature of 55°C, the final PCR products were precipitated in 95% ethanol and then washed with 70% ethanol dried and finally dissolved in water. Then, samples where run on the Applied Biosystems 3130 sequencer.

The pcDNA3.1 vector map is shown in **Figure 77**.

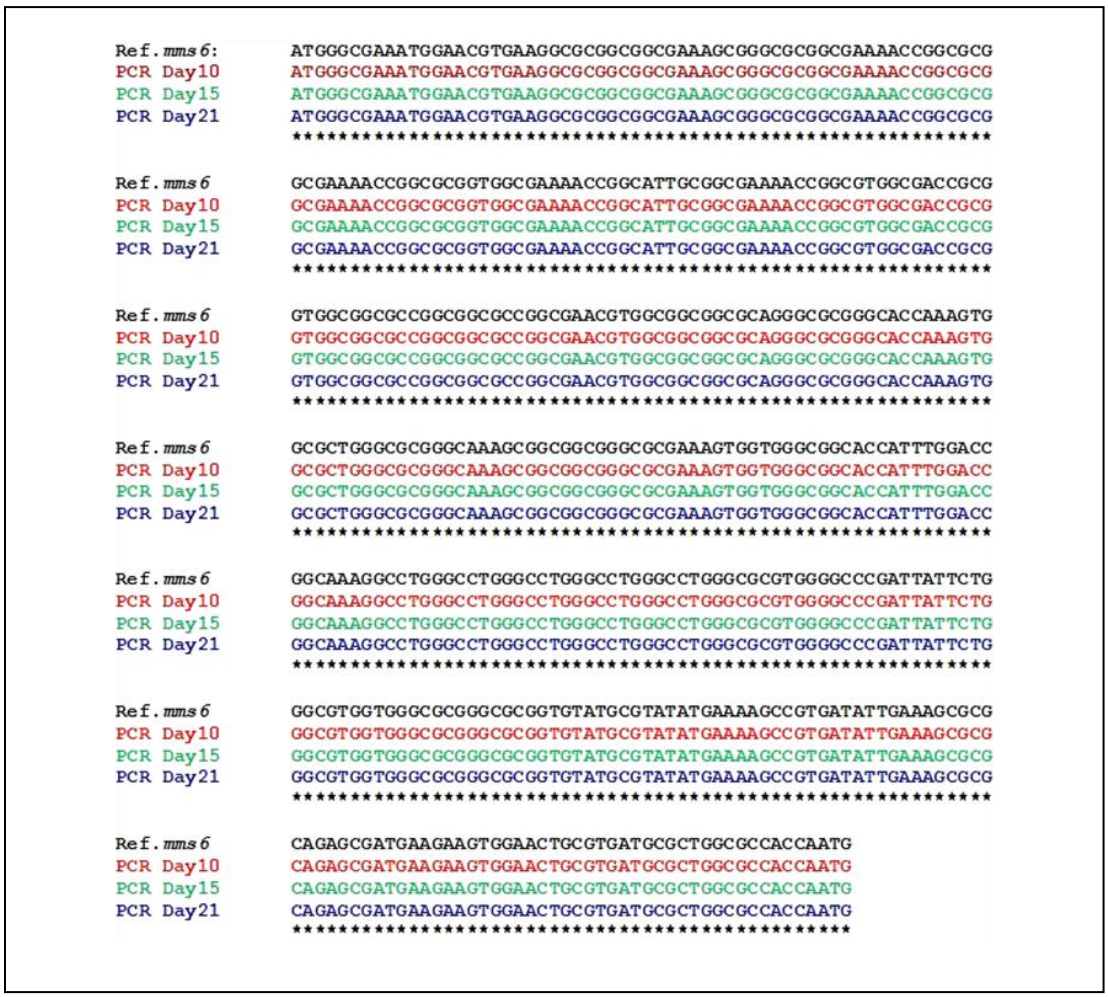

Figure 76. CLUSTAL O (1.2.3) multiple sequence alignment.

The pcDNA3.1 vector used for transfection (Ref.*mms6*) and the gene expressed by MSCs after 10, 15 and 21 days of transfection were aligned confirming 100% identity.

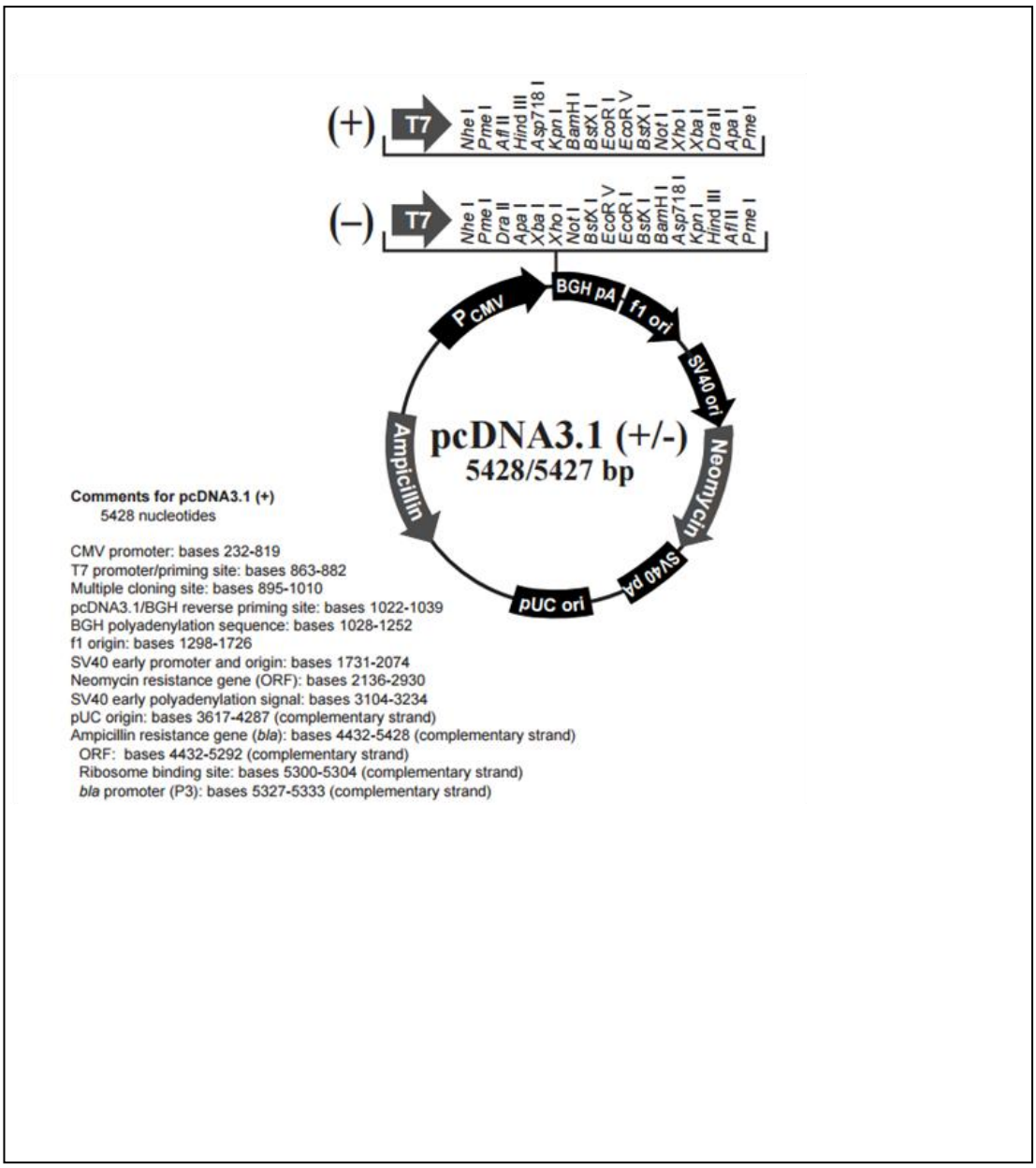

Figure 77. pcDNA™3.1 Vector map.

Original picture taken from: https://tools.thermofisher.com/content/sfs/manuals/pcdna3_1_man.pdf

8.2. *mmsF* ligation into pcDNA4/TO vector

1. mmsF gene PCR amplification

mmsF gene used in this study belongs to *Magnetospirillum gryphiswaldense* bacterium. The genomic DNA of *M. gryphiswaldense* was purchased from DMSZ, Germany (product code: DMS 6361).

The nucleotide sequence of the *mmsF* gene is the following:

ATGAAGAAGTCGAACTGCGCGACGCGCTGTCCTGAACGGGGGGGGGGGG
ACATGGTTGAAGCAATCCTTCGGAGCACTCTTGGCGCGCGCACGACCGTC
ATGGCGGCGCTGTCTTATCTCAGCGTCCTGTGCTTCGTTCCGCTGCTGGTG
GATCGGGACGACGAGTTTGTCTACTTCCACGCCAAGCAGGGTCTGGTGAT
CTGGATGTGGGGCGTGCTGGCGCTGTTCGCGCTGCATGTTCCCGTTCTGG
GGAAGTGGATTTTCGGGTTTTCATCCATGGGGGTCCTGGTATTCTCCCTTC
TGGGCTTGGTCTCCGTGGTGTTCCAGCGGGCATGGAAACTGCCCGTGGTC
AGCTGGGTGGCCGACCGGATCTGA

To clone the *mmsF* gene into pcDNA4/TO vector, a PCR product of 375 bp was amplified by the following primers. The primers were designed in such a way that a EcoRI and NotI sites were added in the forward and reverse primers respectively. Primer Forward was designed to contain the Kozak sequence (gccacc) for improving mammalian translation efficiency.

Primer Forward (5'-3'):
GATCGAATTCGCCACCATGAAGAAGTCGAACTGCGCGACG

Primer Reverse (5'-3'): GATCGCGGCCGCTCAGATCCGGTCGGCCACCCA

EcoRI sequence: GAATTC, NotI sequence: GCGGCCGC, Kozak sequence: GCCACC

Start Codon is ATG and stop codon is TGA. Both the primers contain the hanging sequence (gatc) for the plasmid integration.

Primers lenght was chosen to improve specificity during PCR product amplification. PCR was performed with the use of Q5® High-Fidelity DNA Polymerase (NEB) and

dNTPs (Thermo Fisher Scientific) following the manufacture's protocol, and using the following program:

- initial denaturation at 98°C for 30 seconds,
- denaturation at 98°C for 10 seconds,
- annealing at 60 °C for 30 seconds
- extension at 72 °C for 30 seconds
- final extension at 72 °C for 2 minutes.

35 cycles

The PCR product was analysed by 2% agarose gel electrophoresis (**Figure 78A**).

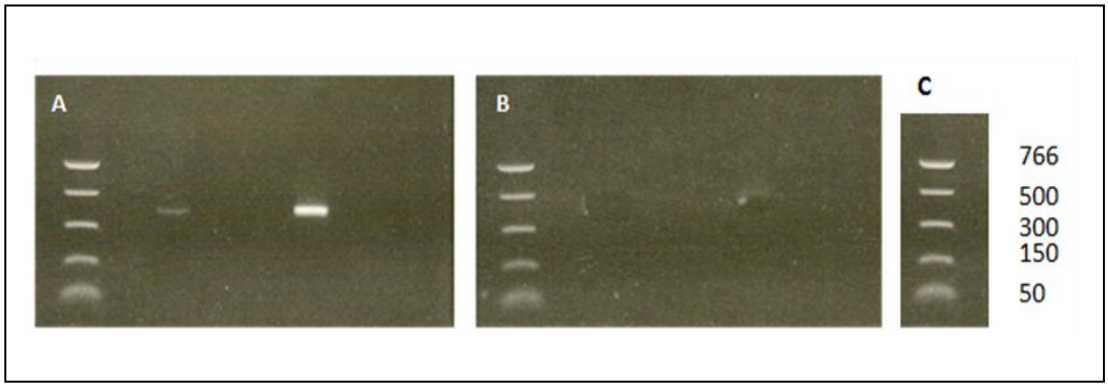

Figure 78. Agarose gel electrophoresis of *mmsF* gene.

A)Two PCR products were run on gel; B) The gene *mmsF* was cut with scalpel following gel UV exposure for gene purification. C) NEB DNA marker with bp indicated.

2. mmsF gene purification from agarose gel

The gene *mmsF* was imaged at the UV image analyser, removed from it with a scalpel (**Figure 78B**), and put in a pre-weight microcentrifuge tube. Then, the excised gel band of *mmsF* gene was purified from the gel using QIAquick Gel Extraction Kit (Qiagen), according to the manufacture's protocol. Briefly, 3 volumes of Buffer QG were added to one volume of gel, incubating at 50 ºC for 10 minutes and vortexing the tube to dissolve the gel. A volume of isopropanol was added to the sample and mixed. The sample was then applied to a spin column containing a DNA-binding membrane. The column was placed in a collection tube, and it was centrifuged for 1 minute at 10,000 xg in a table-top microcentrifuge. The wash-

through was discarded and, to wash the membrane, 0.75 ml of Buffer PE were added to the column, and centrifuge again for 1 minute at 10,000 xg. The column was put in a clean 1.5 ml microcentrifuge tube, and *mmsF* gene was eluted by adding 30 µl of Buffer EB (10mM TrisCl, pH8.5) directly to the centre of the membrane. The column was left to stand at RT for 1 minute and then centrifuged for 1 minute at 10,000 xg. The purified DNA was analysed on a 2% gel, by adding 1 volume of Loading Dye to 5 volumes of DNA (**Figure 79**). DNA concentration and purity were determined by NanoDrop spectrophotometer (Labtech).

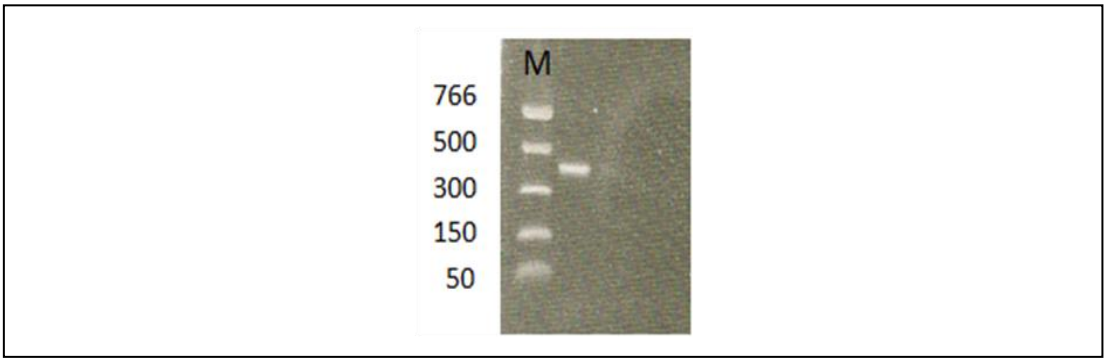

Figure 79. The purified *mmsF* DNA was analyzed on a 2% gel.
M: NEB DNA marker with bp indicated.

3. Restriction enzymes digestion of the purified PCR product and of the pcDNA4/T0 vector

To insert the *mmsF* gene into pcDNA4/TO vector, both the DNA were digested with EcoRI and NotI enzymes (NEB), according to the manufacture's protocol. Briefly, the *mmsF* PCR product (700ng) and pcDNA4/TO vector (2 µg) were put in two separate tubes. Then, the following components were added to each tube: 5µl of NEBuffer 3.1(10x concentrated), 1 µl of EcoRI enzyme, 1 µl of NotI enzyme, 0.5 µl of BSA (100x concentrated) and water up to a final volume of 50 µl. Then, the two solutions were incubated at 37 ºC overnight. The day after, the enzymes activity was inactivated by incubating the solutions at 65 ºC for 5 minutes.

4.Dephosphorylation of the pcDNA4/TO vector only

pcDNA4/TO vector was dephosporylated and ligated to *mmsF* gene using the Rapid DNA ligation kit (Roche), according to the manufacture's protocol. Before the ligation reaction, pcDNA4/TO vector was dephosporylated to prevent self-ligation.

Briefly, 2µl of rAPid Alkaline Phosphatase Buffer and 1µl of rAPid Alkaline Phosphatase were added to 1µg of the vector, adding water to a final volume of 20 µl. Then the solution was mixed thoroughly, briefly centrifuged and incubated at 37°C for 30 minutes. At the end of the incubation time, rAPid Alkaline Phosphatase was inactivated by incubating the solution at 75°C for 2 minutes.

5. Ligation of the pcDNA/4TO vector to the mmsF gene

The dephosphorylated pcDNA4/TO vector and the *mmsF* insert gene were ligated. Briefly, 50 ng of pcDNA4/TO vector and 150 ng of the *mmsF* gene were dissolved in the thoroughly mixed DNA Dilution Buffer (2 µl, 5x concentrated) and water, which was added to a final volume of 10 µl in a sterile reaction vial. Then, 10 µl of T4 DNA Ligation Buffer (2x concentrated) were added to the reaction vial and mixed thoroughly. Lastly, 1 µl of T4 DNA Ligase was added to the reaction vial, mixed thoroughly and let to incubate at RT for 15 minutes. A (negative) control reaction vial was prepared in the same way, omitting the *mmsF* gene insert that was replaced by water. The control reaction was prepared to verify that the vector with the insert ligation had many more colonies, when later transformed into competent bacteria, than the vector alone. The ligation reaction was then transformed into competent cells.

6. Bacteria transformation with the ligation reaction

The ligation reaction was transformed into *E. Coli* bacteria, using Subcloning Efficiency™ DH5α™ Competent Cells (Invitrogen). Aliquots of 50 µl of cells stored at -80°C were thawed on ice for 15 minutes before to use them. Then, 2 µl of ligation reaction were added to the competent cells in a microcentrifuge tube, and gently mixed. The tube was incubated on ice for 30 minutes, followed by heat shock in incubator at 42°C for 70 seconds and again by incubation on ice for 3 minutes. Then, 900 µl of pre-warmed SOC medium (without antibiotic) were added to the cells, which were cultured in shaking incubator at 37°C for 1 hour. In the meanwhile, agar plates containing ampicillin (1µl of 1000x ampicillin /1ml agarose) were warmed up in 37°C incubator bottom up to avoid condensation. The cells were then centrifuged at 5000 rpm for 1 minute. 500 µl of supernatant were removed, and the pellet was

resuspended in the remaining medium and added drop by drop to plates in different concentration (50 µl, 100 µl, 200 µl) near to a Bunsen flame. For a homogenous distribution, drops were distributed with a sterile inoculation loop. Then, plates were incubated at 37°C overnight.

7. Plasmids amplification

The day after, bacteria colonies were visible in the plates, which were put in fridge to stop bacteria replication. 5 single colonies were picked from the plates to be grown overnight in different tubes containing 3 ml of selective LB medium (LB medium containing 1µl of 1000x ampicillin /1ml LB medium). This is called starter culture. The caps of tubes were untied to favour the air passage, and then bacteria were grown at 37°C in a shaking incubator overnight. The day after, early in the morning, the cloudiness of the starter culture was visually inspected, as it is an indicator of the bacteria growth. Then, 100 ml of selective LB medium were inoculated with 100 µl of the starter culture (1/1000 dilution). Bacteria were grown at 37°C for 12–16 h with vigorous shaking (approx. 300 rpm). At the end of the incubation period, the tubes were incubated on ice for 10 minutes to stop bacteria growth. Then, 500 µl of solution were removed from each tube, and added to a 500 µl of a solution of sterile 80% glycerol (80% pure glycerol and 20% sterile water) and then stored at -80°C to preserve transformed bacteria cells aliquots.

8. Plasmid purification

The plasmid was then purified using the "QIAGEN Plasmid Maxi Kit"(QIAGEN). Briefly, the solution contained in the different tubes was centrifuged at 6000 x g, at 4°C for 15 minutes. The supernatant was then removed in a waste bottle containing disinfectant. For each tube, the bacteria pellet was resuspended in 10 ml of buffer P1. Then, 10 ml of buffer P2 were added, mixing vigorously by hand inversion for 4-6 times. The solution was incubated at RT for 5 minutes, followed by addition of 10 ml of prechilled Buffer P3. The mixture was mixed and incubated on ice for 20 minutes, then it was transferred into clean tubes made for high speed and centrifuged at 20000 x g for 30 min at 4°C. The supernatant was re-centrifuged at 20,000 x g for 15 min at 4°C, and applied to a QIAGEN-tip previously equilibrated with 10 ml of

Buffer QBT, allowing it to enter the resin by gravity flow. The QIAGEN-tip was washed twice with 30 ml of Buffer QC, allowing it to move through the QIAGEN-tip by gravity flow. The plasmid was then eluted with 15 ml Buffer QF into a clean 50 ml tube and precipitated by adding 10.5 ml RT isopropanol. Then, it was centrifuged at 20000 x g for 30 min at 4°C and the supernatant was carefully decanted. The pellet (plasmid) was washed with 5 ml of RT 70% ethanol and centrifuged at 20000 x g for 10 minutes, carefully decanting the supernatant. Then, the pellet was air-dried for 10 minutes and redissolved in 50 µl of RNA/DNAse free sterile water. The plasmid concentration and purity were determined using NanoDrop spectrophotometer (Labtech), measuring the absorbance at the 260, 280 and 230 nm wavelength. The absorbance ratio of DNA samples at 260/280nm of ~1.8 and absorbance ratio at 260/230nm in a range of 2.0-2.2 were considered as highly pure.

The presence of the *mmsF* gene in each extracted plasmid was confirmed by PCR, using the same cloning primers. The PCR product was analysed on 2% agarose gel electrophoresis (**Figure 80A**).

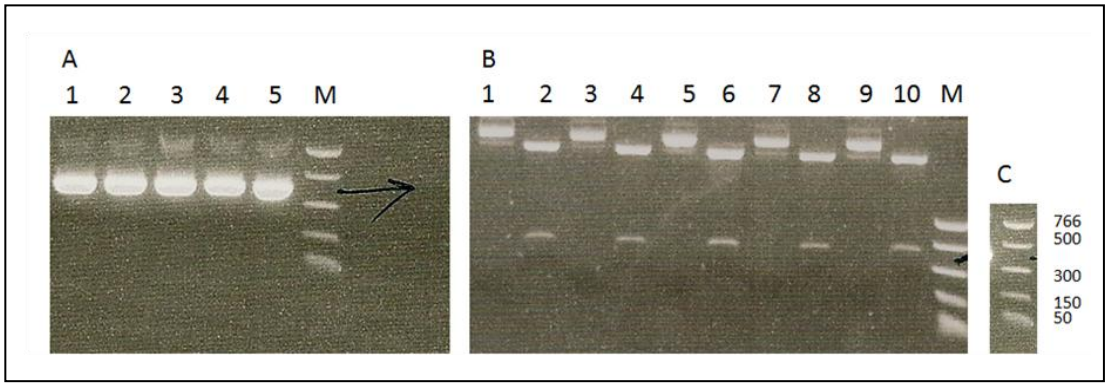

Figure 80. Agarose gel electrophoresis of *mmsF* gene.

A 1-5) Following plasmid purification from bacteria colonies, *mmsF* gene was visualised on 2% agarose gel electrophoresis. Arrow indicates gene size. B) Digestion of pcDNA/4TO vector by NotI and EcoRI enzymes for each colony picked. 1,3,5,7,9: uncut vector; 2,4,6,8,10 cut vector. M: marker C) NEB DNA marker with bp indicated.

For a further confirmation of the success of the ligation reaction, the purified plasmids were digested with EcoRI and NotI enzymes. Briefly, to each tube containing 100 ng of plasmid were added the following components: 5µl of

NEBuffer 3.1(10x concentrated), 1 µl of EcoRI enzyme, 1 µl of NotI enzyme, 0.5 µl of BSA (100x concentrated) and water up to a final volume of 50 µl. Then, the two solutions were incubated at 37 ºC overnight. The day after, the enzymes activity was inactivated by incubating the solutions at 65 ºC for 15 minutes. The digestion reaction was confirmed by agarose gel. In each tube, it was added 1 volume of loading dye for each 9 volumes of plasmid. Then, samples were loaded in a 2% agarose gel (**Figure 80B**).

9. mmsF gene sequencing

To check that the *mmsF* gene did not mutate during plasmid cloning, all the purified plasmids were sequenced by Sanger Sequencing method using the following primers:

Primer Forward (5'-3'): CGCAAATGGGCGGTAGGCGTG

Primer Reverse (5'-3'): TCAGATCCGGTCGGCCACCCA

The protocol used for gene sequencing was the following: sequencing samples were set up using a reaction volume of 0.5 µl BigDye Terminator v3.1 (Applied Biosystems), adding the following reagents: 1.31 µl (x5) buffer, 1µl primer (5µM), 5.19 µl dH_2O, 2 µl of DNA (per reaction). Samples were run on a Peltier thermal cycler with an annealing temperature of 55 °C and then were precipitated using 95% ethanol and washed with 70% ethanol. Then, samples were run on the Applied Biosystems 3130 sequencer.

The sequences were aligned with the original modified *mmsF* gene (Query) using Align Sequences Nucleotide BLAST tool (NCBI), and clone number 4 (Sbjct) was selected for cells transfection as 100% identical to the original modified *mmsF* gene (**Figure 81**). The pcDNA 4/TO vector map is shown in **Figure 82**.

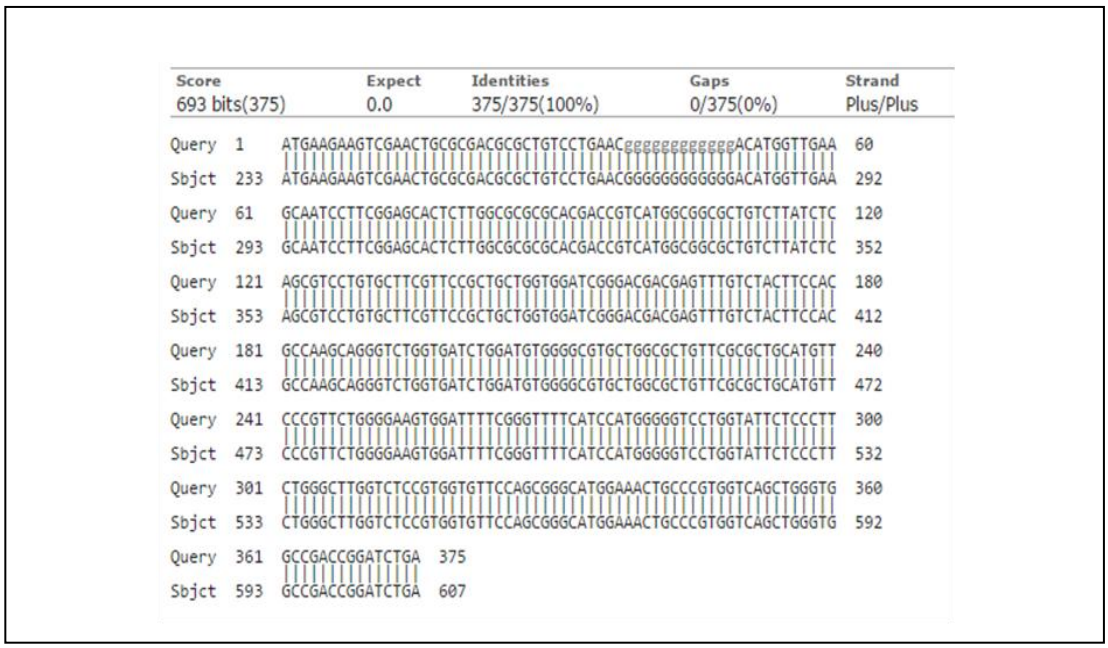

Score	Expect	Identities	Gaps	Strand
693 bits(375)	0.0	375/375(100%)	0/375(0%)	Plus/Plus

```
Query  1    ATGAAGAAGTCGAACTGCGCGACGCGCTGTCCTGAACgggggggggggACATGGTTGAA  60
            ||||||||||||||||||||||||||||||||||||||||||||||||||||||||||||
Sbjct  233  ATGAAGAAGTCGAACTGCGCGACGCGCTGTCCTGAACGGGGGGGGGGGGACATGGTTGAA  292

Query  61   GCAATCCTTCGGAGCACTCTTGGCGCGCGCACGACCGTCATGGCGGCGCTGTCTTATCTC  120
            ||||||||||||||||||||||||||||||||||||||||||||||||||||||||||||
Sbjct  293  GCAATCCTTCGGAGCACTCTTGGCGCGCGCACGACCGTCATGGCGGCGCTGTCTTATCTC  352

Query  121  AGCGTCCTGTGCTTCGTTCCGCTGCTGGTGGATCGGGACGACGAGTTTGTCTACTTCCAC  180
            ||||||||||||||||||||||||||||||||||||||||||||||||||||||||||||
Sbjct  353  AGCGTCCTGTGCTTCGTTCCGCTGCTGGTGGATCGGGACGACGAGTTTGTCTACTTCCAC  412

Query  181  GCCAAGCAGGGTCTGGTGATCTGGATGTGGGGCGTGCTGGCGCTGTTCGCGCTGCATGTT  240
            ||||||||||||||||||||||||||||||||||||||||||||||||||||||||||||
Sbjct  413  GCCAAGCAGGGTCTGGTGATCTGGATGTGGGGCGTGCTGGCGCTGTTCGCGCTGCATGTT  472

Query  241  CCCGTTCTGGGGAAGTGGATTTTCGGGTTTTCATCCATGGGGGTCCTGGTATTCTCCCTT  300
            ||||||||||||||||||||||||||||||||||||||||||||||||||||||||||||
Sbjct  473  CCCGTTCTGGGGAAGTGGATTTTCGGGTTTTCATCCATGGGGGTCCTGGTATTCTCCCTT  532

Query  301  CTGGGCTTGGTCTCCGTGGTGTTCCAGCGGGCATGGAAACTGCCCGTGGTCAGCTGGGTG  360
            ||||||||||||||||||||||||||||||||||||||||||||||||||||||||||||
Sbjct  533  CTGGGCTTGGTCTCCGTGGTGTTCCAGCGGGCATGGAAACTGCCCGTGGTCAGCTGGGTG  592

Query  361  GCCGACCGGATCTGA  375
            |||||||||||||||
Sbjct  593  GCCGACCGGATCTGA  607
```

Figure 81. BLAST alignement.

Clone 4 (Sbjct) was aligned with the original modified *mmsF* gene (Query) using Align Sequences Nucleotide BLAST tool (ncbi).

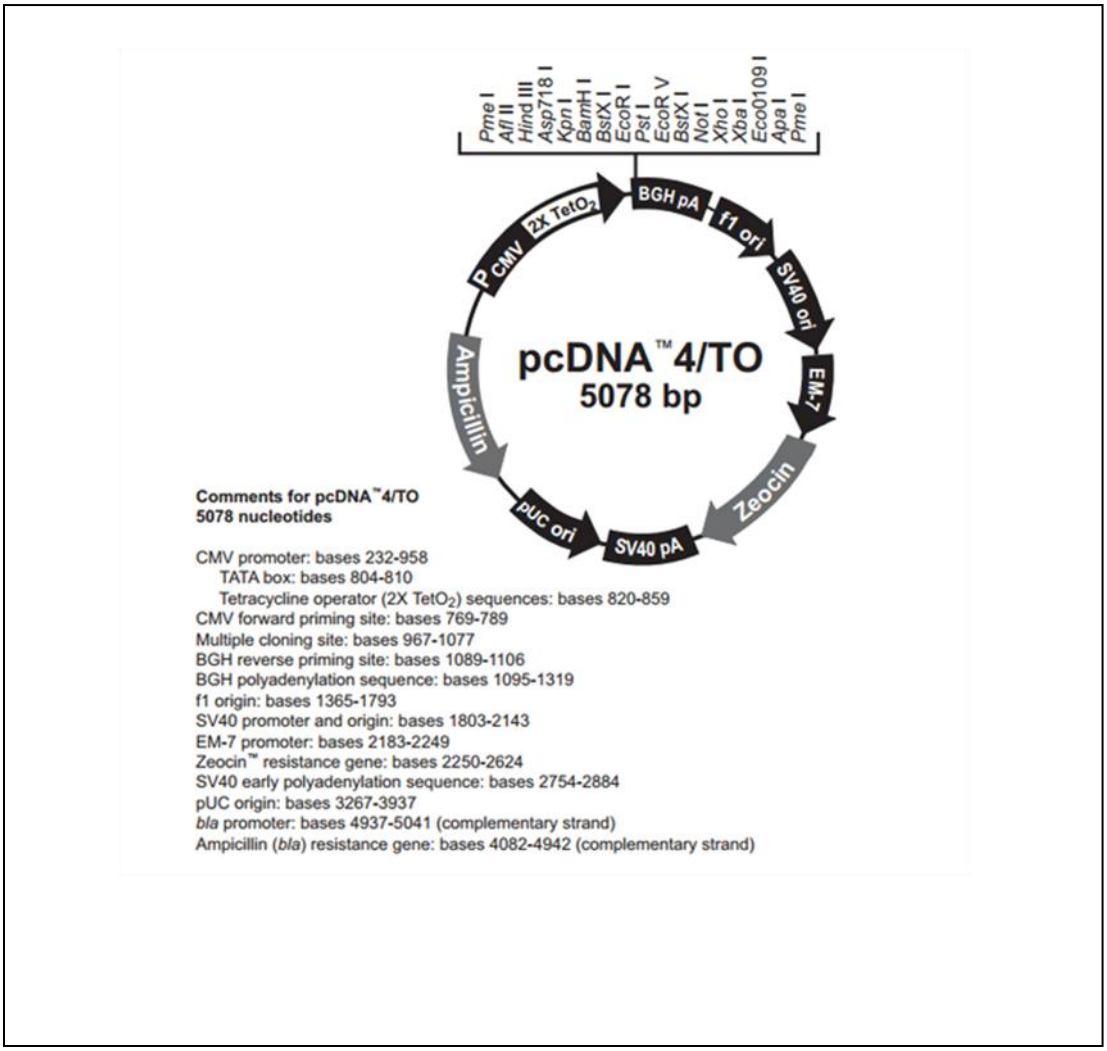

Figure 82. pcDNA4/TO Vector map.

Original picture taken from: https://tools.thermofisher.com/content/sfs/manuals/pcdna3_1_man.pdf

8.3. Transfection S.O.P

Reagents required for two T25 flasks:

1. OptiMem Reduced Serum Medium (Gibco)

2. Plasmid

3. X-tremeGENE HP DNA Transfection Reagent (Roche)

Procedure

1. Keep out all the reagents at RT 1 hour before to start. Cells density in the flask should be around the 80%.
2. Prepare 2 fresh Eppendorf vials (1.5 ml) and put 600 µl of Optimem Medium in each one.
3. Put 6 µl of the plasmid (1000 ng/µl) in each Eppendorf vial and let it equilibrate at RT. In the case of co-transfection, also add the second plasmid.
4. Vortex the Transfection Reagent before to add it.
5. Add 18 µl of Transfection Reagent to each Eppendorf directly in the middle of the medium without touching the Eppendorf's walls and tip gently to mix the compound.

   N.B. *The Transfection reagent should NEVER touch the plastic walls of tube. Otherwise, its activity will be compromised.*
6. Let incubate for 20 minutes. In the meanwhile, change the medium to the flasks T25 with 6 ml of DMEM 20% FBS **NO P/S**.
7. When 10 minutes of incubation are passed, tap gently again the Eppendorf to mix well the compound.
8. When 20 minutes are passed, spin down for 3 sec the compound of each Eppendorf and add it in each flask gently trying to cover all the flask. Incline the flask so that the medium let uncovered the majority of the flask and you can add quickly the reagent drop by drop.
9. Gently swirl the flask for 30 sec.
10. Incubate in incubator O/N.

11. The day after, change the medium with fresh standard medium, without P/S and doped with FeQ (3.4 µl/ml).

8.4. Transfection Efficiency

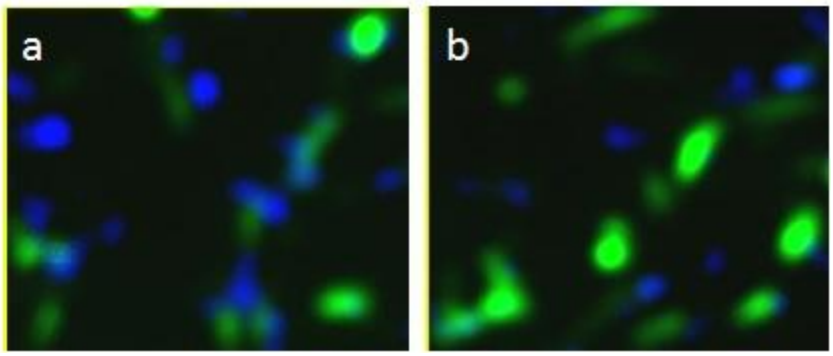

Figure 83. Representative picture of transfection efficiency.

MG63 cells (a) and MSCs (b) were transfected with pmaxGFP plasmid using the X-tremeGENE HP Transfection Reagent and imaged 48 hours after transfection in fluorescence microscopy at 200x magnification, revealing a 70% transfection efficiency for both the cell type studied.

8.5. RNA integrity test.

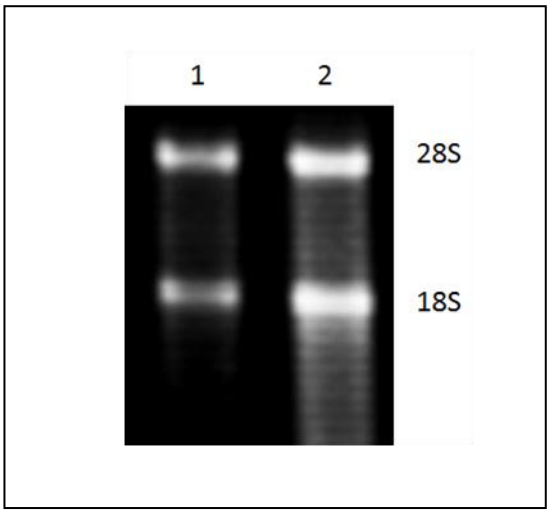

Figure 84. Example of RNA integrity test.
Two main bands of rRNA (28S and 18S respectively) were detected. Lane 1= 500 ng of rRNA loaded; lane2= 1 µg of rRNA loaded.

8.6. Nucleotide sequence of the primers used in this study for RT-PCR.

Table 14. Nucleotide sequence of the primers used in this study for RT-PCR.

Primers were designed using PRIMER3 software.

Gene (product size)	***Forward* Primer 5'-3'**	***Reverse* Primer 5'-3'**
mms6 internal (108 bp)	GTGGGGCCCGATTATTCT	TCACGCAGTTCCACTTCTTC
mms6 for gene expression and Sanger sequencing (408 bp)	ATGGGCGAAATGGAACGTGAAG	CATTGGTGGCGCCAGCGCATC
mmsF for cloning (375 bp)	GATCGAATTCGCCACCATGAAG AAGTCGAACTGCGCGACG	GATCGCGGCCGCTCAGATCCG GTCGGCCACCCA
mmsF for Sanger sequencing (375 bp)	CGCAAATGGGCGGTAGGCGTG	TCAGATCCGGTCGGCCACCCA
*MmsF*A (122 bp)	AGGGTCTGGTGATCTGGATG	CAAGCCCAGAAGGGAGAATA
*MmsF*B (205 bp)	GCAATCCTTCGGAGCACTCT	CGAAAATCCACTTCCCCAGA
GAPDH(210 bp)	GGGAGCCAAAAGGGTCATCA	GTGGCAGTGATGGCATGGAC
eEF2(123 bp)	TGTCAGTCATCGCCCATGTG	CATCCTTGCGAGTGTCAGTGA

8.7. SQUID Protocol

1) The sample should be in the capsule, inserted into the straw.
2) Go to the pc. The temperature on the software shoud be **T=300K**. Click "set".
3) Go to the instrument. There are 2 rings.
4) Unscrew and pull up **SLOWLY**. When it stops and you feel some tension, **ROTATE** and pull it slowly. Never force it.
5) When I can see the sample, switch it on "closed". The black handle is now horizontal.
6) Pull away the long tube. **The white dot should face me**.
7) Put it on the table, open it, push the sample in the orange pot of tube, making sure it doesn't fall.
8) Then put back the blue cover with the dot facing me.
9) Click "close"(the 2 wings should block the sample).
10) Click "**purge airlock"**. When the machine is ready, it appears the "ready" green button.
11) When ready, open chamber (the handle should be vertical). Insert by rotations and grease it.
12) Rotate the second ring and close the black screws
13) Look at the graphic o the software. It should be "**centre**". Then push "**DC**", then "target field", then set field at **100 Oe**, set "**state charging**", actual field **100 Oe**.
14) Put the mass of the sample (in my case is 0.013 g = 13 mg)
15) **DC center** --> **initialise**--> transport--> sample go to button "**Full DC scan**".
16) Adjust position 5 cm. **Adjust automatically.**
17) Adjust automatically until "**Center Position**" is exactly 3 cm--> close.
18) Save on my personal folder.
19) Set field "0", because I need "0" field cool.
20) Cool down to 30K.

8.8. Flow cytometry antibodies

Table 15. Flow cytometry antibodies

Antibody	Product code
APC-conjugated CD34	130-098-139 (MACS Miltenyi Biotec)
VioBlue-conjugated CD45	130-098-136 (MACS Miltenyi Biotec)
PE-conjugated CD73	130-097-943 (MACS Miltenyi Biotec)
PE-conjugated Vio770 CD90	130-099-289 (MACS Miltenyi Biotec)
FITC-conjugated CD105	130-098-778 (MACS Miltenyi Biotec)

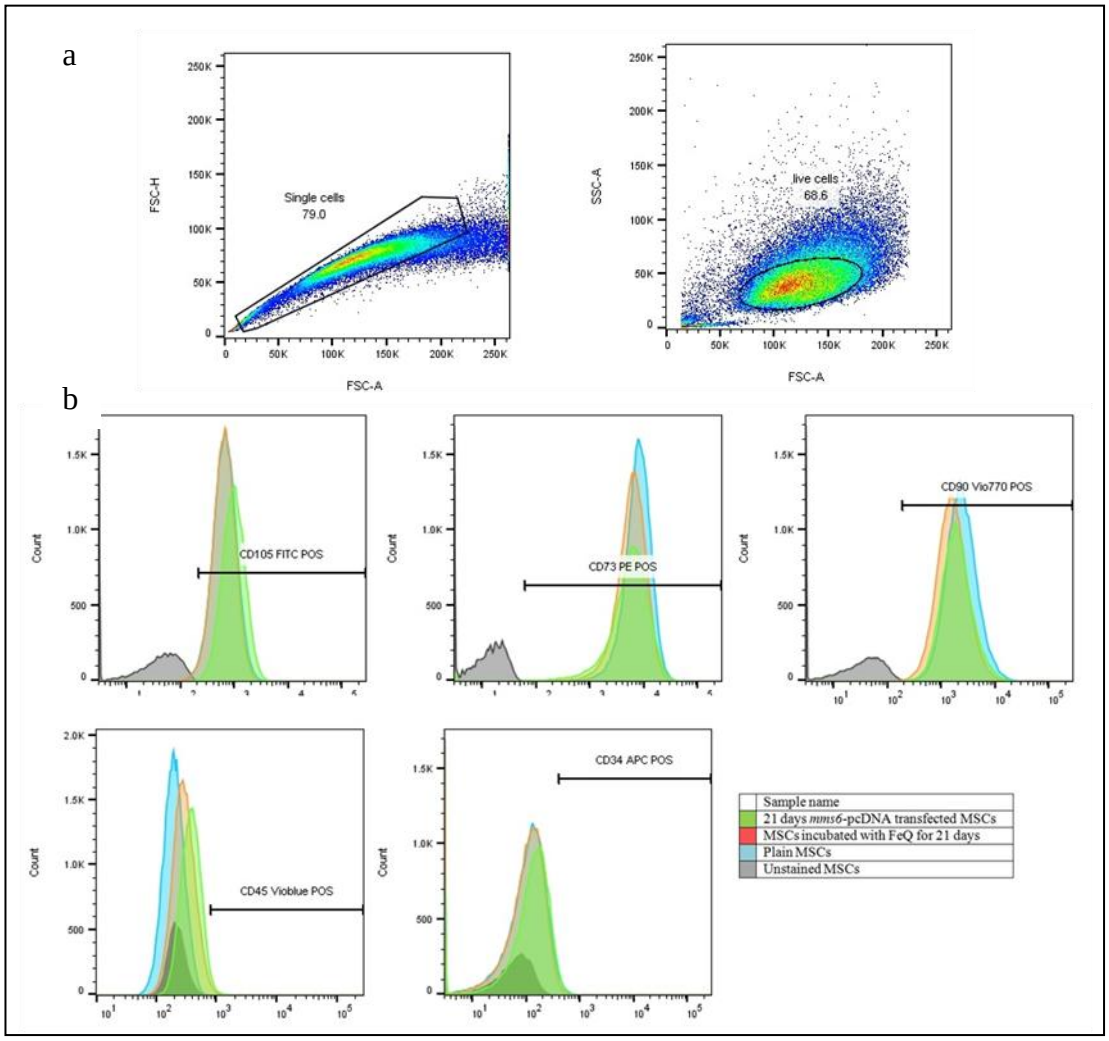

Figure 85. Example of gating strategy and staining for each antibody.

a) Example of gating strategy. Minimum 50000 events were collected using an electronic gate to exclude debris and dead cells, so the data for a minimum of 10000 'live' events occurred in the gate (Live cells gate). Data for all events were collected. b) Example of staining for each antibody.

8.9. S.O.P. magneTherm Treatment

1. Switch on water bath, then all other equipment except the magneTherm.
2. Anaesthetise the mouse, put Lacrilube in the eyes, then put the mouse on the ruler with the face mask on.
3. Slide the ruler into and slightly through the magneTherm to allow rectal probe or thermocouple wire to be inserted (use soft paraffin on these to aid insertion).
4. Push the ruler back into the magneTherm so that the tumours are centrally placed. Note the reading on the ruler to ensure that further treatments are all placed the same.
5. Plug in the magneTherm.
6. On the synthesised function generator (top) press “SHIFT+DUTY”. The reading should flash up as 50. Press “Hz/%” followed by the desired setting e.g. 565.3, then press “KHz”.
7. On the laboratory power supply (middle) turn the “Coarse” and “Fine” dials for the voltage until the reading is ⅓ of the final required power voltage (for 565.3KHz treatment this is approximately 8).
8. On the synthesised function generator (top) adjust the top right dial until the current reading (right) on the laboratory power supply (middle) reads 1.9.
9. On the laboratory power supply (middle) turn the “Coarse” and “Fine” dials for the voltage to the final required power voltage (for 565.3 KHz treatment this is 23.1). This may be approximate – adjust to around this and the current is approximately 5.1.
10. On the oscilloscope (bottom) use the vertical position dial (top left) to adjust the position of the waveform so that it is symmetrical.
11. Treat in the magneTherm for 30 minutes. The magneTherm will take 5 minutes to warm up, so discount the first 5 minutes of the first mouse to be treated.
12. Take skin temperature readings every 5 minutes during treatment. If a rectal thermometer is used take a note of the readings at every 5 minutes also, else if a thermocouple is used just check the reading.
13. After 30 minutes, switch off the laboratory power supply (middle) by turning the “Coarse” and “Fine” dials for the voltage to 0, then unplug the magneTherm.

14. Slide the ruler slightly through the magneTherm to allow rectal probe or thermocouple wire to be removed, then back through the magneTherm to remove the mouse.
15. Place mouse into the recovery box.
16. Repeat for all mice, then switch off all equipment.

8.10. TEM picture of late endosomes

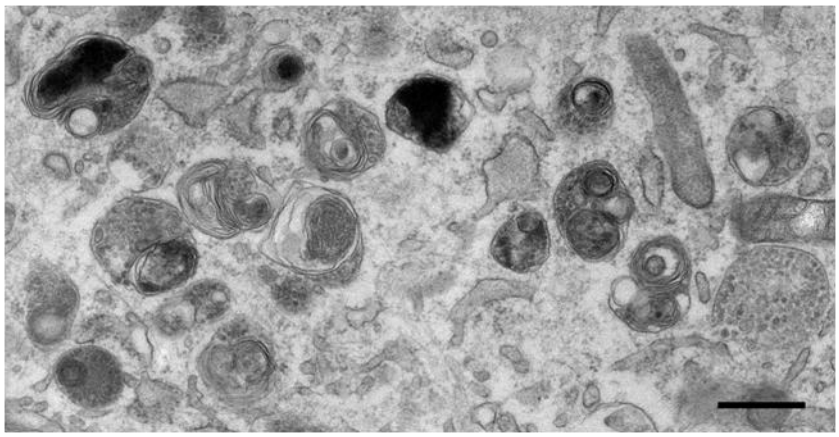

Figure 86. TEM picture of late endosomes.

Cell Biology Gallery, University of Liverpool. http://pcwww.liv.ac.uk/~emunit/gallerycell.html. Bar = 500nm.

8.11. AFM/MFM control experiments

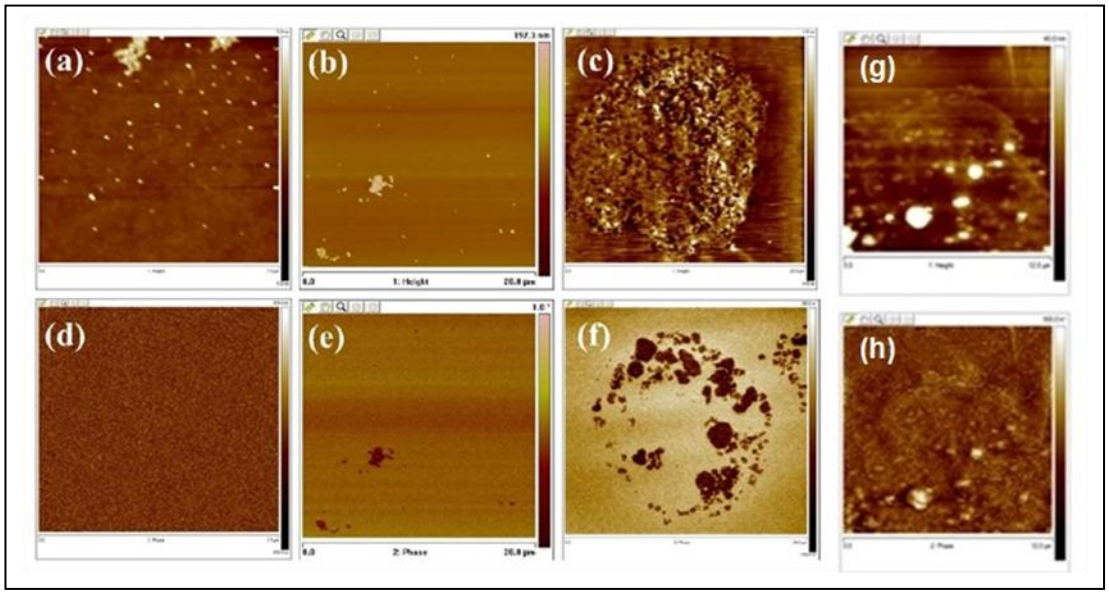

Figure 87. AFM/MFM control experiments.

AFM/MFM of $FeCl_3$ powder (a, d). Fluid Mag DXS nanoparticles (b, e). MSCs incubated with Fluid Mag DXS (c, f). MSCs untransfected (g,h). In the upper row are shown the topographic images (AFM) whilst the in the lower are shown the equivalent MFM images. Magnetic particles are clearly identified in the MFM images as clusters of black spots due to attractive forces, showing the capability of MFM to detect magnetic particles inside the cells. The absence of any features on (d) indicates the non-magnetic nature of $FeCl_3$ powder. Image widths: a,d) 7.1 µm, b,e) 20 µm, c) 25 µm f) 24 µm, g,h)12 µm.

8.12. Negative controls for OCN staining

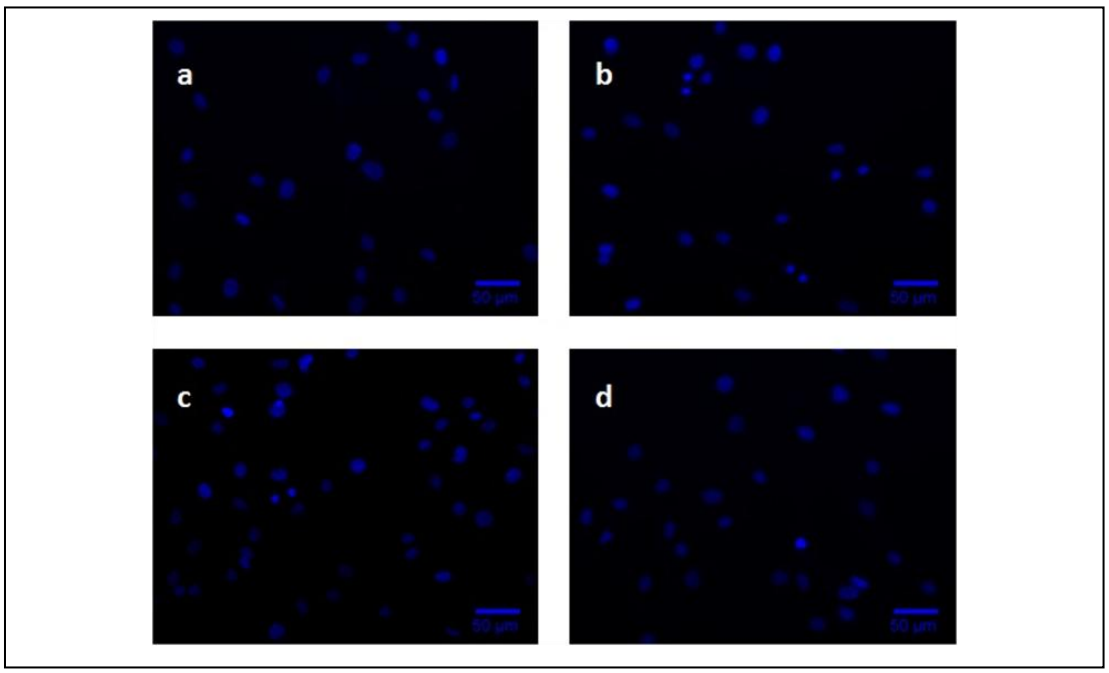

Figure 88. Representative images for negative controls for OCN staining.

Images were obtained by omitting the primary antibody. a) Negative control for wild-type MSCs (Plain), after 10 days of incubation with the osteogenic medium; b) Negative control for *mms6*-pcDNA3.1 transfected MSCs, after 10 days of incubation with the osteogenic medium; c) Negative control for wild-type MSCs (Plain), after 21 days of incubation with the osteogenic medium; d) Negative control for *mms6*-pcDNA3.1 transfected MSCs, after 21 days of incubation with the osteogenic medium. DAPI was used to stain the cell nuclei (blue). Images were taken using the confocal microscope. Scale bar is 50μm.

8.13. Experimental setup determination: choice of the AMF frequency and of the medium FBS percentage

To determine which AMF frequency was the most effective in causing cell death, four AMF frequencies were taken in consideration: 97.8 kHz, 296.4 kHz, 399.9 kHz, and 565.3 kHz.

21 days *mms6*-expressing MSCs were seeded in Petri dishes as indicated in the Materials and Methods Chapter, incubated overnight and exposed at the different frequencies for one hour the following morning. Then, the cell death was determined by Trypan Blue assay (**Figure 89**).

It was noticed that, when cells were cultivated in standard medium, supplemented with 20% FBS, the cell death percentage did not pass the 12% threshold (**Figure 89a**). It was hypothesised that the high concentration of FBS (20%) present in the medium could have a protective effect on AMF exposed cells, and so it was decided to lower it at 10% before the magneTherm exposure. Diminishing the FBS presence in the media, it was noticed a higher rate of cell death, as reported in the experiments below (**Figure 89b**). For this reason, the following experiments were performed using an exposure medium doped with 10% FBS instead of 20% FBS.

Results show that 565.3 kHz is the frequency that provides the highest degree of cell death (21% ± 4.6%), and so this frequency was chosen for the subsequent studies.

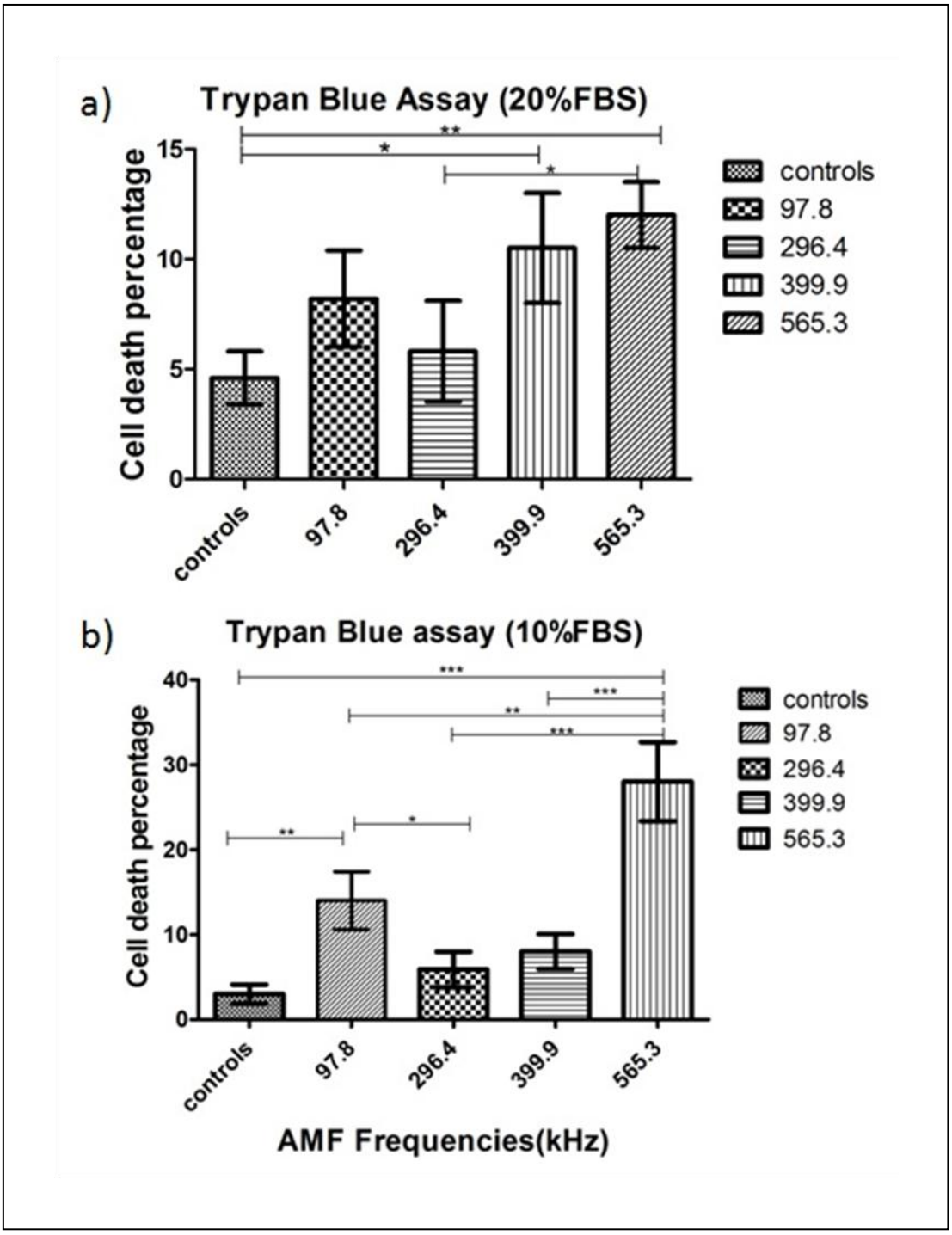

Figure 89. Experimental setup determination for in vitro cells exposure to AMF.

Cell death determination using Trypan Blue assay. a) 21 days *mms6*-expressing MSCs exposed at different AMF frequencies for one hour in presence of 20% FBS. b) 21 days *mms6*-expressing MSCs exposed at different AMF frequencies for one hour in presence of 10% FBS. Three independent experiments were considered. Results were compared using One-way ANOVA test followed by Tukey's test and considered statistically significant when p value <0.05%. Statistically significant results are indicated by asterisks.

8.14. Positive controls for Caspase-3 and Anti-human Nuclei Antibody Clone 3E1.3 staining.

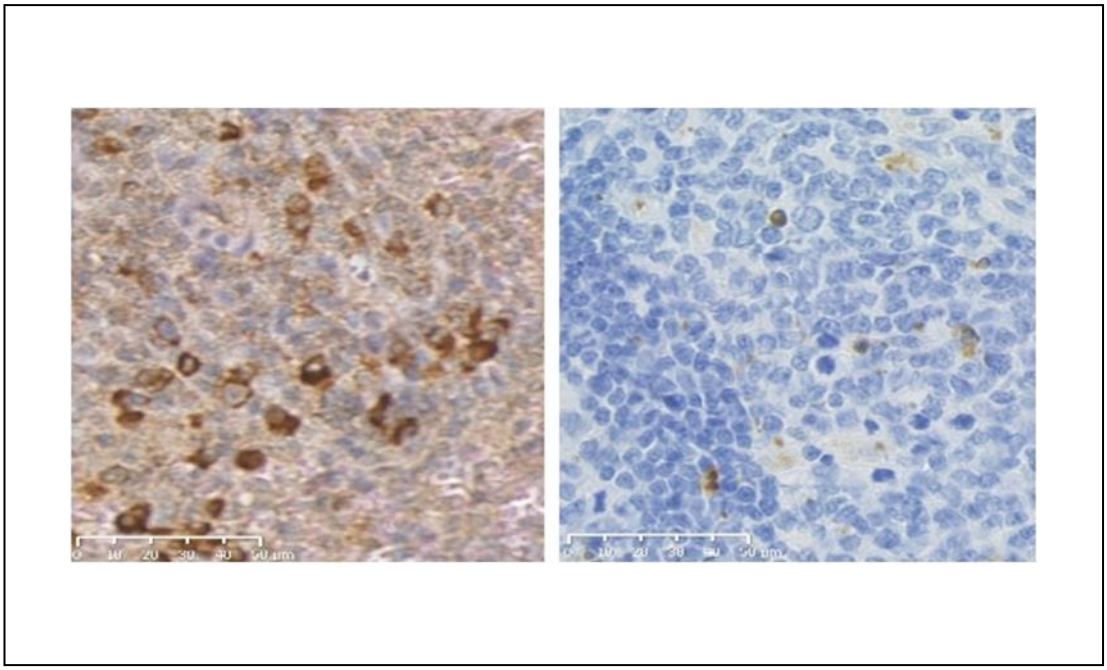

Figure 90. Positive controls for Caspase-3 and Anti-human Nuclei Antibody Clone 3E1.3 staining.

a) Anti-human Nuclei Antibody Clone 3E1.3 staining of formalin-fixed, paraffin-embedded human spleen tissue. b) Caspase-3 staining of formalin-fixed, paraffin-embedded human tonsil tissue. Scale bar=50µm.

8.15. Representation of *Viability Dye eFluor 450* staining followed by Multiphoton microscopy

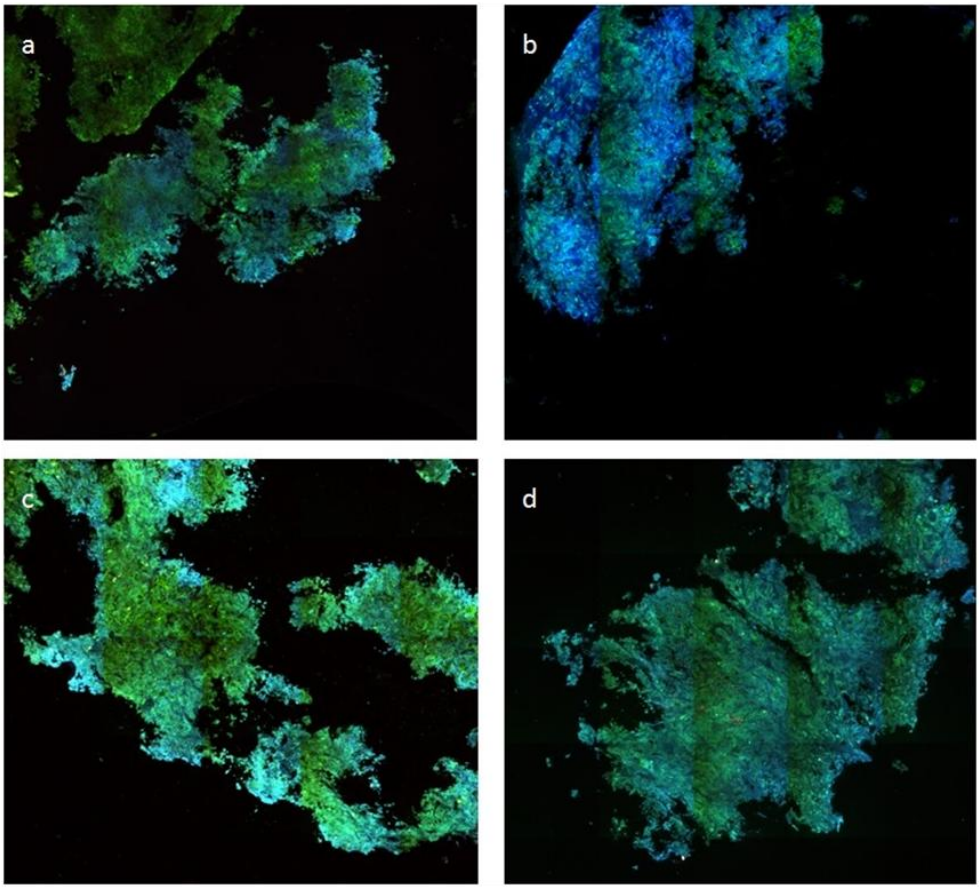

Figure 91. Viability Dye eFluor 450 staining, followed by Multiphoton microscopy.

Group C and Group D tumours were investigated by cellular uptake of Viability Dye eFluor® 450, followed by Multiphoton microscopy. Dead cells are stained in blue, while living cells are green.

a-b) Group C tumour cells. c-d) Group D tumour cells.

8.16. Oral and Poster Presentation

February 2015

Bologna AIMAGN Conference- "MAGNET 2015".

Poster Presentation: " Development and utility of magnetic nanoparticles production by mammalian cells."

March 2015

Glasgow Orthopaedic Research Initiative "GLORI 2015".

Oral Presentation-"Development and utility of magnetic nanoparticles production by mammalian cells."

December 2016

London IET Engineering Biology Conference 2016.
Oral Presentation-"Synthetic Biology for Cell-Based Anti-Cancer Therapies"
Elfick A, Azfer A, Lungaro L, Brunton V, Peault B, Salter D.

8.17. Published Paper

Elfick, A., Rischitor, G., Mouras, R., Azfer, A., Lungaro, L., Uhlarz, M., Herrmannsdörfer, T., Lucocq, J., Gamal, W., Bagnaninchi, P.,Semple, S., Salter, D. M. (2017). Biosynthesis of magnetic nanoparticles by human mesenchymal stem cells following transfection with the magnetotactic bacterial gene mms6. *Sci Rep, 7*, 39755. doi:10.1038/srep39755

9. Bibliography

Aggarwal, S., & Pittenger, M. F. (2005). Human mesenchymal stem cells modulate allogeneic immune cell responses. *Blood, 105*(4), 1815-1822. doi:10.1182/blood-2004-04-1559

Agoff, S. N., Hou, J., Linzer, D. I., & Wu, B. (1993). Regulation of the human hsp70 promoter by p53. *Science, 259*(5091), 84-87.

Ahmed, K., Tabuchi, Y., & Kondo, T. (2015). Hyperthermia: an effective strategy to induce apoptosis in cancer cells. *Apoptosis, 20*(11), 1411-1419. doi:10.1007/s10495-015-1168-3

Alphandery. (2014). Applications of Magnetosomes Synthesized by Magnetotactic Bacteria in Medicine. *Frontiers in Bioengineering and Biotechnology, 2*. doi:10.3389/fbioe.2014.00005

Alphandery, Chebbi, I., Guyot, F., & Durand-Dubief, M. (2013). Use of bacterial magnetosomes in the magnetic hyperthermia treatment of tumours: a review. *Int J Hyperthermia, 29*(8), 801-809. doi:10.3109/02656736.2013.821527

Alphandery, Faure, S., Seksek, O., Guyot, F., & Chebbi, I. (2011). Chains of magnetosomes extracted from AMB-1 magnetotactic bacteria for application in alternative magnetic field cancer therapy. *ACS Nano, 5*(8), 6279-6296. doi:10.1021/nn201290k

Alphandéry, E., Faure, S., Raison, L., Duguet, E., Howse, P. A., & Bazylinski, D. A. (2011). Heat Production by Bacterial Magnetosomes Exposed to an Oscillating Magnetic Field. *The Journal of Physical Chemistry C, 115*(1), 18-22. doi:10.1021/jp104580t

Alphandery, E., Faure, S., Seksek, O., Guyot, F., & Chebbi, I. (2011). Chains of magnetosomes extracted from AMB-1 magnetotactic bacteria for application in alternative magnetic field cancer therapy. *ACS Nano, 5*(8), 6279-6296. doi:10.1021/nn201290k

Alphandery, E., Guyot, F., & Chebbi, I. (2012). Preparation of chains of magnetosomes, isolated from Magnetospirillum magneticum strain AMB-1 magnetotactic bacteria, yielding efficient treatment of tumors using magnetic hyperthermia. *Int J Pharm, 434*(1-2), 444-452. doi:10.1016/j.ijpharm.2012.06.015

Alphandéry, E., Ngo, A. T., Lefèvre, C., Lisiecki, I., Wu, L. F., & Pileni, M. P. (2008). Difference between the Magnetic Properties of the Magnetotactic Bacteria and Those of the Extracted Magnetosomes: Influence of the Distance between the Chains of Magnetosomes. *The Journal of Physical Chemistry C, 112*(32), 12304-12309. doi:10.1021/jp800408t

Alvarez-Berrios, M. P., Castillo, A., Mendez, J., Soto, O., Rinaldi, C., & Torres-Lugo, M. (2013). Hyperthermic potentiation of cisplatin by magnetic nanoparticle heaters is correlated with an increase in cell membrane fluidity. *Int J Nanomedicine, 8*, 1003-1013. doi:10.2147/ijn.s38842

Amado, L. C., Saliaris, A. P., Schuleri, K. H., St John, M., Xie, J. S., Cattaneo, S., . . . Hare, J. M. (2005). Cardiac repair with intramyocardial injection of

allogeneic mesenchymal stem cells after myocardial infarction. *Proc Natl Acad Sci U S A, 102*(32), 11474-11479. doi:10.1073/pnas.0504388102

Amemiya, Y., Arakaki, A., Staniland, S. S., Tanaka, T., & Matsunaga, T. (2007). Controlled formation of magnetite crystal by partial oxidation of ferrous hydroxide in the presence of recombinant magnetotactic bacterial protein Mms6. *Biomaterials, 28*(35), 5381-5389. doi:10.1016/j.biomaterials.2007.07.051

Arakaki, A., Masuda, F., Amemiya, Y., Tanaka, T., & Matsunaga, T. (2010). Control of the morphology and size of magnetite particles with peptides mimicking the Mms6 protein from magnetotactic bacteria. *J Colloid Interface Sci, 343*(1), 65-70. doi:10.1016/j.jcis.2009.11.043

Arakaki, A., Webb, J., & Matsunaga, T. (2003). A novel protein tightly bound to bacterial magnetic particles in Magnetospirillum magneticum strain AMB-1. *J Biol Chem, 278*(10), 8745-8750. doi:10.1074/jbc.M211729200

Arakaki, A., Yamagishi, A., Fukuyo, A., Tanaka, M., & Matsunaga, T. (2014). Co-ordinated functions of Mms proteins define the surface structure of cubo-octahedral magnetite crystals in magnetotactic bacteria. *Mol Microbiol, 93*(3), 554-567. doi:10.1111/mmi.12683

Arango-Rodriguez, M. L., Ezquer, F., Ezquer, M., & Conget, P. (2015). Could cancer and infection be adverse effects of mesenchymal stromal cell therapy? *World J Stem Cells, 7*(2), 408-417. doi:10.4252/wjsc.v7.i2.408

Asin, L., Ibarra, M. R., Tres, A., & Goya, G. F. (2012). Controlled cell death by magnetic hyperthermia: effects of exposure time, field amplitude, and nanoparticle concentration. *Pharm Res, 29*(5), 1319-1327. doi:10.1007/s11095-012-0710-z

Aslan, B., Ozpolat, B., Sood, A. K., & Lopez-Berestein, G. (2013). Nanotechnology in cancer therapy. *J Drug Target, 21*(10), 904-913. doi:10.3109/1061186x.2013.837469

Attar, M. M., & Haghpanahi, M. (2016). Effect of heat dissipation of superparamagnetic nanoparticles in alternating magnetic field on three human cancer cell lines in magnetic fluid hyperthermia. *Electromagn Biol Med, 35*(4), 305-320. doi:10.3109/15368378.2015.1089409

Bae, J.-E., Huh, M.-I., Ryu, B.-K., Do, J.-Y., Jin, S.-U., Moon, M.-J., . . . Chae, K.-S. (2011). The effect of static magnetic fields on the aggregation and cytotoxicity of magnetic nanoparticles. *Biomaterials, 32*(35), 9401-9414. doi:https://doi.org/10.1016/j.biomaterials.2011.08.075

Barber-Zucker, S., Keren-Khadmy, N., & Zarivach, R. (2016). From invagination to navigation: The story of magnetosome-associated proteins in magnetotactic bacteria. *Protein Science, 25*(2), 338-351. doi:10.1002/pro.2827

Barber-Zucker, S., Keren-Khadmy, N., & Zarivach, R. (2016). From invagination to navigation: The story of magnetosome-associated proteins in magnetotactic bacteria. *Protein Science : A Publication of the Protein Society, 25*(2), 338-351. doi:10.1002/pro.2827

Bashir, J., Sherman, A., Lee, H., Kaplan, L., & Hare, J. M. (2014). Mesenchymal stem cell therapies in the treatment of musculoskeletal diseases. *Pm r, 6*(1), 61-69. doi:10.1016/j.pmrj.2013.05.007

Bazylinski, D. A., & Frankel, R. B. (2004). Magnetosome formation in prokaryotes. *Nat Rev Micro, 2*(3), 217-230.

doi:http://www.nature.com/nrmicro/journal/v2/n3/suppinfo/nrmicro842_S1.html

Beckermann, B. M., Kallifatidis, G., Groth, A., Frommhold, D., Apel, A., Mattern, J., . . . Herr, I. (2008). VEGF expression by mesenchymal stem cells contributes to angiogenesis in pancreatic carcinoma. *Br J Cancer, 99*(4), 622-631. doi:10.1038/sj.bjc.6604508

Beckman, J. S., & Koppenol, W. H. (1996). Nitric oxide, superoxide, and peroxynitrite: the good, the bad, and ugly. *Am J Physiol, 271*(5 Pt 1), C1424-1437.

Beik, J., Abed, Z., Ghoreishi, F. S., Hosseini-Nami, S., Mehrzadi, S., Shakeri-Zadeh, A., & Kamrava, S. K. (2016). Nanotechnology in hyperthermia cancer therapy: From fundamental principles to advanced applications. *Journal of Controlled Release, 235*, 205-221. doi:http://dx.doi.org/10.1016/j.jconrel.2016.05.062

Bennet, M., Bertinetti, L., Neely, R. K., Schertel, A., Kornig, A., Flors, C., . . . Faivre, D. (2015). Biologically controlled synthesis and assembly of magnetite nanoparticles. *Faraday Discuss, 181*, 71-83. doi:10.1039/c4fd00240g

Bergfeld, S. A., & DeClerck, Y. A. (2010). Bone marrow-derived mesenchymal stem cells and the tumor microenvironment. *Cancer Metastasis Rev, 29*(2), 249-261. doi:10.1007/s10555-010-9222-7

Bhayani, K. R., Rajwade, J. M., & Paknikar, K. M. (2013). Radio frequency induced hyperthermia mediated by dextran stabilized LSMO nanoparticles: in vitro evaluation of heat shock protein response. *Nanotechnology, 24*(1), 015102. doi:10.1088/0957-4484/24/1/015102

Binhi, V., & Chernavskii, D. (2005). Stochastic dynamics of magnetosomes in cytoskeleton. *EPL (Europhysics Letters), 70*(6), 850.

Birbrair, A., Zhang, T., Wang, Z. M., Messi, M. L., Olson, J. D., Mintz, A., & Delbono, O. (2014). Type-2 pericytes participate in normal and tumoral angiogenesis. *Am J Physiol Cell Physiol, 307*(1), C25-38. doi:10.1152/ajpcell.00084.2014

Bird, S. M., Rawlings, A. E., Galloway, J. M., & Staniland, S. S. (2016). Using a biomimetic membrane surface experiment to investigate the activity of the magnetite biomineralisation protein Mms6. *RSC Adv, 6*(9), 7356-7363. doi:10.1039/c5ra16469a

Blakemore, Frankel, R. B., & Kalmijn, A. J. (1980). South-seeking magnetotactic bacteria in the Southern Hemisphere. *Nature, 286*(5771), 384-385.

Blakemore, R. (1975). Magnetotactic bacteria. *Science, 190*(4212), 377-379.

Bobis-Wozowicz, S., Miekus, K., Wybieralska, E., Jarocha, D., Zawisz, A., Madeja, Z., & Majka, M. (2011). Genetically modified adipose tissue-derived mesenchymal stem cells overexpressing CXCR4 display increased motility, invasiveness, and homing to bone marrow of NOD/SCID mice. *Exp Hematol, 39*(6), 686-696.e684. doi:10.1016/j.exphem.2011.03.004

Bogart, L. K., Pourroy, G., Murphy, C. J., Puntes, V., Pellegrino, T., Rosenblum, D., . . . Levy, R. (2014). Nanoparticles for imaging, sensing, and therapeutic intervention. *ACS Nano, 8*(4), 3107-3122. doi:10.1021/nn500962q

Bonzon, C., Bouchier-Hayes, L., Pagliari, L. J., Green, D. R., & Newmeyer, D. D. (2006). Caspase-2-induced apoptosis requires bid cleavage: a physiological

role for bid in heat shock-induced death. *Mol Biol Cell, 17*(5), 2150-2157. doi:10.1091/mbc.E05-12-1107

Botzler, C., Li, G., Issels, R. D., & Multhoff, G. (1998). Definition of extracellular localized epitopes of Hsp70 involved in an NK immune response. *Cell Stress Chaperones, 3*(1), 6-11.

Botzler, C., Schmidt, J., Luz, A., Jennen, L., Issels, R., & Multhoff, G. (1998). Differential Hsp70 plasma-membrane expression on primary human tumors and metastases in mice with severe combined immunodeficiency. *Int J Cancer, 77*(6), 942-948.

Bouchier-Hayes, L., Oberst, A., McStay, G. P., Connell, S., Tait, S. W., Dillon, C. P., . . . Green, D. R. (2009). Characterization of cytoplasmic caspase-2 activation by induced proximity. *Mol Cell, 35*(6), 830-840. doi:10.1016/j.molcel.2009.07.023

Branquinho, L. C., Carriao, M. S., Costa, A. S., Zufelato, N., Sousa, M. H., Miotto, R., . . . Bakuzis, A. F. (2013). Effect of magnetic dipolar interactions on nanoparticle heating efficiency: implications for cancer hyperthermia. *Sci Rep, 3*, 2887. doi:10.1038/srep02887

Brokx, S. J., Rothery, R. A., Zhang, G., Ng, D. P., & Weiner, J. H. (2005). Characterization of an Escherichia coli sulfite oxidase homologue reveals the role of a conserved active site cysteine in assembly and function. *Biochemistry, 44*(30), 10339-10348. doi:10.1021/bi050621a

Buchner, J. (1996). Supervising the fold: functional principles of molecular chaperones. *Faseb j, 10*(1), 10-19.

Buschmann, I. R., Hoefer, I. E., van Royen, N., Katzer, E., Braun-Dulleaus, R., Heil, M., . . . Schaper, W. (2001). GM-CSF: a strong arteriogenic factor acting by amplification of monocyte function. *Atherosclerosis, 159*(2), 343-356.

Butcher, L. J. P. (1996). Lymphocyte Homing and Homeostasis. *Science, Vol. 272*(Issue 5258), pp. 60-67. doi:DOI: 10.1126/science.272.5258.60

Calderwood, S. K., & Hahn, G. M. (1983). Thermal sensitivity and resistance of insulin-receptor binding. *Biochim Biophys Acta, 756*(1), 1-8.

Caplan, A. I., & Dennis, J. E. (2006). Mesenchymal stem cells as trophic mediators. *J Cell Biochem, 98*(5), 1076-1084. doi:10.1002/jcb.20886

Carrey, J., Connord, V., & Respaud, M. (2013). Ultrasound generation and high-frequency motion of magnetic nanoparticles in an alternating magnetic field: Toward intracellular ultrasound therapy? *Applied Physics Letters, 102*(23), 232404. doi:10.1063/1.4810972

Carrey, J., Mehdaoui, B., & Respaud, M. (2011a). Publisher's Note: "Simple models for dynamic hysteresis loop calculations of magnetic single-domain nanoparticles: Application to magnetic hyperthermia optimization" [J. Appl. Phys. 109, 083921 (2011)]. *Journal of Applied Physics, 110*(3), 039902. doi:10.1063/1.3617122

Carrey, J., Mehdaoui, B., & Respaud, M. (2011b). Simple models for dynamic hysteresis loop calculations of magnetic single-domain nanoparticles: Application to magnetic hyperthermia optimization. *Journal of Applied Physics, 109*(8), 083921. doi:10.1063/1.3551582

Cartmell, S. H., Dobson, J., Verschueren, S. B., & El Haj, A. J. (2002). Development of magnetic particle techniques for long-term culture of bone cells with intermittent mechanical activation. *IEEE transactions on nanobioscience, 99*(2), 92-97.

Chan, F. K., Moriwaki, K., & De Rosa, M. J. (2013). Detection of necrosis by release of lactate dehydrogenase activity. *Methods Mol Biol, 979*, 65-70. doi:10.1007/978-1-62703-290-2_7

Chang, Y. K., Liu, Y. P., Ho, J. H., Hsu, S. C., & Lee, O. K. (2012). Amine-surface-modified superparamagnetic iron oxide nanoparticles interfere with differentiation of human mesenchymal stem cells. *J Orthop Res, 30*(9), 1499-1506. doi:10.1002/jor.22088

Chen, L., Chen, C., Wang, P., & Song, T. (2017). Mechanisms of Cellular Effects Directly Induced by Magnetic Nanoparticles under Magnetic Fields. *Journal of Nanomaterials, 2017*, 13. doi:10.1155/2017/1564634

Chen, X., Lin, X., Zhao, J., Shi, W., Zhang, H., Wang, Y., . . . Zhao, X. (2008). A tumor-selective biotherapy with prolonged impact on established metastases based on cytokine gene-engineered MSCs. *Mol Ther, 16*(4), 749-756. doi:10.1038/mt.2008.3

Chen, X. C., Wang, R., Zhao, X., Wei, Y. Q., Hu, M., Wang, Y. S., . . . Li, J. (2006). Prophylaxis against carcinogenesis in three kinds of unestablished tumor models via IL12-gene-engineered MSCs. *Carcinogenesis, 27*(12), 2434-2441. doi:10.1093/carcin/bgl069

Chen, Y. C., Hsiao, J. K., Liu, H. M., Lai, I. Y., Yao, M., Hsu, S. C., . . . Huang, D. M. (2010). The inhibitory effect of superparamagnetic iron oxide nanoparticle (Ferucarbotran) on osteogenic differentiation and its signaling mechanism in human mesenchymal stem cells. *Toxicol Appl Pharmacol, 245*(2), 272-279. doi:10.1016/j.taap.2010.03.011

Chiu, R. C. (2005). "Stealth immune tolerance" in stem cell transplantation: potential for "universal donors" in myocardial regenerative therapy. *J Heart Lung Transplant, 24*(5), 511-516. doi:10.1016/j.healun.2004.11.010

Ciocca, D. R., Oesterreich, S., Chamness, G. C., McGuire, W. L., & Fuqua, S. A. (1993). Biological and clinical implications of heat shock protein 27,000 (Hsp27): a review. *J Natl Cancer Inst, 85*(19), 1558-1570.

Cole, A. J., Yang, V. C., & David, A. E. (2011). Cancer theranostics: the rise of targeted magnetic nanoparticles. *Trends Biotechnol, 29*(7), 323-332. doi:10.1016/j.tibtech.2011.03.001

Connell, J. J., Patrick, P. S., Yu, Y., Lythgoe, M. F., & Kalber, T. L. (2015). Advanced cell therapies: targeting, tracking and actuation of cells with magnetic particles. *Regen Med, 10*(6), 757-772. doi:10.2217/rme.15.36

Connord, V., Clerc, P., Hallali, N., El Hajj Diab, D., Fourmy, D., Gigoux, V., & Carrey, J. (2015). Real-Time Analysis of Magnetic Hyperthermia Experiments on Living Cells under a Confocal Microscope. *Small, 11*(20), 2437-2445. doi:10.1002/smll.201402669

Corbet, C., & Feron, O. (2017). Tumour acidosis: from the passenger to the driver's seat. *Nat Rev Cancer, 17*(10), 577-593. doi:10.1038/nrc.2017.77

Corcione, A., Benvenuto, F., Ferretti, E., Giunti, D., Cappiello, V., Cazzanti, F., . . . Uccelli, A. (2006). Human mesenchymal stem cells modulate B-cell functions. *Blood, 107*(1), 367-372. doi:10.1182/blood-2005-07-2657

Corselli, M., Chen, C. W., Sun, B., Yap, S., Rubin, J. P., & Peault, B. (2012). The tunica adventitia of human arteries and veins as a source of mesenchymal stem cells. *Stem Cells Dev, 21*(8), 1299-1308. doi:10.1089/scd.2011.0200

Corsten, M. F., & Shah, K. (2008). Therapeutic stem-cells for cancer treatment: hopes and hurdles in tactical warfare. *Lancet Oncol, 9*(4), 376-384. doi:10.1016/s1470-2045(08)70099-8

Cosentino, K., & Garcia-Saez, A. J. (2014). Mitochondrial alterations in apoptosis. *Chem Phys Lipids, 181*, 62-75. doi:10.1016/j.chemphyslip.2014.04.001

Coss, R. A., & Linnemans, W. A. (1996). The effects of hyperthermia on the cytoskeleton: a review. *Int J Hyperthermia, 12*(2), 173-196.

Cousin, B., Ravet, E., Poglio, S., De Toni, F., Bertuzzi, M., Lulka, H., . . . Cordelier, P. (2009). Adult stromal cells derived from human adipose tissue provoke pancreatic cancer cell death both in vitro and in vivo. *PLoS One, 4*(7), e6278. doi:10.1371/journal.pone.0006278

Crisan, M., Corselli, M., Chen, W. C. W., Péault, B., & Moldovan, N. I. (2012). Perivascular cells for regenerative medicine. *Journal of Cellular and Molecular Medicine, 16*(12), 2851-2860. doi:10.1111/j.1582-4934.2012.01617.x

da Silva Meirelles, L., Caplan, A. I., & Nardi, N. B. (2008). In search of the in vivo identity of mesenchymal stem cells. *Stem Cells, 26*(9), 2287-2299. doi:10.1634/stemcells.2007-1122

Damaghi, M., Tafreshi, N. K., Lloyd, M. C., Sprung, R., Estrella, V., Wojtkowiak, J. W., . . . Gillies, R. J. (2015). Chronic acidosis in the tumour microenvironment selects for overexpression of LAMP2 in the plasma membrane. *Nat Commun, 6*, 8752. doi:10.1038/ncomms9752

Dasari, V. R., Kaur, K., Velpula, K. K., Gujrati, M., Fassett, D., Klopfenstein, J. D., . . . Rao, J. S. (2010). Upregulation of PTEN in glioma cells by cord blood mesenchymal stem cells inhibits migration via downregulation of the PI3K/Akt pathway. *PLoS One, 5*(4), e10350. doi:10.1371/journal.pone.0010350

Dasari, V. R., Velpula, K. K., Kaur, K., Fassett, D., Klopfenstein, J. D., Dinh, D. H., . . . Rao, J. S. (2010). Cord blood stem cell-mediated induction of apoptosis in glioma downregulates X-linked inhibitor of apoptosis protein (XIAP). *PLoS One, 5*(7), e11813. doi:10.1371/journal.pone.0011813

De Becker, A., & Riet, I. V. (2016). Homing and migration of mesenchymal stromal cells: How to improve the efficacy of cell therapy? *World J Stem Cells, 8*(3), 73-87. doi:10.4252/wjsc.v8.i3.73

De Becker, A., Van Hummelen, P., Bakkus, M., Vande Broek, I., De Wever, J., De Waele, M., & Van Riet, I. (2007). Migration of culture-expanded human mesenchymal stem cells through bone marrow endothelium is regulated by matrix metalloproteinase-2 and tissue inhibitor of metalloproteinase-3. *Haematologica, 92*(4), 440-449.

De Becker, A., & Van Riet, I. (2015). Mesenchymal Stromal Cell Therapy in Hematology: From Laboratory to Clinic and Back Again. *Stem Cells Dev, 24*(15), 1713-1729. doi:10.1089/scd.2014.0564

Deatsch, A. E., & Evans, B. A. (2014). Heating efficiency in magnetic nanoparticle hyperthermia. *Journal of Magnetism and Magnetic Materials, 354*, 163-172. doi:https://doi.org/10.1016/j.jmmm.2013.11.006

Dembinski, J. L., Spaeth, E. L., Fueyo, J., Gomez-Manzano, C., Studeny, M., Andreeff, M., & Marini, F. C. (2010). Reduction of nontarget infection and systemic toxicity by targeted delivery of conditionally replicating viruses transported in mesenchymal stem cells. *Cancer Gene Ther, 17*(4), 289-297. doi:10.1038/cgt.2009.67

DiBartolomeis, S. M., & Moné, J. P. (2003). Apoptosis: A Four-Week Laboratory Investigation for Advanced Molecular and Cellular Biology Students. *Cell Biology Education, 2*, 275-295. doi:10.1187/cbe.03-06-0027

Ding, Y., Li, J., Liu, J., Yang, J., Jiang, W., Tian, J., . . . Li, J. (2010). Deletion of the ftsZ-like gene results in the production of superparamagnetic magnetite magnetosomes in Magnetospirillum gryphiswaldense. *J Bacteriol, 192*(4), 1097-1105. doi:10.1128/jb.01292-09

Dobson, J., Cartmell, S. H., Keramane, A., & El Haj, A. J. (2006). Principles and design of a novel magnetic force mechanical conditioning bioreactor for tissue engineering, stem cell conditioning, and dynamic in vitro screening. *IEEE transactions on nanobioscience, 5*(3), 173-177.

Domenech, M., Marrero-Berrios, I., Torres-Lugo, M., & Rinaldi, C. (2013). Lysosomal membrane permeabilization by targeted magnetic nanoparticles in alternating magnetic fields. *ACS Nano, 7*(6), 5091-5101. doi:10.1021/nn4007048

Dominici, M., Le Blanc, K., Mueller, I., Slaper-Cortenbach, I., Marini, F., Krause, D., . . . Horwitz, E. (2006). Minimal criteria for defining multipotent mesenchymal stromal cells. The International Society for Cellular Therapy position statement. *Cytotherapy, 8*(4), 315-317. doi:10.1080/14653240600855905

Draper, O., Byrne, M. E., Li, Z., Keyhani, S., Barrozo, J. C., Jensen, G., & Komeili, A. (2011). MamK, a bacterial actin, forms dynamic filaments in vivo that are regulated by the acidic proteins MamJ and LimJ. *Mol Microbiol, 82*(2), 342-354. doi:10.1111/j.1365-2958.2011.07815.x

Du, J., Zhou, L., Chen, X., Yan, S., Ke, M., Lu, X., . . . Xiang, A. P. (2012). IFN-gamma-primed human bone marrow mesenchymal stem cells induce tumor cell apoptosis in vitro via tumor necrosis factor-related apoptosis-inducing ligand. *Int J Biochem Cell Biol, 44*(8), 1305-1314. doi:10.1016/j.biocel.2012.04.015

Durinikova, E., Kucerova, L., & Matuskova, M. (2014). Mesenchymal stromal cells retrovirally transduced with prodrug-converting genes are suitable vehicles for cancer gene therapy. *Acta Virol, 58*(1), 1-13.

Dutz, S., & Hergt, R. (2014). Magnetic particle hyperthermia--a promising tumour therapy? *Nanotechnology, 25*(45), 452001. doi:10.1088/0957-4484/25/45/452001

Dutz, S., Hergt, R., Mürbe, J., Müller, R., Zeisberger, M., Andrä, W., . . . Bellemann, M. E. (2007). Hysteresis losses of magnetic nanoparticle powders in the single domain size range. *Journal of Magnetism and Magnetic Materials, 308*(2), 305-312. doi:http://doi.org/10.1016/j.jmmm.2006.06.005

Eggenhofer, E., Benseler, V., Kroemer, A., Popp, F. C., Geissler, E. K., Schlitt, H. J., . . . Hoogduijn, M. J. (2012). Mesenchymal stem cells are short-lived and do not migrate beyond the lungs after intravenous infusion. *Front Immunol, 3*, 297. doi:10.3389/fimmu.2012.00297

El-Orabi, N. F., Rogers, C. B., Gray Edwards, H., & Schwartz, D. D. (2011). Heat-induced inhibition of superoxide dismutase and accumulation of reactive oxygen species leads to HT-22 neuronal cell death. *Journal of Thermal Biology, 36*(1), 49-56. doi:http://doi.org/10.1016/j.jtherbio.2010.11.002

Elfick, A., Rischitor, G., Mouras, R., Azfer, A., Lungaro, L., Uhlarz, M., . . . Salter, D. M. (2017). Biosynthesis of magnetic nanoparticles by human mesenchymal stem cells following transfection with the magnetotactic bacterial gene mms6. *Sci Rep, 7*, 39755. doi:10.1038/srep39755

Eliopoulos, N., Francois, M., Boivin, M. N., Martineau, D., & Galipeau, J. (2008). Neo-organoid of marrow mesenchymal stromal cells secreting interleukin-12 for breast cancer therapy. *Cancer Res, 68*(12), 4810-4818. doi:10.1158/0008-5472.can-08-0160

Engelman, J. A., Luo, J., & Cantley, L. C. (2006). The evolution of phosphatidylinositol 3-kinases as regulators of growth and metabolism. *Nat Rev Genet, 7*(8), 606-619. doi:10.1038/nrg1879

Erta, M., Quintana, A., & Hidalgo, J. (2012). Interleukin-6, a major cytokine in the central nervous system. *Int J Biol Sci, 8*(9), 1254-1266. doi:10.7150/ijbs.4679

Estevanato, L. L. C., Silva, J. R. D., Falqueiro, A. M., Mosiniewicz-Szablewska, E., Suchocki, P., Tedesco, A. C., . . . Lacava, Z. G. M. (2012). Co-nanoencapsulation of magnetic nanoparticles and selol for breast tumor treatment: in vitro evaluation of cytotoxicity and magnetohyperthermia efficacy. *Int J Nanomedicine, 7*, 5287-5299. doi:10.2147/IJN.S35279

Faini, M., Beck, R., Wieland, F. T., & Briggs, J. A. (2013). Vesicle coats: structure, function, and general principles of assembly. *Trends Cell Biol, 23*(6), 279-288. doi:10.1016/j.tcb.2013.01.005

Faivre, D., & Godec, T. U. (2015). From bacteria to mollusks: the principles underlying the biomineralization of iron oxide materials. *Angew Chem Int Ed Engl, 54*(16), 4728-4747. doi:10.1002/anie.201408900

Farrell, E., Wielopolski, P., Pavljasevic, P., van Tiel, S., Jahr, H., Verhaar, J., . . . Bernsen, M. (2008). Effects of iron oxide incorporation for long term cell tracking on MSC differentiation in vitro and in vivo. *Biochem Biophys Res Commun, 369*(4), 1076-1081. doi:10.1016/j.bbrc.2008.02.159

Ferraro, F., Celso, C. L., & Scadden, D. (2010). ADULT STEM CELLS AND THEIR NICHES. *Advances in experimental medicine and biology, 695*, 155-168. doi:10.1007/978-1-4419-7037-4_11

Finlay, C. A., Hinds, P. W., Tan, T. H., Eliyahu, D., Oren, M., & Levine, A. J. (1988). Activating mutations for transformation by p53 produce a gene product that forms an hsc70-p53 complex with an altered half-life. *Mol Cell Biol, 8*(2), 531-539.

Fortin, J.-P., Wilhelm, C., Servais, J., Ménager, C., Bacri, J.-C., & Gazeau, F. (2007). Size-Sorted Anionic Iron Oxide Nanomagnets as Colloidal Mediators for Magnetic Hyperthermia. *Journal of the American Chemical Society, 129*(9), 2628-2635. doi:10.1021/ja067457e

Fouillard, L., Chapel, A., Bories, D., Bouchet, S., Costa, J. M., Rouard, H., . . . Gorin, N. C. (2007). Infusion of allogeneic-related HLA mismatched mesenchymal stem cells for the treatment of incomplete engraftment following autologous haematopoietic stem cell transplantation. *Leukemia, 21*(3), 568-570. doi:10.1038/sj.leu.2404550

Frankel, R. B., & Bazylinski, D. A. (2006). How magnetotactic bacteria make magnetosomes queue up. *Trends Microbiol, 14*(8), 329-331. doi:10.1016/j.tim.2006.06.004

Frankel, R. B., Bazylinski, D. A., Johnson, M. S., & Taylor, B. L. (1997). Magneto-aerotaxis in marine coccoid bacteria. *Biophysical Journal, 73*(2), 994-1000.

Frankel, R. B., Blakemore, R. P., FF, D. E. A., Esquivel, D. M., & Danon, J. (1981). Magnetotactic bacteria at the geomagnetic equator. *Science, 212*(4500), 1269-1270. doi:10.1126/science.212.4500.1269

Fukuda, Y., Okamura, Y., Takeyama, H., & Matsunaga, T. (2006). Dynamic analysis of a genomic island in Magnetospirillum sp. strain AMB-1 reveals how magnetosome synthesis developed. *FEBS Lett, 580*(3), 801-812. doi:10.1016/j.febslet.2006.01.003

Fuller, K. J., Issels, R. D., Slosman, D. O., Guillet, J. G., Soussi, T., & Polla, B. S. (1994). Cancer and the heat shock response. *Eur J Cancer, 30a*(12), 1884-1891.

Furusawa, Y., Iizumi, T., Fujiwara, Y., Zhao, Q. L., Tabuchi, Y., Nomura, T., & Kondo, T. (2012). Inhibition of checkpoint kinase 1 abrogates G2/M checkpoint activation and promotes apoptosis under heat stress. *Apoptosis, 17*(1), 102-112. doi:10.1007/s10495-011-0660-7

Galloway J.M., Bramble J.P., Rawlings A.E., Burnell G., Evans S.D., & S.S., S. (2012). Nanomagnetic arrays formed with the biomineralization protein Mms6. . *J. Nano. Res., 17*, 127–146. doi:doi:10.4028/www.scientific.net/JNanoR.17.127

Gao, P., Ding, Q., Wu, Z., Jiang, H., & Fang, Z. (2010). Therapeutic potential of human mesenchymal stem cells producing IL-12 in a mouse xenograft model of renal cell carcinoma. *Cancer Lett, 290*(2), 157-166. doi:10.1016/j.canlet.2009.08.031

Giorgi, C., Bonora, M., Sorrentino, G., Missiroli, S., Poletti, F., Suski, J. M., . . . Pinton, P. (2015). p53 at the endoplasmic reticulum regulates apoptosis in a Ca2+-dependent manner. *Proc Natl Acad Sci U S A, 112*(6), 1779-1784. doi:10.1073/pnas.1410723112

Glennie, S., Soeiro, I., Dyson, P. J., Lam, E. W., & Dazzi, F. (2005). Bone marrow mesenchymal stem cells induce division arrest anergy of activated T cells. *Blood, 105*(7), 2821-2827. doi:10.1182/blood-2004-09-3696

Glish, G. L., & Vachet, R. W. (2003). The basics of mass spectrometry in the twenty-first century. *Nat Rev Drug Discov, 2*(2), 140-150. doi:10.1038/nrd1011

Goldhawk, D. E., Lemaire, C., McCreary, C. R., McGirr, R., Dhanvantari, S., Thompson, R. T., . . . Prato, F. S. (2009). Magnetic resonance imaging of cells overexpressing MagA, an endogenous contrast agent for live cell imaging. *Mol Imaging, 8*(3), 129-139.

Goldman, D., & Domschke, K. (2014). Making sense of deep sequencing. *International Journal of Neuropsychopharmacology, 17*(10), 1717-1725. doi:10.1017/S1461145714000789

Goldstein, R. H., Reagan, M. R., Anderson, K., Kaplan, D. L., & Rosenblatt, M. (2010). Human bone marrow-derived MSCs can home to orthotopic breast cancer tumors and promote bone metastasis. *Cancer Res, 70*(24), 10044-10050. doi:10.1158/0008-5472.can-10-1254

Gorby, Y. A., Beveridge, T. J., & Blakemore, R. P. (1988). Characterization of the bacterial magnetosome membrane. *Journal of Bacteriology, 170*(2), 834-841.

Gorojod, R. M., Alaimo, A., Porte Alcon, S., Saravia, F., & Kotler, M. L. (2017). Interplay between lysosomal, mitochondrial and death receptor pathways during manganese-induced apoptosis in glial cells. *Archives of Toxicology, 91*(9), 3065-3078. doi:10.1007/s00204-017-1936-7

Grunberg, K., Muller, E. C., Otto, A., Reszka, R., Linder, D., Kube, M., . . . Schuler, D. (2004). Biochemical and proteomic analysis of the magnetosome membrane in Magnetospirillum gryphiswaldense. *Appl Environ Microbiol, 70*(2), 1040-1050.

Grunberg, K., Wawer, C., Tebo, B. M., & Schuler, D. (2001). A large gene cluster encoding several magnetosome proteins is conserved in different species of magnetotactic bacteria. *Appl Environ Microbiol, 67*(10), 4573-4582.

Gu, G., Qi, H., Jiang, T., Ma, B., Fang, Z., Xu, H., & Zhang, Q. (2017). Investigation of the cytotoxicity, apoptosis and pharmacokinetics of Raddeanin A. *Oncology Letters, 13*(3), 1365-1369. doi:10.3892/ol.2017.5588

Gudoshnikov, S. A., Liubimov, B. Y., & Usov, N. A. (2012). Hysteresis losses in a dense superparamagnetic nanoparticle assembly. *AIP Advances, 2*(1), 012143. doi:10.1063/1.3688084

Guo, F. F., Yang, W., Jiang, W., Geng, S., Peng, T., & Li, J. L. (2012). Magnetosomes eliminate intracellular reactive oxygen species in Magnetospirillum gryphiswaldense MSR-1. *Environ Microbiol, 14*(7), 1722-1729. doi:10.1111/j.1462-2920.2012.02707.x

Haase, C., & Nowak, U. (2012). Role of dipole-dipole interactions for hyperthermia heating of magnetic nanoparticle ensembles. *Physical Review B, 85*(4), 045435.

Habash, R. W., Bansal, R., Krewski, D., & Alhafid, H. T. (2006). Thermal therapy, part 2: hyperthermia techniques. *Crit Rev Biomed Eng, 34*(6), 491-542.

Hakkarainen, T., Sarkioja, M., Lehenkari, P., Miettinen, S., Ylikomi, T., Suuronen, R., . . . Hemminki, A. (2007). Human mesenchymal stem cells lack tumor tropism but enhance the antitumor activity of oncolytic adenoviruses in orthotopic lung and breast tumors. *Hum Gene Ther, 18*(7), 627-641. doi:10.1089/hum.2007.034

Hamada, H., Kobune, M., Nakamura, K., Kawano, Y., Kato, K., Honmou, O., . . . Niitsu, Y. (2005). Mesenchymal stem cells (MSC) as therapeutic cytoreagents for gene therapy. *Cancer Sci, 96*(3), 149-156. doi:10.1111/j.1349-7006.2005.00032.x

Hammer, K., Kazcorowski, A., Liu, L., Behr, M., Schemmer, P., Herr, I., & Nettelbeck, D. M. (2015). Engineered adenoviruses combine enhanced oncolysis with improved virus production by mesenchymal stromal carrier cells. *Int J Cancer, 137*(4), 978-990. doi:10.1002/ijc.29442

Han, J., Back, S. H., Hur, J., Lin, Y. H., Gildersleeve, R., Shan, J., . . . Kaufman, R. J. (2013). ER-stress-induced transcriptional regulation increases protein synthesis leading to cell death. *Nat Cell Biol, 15*(5), 481-490. doi:10.1038/ncb2738

He, S., Nakada, D., & Morrison, S. J. (2009). Mechanisms of stem cell self-renewal. *Annu Rev Cell Dev Biol, 25*, 377-406. doi:10.1146/annurev.cellbio.042308.113248

Heider, F., Dunlop, D. J., & Sugiura, N. (1987). Magnetic properties of hydrothermally recrystallized magnetite crystals. *Science, 236*(4806), 1287-1290. doi:10.1126/science.236.4806.1287

Hergt, R., Dutz, S., & Röder, M. (2008). Effects of size distribution on hysteresis losses of magnetic nanoparticles for hyperthermia. *Journal of Physics: Condensed Matter, 20*(38), 385214.

Hergt, R., Hiergeist, R., Zeisberger, M., Schüler, D., Heyen, U., Hilger, I., & Kaiser, W. A. (2005). Magnetic properties of bacterial magnetosomes as potential diagnostic and therapeutic tools. *Journal of Magnetism and Magnetic Materials, 293*(1), 80-86. doi:http://doi.org/10.1016/j.jmmm.2005.01.047

Hernandez, R., Sacristan, J., Asin, L., Torres, T. E., Ibarra, M. R., Goya, G. F., & Mijangos, C. (2010). Magnetic hydrogels derived from polysaccharides with improved specific power absorption: potential devices for remotely triggered drug delivery. *J Phys Chem B, 114*(37), 12002-12007. doi:10.1021/jp105556e

Hervault, A., & Thanh, N. T. (2014). Magnetic nanoparticle-based therapeutic agents for thermo-chemotherapy treatment of cancer. *Nanoscale, 6*(20), 11553-11573. doi:10.1039/c4nr03482a

Hildebrandt, B., Wust, P., Ahlers, O., Dieing, A., Sreenivasa, G., Kerner, T., . . . Riess, H. (2002). The cellular and molecular basis of hyperthermia. *Crit Rev Oncol Hematol, 43*(1), 33-56.

Ho, L. H., Read, S. H., Dorstyn, L., Lambrusco, L., & Kumar, S. (2008). Caspase-2 is required for cell death induced by cytoskeletal disruption. *Oncogene, 27*(24), 3393-3404. doi:10.1038/sj.onc.1211005

Hong, I. S., Lee, H. Y., & Kang, K. S. (2014). Mesenchymal stem cells and cancer: friends or enemies? *Mutat Res, 768*, 98-106. doi:10.1016/j.mrfmmm.2014.01.006

Horie, M., Tripathi, A., Ito, A., Kawabe, Y., & Kamihira, M. (2017). Magnetic Nanoparticles: Functionalization and Manufacturing of Pluripotent Stem Cells. In A. Tripathi & J. S. Melo (Eds.), *Advances in Biomaterials for Biomedical Applications* (pp. 363-383). Singapore: Springer Singapore.

Hou, C. H., Lin, F. L., Hou, S. M., & Liu, J. F. (2014). Hyperthermia induces apoptosis through endoplasmic reticulum and reactive oxygen species in human osteosarcoma cells. *Int J Mol Sci, 15*(10), 17380-17395. doi:10.3390/ijms151017380

Huang, H., Delikanli, S., Zeng, H., Ferkey, D. M., & Pralle, A. (2010). Remote control of ion channels and neurons through magnetic-field heating of nanoparticles. *Nat Nanotechnol, 5*(8), 602-606. doi:10.1038/nnano.2010.125

Hung, S. C., Deng, W. P., Yang, W. K., Liu, R. S., Lee, C. C., Su, T. C., . . . Gelovani, J. G. (2005). Mesenchymal stem cell targeting of microscopic tumors and tumor stroma development monitored by noninvasive in vivo positron emission tomography imaging. *Clin Cancer Res, 11*(21), 7749-7756. doi:10.1158/1078-0432.ccr-05-0876

Jaattela, M. (1999). Heat shock proteins as cellular lifeguards. *Ann Med, 31*(4), 261-271.

Jang, J. T., Jeoung, J. W., Park, J. H., Lee, W. J., Kim, Y. J., Seon, J., . . . Bae, S. (2017). Effects of Recovery Time during Magnetic Nanofluid Hyperthermia on the Induction Behavior and Efficiency of Heat Shock Proteins 72. *Sci Rep, 7*(1), 13942. doi:10.1038/s41598-017-14348-2

Jia, H. L., Wang, C., Li, Y., Lu, Y., Wang, P. P., Pan, W. D., & Song, T. (2014). Combined effects of 50 Hz magnetic field and magnetic nanoparticles on the proliferation and apoptosis of PC12 cells. *Biomed Environ Sci, 27*(2), 97-105. doi:10.3967/bes2014.022

Jogler, C., & Schuler, D. (2009). Genomics, genetics, and cell biology of magnetosome formation. *Annu Rev Microbiol, 63*, 501-521. doi:10.1146/annurev.micro.62.081307.162908

Jogler, C., Wanner, G., Kolinko, S., Niebler, M., Amann, R., Petersen, N., . . . Schuler, D. (2011). Conservation of proteobacterial magnetosome genes and structures in an uncultivated member of the deep-branching Nitrospira phylum. *Proc Natl Acad Sci U S A, 108*(3), 1134-1139. doi:10.1073/pnas.1012694108

Jones, S. R., Wilson, T. D., Brown, M. E., Rahn-Lee, L., Yu, Y., Fredriksen, L. L., . . . Chang, M. C. (2015). Genetic and biochemical investigations of the role of MamP in redox control of iron biomineralization in Magnetospirillum magneticum. *Proc Natl Acad Sci U S A, 112*(13), 3904-3909. doi:10.1073/pnas.1417614112

Jordan, A., Scholz, R., Maier-Hauff, K., Johannsen, M., Wust, P., Nadobny, J., . . . Felix, R. (2001). Presentation of a new magnetic field therapy system for the treatment of human solid tumors with magnetic fluid hyperthermia. *Journal of Magnetism and Magnetic Materials, 225*(1–2), 118-126. doi:http://doi.org/10.1016/S0304-8853(00)01239-7

Kamiya, H., Kanno, T., Fujita, Y., Gotoh, A., Nakano, T., & Nishizaki, T. (2012). Apoptosis-Related Gene Transcription in Human A549 Lung Cancer Cells via A₃ Adenosine Receptor. *Cellular Physiology and Biochemistry, 29*(5-6), 687-696.

Karino, T., Koga, S., & Maeta, M. (1988). Experimental studies of the effects of local hyperthermia on blood flow, oxygen pressure and pH in tumors. *Jpn J Surg, 18*(3), 276-283.

Karnoub, A. E., Dash, A. B., Vo, A. P., Sullivan, A., Brooks, M. W., Bell, G. W., . . . Weinberg, R. A. (2007). Mesenchymal stem cells within tumour stroma promote breast cancer metastasis. *Nature, 449*(7162), 557-563. doi:10.1038/nature06188

Kashyap, S., Woehl, T. J., Liu, X., Mallapragada, S. K., & Prozorov, T. (2014). Nucleation of iron oxide nanoparticles mediated by Mms6 protein in situ. *ACS Nano, 8*(9), 9097-9106. doi:10.1021/nn502551y

Katzmann, E., Scheffel, A., Gruska, M., Plitzko, J. M., & Schuler, D. (2010). Loss of the actin-like protein MamK has pleiotropic effects on magnetosome formation and chain assembly in Magnetospirillum gryphiswaldense. *Mol Microbiol, 77*(1), 208-224. doi:10.1111/j.1365-2958.2010.07202.x

Kaur, J., Kaur, J., & Ralhan, R. (2000). Induction of apoptosis by abrogation of HSP70 expression in human oral cancer cells. *Int J Cancer, 85*(1), 1-5.

Khakoo, A. Y., Pati, S., Anderson, S. A., Reid, W., Elshal, M. F., Rovira, II, . . . Finkel, T. (2006). Human mesenchymal stem cells exert potent antitumorigenic effects in a model of Kaposi's sarcoma. *J Exp Med, 203*(5), 1235-1247. doi:10.1084/jem.20051921

Kim, J. H., & Lee, J. (2014). Induced Neural Stem Cells Protect Neuronal Cells against Apoptosis. *Medical Science Monitor : International Medical Journal*

of Experimental and Clinical Research, 20, 2759-2766. doi:10.12659/MSM.891343

Kolinko, I., Lohsse, A., Borg, S., Raschdorf, O., Jogler, C., Tu, Q., . . . Schuler, D. (2014). Biosynthesis of magnetic nanostructures in a foreign organism by transfer of bacterial magnetosome gene clusters. *Nat Nanotechnol, 9*(3), 193-197. doi:10.1038/nnano.2014.13

Komarova, S., Kawakami, Y., Stoff-Khalili, M. A., Curiel, D. T., & Pereboeva, L. (2006). Mesenchymal progenitor cells as cellular vehicles for delivery of oncolytic adenoviruses. *Mol Cancer Ther, 5*. doi:10.1158/1535-7163.mct-05-0334

Komarova, S., Roth, J., Alvarez, R., Curiel, D. T., & Pereboeva, L. (2010). Targeting of mesenchymal stem cells to ovarian tumors via an artificial receptor. *J Ovarian Res, 3*, 12. doi:10.1186/1757-2215-3-12

Komeili, A. (2012). Molecular mechanisms of compartmentalization and biomineralization in magnetotactic bacteria. *FEMS Microbiol Rev, 36*(1), 232-255. doi:10.1111/j.1574-6976.2011.00315.x

Komeili, A., Li, Z., Newman, D. K., & Jensen, G. J. (2006). Magnetosomes are cell membrane invaginations organized by the actin-like protein MamK. *Science, 311*(5758), 242-245. doi:10.1126/science.1123231

Komeili, A., Vali, H., Beveridge, T. J., & Newman, D. K. (2004). Magnetosome vesicles are present before magnetite formation, and MamA is required for their activation. *Proc Natl Acad Sci U S A, 101*(11), 3839-3844. doi:10.1073/pnas.0400391101

Konings, A. W., & Ruifrok, A. C. (1985). Role of membrane lipids and membrane fluidity in thermosensitivity and thermotolerance of mammalian cells. *Radiat Res, 102*(1), 86-98.

Kopp, R. E., & Kirschvink, J. L. (2008). The identification and biogeochemical interpretation of fossil magnetotactic bacteria. . *Earth-Science Reviews, 86* (1-4), pp. 42-61. .

Körnig, A., Dong, J., Bennet, M., Widdrat, M., Andert, J., Müller, F. D., . . . Faivre, D. (2014). Probing the Mechanical Properties of Magnetosome Chains in Living Magnetotactic Bacteria. *Nano Letters, 14*(8), 4653-4659. doi:10.1021/nl5017267

Kostura, L., Kraitchman, D. L., Mackay, A. M., Pittenger, M. F., & Bulte, J. W. (2004). Feridex labeling of mesenchymal stem cells inhibits chondrogenesis but not adipogenesis or osteogenesis. *NMR Biomed, 17*(7), 513-517. doi:10.1002/nbm.925

Kuai, W. X., Wang, Q., Yang, X. Z., Zhao, Y., Yu, R., & Tang, X. J. (2012). Interleukin-8 associates with adhesion, migration, invasion and chemosensitivity of human gastric cancer cells. *World J Gastroenterol, 18*(9), 979-985. doi:10.3748/wjg.v18.i9.979

Kucerova, L., Matuskova, M., Pastorakova, A., Tyciakova, S., Jakubikova, J., Bohovic, R., . . . Altaner, C. (2008a). Cytosine deaminase expressing human mesenchymal stem cells mediated tumour regression in melanoma bearing mice. *J Gene Med, 10*. doi:10.1002/jgm.1239

Kucerova, L., Matuskova, M., Pastorakova, A., Tyciakova, S., Jakubikova, J., Bohovic, R., . . . Altaner, C. (2008b). Cytosine deaminase expressing human

mesenchymal stem cells mediated tumour regression in melanoma bearing mice. *J Gene Med, 10*(10), 1071-1082. doi:10.1002/jgm.1239

Kumar, C. S., & Mohammad, F. (2011). Magnetic nanomaterials for hyperthermia-based therapy and controlled drug delivery. *Adv Drug Deliv Rev, 63*(9), 789-808. doi:10.1016/j.addr.2011.03.008

Kunisaki, Y., Bruns, I., Scheiermann, C., Ahmed, J., Pinho, S., Zhang, D., . . . Frenette, P. S. (2013). Arteriolar niches maintain haematopoietic stem cell quiescence. *Nature, 502*(7473), 637-643. doi:10.1038/nature12612

Kuwana, T., Bouchier-Hayes, L., Chipuk, J. E., Bonzon, C., Sullivan, B. A., Green, D. R., & Newmeyer, D. D. (2005). BH3 domains of BH3-only proteins differentially regulate Bax-mediated mitochondrial membrane permeabilization both directly and indirectly. *Mol Cell, 17*(4), 525-535. doi:10.1016/j.molcel.2005.02.003

Lacava, L. M., Garcia, V. A. P., Kückelhaus, S., Azevedo, R. B., Sadeghiani, N., Buske, N., . . . Lacava, Z. G. M. (2004). Long-term retention of dextran-coated magnetite nanoparticles in the liver and spleen. *Journal of Magnetism and Magnetic Materials, 272–276, Part 3*, 2434-2435. doi:http://doi.org/10.1016/j.jmmm.2003.12.852

Lang, C., & Schüler, D. (2008). Expression of Green Fluorescent Protein Fused to Magnetosome Proteins in Microaerophilic Magnetotactic Bacteria. *Appl Environ Microbiol, 74*(15), 4944-4953. doi:10.1128/AEM.00231-08

Le Blanc, K., & Ringden, O. (2005). Immunobiology of human mesenchymal stem cells and future use in hematopoietic stem cell transplantation. *Biol Blood Marrow Transplant, 11*(5), 321-334. doi:10.1016/j.bbmt.2005.01.005

Lepock, J. R. (2003). Cellular effects of hyperthermia: relevance to the minimum dose for thermal damage. *Int J Hyperthermia, 19*(3), 252-266. doi:10.1080/0265673031000065042

Li, F. J., Kondo, T., Zhao, Q. L., Tanabe, K., Ogawa, R., Li, M., & Arai, Y. (2001). Enhancement of hyperthermia-induced apoptosis by a free radical initiator, 2,2'-azobis (2-amidinopropane) dihydrochloride, in human histiocytic lymphoma U937 cells. *Free Radic Res, 35*(3), 281-299.

Li, G. C., Zhang, H. W., Zhao, Q. C., Sun, L. I., Yang, J. J., Hong, L., . . . Cai, L. (2016). Mesenchymal stem cells promote tumor angiogenesis via the action of transforming growth factor beta1. *Oncol Lett, 11*(2), 1089-1094. doi:10.3892/ol.2015.3997

Li, L., Guan, Y., Liu, H., Hao, N., Liu, T., Meng, X., . . . Tang, F. (2011). Silica nanorattle-doxorubicin-anchored mesenchymal stem cells for tumor-tropic therapy. *ACS Nano, 5*(9), 7462-7470. doi:10.1021/nn202399w

Liu R-T, Liu J, Tong J-Q, T. T., Kong W-C, Wang X-W, & al., e. (2012). Heating effect and biocompatibility of bacterial magnetosomes as potential materials used in magnetic fluid hyperthermia. *Prog Nat Sci Mater Int, 22*(1), 31-39.

Liu, S., Ginestier, C., Ou, S. J., Clouthier, S. G., Patel, S. H., Monville, F., . . . Wicha, M. S. (2011). Breast cancer stem cells are regulated by mesenchymal stem cells through cytokine networks. *Cancer Res, 71*(2), 614-624. doi:10.1158/0008-5472.can-10-0538

Loebinger, M. R., Eddaoudi, A., Davies, D., & Janes, S. M. (2009). Mesenchymal stem cell delivery of TRAIL can eliminate metastatic cancer. *Cancer Res, 69*(10), 4134-4142. doi:10.1158/0008-5472.can-08-4698

Loebinger, M. R., Kyrtatos, P. G., Turmaine, M., Price, A. N., Pankhurst, Q., Lythgoe, M. F., & Janes, S. M. (2009). Magnetic resonance imaging of mesenchymal stem cells homing to pulmonary metastases using biocompatible magnetic nanoparticles. *Cancer Res, 69*(23), 8862-8867. doi:10.1158/0008-5472.can-09-1912

Lohsse, A., Borg, S., Raschdorf, O., Kolinko, I., Tompa, E., Posfai, M., . . . Schuler, D. (2014). Genetic dissection of the mamAB and mms6 operons reveals a gene set essential for magnetosome biogenesis in Magnetospirillum gryphiswaldense. *J Bacteriol, 196*(14), 2658-2669. doi:10.1128/jb.01716-14

Lu, Y. R., Yuan, Y., Wang, X. J., Wei, L. L., Chen, Y. N., Cong, C., . . . Cheng, J. Q. (2008). The growth inhibitory effect of mesenchymal stem cells on tumor cells in vitro and in vivo. *Cancer Biol Ther, 7*(2), 245-251.

Lucien, F., Harper, K., Pelletier, P.-P., Volkov, L., & Dubois, C. M. (2014). Simultaneous pH Measurement in Endocytic and Cytosolic Compartments in Living Cells using Confocal Microscopy. *Journal of Visualized Experiments : JoVE*(86), 51395. doi:10.3791/51395

Luheshi, N. M., Rothwell, N. J., & Brough, D. (2009). Dual functionality of interleukin-1 family cytokines: implications for anti-interleukin-1 therapy. *British Journal of Pharmacology, 157*(8), 1318-1329. doi:10.1111/j.1476-5381.2009.00331.x

Lunov, O., Zablotskii, V., Syrovets, T., Rocker, C., Tron, K., Nienhaus, G. U., & Simmet, T. (2011). Modeling receptor-mediated endocytosis of polymer-functionalized iron oxide nanoparticles by human macrophages. *Biomaterials, 32*(2), 547-555. doi:10.1016/j.biomaterials.2010.08.111

Lysko, D. E., Putt, M., & Golden, J. A. (2011). SDF1 regulates leading process branching and speed of migrating interneurons. *J Neurosci, 31*(5), 1739-1745. doi:10.1523/jneurosci.3118-10.2011

Madrigal, M., Rao, K. S., & Riordan, N. H. (2014). A review of therapeutic effects of mesenchymal stem cell secretions and induction of secretory modification by different culture methods. *J Transl Med, 12*, 260. doi:10.1186/s12967-014-0260-8

Maeda, H., Greish, K., & Fang, J. (2006). The EPR Effect and Polymeric Drugs: A Paradigm Shift for Cancer Chemotherapy in the 21st Century. In R. Satchi-Fainaro & R. Duncan (Eds.), *Polymer Therapeutics II* (pp. 103-121). Berlin, Heidelberg: Springer Berlin Heidelberg.

Maier-Hauff, K., Rothe, R., Scholz, R., Gneveckow, U., Wust, P., Thiesen, B., . . . Jordan, A. (2007). Intracranial Thermotherapy using Magnetic Nanoparticles Combined with External Beam Radiotherapy: Results of a Feasibility Study on Patients with Glioblastoma Multiforme. *J Neurooncol, 81*(1), 53-60. doi:10.1007/s11060-006-9195-0

Majda, J. A., Gerner, E. W., Vanlandingham, B., Gehlsen, K. R., & Cress, A. E. (1994). Heat shock-induced shedding of cell surface integrins in A549 human lung tumor cells in culture. *Exp Cell Res, 210*(1), 46-51. doi:10.1006/excr.1994.1007

Majesky, M. W., Dong, X. R., Hoglund, V., Mahoney, W. M., & Daum, G. (2011). The Adventitia: A Dynamic Interface Containing Resident Progenitor Cells. *Arteriosclerosis, Thrombosis, and Vascular Biology, 31*(7), 1530-1539. doi:10.1161/ATVBAHA.110.221549

Mallory, M., Gogineni, E., Jones, G. C., Greer, L., & Simone, C. B., II. (2016). Therapeutic hyperthermia: The old, the new, and the upcoming. *Critical Reviews in Oncology / Hematology, 97*, 56-64. doi:10.1016/j.critrevonc.2015.08.003

Mannucci, S., Ghin, L., Conti, G., Tambalo, S., Lascialfari, A., Orlando, T., . . . Sbarbati, A. (2014). Magnetic Nanoparticles from Magnetospirillum gryphiswaldense Increase the Efficacy of Thermotherapy in a Model of Colon Carcinoma. *PLoS One, 9*(10), e108959. doi:10.1371/journal.pone.0108959

Mathieu, M. E., Saucourt, C., Mournetas, V., Gauthereau, X., Theze, N., Praloran, V., . . . Boeuf, H. (2012). LIF-dependent signaling: new pieces in the Lego. *Stem Cell Rev, 8*(1), 1-15. doi:10.1007/s12015-011-9261-7

Matsumoto, H., Shimura, M., Omatsu, T., Okaichi, K., Majima, H., & Ohnishi, T. (1994). p53 proteins accumulated by heat stress associate with heat shock proteins HSP72/HSC73 in human glioblastoma cell lines. *Cancer Lett, 87*(1), 39-46.

Matsumoto, H., Takahashi, A., Wang, X., Ohnishi, K., & Ohnishi, T. (1997). Transfection of p53-knockout mouse fibroblasts with wild-type p53 increases the thermosensitivity and stimulates apoptosis induced by heat stress. *Int J Radiat Oncol Biol Phys, 39*(1), 197-203.

Matuskova, M., Hlubinova, K., Pastorakova, A., Hunakova, L., Altanerova, V., Altaner, C., & Kucerova, L. (2010). HSV-tk expressing mesenchymal stem cells exert bystander effect on human glioblastoma cells. *Cancer Lett, 290*(1), 58-67. doi:10.1016/j.canlet.2009.08.028

Meenach, S. A., Otu, C. G., Anderson, K. W., & Hilt, J. Z. (2012). Controlled synergistic delivery of paclitaxel and heat from poly(beta-amino ester)/iron oxide-based hydrogel nanocomposites. *Int J Pharm, 427*(2), 177-184. doi:10.1016/j.ijpharm.2012.01.052

Menon, L. G., Kelly, K., Yang, H. W., Kim, S. K., Black, P. M., & Carroll, R. S. (2009). Human bone marrow-derived mesenchymal stromal cells expressing S-TRAIL as a cellular delivery vehicle for human glioma therapy. *Stem Cells, 27*(9), 2320-2330. doi:10.1002/stem.136

Menon, L. G., Picinich, S., Koneru, R., Gao, H., Lin, S. Y., Koneru, M., . . . Banerjee, D. (2007). Differential gene expression associated with migration of mesenchymal stem cells to conditioned medium from tumor cells or bone marrow cells. *Stem Cells, 25*(2), 520-528. doi:10.1634/stemcells.2006-0257

Menoret, A., & Chandawarkar, R. (1998). Heat-shock protein-based anticancer immunotherapy: an idea whose time has come. *Semin Oncol, 25*(6), 654-660.

Mertz, D., Sandre, O., & Bégin-Colin, S. (2017). Drug releasing nanoplatforms activated by alternating magnetic fields. *Biochimica et Biophysica Acta (BBA) - General Subjects, 1861*(6), 1617-1641. doi:https://doi.org/10.1016/j.bbagen.2017.02.025

Moll, N. M., & Ransohoff, R. M. (2010). CXCL12 and CXCR4 in bone marrow physiology. *Expert Rev Hematol, 3*(3), 315-322. doi:10.1586/ehm.10.16

Momin, E. N., Vela, G., Zaidi, H. A., & Quinones-Hinojosa, A. (2010). The Oncogenic Potential of Mesenchymal Stem Cells in the Treatment of Cancer: Directions for Future Research. *Curr Immunol Rev, 6*(2), 137-148. doi:10.2174/157339510791111718

Mornet, S. p., Vasseur, S. b., Grasset, F., & Duguet, E. (2004). Magnetic nanoparticle design for medical diagnosis and therapy. *Journal of Materials Chemistry, 14*(14), 2161. doi:10.1039/b402025a

Moros, E. (2012). *Physics of thermal therapy: fundamentals and clinical applications*: Taylor & Francis.

Moros, M., Ambrosone, A., Stepien, G., Fabozzi, F., Marchesano, V., Castaldi, A., . . . Tortiglione, C. (2015). Deciphering intracellular events triggered by mild magnetic hyperthermia in vitro and in vivo. *Nanomedicine (Lond), 10*(14), 2167-2183. doi:10.2217/nnm.15.70

Mouiseddine, M., Francois, S., Semont, A., Sache, A., Allenet, B., Mathieu, N., . . . Chapel, A. (2007). Human mesenchymal stem cells home specifically to radiation-injured tissues in a non-obese diabetes/severe combined immunodeficiency mouse model. *Br J Radiol, 80 Spec No 1*, S49-55. doi:10.1259/bjr/25927054

Moy, A. J., & Tunnell, J. W. (2017). Combinatorial immunotherapy and nanoparticle mediated hyperthermia. *Advanced Drug Delivery Reviews, 114*(Supplement C), 175-183. doi:https://doi.org/10.1016/j.addr.2017.06.008

Mukhopadhyay, D. A. (2017). Regenerative Medicine: Laboratory to Clinic. doi:DOI10.1007/978-981-10-3701-6

Mukhopadhyay, S., Panda, P. K., Sinha, N., Das, D. N., & Bhutia, S. K. (2014). Autophagy and apoptosis: where do they meet? *Apoptosis, 19*(4), 555-566. doi:10.1007/s10495-014-0967-2

Müller, F. D., Raschdorf, O., Nudelman, H., Messerer, M., Katzmann, E., Plitzko, J. M., . . . Schüler, D. (2014). The FtsZ-Like Protein FtsZm of Magnetospirillum gryphiswaldense Likely Interacts with Its Generic Homolog and Is Required for Biomineralization under Nitrate Deprivation. *Journal of Bacteriology, 196*(3), 650-659. doi:10.1128/JB.00804-13

Multhoff, G., Botzler, C., Jennen, L., Schmidt, J., Ellwart, J., & Issels, R. (1997). Heat shock protein 72 on tumor cells: a recognition structure for natural killer cells. *J Immunol, 158*(9), 4341-4350.

Multhoff, G., Botzler, C., Wiesnet, M., Muller, E., Meier, T., Wilmanns, W., & Issels, R. D. (1995). A stress-inducible 72-kDa heat-shock protein (HSP72) is expressed on the surface of human tumor cells, but not on normal cells. *Int J Cancer, 61*(2), 272-279.

Multhoff, G., Mizzen, L., Winchester, C. C., Milner, C. M., Wenk, S., Eissner, G., . . . Johnson, J. (1999). Heat shock protein 70 (Hsp70) stimulates proliferation and cytolytic activity of natural killer cells. *Exp Hematol, 27*(11), 1627-1636.

Munoz de Escalona, M., Saez-Fernandez, E., Prados, J. C., Melguizo, C., & Arias, J. L. (2016). Magnetic solid lipid nanoparticles in hyperthermia against colon cancer. *Int J Pharm, 504*(1-2), 11-19. doi:10.1016/j.ijpharm.2016.03.005

Murat, D., Falahati, V., Bertinetti, L., Csencsits, R., Kornig, A., Downing, K., . . . Komeili, A. (2012). The magnetosome membrane protein, MmsF, is a major regulator of magnetite biomineralization in Magnetospirillum magneticum AMB-1. *Mol Microbiol, 85*(4), 684-699. doi:10.1111/j.1365-2958.2012.08132.x

Murat, D., Quinlan, A., Vali, H., & Komeili, A. (2010). Comprehensive genetic dissection of the magnetosome gene island reveals the step-wise assembly of

a prokaryotic organelle. *Proc Natl Acad Sci U S A, 107*(12), 5593-5598. doi:10.1073/pnas.0914439107

Murphy, M. B., Moncivais, K., & Caplan, A. I. (2013). Mesenchymal stem cells: environmentally responsive therapeutics for regenerative medicine. *Exp Mol Med, 45*, e54. doi:10.1038/emm.2013.94

Nagase, H., & Woessner, J. F., Jr. (1999). Matrix metalloproteinases. *J Biol Chem, 274*(31), 21491-21494.

Nakamae, T., Adachi, N., Kobayashi, T., Nagata, Y., Nakasa, T., Tanaka, N., & Ochi, M. (2010). The effect of an external magnetic force on cell adhesion and proliferation of magnetically labeled mesenchymal stem cells. *Sports Med Arthrosc Rehabil Ther Technol, 2*(1), 5. doi:10.1186/1758-2555-2-5

Nakamizo, A., Marini, F., Amano, T., Khan, A., Studeny, M., Gumin, J., . . . Lang, F. F. (2005). Human bone marrow-derived mesenchymal stem cells in the treatment of gliomas. *Cancer Res, 65*(8), 3307-3318. doi:10.1158/0008-5472.can-04-1874

Nakamura, K., Ito, Y., Kawano, Y., Kurozumi, K., Kobune, M., Tsuda, H., . . . Hamada, H. (2004). Antitumor effect of genetically engineered mesenchymal stem cells in a rat glioma model. *Gene Ther, 11*(14), 1155-1164. doi:10.1038/sj.gt.3302276

Nancarrow-Lei, R., Mafi, P., Mafi, R., & Khan, W. (2017). A Systemic Review of Adult Mesenchymal Stem Cell Sources and their Multilineage Differentiation Potential Relevant to Musculoskeletal Tissue Repair and Regeneration. *Curr Stem Cell Res Ther, 12*(8), 601-610. doi:10.2174/1574888x12666170608124303

Nandwana, V., De, M., Chu, S., Jaiswal, M., Rotz, M., Meade, T. J., & Dravid, V. P. (2015). Theranostic Magnetic Nanostructures (MNS) for Cancer. *Cancer Treat Res, 166*, 51-83. doi:10.1007/978-3-319-16555-4_3

Nold, P., Hartmann, R., Feliu, N., Kantner, K., Gamal, M., Pelaz, B., . . . Brendel, C. (2017). Optimizing conditions for labeling of mesenchymal stromal cells (MSCs) with gold nanoparticles: a prerequisite for in vivo tracking of MSCs. *J Nanobiotechnology, 15*(1), 24. doi:10.1186/s12951-017-0258-5

Norozi, Ahmadzadeh, A., Shahjahani, M., Shahrabi, S., & Saki, N. (2016). Twist as a new prognostic marker in hematological malignancies. *Clin Transl Oncol, 18*(2), 113-124. doi:10.1007/s12094-015-1357-0

Norozi, Ahmadzadeh, A., Shahrabi, S., Vosoughi, T., & Saki, N. (2016). Mesenchymal stem cells as a double-edged sword in suppression or progression of solid tumor cells. *Tumor Biology, 37*(9), 11679-11689. doi:10.1007/s13277-016-5187-7

Nudelman, H., & Zarivach, R. (2014). Structure prediction of magnetosome-associated proteins. *Frontiers in Microbiology, 5*(9). doi:10.3389/fmicb.2014.00009

Oh, M., & Nör, J. E. (2015). The Perivascular Niche and Self-Renewal of Stem Cells. *Frontiers in Physiology, 6*(367). doi:10.3389/fphys.2015.00367

Oh, Y., Moorthy, M. S., Manivasagan, P., Bharathiraja, S., & Oh, J. (2017). Magnetic hyperthermia and pH-responsive effective drug delivery to the sub-cellular level of human breast cancer cells by modified CoFe2O4 nanoparticles. *Biochimie, 133*, 7-19. doi:https://doi.org/10.1016/j.biochi.2016.11.012

Ohlsson, L. B., Varas, L., Kjellman, C., Edvardsen, K., & Lindvall, M. (2003). Mesenchymal progenitor cell-mediated inhibition of tumor growth in vivo and in vitro in gelatin matrix. *Exp Mol Pathol, 75*(3), 248-255.

Olaso, E., Santisteban, A., Bidaurrazaga, J., Gressner, A. M., Rosenbaum, J., & Vidal-Vanaclocha, F. (1997). Tumor-dependent activation of rodent hepatic stellate cells during experimental melanoma metastasis. *Hepatology, 26*(3), 634-642. doi:10.1002/hep.510260315

Otani, K., Yamahara, K., Ohnishi, S., Obata, H., Kitamura, S., & Nagaya, N. (2009). Nonviral delivery of siRNA into mesenchymal stem cells by a combination of ultrasound and microbubbles. *J Control Release, 133*(2), 146-153. doi:10.1016/j.jconrel.2008.09.088

Pan, W., Xie, C., & Lv, J. (2012). Screening for the interacting partners of the proteins MamK & MamJ by two-hybrid genomic DNA library of Magnetospirillum magneticum AMB-1. *Curr Microbiol, 64*(6), 515-523. doi:10.1007/s00284-012-0099-2

Park, J. S., Suryaprakash, S., Lao, Y. H., & Leong, K. W. (2015). Engineering mesenchymal stem cells for regenerative medicine and drug delivery. *Methods, 84*, 3-16. doi:10.1016/j.ymeth.2015.03.002

Pawlik, A., Nowak, J. M., Grzanka, D., Gackowska, L., Michalkiewicz, J., & Grzanka, A. (2013). Hyperthermia induces cytoskeletal alterations and mitotic catastrophe in p53-deficient H1299 lung cancer cells. *Acta Histochem, 115*(1), 8-15. doi:10.1016/j.acthis.2012.02.006

Peeken, J. C., Vaupel, P., & Combs, S. E. (2017). Integrating Hyperthermia into Modern Radiation Oncology: What Evidence Is Necessary? *Frontiers in Oncology, 7*(132). doi:10.3389/fonc.2017.00132

Pereira, R. F., O'Hara, M. D., Laptev, A. V., Halford, K. W., Pollard, M. D., Class, R., . . . Prockop, D. J. (1998). Marrow stromal cells as a source of progenitor cells for nonhematopoietic tissues in transgenic mice with a phenotype of osteogenesis imperfecta. *Proc Natl Acad Sci U S A, 95*(3), 1142-1147.

Pereira, S. M., Moss, D., Williams, S. R., Murray, P., & Taylor, A. (2015). Overexpression of the MRI Reporter Genes Ferritin and Transferrin Receptor Affect Iron Homeostasis and Produce Limited Contrast in Mesenchymal Stem Cells. *International Journal of Molecular Sciences, 16*(7), 15481-15496. doi:10.3390/ijms160715481

Perron, J. C., & Dodd, J. (2012). Structural distinctions in BMPs underlie divergent signaling in spinal neurons. *Neural Development, 7*, 16-16. doi:10.1186/1749-8104-7-16

Philippe, N., & Wu, L. F. (2010). An MCP-like protein interacts with the MamK cytoskeleton and is involved in magnetotaxis in Magnetospirillum magneticum AMB-1. *J Mol Biol, 400*(3), 309-322. doi:10.1016/j.jmb.2010.05.011

Pollert, E., Veverka, P., Veverka, M., Kaman, O., Závěta, K., Vasseur, S., . . . Duguet, E. (2009). Search of new core materials for magnetic fluid hyperthermia: Preliminary chemical and physical issues. *Progress in Solid State Chemistry, 37*(1), 1-14. doi:http://doi.org/10.1016/j.progsolidstchem.2009.02.001

Ponomaryov, T., Peled, A., Petit, I., Taichman, R. S., Habler, L., Sandbank, J., . . . Lapidot, T. (2000). Induction of the chemokine stromal-derived factor-1

following DNA damage improves human stem cell function. *J Clin Invest, 106*(11), 1331-1339. doi:10.1172/jci10329

Pradel, N., Santini, C. L., Bernadac, A., Fukumori, Y., & Wu, L. F. (2006). Biogenesis of actin-like bacterial cytoskeletal filaments destined for positioning prokaryotic magnetic organelles. *Proc Natl Acad Sci U S A, 103*(46), 17485-17489. doi:10.1073/pnas.0603760103

Prozorov, T., Mallapragada, S. K., Narasimhan, B., Wang, L., Palo, P., Nilsen-Hamilton, M., . . . Canfield, P. C. (2007). Protein-Mediated Synthesis of Uniform Superparamagnetic Magnetite Nanocrystals. *Advanced Functional Materials, 17*(6), 951-957. doi:10.1002/adfm.200600448

Qiao, B., Shui, W., Cai, L., Guo, S., & Jiang, D. (2015). Human mesenchymal stem cells as delivery of osteoprotegerin gene: homing and therapeutic effect for osteosarcoma. *Drug Des Devel Ther, 9*, 969-976. doi:10.2147/dddt.s77116

Qiao, L., Xu, Z., Zhao, T., Zhao, Z., Shi, M., Zhao, R. C., . . . Zhang, X. (2008). Suppression of tumorigenesis by human mesenchymal stem cells in a hepatoma model. *Cell Res, 18*(4), 500-507. doi:10.1038/cr.2008.40

Qiao, L., Xu, Z. L., Zhao, T. J., Ye, L. H., & Zhang, X. D. (2008). Dkk-1 secreted by mesenchymal stem cells inhibits growth of breast cancer cells via depression of Wnt signalling. *Cancer Lett, 269*(1), 67-77. doi:10.1016/j.canlet.2008.04.032

Quinlan, A., Murat, D., Vali, H., & Komeili, A. (2011). The HtrA/DegP family protease MamE is a bifunctional protein with roles in magnetosome protein localization and magnetite biomineralization. *Mol Microbiol, 80*(4), 1075-1087. doi:10.1111/j.1365-2958.2011.07631.x

Quinto, C. A., Mohindra, P., Tong, S., & Bao, G. (2015). Multifunctional superparamagnetic iron oxide nanoparticles for combined chemotherapy and hyperthermia cancer treatment. *Nanoscale, 7*(29), 12728-12736. doi:10.1039/c5nr02718g

Rabin, Y. (2002). Is intracellular hyperthermia superior to extracellular hyperthermia in the thermal sense? *Int J Hyperthermia, 18*(3), 194-202. doi:10.1080/02656730110116713

Ramasamy, R., Lam, E. W., Soeiro, I., Tisato, V., Bonnet, D., & Dazzi, F. (2007). Mesenchymal stem cells inhibit proliferation and apoptosis of tumor cells: impact on in vivo tumor growth. *Leukemia, 21*(2), 304-310. doi:10.1038/sj.leu.2404489

Raschdorf, O., Muller, F. D., Posfai, M., Plitzko, J. M., & Schuler, D. (2013). The magnetosome proteins MamX, MamZ and MamH are involved in redox control of magnetite biomineralization in Magnetospirillum gryphiswaldense. *Mol Microbiol, 89*(5), 872-886. doi:10.1111/mmi.12317

Rawlings, A. E., Bramble, J. P., Hounslow, A. M., Williamson, M. P., Monnington, A. E., Cooke, D. J., & Staniland, S. S. (2016). Ferrous Iron Binding Key to Mms6 Magnetite Biomineralisation: A Mechanistic Study to Understand Magnetite Formation Using pH Titration and NMR Spectroscopy. *Chemistry, 22*(23), 7885-7894. doi:10.1002/chem.201600322

Reagan, M. R., & Kaplan, D. L. (2011). Concise review: Mesenchymal stem cell tumor-homing: detection methods in disease model systems. *Stem Cells, 29*(6), 920-927. doi:10.1002/stem.645

Reap, E. A., Roof, K., Maynor, K., Borrero, M., Booker, J., & Cohen, P. L. (1997). Radiation and stress-induced apoptosis: a role for Fas/Fas ligand interactions. *Proc Natl Acad Sci U S A, 94*(11), 5750-5755.

Reinhold, H. S., & Endrich, B. (1986). Tumour microcirculation as a target for hyperthermia. *Int J Hyperthermia, 2*(2), 111-137.

Ren, C., Kumar, S., Chanda, D., Kallman, L., Chen, J., Mountz, J. D., & Ponnazhagan, S. (2008). Cancer gene therapy using mesenchymal stem cells expressing interferon-beta in a mouse prostate cancer lung metastasis model. *Gene Ther, 15*. doi:10.1038/gt.2008.101

Rhee, K. J., Lee, J. I., & Eom, Y. W. (2015). Mesenchymal Stem Cell-Mediated Effects of Tumor Support or Suppression. *Int J Mol Sci, 16*(12), 30015-30033. doi:10.3390/ijms161226215

Richter, M., Kube, M., Bazylinski, D. A., Lombardot, T., Glockner, F. O., Reinhardt, R., & Schuler, D. (2007). Comparative genome analysis of four magnetotactic bacteria reveals a complex set of group-specific genes implicated in magnetosome biomineralization and function. *J Bacteriol, 189*(13), 4899-4910. doi:10.1128/jb.00119-07

Riedinger, A., Guardia, P., Curcio, A., Garcia, M. A., Cingolani, R., Manna, L., & Pellegrino, T. (2013). Subnanometer local temperature probing and remotely controlled drug release based on azo-functionalized iron oxide nanoparticles. *Nano Lett, 13*(6), 2399-2406. doi:10.1021/nl400188q

Rioux, J. B., Philippe, N., Pereira, S., Pignol, D., Wu, L. F., & Ginet, N. (2010). A second actin-like MamK protein in Magnetospirillum magneticum AMB-1 encoded outside the genomic magnetosome island. *PLoS One, 5*(2), e9151. doi:10.1371/journal.pone.0009151

Rohban, R., & Pieber, T. R. (2017a). Mesenchymal Stem and Progenitor Cells in Regeneration: Tissue Specificity and Regenerative Potential. *Stem Cells International, 2017*, 5173732. doi:10.1155/2017/5173732

Rohban, R., & Pieber, T. R. (2017b). Mesenchymal Stem and Progenitor Cells in Regeneration: Tissue Specificity and Regenerative Potential. *Stem Cells International, 2017*, 16. doi:10.1155/2017/5173732

Roigas, J., Wallen, E. S., Loening, S. A., & Moseley, P. L. (1998). Heat shock protein (HSP72) surface expression enhances the lysis of a human renal cell carcinoma by IL-2 stimulated NK cells. *Adv Exp Med Biol, 451*, 225-229.

Rong, C., Zhang, C., Zhang, Y., Qi, L., Yang, J., Guan, G., . . . Li, J. (2012). FeoB2 Functions in magnetosome formation and oxidative stress protection in Magnetospirillum gryphiswaldense strain MSR-1. *J Bacteriol, 194*(15), 3972-3976. doi:10.1128/jb.00382-12

Roson-Burgo, B., Sanchez-Guijo, F., Del Cañizo, C., & De Las Rivas, J. (2014). Transcriptomic portrait of human Mesenchymal Stromal/Stem cells isolated from bone marrow and placenta. *BMC Genomics, 15*(1), 910. doi:10.1186/1471-2164-15-910

Ruster, B., Gottig, S., Ludwig, R. J., Bistrian, R., Muller, S., Seifried, E., . . . Henschler, R. (2006). Mesenchymal stem cells display coordinated rolling and adhesion behavior on endothelial cells. *Blood, 108*(12), 3938-3944. doi:10.1182/blood-2006-05-025098

Ryu, H., Oh, J. E., Rhee, K. J., Baik, S. K., Kim, J., Kang, S. J., . . . Eom, Y. W. (2014). Adipose tissue-derived mesenchymal stem cells cultured at high

density express IFN-beta and suppress the growth of MCF-7 human breast cancer cells. *Cancer Lett, 352*(2), 220-227. doi:10.1016/j.canlet.2014.06.018

Sackstein, R. (2004). The bone marrow is akin to skin: HCELL and the biology of hematopoietic stem cell homing. *J Investig Dermatol Symp Proc, 9*(3), 215-223. doi:10.1111/j.0022-202X.2004.09301.x

Sadat, M. E., Baghbador, M. K., Dunn, A. W., Wagner, H. P., Ewing, R. C., Zhang, J., . . . Shi, D. (2014). Photoluminescence and photothermal effect of Fe3O4 nanoparticles for medical imaging and therapy. *Applied Physics Letters, 105*(9), 091903. doi:10.1063/1.4895133

Sadhasivam, S., Savitha, S., Wu, C.-J., Lin, F.-H., & Stobiński, L. (2015). Carbon encapsulated iron oxide nanoparticles surface engineered with polyethylene glycol-folic acid to induce selective hyperthermia in folate over expressed cancer cells. *Int J Pharm, 480*(1–2), 8-14. doi:http://doi.org/10.1016/j.ijpharm.2015.01.029

Samali, A., Holmberg, C. I., Sistonen, L., & Orrenius, S. (1999). Thermotolerance and cell death are distinct cellular responses to stress: dependence on heat shock proteins. *FEBS Lett, 461*(3), 306-310.

Sarkar, D., Vemula, P. K., Zhao, W., Gupta, A., Karnik, R., & Karp, J. M. (2010). Engineered mesenchymal stem cells with self-assembled vesicles for systemic cell targeting. *Biomaterials, 31*(19), 5266-5274. doi:10.1016/j.biomaterials.2010.03.006

Sato, A., Tamura, Y., Sato, N., Yamashita, T., Takada, T., Sato, M., . . . Jimbow, K. (2010). Melanoma-targeted chemo-thermo-immuno (CTI)-therapy using N-propionyl-4-S-cysteaminylphenol-magnetite nanoparticles elicits CTL response via heat shock protein-peptide complex release. *Cancer Sci, 101*(9), 1939-1946. doi:10.1111/j.1349-7006.2010.01623.x

Sauvage, F., Messaoudi, S., Fattal, E., Barratt, G., & Vergnaud-Gauduchon, J. (2017). Heat shock proteins and cancer: How can nanomedicine be harnessed? *Journal of Controlled Release, 248*, 133-143. doi:https://doi.org/10.1016/j.jconrel.2017.01.013

Schäfer, R., Bantleon, R., Kehlbach, R., Siegel, G., Wiskirchen, J., Wolburg, H., . . . Schlemmer, H.-P. (2010). Functional investigations on human mesenchymal stem cells exposed to magnetic fields and labeled with clinically approved iron nanoparticles. *BMC Cell Biology, 11*(1), 22. doi:10.1186/1471-2121-11-22

Scheffel, A., Gruska, M., Faivre, D., Linaroudis, A., Plitzko, J. M., & Schüler, D. (2006). An acidic protein aligns magnetosomes along a filamentous structure in magnetotactic bacteria. *Nature, 440*(7080), 110-114. doi:http://www.nature.com/nature/journal/v440/n7080/suppinfo/nature04382_S1.html

Schreiber, S., Savla, M., Pelekhov, D. V., Iscru, D. F., Selcu, C., Hammel, P. C., & Agarwal, G. (2008). Magnetic force microscopy of superparamagnetic nanoparticles. *Small, 4*(2), 270-278. doi:10.1002/smll.200700116

Schuh, C. D., Haenni, D., Craigie, E., Ziegler, U., Weber, B., Devuyst, O., & Hall, A. M. (2016). Long wavelength multiphoton excitation is advantageous for intravital kidney imaging. *Kidney Int, 89*(3), 712-719. doi:10.1038/ki.2015.323

Schuler, D. (2008). Genetics and cell biology of magnetosome formation in magnetotactic bacteria. *FEMS Microbiol Rev, 32*(4), 654-672. doi:10.1111/j.1574-6976.2008.00116.x

Schüler, D. (2006). *Magnetoreception and Magnetosomes in Bacteria*: Springer Berlin Heidelberg.

Secchiero, P., Zorzet, S., Tripodo, C., Corallini, F., Melloni, E., Caruso, L., . . . Zauli, G. (2010). Human bone marrow mesenchymal stem cells display anti-cancer activity in SCID mice bearing disseminated non-Hodgkin's lymphoma xenografts. *PLoS One, 5*(6), e11140. doi:10.1371/journal.pone.0011140

Segers, V. F., Van Riet, I., Andries, L. J., Lemmens, K., Demolder, M. J., De Becker, A. J., . . . De Keulenaer, G. W. (2006). Mesenchymal stem cell adhesion to cardiac microvascular endothelium: activators and mechanisms. *Am J Physiol Heart Circ Physiol, 290*(4), H1370-1377. doi:10.1152/ajpheart.00523.2005

Sekihara, K., Harashima, N., Tongu, M., Tamaki, Y., Uchida, N., Inomata, T., & Harada, M. (2013). Pifithrin-mu, an inhibitor of heat-shock protein 70, can increase the antitumor effects of hyperthermia against human prostate cancer cells. *PLoS One, 8*(11), e78772. doi:10.1371/journal.pone.0078772

Sengupta, A., Quiaoit, K., Thompson, R., Prato, F., Gelman, N., & Goldhawk, D. (2014). Biophysical features of MagA expression in mammalian cells: implications for MRI contrast. *Frontiers in Microbiology, 5*(29). doi:10.3389/fmicb.2014.00029

Shapiro, O. H., Hatzenpichler, R., Buckley, D. H., Zinder, S. H., & Orphan, V. J. (2011). Multicellular photo-magnetotactic bacteria. *Environ Microbiol Rep, 3*(2), 233-238. doi:10.1111/j.1758-2229.2010.00215.x

Shaterabadi, Z., Nabiyouni, G., & Soleymani, M. (2017). Physics responsible for heating efficiency and self-controlled temperature rise of magnetic nanoparticles in magnetic hyperthermia therapy. *Prog Biophys Mol Biol*. doi:10.1016/j.pbiomolbio.2017.10.001

Shi, Z., Neoh, K. G., Kang, E. T., Shuter, B., Wang, S. C., Poh, C., & Wang, W. (2009). (Carboxymethyl)chitosan-modified superparamagnetic iron oxide nanoparticles for magnetic resonance imaging of stem cells. *ACS Appl Mater Interfaces, 1*(2), 328-335. doi:10.1021/am8000538

Silva, A. C., Oliveira, T. R., Mamani, J. B., Malheiros, S. M., Malavolta, L., Pavon, L. F., . . . Gamarra, L. F. (2011). Application of hyperthermia induced by superparamagnetic iron oxide nanoparticles in glioma treatment. *Int J Nanomedicine, 6*, 591-603. doi:10.2147/ijn.s14737

Silva, L. H. A., Cruz, F. F., Morales, M. M., Weiss, D. J., & Rocco, P. R. M. (2017). Magnetic targeting as a strategy to enhance therapeutic effects of mesenchymal stromal cells. *Stem Cell Research & Therapy, 8*, 58. doi:10.1186/s13287-017-0523-4

Simmons, S. L., Bazylinski, D. A., & Edwards, K. J. (2006). South-seeking magnetotactic bacteria in the Northern Hemisphere. *Science, 311*(5759), 371-374. doi:10.1126/science.1122843

Siponen, M. I., Adryanczyk, G., Ginet, N., Arnoux, P., & Pignol, D. (2012). Magnetochrome: a c-type cytochrome domain specific to magnetotatic bacteria. *Biochem Soc Trans, 40*(6), 1319-1323. doi:10.1042/bst20120104

Siponen, M. I., Legrand, P., Widdrat, M., Jones, S. R., Zhang, W. J., Chang, M. C., . . . Pignol, D. (2013). Structural insight into magnetochrome-mediated

magnetite biomineralization. *Nature, 502*(7473), 681-684. doi:10.1038/nature12573

Song, C. W., Choi, I. B., Nah, B. S., Sahu, S. K., & Osborn, J. L. (1995). Microvasculature and Perfusion in Normal Tissues and Tumors. In M. H. Seegenschmiedt, P. Fessenden, & C. C. Vernon (Eds.), *Thermoradiotherapy and Thermochemotherapy: Biology, Physiology, Physics* (pp. 139-156). Berlin, Heidelberg: Springer Berlin Heidelberg.

Sotiropoulou, P. A., Perez, S. A., Gritzapis, A. D., Baxevanis, C. N., & Papamichail, M. (2006). Interactions between human mesenchymal stem cells and natural killer cells. *Stem Cells, 24*(1), 74-85. doi:10.1634/stemcells.2004-0359

Spring, S., Amann, R., Ludwig, W., Schleifer, K.-H., van Gemerden, H., & Petersen, N. (1993). Dominating Role of an Unusual Magnetotactic Bacterium in the Microaerobic Zone of a Freshwater Sediment. *Appl Environ Microbiol, 59*(8), 2397-2403.

Stagg, J., Lejeune, L., Paquin, A., & Galipeau, J. (2004). Marrow stromal cells for interleukin-2 delivery in cancer immunotherapy. *Hum Gene Ther, 15*(6), 597-608. doi:10.1089/104303404323142042

Staniland, Sarah S., & Rawlings, Andrea E. (2016). Crystallizing the function of the magnetosome membrane mineralization protein Mms6. *Biochemical Society Transactions, 44*(3), 883-890. doi:10.1042/BST20160057

Steingen, C., Brenig, F., Baumgartner, L., Schmidt, J., Schmidt, A., & Bloch, W. (2008). Characterization of key mechanisms in transmigration and invasion of mesenchymal stem cells. *J Mol Cell Cardiol, 44*(6), 1072-1084. doi:10.1016/j.yjmcc.2008.03.010

Stevenson, M. A., Minton, K. W., & Hahn, G. M. (1981). Survival and Concanavalin-A-Induced Capping in CHO Fibroblasts after Exposure to Hyperthermia, Ethanol, and X Irradiation. *Radiat Res, 86*(3), 467-478. doi:10.2307/3575463

Stoff-Khalili, M. A., Rivera, A. A., Mathis, J. M., Banerjee, N. S., Moon, A. S., Hess, A., . . . Curiel, D. T. (2007). Mesenchymal stem cells as a vehicle for targeted delivery of CRAds to lung metastases of breast carcinoma. *Breast Cancer Res Treat, 105*. doi:10.1007/s10549-006-9449-8

Studeny, M., Marini, F. C., Champlin, R. E., Zompetta, C., Fidler, I. J., & Andreeff, M. (2002). Bone marrow-derived mesenchymal stem cells as vehicles for interferon-beta delivery into tumors. *Cancer Res, 62*.

Studeny, M., Marini, F. C., Dembinski, J. L., Zompetta, C., Cabreira-Hansen, M., Bekele, B. N., . . . Andreeff, M. (2004a). Mesenchymal stem cells: potential precursors for tumor stroma and targeted-delivery vehicles for anticancer agents. *J Natl Cancer Inst, 96*. doi:10.1093/jnci/djh299

Studeny, M., Marini, F. C., Dembinski, J. L., Zompetta, C., Cabreira-Hansen, M., Bekele, B. N., . . . Andreeff, M. (2004b). Mesenchymal stem cells: potential precursors for tumor stroma and targeted-delivery vehicles for anticancer agents. *J Natl Cancer Inst, 96*(21), 1593-1603. doi:10.1093/jnci/djh299

Sun, J. B., Wang, Z. L., Duan, J. H., Ren, J., Yang, X. D., Dai, S. L., & Li, Y. (2009). Targeted distribution of bacterial magnetosomes isolated from Magnetospirillum gryphiswaldense MSR-1 in healthy Sprague-Dawley rats. *J Nanosci Nanotechnol, 9*(3), 1881-1885.

Suriyanto, Ng, E. Y., & Kumar, S. D. (2017). Physical mechanism and modeling of heat generation and transfer in magnetic fluid hyperthermia through Neelian and Brownian relaxation: a review. *Biomed Eng Online, 16*(1), 36. doi:10.1186/s12938-017-0327-x

Suto, R., & Srivastava, P. K. (1995). A mechanism for the specific immunogenicity of heat shock protein-chaperoned peptides. *Science, 269*(5230), 1585-1588.

Swedenborg, J., Mayranpaa, M. I., & Kovanen, P. T. (2011). Mast cells: important players in the orchestrated pathogenesis of abdominal aortic aneurysms. *Arterioscler Thromb Vasc Biol, 31*(4), 734-740. doi:10.1161/atvbaha.110.213157

Tamura, Y., Peng, P., Liu, K., Daou, M., & Srivastava, P. K. (1997). Immunotherapy of tumors with autologous tumor-derived heat shock protein preparations. *Science, 278*(5335), 117-120.

Tanaka, M., Arakaki, A., & Matsunaga, T. (2010). Identification and functional characterization of liposome tubulation protein from magnetotactic bacteria. *Mol Microbiol, 76*(2), 480-488. doi:10.1111/j.1365-2958.2010.07117.x

Tanaka, M., Mazuyama, E., Arakaki, A., & Matsunaga, T. (2011). MMS6 protein regulates crystal morphology during nano-sized magnetite biomineralization in vivo. *J Biol Chem, 286*(8), 6386-6392. doi:10.1074/jbc.M110.183434

Tang, C., Russell, P. J., Martiniello-Wilks, R., Rasko, J. E., & Khatri, A. (2010). Concise review: Nanoparticles and cellular carriers-allies in cancer imaging and cellular gene therapy? *Stem Cells, 28*(9), 1686-1702. doi:10.1002/stem.473

Tang, T., Zhang, L., Gao, R., Dai, Y., Meng, F., & Li, Y. (2012). Fluorescence imaging and targeted distribution of bacterial magnetic particles in nude mice. *Appl Microbiol Biotechnol, 94*(2), 495-503. doi:10.1007/s00253-012-3981-8

Taoka, A., Eguchi, Y., Mise, S., Oestreicher, Z., Uno, F., & Fukumori, Y. (2014). A magnetosome-associated cytochrome MamP is critical for magnetite crystal growth during the exponential growth phase. *FEMS Microbiol Lett, 358*(1), 21-29. doi:10.1111/1574-6968.12541

Timko, M., Dzarova, A., Kovac, J., Skumiel, A., Józefczak, A., Hornowski, T., . . . Tomasovicova, N. (2009). Magnetic properties and heating effect in bacterial magnetic nanoparticles. *Journal of Magnetism and Magnetic Materials, 321*(10), 1521-1524. doi:10.1016/j.jmmm.2009.02.077

Tocheva, E. I., Li, Z., & Jensen, G. J. (2010). Electron cryotomography. *Cold Spring Harb Perspect Biol, 2*(6), a003442. doi:10.1101/cshperspect.a003442

Toraya-Brown, S., & Fiering, S. (2014). Local tumour hyperthermia as immunotherapy for metastatic cancer. *International Journal of Hyperthermia, 30*(8), 531-539. doi:10.3109/02656736.2014.968640

Tran, S. E., Meinander, A., Holmstrom, T. H., Rivero-Muller, A., Heiskanen, K. M., Linnau, E. K., . . . Eriksson, J. E. (2003). Heat stress downregulates FLIP and sensitizes cells to Fas receptor-mediated apoptosis. *Cell Death Differ, 10*(10), 1137-1147. doi:10.1038/sj.cdd.4401278

Tu, S., McStay, G. P., Boucher, L. M., Mak, T., Beere, H. M., & Green, D. R. (2006). In situ trapping of activated initiator caspases reveals a role for caspase-2 in heat shock-induced apoptosis. *Nat Cell Biol, 8*(1), 72-77. doi:10.1038/ncb1340

Uchibori, R., Okada, T., Ito, T., Urabe, M., Mizukami, H., Kume, A., & Ozawa, K. (2009). Retroviral vector-producing mesenchymal stem cells for targeted suicide cancer gene therapy. *J Gene Med, 11*(5), 373-381. doi:10.1002/jgm.1313

Uebe, R., Junge, K., Henn, V., Poxleitner, G., Katzmann, E., Plitzko, J. M., . . . Schuler, D. (2011). The cation diffusion facilitator proteins MamB and MamM of Magnetospirillum gryphiswaldense have distinct and complex functions, and are involved in magnetite biomineralization and magnetosome membrane assembly. *Mol Microbiol, 82*(4), 818-835. doi:10.1111/j.1365-2958.2011.07863.x

Uebe, R., & Schuler, D. (2016). Magnetosome biogenesis in magnetotactic bacteria. *Nat Rev Microbiol, 14*(10), 621-637. doi:10.1038/nrmicro.2016.99

Ullrich, S., Kube, M., Schubbe, S., Reinhardt, R., & Schuler, D. (2005). A hypervariable 130-kilobase genomic region of Magnetospirillum gryphiswaldense comprises a magnetosome island which undergoes frequent rearrangements during stationary growth. *J Bacteriol, 187*(21), 7176-7184. doi:10.1128/jb.187.21.7176-7184.2005

Urtizberea, A., Natividad, E., Arizaga, A., Castro, M., & Mediano, A. (2010). Specific Absorption Rates and Magnetic Properties of Ferrofluids with Interaction Effects at Low Concentrations. *The Journal of Physical Chemistry C, 114*(11), 4916-4922. doi:10.1021/jp912076f

Valverde-Tercedor, C., Montalban-Lopez, M., Perez-Gonzalez, T., Sanchez-Quesada, M. S., Prozorov, T., Pineda-Molina, E., . . . Jimenez-Lopez, C. (2015). Size control of in vitro synthesized magnetite crystals by the MamC protein of Magnetococcus marinus strain MC-1. *Appl Microbiol Biotechnol, 99*(12), 5109-5121. doi:10.1007/s00253-014-6326-y

van Bree, C., van der Maat, B., Ceha, H. M., Franken, N. A., Haveman, J., & Bakker, P. J. (1999). Inactivation of p53 and of pRb protects human colorectal carcinoma cells against hyperthermia-induced cytotoxicity and apoptosis. *J Cancer Res Clin Oncol, 125*(10), 549-555.

van Loo, G., Saelens, X., van Gurp, M., MacFarlane, M., Martin, S. J., & Vandenabeele, P. (2002). The role of mitochondrial factors in apoptosis: a Russian roulette with more than one bullet. *Cell Death Differ, 9*(10), 1031-1042. doi:10.1038/sj.cdd.4401088

Vaupel, P. W., & Kelleher, D. K. (1995). Metabolic Status and Reaction to Heat of Normal and Tumor Tissue. In M. H. Seegenschmiedt, P. Fessenden, & C. C. Vernon (Eds.), *Thermoradiotherapy and Thermochemotherapy: Biology, Physiology, Physics* (pp. 157-176). Berlin, Heidelberg: Springer Berlin Heidelberg.

Velichko, A. K., Petrova, N. V., Kantidze, O. L., & Razin, S. V. (2012). Dual effect of heat shock on DNA replication and genome integrity. *Mol Biol Cell, 23*(17), 3450-3460. doi:10.1091/mbc.E11-12-1009

Villanueva, A., de la Presa, P., Alonso, J. M., Rueda, T., Martínez, A., Crespo, P., . . . Rivero, G. (2010). Hyperthermia HeLa Cell Treatment with Silica-Coated Manganese Oxide Nanoparticles. *The Journal of Physical Chemistry C, 114*(5), 1976-1981. doi:10.1021/jp907046f

Wang, L., Dong, J., Ouyang, W., Wang, X., & Tang, J. (2012). Anticancer effect and feasibility study of hyperthermia treatment of pancreatic cancer using

magnetic nanoparticles. *Oncol Rep, 27*(3), 719-726. doi:10.3892/or.2011.1567

Wang, L., Pan, J., Wang, T., Song, M., & Chen, W. (2013). Pathological Cyclic Strain-Induced Apoptosis in Human Periodontal Ligament Cells through the RhoGDIα/Caspase-3/PARP Pathway. *PLoS ONE, 8*(10), e75973. doi:10.1371/journal.pone.0075973

Wang, L., Prozorov, T., Palo, P. E., Liu, X., Vaknin, D., Prozorov, R., . . . Nilsen-Hamilton, M. (2012). Self-assembly and biphasic iron-binding characteristics of Mms6, a bacterial protein that promotes the formation of superparamagnetic magnetite nanoparticles of uniform size and shape. *Biomacromolecules, 13*(1), 98-105. doi:10.1021/bm201278u

Wang, N., Fallavollita, L., Nguyen, L., Burnier, J., Rafei, M., Galipeau, J., . . . Brodt, P. (2009). Autologous Bone Marrow Stromal Cells Genetically Engineered to Secrete an IGF-I Receptor Decoy Prevent the Growth of Liver Metastases. *Molecular Therapy, 17*(7), 1241-1249. doi:http://doi.org/10.1038/mt.2009.82

White, E. E., Pai, A., Weng, Y., Suresh, A. K., Van Haute, D., Pailevanian, T., . . . Berlin, J. M. (2015). Functionalized iron oxide nanoparticles for controlling the movement of immune cells. *Nanoscale, 7*(17), 7780-7789. doi:10.1039/c3nr04421a

Wiehe, J. M., Kaya, Z., Homann, J. M., Wohrle, J., Vogt, K., Nguyen, T., . . . Zimmermann, O. (2013). GMP-adapted overexpression of CXCR4 in human mesenchymal stem cells for cardiac repair. *Int J Cardiol, 167*(5), 2073-2081. doi:10.1016/j.ijcard.2012.05.065

Won, Y. W., Patel, A. N., & Bull, D. A. (2014). Cell surface engineering to enhance mesenchymal stem cell migration toward an SDF-1 gradient. *Biomaterials, 35*(21), 5627-5635. doi:10.1016/j.biomaterials.2014.03.070

Wydra, R. J., Oliver, C. E., Anderson, K. W., Dziubla, T. D., & Hilt, J. Z. (2015). Accelerated generation of free radicals by iron oxide nanoparticles in the presence of an alternating magnetic field. *RSC advances, 5*(24), 18888-18893. doi:10.1039/C4RA13564D

Xiao, Q., Ye, S., Oberhollenzer, F., Mayr, A., Jahangiri, M., Willeit, J., . . . Xu, Q. (2009). SDF1 Gene Variation Is Associated with Circulating SDF1α Level and Endothelial Progenitor Cell Number–The Bruneck Study. *PLoS One, 3*(12), e4061. doi:10.1371/journal.pone.0004061

Xin, H., Kanehira, M., Mizuguchi, H., Hayakawa, T., Kikuchi, T., Nukiwa, T., & Saijo, Y. (2007). Targeted delivery of CX3CL1 to multiple lung tumors by mesenchymal stem cells. *Stem Cells, 25*. doi:10.1634/stemcells.2006-0461

Xin, H., Sun, R., Kanehira, M., Takahata, T., Itoh, J., Mizuguchi, H., & Saijo, Y. (2009). Intratracheal delivery of CX3CL1-expressing mesenchymal stem cells to multiple lung tumors. *Mol Med, 15*(9-10), 321-327. doi:10.2119/molmed.2009.00059

Yamamoto, D., Taoka, A., Uchihashi, T., Sasaki, H., Watanabe, H., Ando, T., & Fukumori, Y. (2010). Visualization and structural analysis of the bacterial magnetic organelle magnetosome using atomic force microscopy. *Proc Natl Acad Sci U S A, 107*(20), 9382-9387. doi:10.1073/pnas.1001870107

Yan, S. Y., Chen, M. M., Fan, J. G., Wang, Y. Q., Du, Y. Q., Hu, Y., & Xu, L. M. (2014). Therapeutic mechanism of treating SMMC-7721 liver cancer cells with magnetic fluid hyperthermia using Fe(2)O(3) nanoparticles. *Brazilian*

Journal of Medical and Biological Research, 47(11), 947-959. doi:10.1590/1414-431X20143808

Yang, J., Li, S., Huang, X., Li, J., Li, L., Pan, Y., & Li, Y. (2013). MamX encoded by the mamXY operon is involved in control of magnetosome maturation in Magnetospirillum gryphiswaldense MSR-1. *BMC Microbiol, 13*, 203. doi:10.1186/1471-2180-13-203

Yang, R., Tang, Q., Miao, F., An, Y., Li, M., Han, Y., . . . Chen, R. (2015). Inhibition of heat-shock protein 90 sensitizes liver cancer stem-like cells to magnetic hyperthermia and enhances anti-tumor effect on hepatocellular carcinoma-burdened nude mice. *Int J Nanomedicine, 10*, 7345-7358. doi:10.2147/ijn.s93758

Yang, W., Li, R., Peng, T., Zhang, Y., Jiang, W., Li, Y., & Li, J. (2010). mamO and mamE genes are essential for magnetosome crystal biomineralization in Magnetospirillum gryphiswaldense MSR-1. *Res Microbiol, 161*(8), 701-705. doi:10.1016/j.resmic.2010.07.002

Yoo, J., & Lee, Y. J. (2007). Effect of hyperthermia on TRAIL-induced apoptotic death in human colon cancer cells: development of a novel strategy for regional therapy. *J Cell Biochem, 101*(3), 619-630. doi:10.1002/jcb.21203

Zeytuni, N., Ozyamak, E., Ben-Harush, K., Davidov, G., Levin, M., Gat, Y., . . . Zarivach, R. (2011). Self-recognition mechanism of MamA, a magnetosome-associated TPR-containing protein, promotes complex assembly. *Proc Natl Acad Sci U S A, 108*(33), E480-487. doi:10.1073/pnas.1103367108

Zhang, H., Liu, X., Feng, S., Wang, W., Schmidt-Rohr, K., Akinc, M., . . . Mallapragada, S. (2015). Morphological transformations in the magnetite biomineralizing protein Mms6 in iron solutions: a small-angle X-ray scattering study. *Langmuir, 31*(9), 2818-2825. doi:10.1021/la5044377

Zhang, J., Dewilde, A. H., Chinn, P., Foreman, A., Barry, S., Kanne, D., & Braunhut, S. J. (2011). Herceptin-directed nanoparticles activated by an alternating magnetic field selectively kill HER-2 positive human breast cells in vitro via hyperthermia. *Int J Hyperthermia, 27*(7), 682-697. doi:10.3109/02656736.2011.609863

Zischek, C., Niess, H., Ischenko, I., Conrad, C., Huss, R., Jauch, K. W., . . . Bruns, C. (2009). Targeting tumor stroma using engineered mesenchymal stem cells reduces the growth of pancreatic carcinoma. *Ann Surg, 250*(5), 747-753. doi:10.1097/SLA.0b013e3181bd62d0

Zurkiya, O., Chan, A. W. S., & Hu, X. (2008). MagA Is Sufficient for Producing Magnetic Nanoparticles in Mammalian Cells, Making it an MRI Reporter. *Magnetic resonance in medicine : official journal of the Society of Magnetic Resonance in Medicine / Society of Magnetic Resonance in Medicine, 59*(6), 1225-1231. doi:10.1002/mrm.21606

Information retrieved from websites:

Ampere's Law: Definition & Examples. (2017, June). Retrieved from *http://study.com/academy/lesson/amperes-law-definition-examples.html*